NONLINEAR OPTICAL TECHNIQUES FOR IMAGING AND MANIPULATING THE MOUSE CENTRAL NERVOUS SYSTEM

A Dissertation

Presented to the Faculty of the Graduate School

of Cornell University

in Partial Fulfillment of the Requirements for the Degree of

Doctor of Philosophy

by

Matthew John Farrar

August 2012

NONLINEAR OPTICAL TECHNIQUES FOR IMAGING AND MANIPULATING THE MOUSE CENTRAL NERVOUS SYSTEM

Matthew John Farrar, Ph.D.

Cornell University 2012

The spinal cord of vertebrates serves as the conduit for somatosensory information and motor control, as well as being the locus of neural circuits that govern fast reflexes and patterned behaviors, such as walking in mammals or swimming in fish. Consequently, pathologies of the spinal cord –such as spinal cord injury (SCI)– lead to loss of motor control and sensory perception, with accompanying decline in life expectancy and quality of life. Despite the devastating effects of these diseases, few therapies exist to substantially ameliorate patient outcome.

In part, studies of spinal cord pathology have been limited by the inability to perform *in vivo* imaging at the level of cellular processes. The focus of this thesis is to present the underlying theory for and demonstration of novel multi-photon microscopy (MPM) and optical manipulation techniques as they apply to studies the mouse central nervous system (CNS), with an emphasis on the spinal cord. The scientific findings which have resulted from the implementation of these techniques are also presented.

In particular, we have demonstrated that third harmonic generation is a dye-free method of imaging CNS myelin, a fundamental constituent of the spinal cord that is difficult to label using exogenous dyes and/or transgenic constructs. Since gaining optical access to the spinal cord is a prerequisite for spinal cord imaging, we review our development of a novel spinal cord imaging chamber

and surgical procedure which allowed us to image for multiple weeks following implantation without the need for repeated surgeries. We also have used MPM to characterize spinal venous blood flow before and after point occlusions. We review a novel nonlinear microscopy technique that may serve to show optical interfaces in three dimensions inside scattering tissue. Finally, we discuss a model and show results of optoporation, a means of transfecting cells with genetic constructs. Brief reviews of MPM and SCI are also presented.

BIOGRAPHICAL SKETCH

Matthew John Farrar was born in Hamilton, Ontario, Canada on December 23, 1985 to William Henry and Judith Eileen, and is the younger brother of Nathan Robert. He graduated from Hill Park Secondary School in 2003 and was awarded the Governor General's Bronze Medal, awarded to the student in highest academic standing within the graduating class. He attended McMaster University in Hamilton, Ontario, Canada, initially entering the Engineering program. At the beginning of his second year, he transferred his major to Physics. During his tenure at McMaster, he worked in the research groups of Drs. Peter Mascher, Kari Dalnoki-Veress, and Duncan O'Dell. In 2007, he graduated summa cum laude with his Hons. BSc. in Physics, and was awarded the Governor General's Silver Medal, awarded to the top two students in the graduating class, university-wide. He came to Cornell University in August 2007, where he began his doctoral dissertation. Having successfully passed his admission to candidacy exam, he was awarded a MS in Physics in Fall of 2010. In August 2010, he met Emily Jean Howell in the Biomedical Engineering Department, and after a brief courtship, married her on December 17, 2011. After he graduates, his plans are to pursue postdoctoral research in the lab of Joseph Fetcho in the Department of Neurobiology and Behavior at Cornell University.

Soli Deo Gloria

ACKNOWLEDGEMENTS

This thesis is dedicated to the vast number of people who have made its accomplishment possible. While impossible to mention all of them, I will mention those who impact is most memorable.

First, I would like to recognize members of my family. The support from my parents has played a powerfully formative role in my life, and I owe them a debt of gratitude that can never be repaid. Their continued love and encouragement helped to bear me through the most difficult times in my studies, and I am truly grateful for their aid. I also thank my brother for challenging me to grow on multiple levels and encompassing all aspects of what the Irish Catholic Church once termed *anam cara*, a "soul friend". His scientific encouragement, personal friendship, and his guidance towards my belief in the historic Christian faith have resulted in life changes that have given rise to whatever modest virtues I may possess. My grandparents, Ted and Catharine Evans, have also played a supportive role, going well beyond the call of duty, including weekly conversations and words of encouragement in addition to their more than generous financial support over the years. Finally, though not in any way least, I am extremely grateful for the friendship, support, correction, and overflowing love from my wife, Emily. Her emotional warmth and intellectual depth have provided and continue to provide both a caring companion and a trustworthy sounding board. I love her dearly, and am grateful for the time with which we have been blessed to share together.

Second, I would like to recognize the faculty whose impact has shaped my research over the last several years. Upon my first coming to Cornell, I was fortunate to have the opportunity to carry out a lab rotation under the guidance of Drs. Itai Cohen and Larry Bonassar, where I was able to apply my training in

physics to tissue-level biology. I am grateful for the inspiration and training I received under their tutelage. My third and final rotation was under Dr. Chris Schaffer, under whose supervision the body of the work presented in this thesis was performed. Chris' depth of knowledge, patience, and mentoring style have made both for an extremely fulfilling and immensely enjoyable time in his group. In addition, I have had the pleasure of getting to know Chris outside the laboratory setting, and his joy for life, generosity, and amicability are qualities I seek to emulate in my life more generally. I am also grateful for the collaborations we have shared with Dr. Joseph Fetcho, in whose lab it is my intention to pursue postdoctoral studies. Joe has been a strong source of experimental direction, background knowledge, and professional instruction. It is my great privilege to be continuing under his guidance.

My gratitude also extends to the members of the Schaffer lab, past and present for their morale support, scientific dialogue, and personal friendships. In particular, Dr. Nozomi Nishimura has often been the one "holding up the pillars" of the lab, as it were. She has been a considerable intellectual support, an encourager, and a fantastic manager of both her own projects and the lab in general. I am also grateful for the friendship I have shared in particular with Dr. John Nguyen and Puifai Santisakultarm, who have done more than their fair share of listening to my griping, drawing me out, and encouraging my success. I have been fortunate to work with several talented undergraduate students, whose hard work has contributed to the results of this thesis. My thanks goes out to Ida Bernstein, Darcy Diago, Jonathan Rubin, and Gabrielle van Paten.

Finally, I thank the members of both my church, Bethel Grove Bible Church, and members of both the Cornell International Christian Fellowship and Graduate Christian Fellowship for their love, their encouragement, and their

community (*koinonia*) together over the last several years. In times of emotional and spiritual dryness they have often refreshed me, and have been my family to the extent that it is hard to miss home. The international fellowship has also served to remind me in no small way that the Church goes far beyond its local manifestation in one culture, but truly encompasses people of "every tribe, nation and tongue".

I would like to thank the National Science and Engineering Research Council of Canada (NSERC) for their continued support throughout my graduate career, awarding both funding in the forms of Postgraduate Scholarships at the Master's and Doctoral levels (PGS-M and PGS-D, respectively). It is truly an honour to represent Canada at Cornell, and I am grateful for their financial support. This work was also funded by the National Institutes of Health: Grant numbers RO1 EB002019 (Chris B. Schaffer) and DP1 OD006411(Joseph R. Fetcho).

TABLE OF CONTENTS

LIST OF FIGURES

CHAPTER 1

INTRODUCTION

The writing of a thesis is, by nature, the woeful attempt to compress several years of learning, experiments, insights, and frustrations into a small number of pages in such a way that one reasonably demonstrates all of the above in a meaningful way. Doubtless, much that could be said has been left out, and there are perhaps a few items that may have been included that have gotten lost in the shuffle. However, as a whole, this dissertation captures the essence of my work over the last 5 years.

My motivation for this thesis dates back to the summer after 6th grade. A classmate and friend of mine–I shall call her Brianne out of respect for her privacy–who was athletic, fit (a dancer, as I recall), and good looking had been swimming at her family's pool. As is wont for athletic youth, Brianne decided to dive backwards into the pool, which tragically was not deep enough sufficiently to slow her descent. We got word that summer that Brianne had suffered a severe spinal cord injury (SCI) in the cervical spine, resulting in tetraplegia. I cannot begin to tell you the profound impact that going to school with a paralyzed friend can have on a 7th grade boy. Six years later, I received word that a childhood friend and high school classmate had been tackled onto the ball playing rugby, resulting in a lumbar SCI and subsequent paraplegia. Both people have continued to face life with optimism, courage, and pride despite drastically changed lifestyles. Their persistence in the face of difficulty continues to inspire me.

Nevertheless, as a student fresh out of undergraduate physics, my desire to help was limited to distant hoping and prayer. After all, my undergraduate work had focused on di-block copolymer dewetting experiments and Bose-

Einstein interferometry theory, making any contribution to helping paralytics an unlikely outcome. It thus came as a great surprise to me when in the spring of 2008, Dr. Chris Schaffer approached me with an offer to join his lab and develop a project on spinal cord imaging with an immediate application to SCI. The project was a collaboration with Dr. Joseph Fetcho, who only a few short years earlier had effectively cured SCI in zebrafish larvae. The project would rely on my physics background to develop and interpret new imaging techniques, perform quantitative image analysis, and develop mathematical models of the observed phenomena, while simultaneously requiring me to enter headlong into the world of biological sciences, a field that I hadn't studied since 11^{th} grade.

This thesis summarizes the techniques developed, results observed, and insights obtained over the last 5 years. This thesis is comprised of 9 chapters, including this introduction. The first two chapters provide background material which provide context and serve as a reference for the rest of the thesis. Chapter 2 takes a look at the current state of SCI, including clinical outcome and pre-clinical animal studies, with a spotlight on *in vivo* imaging and what it offers SCI research. Chapter 3 examines multi-photon microscopy, discussing its value and significance to biology, basic experimental techniques and the achievement of optical sectioning, as well as a more detailed look at the individual processes of 2-photon excited fluorescence (2PEF), and second and third harmonic generation (SHG and THG, respectively). The chapter concludes with a discussion of optical damage mechanisms.

Chapters 4-7 are formatted as stand-alone papers, whether they are published as of yet or whether they contain work in progress, including supplementary files and information. Chapter 4 contains the re-formatted published manuscript of our work on THG imaging of myelin the mouse CNS.

Chapter 5 contains the re-formatted published manuscript of our paper on a novel spinal chamber that allowed for 2PEF imaging of the spinal cord for as long as 5 months.

Chapters 6-7 are works in progress, and thus will likely be out of date even at the time of final submission of this thesis. Chapter 6 includes unpublished work on blood flow and the microvascular network of the spinal cord, consisting both of theoretical modeling, blood flow measurements, and topographical mapping. Chapter 7 presents unpublished work on a novel imaging modality that is designed to map optical interfaces, which we have titled Nonlinear Optical Reflection Microscopy (NORM).

Chapter 8 contains the prepared manuscript of a project on optimizing laser parameters for targeted optoporation, a technique for transfecting exogenous DNA into cells. My contribution to this chapter was primarily through mathematical modeling, writing custom software to streamline analysis, and contributing to the intellectual material of the study, while Andrew Davis, a former undergraduate researcher in the lab, completed the experimental data taking. It is last in this thesis primarily because I am not the first author on this work and thus consider it a secondary contribution which stands somewhat apart from the rest.

Finally, in Chapter 9, we close the thesis with a brief summary of and reflection on what has been successfully completed in the results of this thesis, as well as offering some insights for future project directions for whomever picks this project up where I must inevitably leave off.

CHAPTER 2

SPINAL CORD INJURY: AN OVERVIEW

In this chapter, we review the current outlook on spinal cord injury (SCI) from a clinical and scientific perspective. This chapter is divided into three sections. In the first section, we review the current state of clinical SCI and its economic and quality of life impact on SCI victims. In the second section, we consider the key challenges to regeneration in the spinal cord identified through animal studies and the progress made to date towards overcoming these barriers in pre-clinical (animal) trials, the vast majority of which have used histological sectioning, behavioral, and/or *in vitro* analysis to arrive at their conclusions. Finally, we examine the growing role of *in vivo* optical microscopy in understanding disease mechanisms of SCI and evaluating the therapeutic efficacy of treatment strategies.

2.1 Clinical Perspective

2.1.1 Epidemiology and Impact

Paralysis affects nearly 6 million people in the United States alone, with SCI accounting for 23% of known incidents, with the mean age paralytics being 52 years of age [1]. Tragically, current estimates place the number of SCIs at over 12,000 annually with the mean age at time of injury being 37 years of age, although the late teens to early twenties age bracket exhibited the highest rate of injury [2]. According to the National Spinal Cord Injury Statistical Center (NSCISC), more that 40% of SCI cases occur due to motor vehicle accidents,

30% due to falls, and 15% due to violence, while sports-related injuries account only for less than 10% of SCIs [3]. Within the entirety of the four branches of US military, 5928 servicemembers of approximately 13 million at-risk were identified with SCI over a 10-year period (43 per-million-persons/year), with white males being the highest at-risk population [4]. In the overall population of North America, incidents of SCI occur in males at approximately a 4:1 ration compared to females [5,6], with Caucasians accounting for 66% of cases [5], with an estimated 43-51 per-million-persons/year [2, 3, 6]. Curiously, this incidence rate is less than 20 per-million-persons/year in Europe [6].

Considerable improvements have been realized in post-injury mortality, with a 40% decrease in the 2-year mortality rate between 1973 and 2004 [7]. In contrast to the 2-year mortality rate, little change has occurred in the life expectancy of SCI patients, which for a Grade A[1] high-level (C1-C3) cervical injury (tetraplegia; see Fig. 2.1) occurring in one's twenties is estimated at 25-37 years[2] compared to 50.9 years in the general population, while for injuries below the cervical level the life expectancy rises to $\sim$ 75% of the general population [3, 7]. These survival ratings included only patients who were non-ventilator dependent, while for ventilator-dependent victims the life expectancy drops to just under 24 years [3]. Incidence of complete (Grade A) SCI is estimated at over 50% of SCI cases [5, 6], with tetraplegia being the clinical outcome in more than 55% [5] in the general population, while within the US military, cervical injury was present in $\sim$ 38% of SCIs [4].

SCI costs the health care system an estimated $40.5 billion per year [1], with

[1]The American Spinal Cord Injury Association (ASIA) has systematized the classification of spinal cord injury [8], ranging from complete injury resulting in total sensorimotor loss (Grade A) through (Grade E), wherein sensory and motor control are preserved in totality despite injury.

[2]Measured as time post-injury. For for an injury at age 25, the age expected to be attained would be 50-62 years of age.

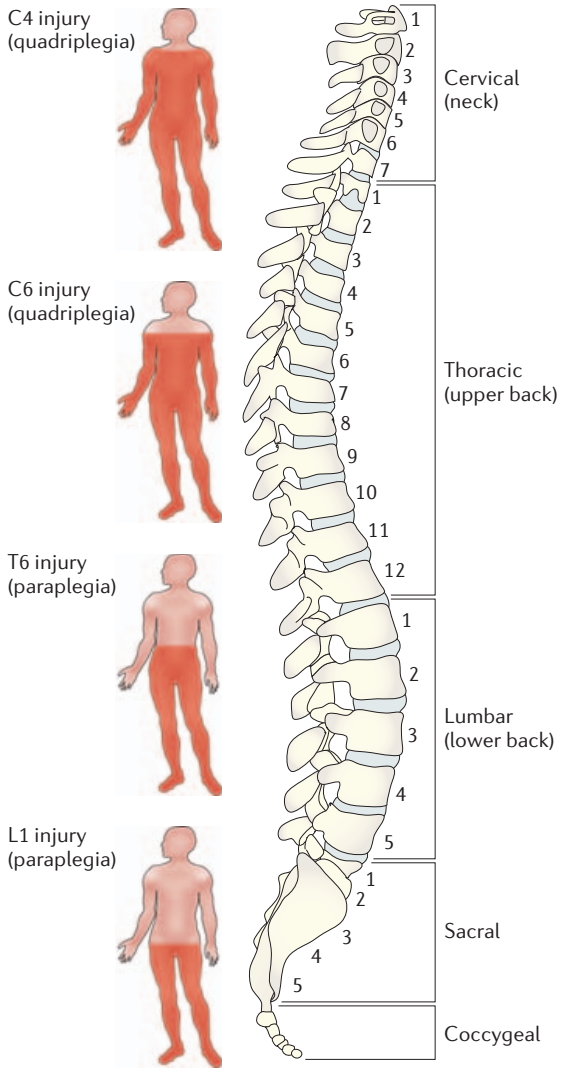

Figure 2.1: Functional impairment correlates with level of spinal cord injury. The spinal cord is divided up into 7 cervical (C), 12 thoracic (T), 5 lumbar (L), and 5 sacral (S) vertebrae, terminated at the coccyx. Cervical injury correlate with quadriplegia while thoracic and lumbar injuries correlate with paraplegia. The spinal cord ends at the L1-L2 level in humans [9]. Reprinted by permission from Macmillan Publishers Ltd: *Nature Reviews Neuroscience*,Thuret, S., Moon, L.D.F. and Gage, F.H., Therapeutic interventions after spinal cord injury, **7**, 628-643, Copyright 2006. [10]

estimated lifetime costs ranging from $\sim$ \$1.4-4.4 million, with approximately 20% of costs occurring in the first year following injury [3]. In addition to the direct cost of health care, SCI also results in a broader economic impact on the victim. A recent survey in Taiwain [11] showed that less than one third of previously employed SCI patients had returned to work in a 3-year follow up study, with only 68% of those returning to the same position. However, a considerable range of employment statistics have been reported, with as low as 11% and as high as 75% returning to work (reviewed in [12]). Differential employment rates were seen when compared across age of injury, extent of injury, time after injury, and educational background, with favorable outcomes in each of these comparison groups for younger age, lesser extent of injury, longer time following injury, and greater education. Other key factors in employment were the availability of transportation, physical limitations, architectural difficulties, and recurring health problems [11–13].

In addition to the paralysis, SCI victims face a plethora of related co-morbidities. For example, in a study [14] of 408 patients, over 65% of SCI patients were overweight, with approximately 30% being considered obese. Counterintuitively, Grade A injuries showed the lowest obesity at 22.91%, while Grade C had the highest obesity (38.3%) and Grade D had the highest overweight population (74.14%). In turn, being overweight was correlated with an increased incidence of overuse injuries in the upper limbs, increased fatigue, and a decline in subjective well-being [15].

Urinary complications have been significantly mitigated by the use of clean intermittent cauterization (CIC)–the insertion of a temporary cannula to drain the bladder–over and against traditional methods of indwelling and condom catheters [16]. Nevertheless, complications are reported to occur at a rate of

71% for patients using CIC, compared to 100% in patients using indwelling catheters [17]. CIC must also be performed as many as 6-7 times per day [17].

Autonomic dysreflexia (AD) results from the loss of supra spinal control of autonomic reflexes [18–20], resulting in periodic bouts of severe hypertension, headache, bradycardia, and possible complications including stroke, seizures, and death [21]. AD presents in 91% of tetraplegic patients with Grade A SCI, while being absent in paraplegic patients [18]. AD has been seen to occur only in injuries above T6 [22]. Unfortunately, there is evidence to suggest that the same mechanisms that give rise to neuroplasticity–and thus functional recovery– may also be at the root cause of AD [21]. Finally, other complications include chronic pain [21, 23, 24], pressure ulcers [25], respiratory complications [25–28] including pneumonia in as many as 50% of patients within the first 30 days post-SCI [29] , and a significantly increased incidence of suicide [26, 30, 31].

2.1.2 Current Therapies

Despite its devastating effects, no efficacious regenerative therapies exist [32, 33]. Broadly speaking, most approaches seek to minimize the extent of direct damage and/or mitigate secondary injury effects (e.g. ischemic and/or inflammatory insult) [33–35]. Despite numerous trials [35], the only approved drug therapy is the administration of methylprednisolone [35]–an anti-inflammatory steroid–within 8 hours following injury, despite contraindications [36] and recommendations against the practice [36–38]. No conclusive evidence exists for pharmacological neuroprotective therapies in clinical trials [33]. Inhibition of the Rho pathway by the drug Cethrin has recently shown promise in Phase I/IIa clinical trials, with as many as

66% of Grade A cervical injuries being downgraded to Grade C or D [39]. Cellular transplantation therapies (reviewed in [33] and [40]) hold promise in Phase I studies, but definitive improvement remains unclear [40, 41]. Recent evidence [42, 43] also suggests that early (<72 hours following injury) decompressive spinal stabilization surgery correlates strongly with improved clinical outcome. Various exercise regimes–both assisted and independent–appear to have profound effects, both in improving functional recovery and mitigating secondary complications (for a review, see [44]).

2.2 Key Challenges in SCI Therapy

In spite of the gloomy outlook of current clinical practice and outcome, considerable and promising advances have been made in animal models, both in understanding disease mechanisms as well as explorations of possible therapeutic interventions. The loss of function in SCI owes to disruption and loss of axonal pathways to and from the brain, in some ways analogous to destroying an electronic circuit by severing the wires that connect the various components. While there is, of course, spinal neuron loss, demyelination, and vascular insult, axon loss lies at the heart of this devastating pathology, and will form the focus of our review. As such, there are two parallel approaches to treating axonal loss in SCI: axonal regeneration and/or tissue sparing. In this section, we shall focus only on the former, since neuroprotective mechanisms are preventative rather than restorative in nature and do not mitigate the primary damage (i.e. trauma)[3].

[3]They also range over quite a spectrum of differing effects, from an anti-oxidant raspberry extract [45] to Omega-3 fatty acids [46].

Compared to axons in the peripheral nervous system(PNS), which undergo robust regeneration following nerve damage, axons in the CNS have greatly reduced regenerative potential. One key difference is the local microenvironment of the CNS. We begin our review of this microenvironment with CNS myelin, a fatty lipid sheath produced by the wrapping of oligodendrocytes around long axons, thereby enabling fast action potential transmission via saltatory conduction [47]. Myelin is also produced in the PNS, but the cell type giving rise to it is the Schwann cell, which has salient differences from CNS myelin. While essential for function, CNS myelin also acts as a growth-inhibitor, and we will review both the problem and some proposed solutions.

Furthermore, the CNS is composed of both neurons and glia, the latter of which play a multi-functional role in the CNS. Once again, there is a physiological role of these cell types, but their recruitment to the lesion site to form an aggregate or "scar" has shown to be simultaneously beneficial to tissue sparing and detrimental to axonal regeneration. We will touch on both aspects and attempts to mitigate the inhibitory effects of the scar.

Along with external factors in the microenvironment, there are fundamental differences between the developing CNS in which growth is essential and the adult CNS in which growth and plasticity are more limited. The intrinsic state of neurons appears to be governed, in part, by developmental "switches" that are responsible for developmental growth but turned off in the adult CNS. Thus, reactivation of these pathways promises to be of benefit to regeneration in the injured CNS, and we will review some important studies which have demonstrated the efficacy of this strategy. However, we will also discuss some caveats of this approach, including organizational differences between the adult

and developing CNS which affect axonal guidance cues and the establishment of useful synaptic connections.

Finally, in the vast majority of the above approaches, studies were performed using plated cells *in vitro*, or by using fixed-time-point histology and behavioral analysis in animal models. While much can and has been learned by these approaches, each has its associated drawbacks. Although *in vitro* studies allow for high reproducibility and straightforward analysis, they lack the necessary context to account for the complicated milieu of the injured CNS. Histology, on the other hand, while showing multiple tissue constituents, leaves a great deal of ambiguity in determining regenerative and degenerative dynamics, since only a single time point can be captured per animal. Behavioral assays allow for multi-time-point longitudinal studies, but offer little in the way of elucidating mechanisms and are complicated by spontaneous recovery that occurs independent of modulation in the target pathway. In contrast to these assays, a number of time-lapsed *in vivo* imaging studies have been performed which circumvent these drawbacks by allowing for repeated imaging of cellular dynamics, enabling direct and unambiguous visualization of disease progress and therapeutic efficacy. We will highlight several recent studies using this approach and offer some concluding thoughts for the value of this approach for future pre-clinical studies.

2.2.1 Growth Inhibition by CNS Myelin

The developing nervous system, by necessity, must be growth permissive. However, following early stages of development, large-scale-neurotrophin-modulated apoptosis [48] and synaptic pruning [49] result in significant loss

of redundant or ineffective neurons and their processes. Some of these developmental processes may share common mechanisms with disease (for a review, see [49]). Somewhere in this complex milieu of neuron proliferation, pruning, and maturation of the CNS, this growth permissiveness to large neurite outgrowth is lost. The adult CNS retains plasticity by the rescaling of synaptic strengths [50, 51], and even learning-associated synapse formation [52–55]. However, this growth is localized [53] and does not lead to the same extent of neurite outgrowth necessary for post-injury regeneration or *de novo* circuit formation.

One component that has received considerable attention in creating the semi-static CNS is CNS myelin, in which Nogo, myelin-associated glycoprotein (MAG), and oligodendrocyte myelin glycoprotein (OMgp) have been identified as growth-inhibitory substrates (for a recent review see [56]). For example, Li et al. [57] showed that the growth cone of plated neurons collapsed upon coming into contact with a MAG coated bead. All three elements share common receptors [56, 58], namely Nogo Receptor (NgR) and paired immunoglobulin-like receptor B (PIR-B), which led to the hypothesis that NgR/PIR-B antagonists would promote axon growth. Conflicting results have been found [56], especially between the Strittmatter group [59, 60], which showed robust regeneration after antagonization of the NgR1 receptor using the peptide NEP1-40, and a subsequent study by Nakamura et al. [61] which showed that dual NgR/PIR-B knockout mice and NEP1-40 administration in PIR-B mice failed to induce a robust regenerative response. To complicate matters further, there is a growing body of evidence that suggests some of these and other molecules play important physiological functions in preventing aberrant sprouting in the adult CNS, as well as providing both attractive and

repulsive guidance cues [62].

However, some research would suggest that the growth-inhibitory role of myelin is overstated. The research group of Marie Filbin has been particularly diligent in exploring how the intrinsic state of the neuron may be significant for how these growth-inhibitory molecules have their effect (for a review of myelin inhibition and therapeutic approaches, see [63]). Chai et al. [64] showed that cerebellar neurons co-cultured in the presence of neurotrophins (brain-derived neurotrophic factor (BDNF) or glial-derived neurotrophic factor (GDNF)) and plated on a monolayer of MAG-expressing Chinese Hamster Ovary (CHO) cells or isolated myelin are able to overcome the growth-inhibitory effects of these substrates. Moreover, they demonstrated that this priming with neurotrophins resulted in an increase of intracellular cyclic adenosine monophosphate (cAMP), and that treatment with membrane-permeable cAMP directly–that is, without neurotrophin incubation–was sufficient to generate the same ability to overcome myelin-associated growth inhibition. Downstream inhibition of the protein kinase A (PKA) pathway–one of the primary targets of cAMP–destroyed the effect of both neurotophin and cAMP treatments, further suggesting that an elevated intracellular cAMP level is the driving factor in overcoming inhibition. In subsequent studies [65], they found that immature neurons capable of sustained growth had increased levels of intracellular cAMP, and that MAG and myelin are actually growth promoting under these circumstances. Again, subsequent inhibition of PKA resulted in growth inhibition and artificial cAMP elevation resulted in growth promotion. Subsequent *in vivo* studies [66, 67] in the rat spinal cord have confirmed the efficacy of this treatment strategy, although this therapy has not constituted a "magic bullet" cure. Similar results have been seen by Neumann et al. [68]. The exception to these findings of

incomplete efficacy is a study by Bhatt et al. [69] in zebrafish larvae, involving treatment of the Mauthner cell soma following axotomy with cAMP. In this case, complete axon regeneration with a normal trajectory after treatment with cAMP was visualized *in vivo* following injury. Recovery of synaptic connectivity was determined by performing calcium imaging of spinal interneurons activated by Mauthner cell axon, with loss of downstream interneuron activation after injury and return of activation after complete axon regeneration was observed. Subsequent behavioral testing confirmed functional restoration. This approach to SCI, which shall be reviewed later in this chapter has much to offer. However, the inability to reproduce these results in mammals may depend on a number of factors, including differences between species and the fact that zebrafish larvae–in contrast to adult zebrafish– may still possess certain directional and developmental cues that are subsequently abrogated in adults. Nevertheless, inducing changes to the intrinsic neuronal phenotype remains a promising therapeutic target. Rho kinase inhibition has also been seen [70, 71] to have similar effects with respect to myelin-associated inhibition, and has entered clinical trials as noted above.

2.2.2 The Glial Scar

Following spinal cord injury, microglia and reactive astrocytes invade the lesion site, forming the so-called "glial scar", the latter of which was discovered [72,73] to secrete growth-inhibitory chondroitin sulfate proteoglycans (CSPGs). CSPGs play many important physiological roles, including the establishment of perineuronal nets (PNN) which stabilize synapses and limit neuronal plasticity in the mature CNS (see Fig. 2.2), but simultaneously restrict regeneration

following SCI (for a detailed review, see [74]). The efficacy of CSPGs digestion by the bacterial enzyme chondroitinase ABC (chABC) was demonstrated in the hallmark study by Bradbury et al. [75]. In this study, intrathecal delivery of chABC to the injured rat spinal cord led to digestion of CSPGs *in vivo*, increased growth into the lesion site, improved motor function, and a nearly two-fold recovery (compared to controls) of spinal potentials below the lesion site to supraspinal inputs. These findings were confirmed in a similar study [76] using a drug delivery method that enabled sustained chABC delivery as opposed to a single microinjection. To address the concern of aberrant sprouting, a follow-up study [77] was performed, in which both spared and injured axons showed aberrant sprouting following chABC treatment in injured, but not control animals. Despite the failure to develop nociceptive connections–the type that could potentially contribute to the observation of chronic pain in rat models of SCI–the aberrant sprouting of these axons is nevertheless a concern for the use of chABC clinically. Moreover, like myelin, the extent to which CSPGs inhibit growth depends strongly on neuron age, type, and CSPG concentration [78].

It is also worth noting that considerable work has been done to investigate the positive effects of the formation of a glial scar (for a review, see [79]). For example, the selective ablation of dividing reactive astrocytes [80] led to increased leukocyte infiltration, loss of myelin, increased neuron degeneration, and reduced motor score following SCI compared to control mice. Thus, despite its effects on growth inhibition, it would appear that the glial scar has a neuroprotective effect, and may substantially mitigate the secondary injury phase of SCI. Rolls et al. [79] hypothesize that an optimal therapeutic strategy would aim to strike a balance between early, protective glial scarring and late,

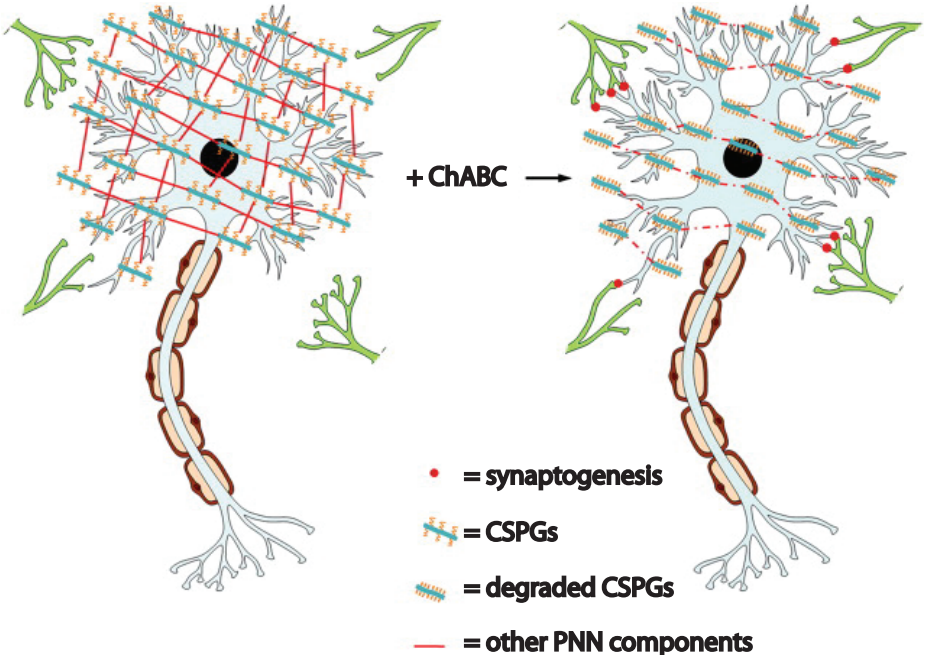

Figure 2.2: Illustration of the role of CSPGs in regulating synaptic contacts as PNNs. In the adult CNS, CSPGs help maintain the mature CNS and protect against aberrant synapse formation by forming the PNN (*left*). Subsequent digestion by chABC leads to increased synaptic plasticity (*right*) and may be important for regeneration within the adult CNS. Reprinted from *Experimental Neurology*, **235**, Bartus, K. et al. Chondroitin sulphate proteoglycans: Key modulators of spinal cord and brain plasticity, 5-17, Copyright 2012, with permission from Elsevier.

growth-inhibitory glial microenvironment. In fact, some recent evidence [81,82] would suggest that the glial scar can promote axonal regeneration, although this is strongly dependent on astrocyte phenotype.

2.2.3 Fundamental Differences Between the Developing and Adult CNS

As mentioned previously, the adult CNS, while not static, is decidedly less plastic than the developing CNS. As a rather striking example of this phenomenon, Saunders et al. [83] subjected neonatal opossums to spinal cord crush or complete transection injuries. These animals were then characterized behaviorally, functionally, and histologically months to years following injury and found to be substantially normal in both aspects, while similar injuries in an adult would result in permanent paralysis with drastic differences in tissue morphology. Although this study showed the importance of innate differences between the neonatal[4] and adult CNS, it did not elucidate key biological markers or pathways to target.

With respect to bimolecular pathways, promising work [84, 85] has also been done in studies focused on the PTEN/mTOR pathway. In their ground-breaking study, Park et al. [84] showed that the mammalian target of rapamycin (mTOR) pathway is highly active in early neonates but is down-regulated in the adult CNS by the downstream effects of phosphatase and tension homolog (PTEN). The mTOR pathway is responsible for promoting cell growth, among other things (see [86] for a review). Moreover, deletion of PTEN resulted in

[4]It should be noted that "neonatal" is a qualitative descriptor, as the stage of development at birth is not conserved across species.

subsequent up-regulation of the mTOR pathway in retinal ganglion cells and increased survival and regeneration following axotomy [84]. A subsequent study by Liu et al. [85] of the corticospinal neurons–neurons projecting axons into the spinal cord and responsible for voluntary motor function–showed not only enhanced sprouting of injured and uninjured axons, but evidence for excitatory synapse formation in many of the regenerating CST axons. However, as might be guessed by the inhibitory effects of PTEN on a growth-promoting target, PTEN is a tumor suppressor gene whose inactivation, mutation, or deletion is common to many cancers, including glioblastoma (reviewed in [87]). Thus, despite the pro-regenerative effects of PTEN deletion/suppression, its permanent deletion/suppression is ill-advised.

Studies of the nature just described,combined with the comparisons between cAMP levels in immature and mature neurons [65] discussed previously, lend support to the "regeneration recapitulates development" paradigm of regenerative medicine. However, the scope of this paradigm is not without bounds. For example, recent work in the Fetcho group [88] demonstrated that in the hindbrain and spinal cord of zebrafish larvae, neurons are initially organized into relatively simple "neurotransmitter stripes", whereby functional circuits form from simple neuron subtype pools and subsequently migrate to form nuclei in the more complex mosaic structure of the adult CNS. While shedding light on developmental biology, the study also reveals the one-way nature of neural development in complex organisms.

With this limitation in mind, one intriguing possibility for axonal regeneration focuses on mechanisms of angiogenesis. A growing body of evidence (reviewed in [89–91]) shows that there is a dynamic interplay between angiogenesis and axonal guidance. In particular, axonal growth cones and

endothelial tip cells share common ligands, including vascular endothelial growth factor (VEGF), which enables a synergistic growth of axons and nerves [89, 90]. While most of this synergism has been identified in the peripheral nervous system (PNS), which regenerates robustly, there is reason to think that angiogenesis may play an important role in CNS regeneration as well [91, 92]. However, the role of VEGF as a therapy for SCI remains somewhat controversial, with some studies [93, 94] having showed the positive outcomes of vascular growth promotion, mitigation of secondary injury, tissue sparing, and improved behavioral outcome, while others showed the negative outcomes of leaky vessels [95, 96] and subsequent behavioral and neurological deficits [95]. Despite the open controversy on the matter, convincing evidence for axon regeneration along blood vessels has been presented by Dray et al. [97]. They performed repeated *in vivo* imaging studies of the mouse spinal cord out to as long as 120 days post-injury, and found that a peak of approximately 50% of endogenously regenerating axons were found to be following blood vessel trajectories approximately one week after injury, with significantly longer neurite outgrowth compared to axons not observed to be following vascular trajectories. This work demonstrates the critical value of *in vivo* imaging for eliminating ambiguity and identifying therapeutic targets, a topic to which we now turn our attention.

2.3 What *In Vivo* Optical Microscopy Has to Offer

One of the drawbacks to clinical trials is that data is based on either motor skills, subjective patient self-assessment, or tissue level imaging (e.g. MRI), making cellular-level mechanistic understandings of any reported efficacy ambiguous,

at best. Furthermore, spontaneous recovery of sensory and motor skills in the absence of therapy and/or regeneration, such as spontaneous rewiring of the propriospinal pathway demonstrated in the mouse spinal cord by Courtine et al. [98], can further obscure measures of efficacy. Traditional animal studies allow for the addition of fixed-time-point histology to behavioral assays, adding tissue characterization at the cellular level to the knowledge base, but fail to capture information of disease progression. *In vivo* imaging holds great promise in providing this missing information.

Axon Degeneration and Sprouting

In addition to providing insights into complex and dynamic inter-cellular interactions, this information is of critical importance for resolving ambiguities in therapeutic strategies targeted at axon regrowth, as single time point images do not allow one to distinguish between axons that are in the processes of degenerating and regenerating, or between axons that have fully regenerated and axons that were spared from injury altogether [99, 100] (see Fig. 2.3a). Similar studies could bring new insights to etiological studies of neuroinflammatory disorders, such as multiple sclerosis (MS) (see Fig. 2.3b).

In a commentary [100] on setting standards for evaluation of the efficacy of therapeutic strategies targeted towards axon regeneration, the authors state that "Obviously, the best solution to this problem would be to develop techniques to visualize the response of living axons after injury *in vivo*." It is this "obvious solution" that our work presented in this thesis has sought to make possible, following the pattern of the watershed study by Bhatt et al. discussed previously [69]. A review of recent work done to this effect is presented in the

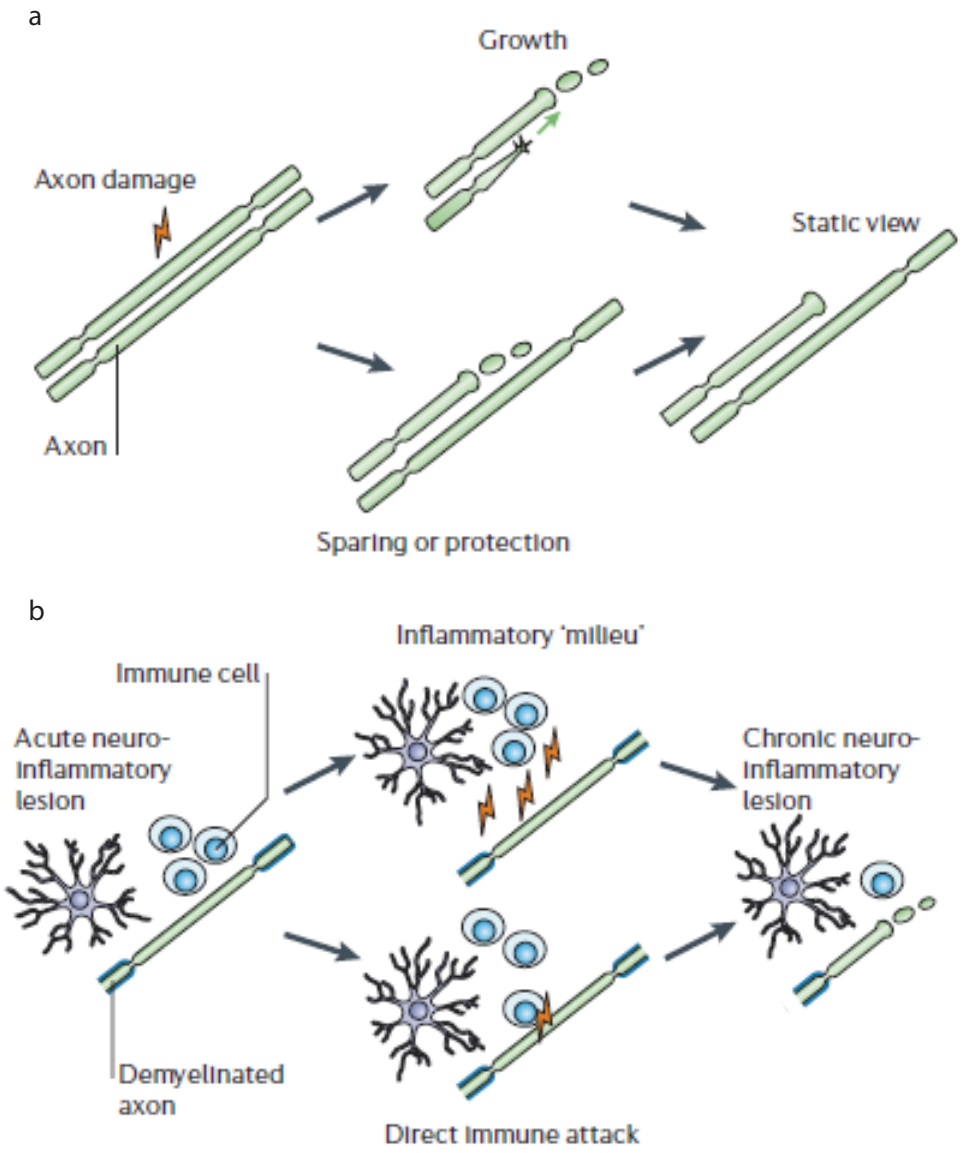

Figure 2.3: Illustration of the advantages of dynamic in vivo imaging in spinal cord pathology

In contrast to static images, *in vivo* imaging allows for the capture of important transients, enabling the identification of axonal phenotypes following injury, whether spared, regenerating, or dying (a). In the same vein, mechanisms of neuroinflammatory injury may be distinguished by detecting loss of axonal integrity either in association with direct immunological attack or by a neurotoxic inflammatory microenvironment (b). Reprinted by permission from Macmillan Publishers Ltd: *Nature Methods*, Misgeld, T. and Kerschensteiner, M., *In vivo* imaging of the diseased nervous system, **7**, 449-463, Copyright 2006.

"Introduction" section of later chapters of this thesis containing our published work on spinal cord imaging. However, we shall here review in greater detail key scientific[5] observations made to date by *in vivo* optical imaging of the spinal cord.

The first group to achieve this "best solution" considered afferent axons of the dorsal root ganglia (DRG), and discovered a new phenomenon known as acute axonal degeneration (AAD), in which axons of the mouse spinal cord degenerate up to 100s of micrometers within minutes of traumatic injury [101]. They also showed that this mechanism was calpain-mediated, and shared at least some common mechanisms with Wallerian degeneration, the progressive fragmentation of the distal segment of an axon following axotomy of a peripheral nerve [47]. Within 24 hours, they saw many injured axons undergo aberrant growth [101]. We have also seen this response [102], but observe fewer axons regenerating. Possible resolutions for discrepancy in growth response include our mechanism of injury and/or the location relative to the cell bodies, which we did not standardize in our dorsal column lesions. Our results are in closer agreement with the results in a follow-up paper [103], reducing the number of regenerating axons from 30% to 9% [101]. While we observed this growth to occur within the first three days post-injury, we also noticed that these axons subsequently disintegrated within the first week after injury [102]. These previous studies had only considered 1-2 days post-injury, emphasizing the importance of imaging across a range of timescales.

It should also be pointed out that imaging can provide qualitatively different conclusions on regenerative mechanisms than fixed-point histology. In the previously-mentioned follow-up study [103], Bareyre et al. demonstrated

[5]We shall also here omit articles which simply present a new methodology without presenting scientific findings, though these are reviewed in later chapters

that the transcription factor, STAT3, is upregulated in peripheral nerve lesions–which regenerated well–yet is not upregulated in CNS axonal injury, accompanied by a lack of regenerative capacity. Moreover, inhibition of STAT3 resulted in failure of peripheral nerves to regenerate. However, one of the critical findings of this study was that while STAT3 over-expression by exogenous transduction substantially improved axon *sprouting* (over 50% of axons sprouted compared to 9% in controls), it was not able to *sustain* axon growth. This latter finding was deduced by *repeated* imaging of the *same* axons in the *same* animal. Their conclusion rested on (a) the ability to see key morphological *differences* between day 0 and day 2 post-injury and (b) the ability to see that this early response did not result in a regenerative net-gain at day 10 post-injury. Anecdotally, a similar finding was discovered in our own work where chABC and cAMP were delivered to the spinal cord via intrathecal catheter following a laser injury (see Fig. 2.4).

In contrast, traditional histological studies which allow for the examination of only a single time-point would likely lead to a false conclusion that STAT3 was ineffective on the basis of lack of axonal elongation at later time points, or else would lead to false conclusion that STAT3 was highly-effective on the basis of an early sprouting response. Even if it were possible to arrive at the same conclusion as Bareyre et al. using traditional methods alone, each time point would require a cohort of animals in both experimental and control groups, easily tripling the numbers of animals required. Thus, not only does *in vivo* imaging allow for findings likely to be missed by traditional studies, but it is also more humane. Nevertheless, Bareyre et al. were limited in the number of time-points and longitudinal extent of imaging by the need for invasive surgery at every time point, a problem that we have attempted to solve with our spinal

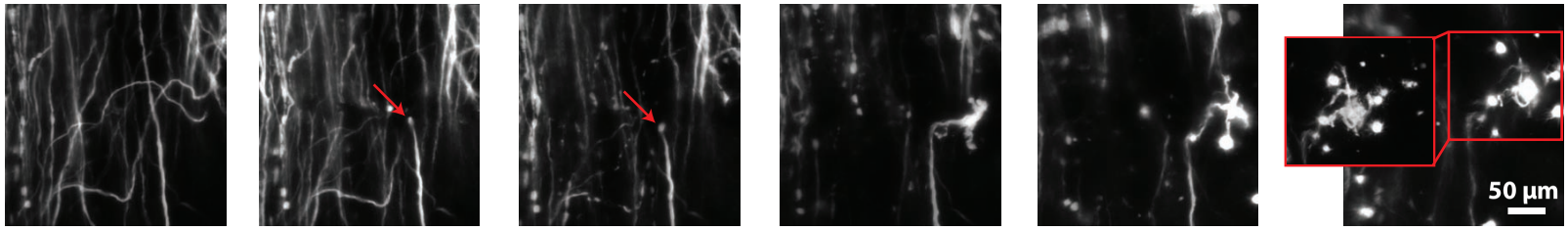

Figure 2.4: Axonal response to treatment with cABC and chABC.
We delivered 12.5 μL of 20mM cAMP and 12.5 μL of 2 U/mL chABC in 1 M trehalose intrathecally immediately following a laser axotomy (*red arrows*) to the spinal cord of a mouse strain expressing EGFP in a subset of DRG axons, with re-injections every 24 hours for 3 days (unpublished data). Anecdotally, we observed a robust sprouting response on the first day following treatment, but little change following subsequent treatments. All growth was aberrant in that it did not cross the lesion site.

chamber [102].

Microglial Activation and Migration

Moving away from studies of axon dynamics, Dibaj et al. have devoted a significant amount of effort to understanding the reactions of microglia to SCI in mouse models [104]. In particular, they have shown [104] that nitric oxide (NO) and ATP are released following SCI and co-dependently recruit microglia and alter their phenotype. This study demonstrated the need for *in vivo* imaging, since the study was essentially a study of the dynamic process of chemotaxis–the migration of cells and/or cellular processes in response to a chemical gradient– in the complex milieu of the injured mouse spinal cord. The proposed timescales in this study also agree well with our observations [102], in which the number of microglia at the lesion site were seen to increase by as much as five-fold within the first 24 hours.

Microglial dynamics are important for therapeutic design since their positive or negative effects on regeneration depend critically on timing. For example, neuronal fractalkine (CX3-CL1) binds its receptor (CX3-CR1) expressed on the surface of microglia [105], and can serve to limit the extent of their activation and subsequent neurotoxicity [106]. Thus, increasing CX3-CL1 levels would appear to have a positive effect in down-regulating the release of pro-inflammatory cytokines, thereby limiting the migration [107] of potentially destructive immune cells into the spinal cord and preventing axonal loss (Fig. 2.3b). The catch-22 comes from the fact that axon regeneration is inhibited by axonal fragments [108] which are removed by the resident macrophages, namely phagocytic microglia. The scenario is further complicated by the

observation that macrophages (microglia and differentiated monocytes) are phenotypically diverse. A neurotoxic M1 macrophage will tend to result in neurotoxicity while M2 macrophages are growth promoting [109]. The precise determination of a "therapeutic window" and cellular phenotype selection requires a precise understanding of the temporal profile of mutli-cellular dynamic interactions, a study for which *in vivo* microscopy is ideally suited.

Myelin

Loss and/or recovery of CNS myelin in SCI and demyelinating disorders, like multiple sclerosis (MS), are also dynamic processes whose study has and will continue to benefit from *in vivo* imaging. Coherent Anti-Stokes Raman Scattering (CARS) microscopy has been the predominant source of myelin contrast [110–112], and we have demonstrated [113] that third harmonic generation (THG; reviewed in later chapters) is also well-suited to imaging CNS myelin. As was previously mentioned, chronic pain is a common complication of SCI, and electrical stimulation of spinal tissues has been observed to cause significant reduction in pain [114], even though the mechanisms of this relief remain largely unknown. Huff et al. [112] have shown that this stimulation in spinal axons results in myelin retraction at the nodes of Ranvier, which recovers within a few hours post-stimulation. Such an observation would be next to impossible using immunohistological methods alone. They also showed that this mechanism was calcium-activated and calpain-dependent. The authors suggest that one potential mechanism of action is that myelin retraction exposes voltage-gated potassium channels, whose exposure results

in a greater polarization of the cell and thereby suppresses hyperactivity.

In Vivo Imaging Beyond SCI

Finally, the value of *in vivo* imaging in the spinal cord extends beyond studies of SCI. Amytrophic lateral sclerosis (ALS), also known as Lou Gehrig's disease, is a debilitating neurological disease that results in progressive loss of spinal cord motor neurons, with consequent weakness, paralysis, and death [115]. Familial ALS (fALS) is genetically linked and accounts for between 5 and 10 % of ALS cases, while the etiology of the remaining cases remains poorly understood [115].

In vivo imaging has helped aid progress in our understanding of this disease. For example, in contrast to microglia, wild-type astrocytes showed little acute response to axonal injury in healthy animals [116]. Yet in superoxide dismutase-1 (SOD-1) mutant mice (a leading model of fALS [117]), imaging revealed rapid astrocyte invasion of the injury site [116]. An analogous study of microglia [118] in SOD-1 mutant mice showed that pre-clinical ALS (i.e. limited loss of motor neurons) showed hyper-reactive microglia while clinical ALS showed hyper-activation of microglia, but with an untargeted response to injury. In both studies, a hypersensitivity of microglia and astrocytes was seen in response to injury, consistent with previous studies [119] which showed that transplanted wild-type glial cells in a SOD-1 mutant mouse do not have the same immune activation and show diminished neurodegenerative phenotype. Another *in vivo* study of ALS [120] has challenged the long-standing assumption that deficits in axonal transport lead to axon degeneration. In this study, they used a combination of mice expressing Kaede–a fluorescent protein that

changes in emission wavelength from green to red upon exposure to UV light (for a review of photoactivatable color-change proteins, see [121])–in neuronal mitochondria along with different mouse models of familial ALS. By tracking of mitochrondrial migration and densities, Marinkovic et al. [120] found that impaired axonal transport could occur without axonal degeneration and vice versa. In all cases, these observations required imaging of dynamic processes inaccessible to traditional methods of study.

2.4 Conclusion

On the face of it, SCI seems like an insurmountable biomedical problem, with very little improvement in treating the core pathology despite decades of research. However, as we have considered, new insights as well as improvements in cellular technologies and gene therapies have led to and are making possible the identification of new targets and novel therapeutic strategies. In addition, the availability of transgenic mice and *in vivo* imaging platforms create a powerful platform, both for identifying disease mechanisms and evaluating therapeutic strategies. In most of the imaging studies discussed above, imaging was performed by the use of one or more modes of nonlinear laser scanning microscopy. It is this form of microscopy which makes possible the acquisition of high-resolution optical images inside of highly scattering tissue, and a good deal of our work has focused on the use and development of these techniques. The next chapter will focus on the physical mechanisms underlying this class of microscopy.

REFERENCES

[1] One Degree of Separation: Paralysis and Spinal Cord Injury in the United States. Technical report, 2009.

[2] MJ DeVivo. Epidemiology of traumatic spinal cord injury: trends and future implications. *Spinal Cord*, 50(5):365–372, 2012.

[3] S.C.I. Facts. Figures at a Glance. Birmingham, AL: National Spinal Cord Injury Statistical Center; 2011. 2011.

[4] A J Schoenfeld, B McCriskin, M Hsiao, and R Burks. Incidence and epidemiology of spinal cord injury within a closed American population: the United States military (2000–2009). *Spinal Cord*, 49(8):874–879, 2011.

[5] Amie B Jackson, Marcel Dijkers, Michael J DeVivo, and Robert B Poczatek. A demographic profile of new traumatic spinal cord injuries: Change and stability over 30 years. *Archives of Physical Medicine and Rehabilitation*, 85(11):1740–1748, 2004.

[6] M Wyndaele and JJ Wyndaele. Incidence, prevalence and epidemiology of spinal cord injury: what learns a worldwide literature survey? *Spinal Cord*, 44(9):523–529, 2006.

[7] David J Strauss, Michael J DeVivo, David R Paculdo, and Robert M Shavelle. Trends in Life Expectancy After Spinal Cord Injury. *Archives of Physical Medicine and Rehabilitation*, 87(8):1079–1085, 2006.

[8] FMJ Maynard, MB Bracken, G Creasey, JFJ Ditunno, and WH Donovan. TB ducker, SL Garber, RJ Marino, SL Stover, CH Tator, JE Wilberg and W. Young, International Standards for Neurological and Functional Classification of Spinal Cord Injury, American Spinal Injury Association. *Spinal Cord*, 35:266–274, 1997.

[9] Charles Watson, George Paxinos, and Gulgun Kayalioglu. *The Spinal Cord*. Elsevier Ltd., Burlington, MA, 2009.

[10] Sandrine Thuret, Lawrence DF Moon, and Fred H Gage. Therapeutic interventions after spinal cord injury. *Nat Rev Neurosci*, 7(8):628–643, 2006.

[11] M R Lin, H F Hwang, W Y Yu, and C Y Chen. A Prospective Study of Factors Influencing Return to Work After Traumatic Spinal Cord Injury in Taiwan. *YAPMR*, 90(10):1716–1722, 2009.

[12] Ingeborg Beate Lidal, Tuan Khai Huynh, and Fin Biering-Sørensen. Return to work following spinal cord injury: a review. *Disabil Rehabil*, 29(17):1341–1375, 2007.

[13] M Franceschini, MC Pagliacci, T Russo, G Felzani, S Aito, and C Marini. Occurrence and predictors of employment after traumatic spinal cord injury: the GISEM Study. 50(3):238–242, 2011.

[14] N Gupta, K T White, and P R Sandford. Body mass index in spinal cord injury – a retrospective study. *Spinal Cord*, 44(2):92–94, 2005.

[15] S P Hetz, A E Latimer, K P Arbour-Nicitopoulos, K A Martin Ginis, and SHAPE-SCI Research Group. Secondary complications and subjective well-being in individuals with chronic spinal cord injury: associations with self-reported adiposity. *Spinal Cord*, 49(2):266–272, 2010.

[16] A P Cameron, L P Wallner, D G Tate, A V Sarma, G M Rodriguez, and J Q Clemens. Bladder Management After Spinal Cord Injury in the United States 1972 to 2005. *JURO*, 184(1):213–217, 2010.

[17] P Gallien, B Nicolas, S Robineau, MP Le Bot, A. Durufle, and R. Brissot. Influence of urinary management on urologic complications in a cohort of spinal cord injury patients. *YAPMR*, 79(10):1206–1209, 1998.

[18] A Curt, B Nitsche, B Rodic, B Schurch, and V Dietz. Assessment of autonomic dysreflexia in patients with spinal cord injury. *Journal of Neurology, Neurosurgery & Psychiatry*, 62(5):473–477, 1997.

[19] Robert W Teasell, J Malcolm O Arnold, Andrei Krassioukov, and Gail A Delaney. Cardiovascular consequences of loss of supraspinal control of the sympathetic nervous system after spinal cord injury. *Archives of Physical Medicine and Rehabilitation*, 81(4):506–516, 2000.

[20] A Krassioukov, D E Warburton, R Teasell, J J Eng, and Spinal Cord Injury Rehabilitation Evidence Research Team. A Systematic Review of the Management of Autonomic Dysreflexia After Spinal Cord Injury. *YAPMR*, 90(4):682–695, 2009.

[21] Arthur Brown and Lynne C Weaver. The dark side of neuroplasticity. *Exp Neurol*, 235(1):133–141, 2012.

[22] Lynne C Weaver, Daniel R Marsh, Denis Gris, Arthur Brown, and Gregory A Dekaban. *Progress in Brain Research*, volume 152 of *Progress in Brain Research*. Elsevier, 2006.

[23] M P Jensen, A J Hoffman, and D D Cardenas. Chronic pain in individuals with spinal cord injury: a survey and longitudinal study. *Spinal Cord*, 43(12):704–712, 2005.

[24] Ehsan Modirian, Pirouz Pirouzi, MohammadReza Soroush, Sima Karbalaei-Esmaeili, Hadi Shojaei, and HamidReza Zamani. Chronic Pain after Spinal Cord Injury: Results of a Long-Term Study. *Pain Med*, 11(7):1037–1043, 2010.

[25] WO McKinley, AB Jackson, DD Cardenas, and MJ DeVivo. Long-term medical complications after traumatic spinal cord injury: A regional model systems analysis. *Archives of Physical Medicine and Rehabilitation*, 80(11):1402–1410, 1999.

[26] RJ Soden, J Walsh, JW Middleton, ML Craven, SB Rutkowski, and JD Yeo. Causes of death after spinal cord injury. *Spinal Cord*, 38(10):604–610, 2000.

[27] C.P. Cardozo. Respiratory complications of spinal cord injury. *The Journal of Spinal Cord Medicine*, 30(4):307, 2007.

[28] Christopher Winslow and Julia Rozovsky. Effect of Spinal Cord Injury on the Respiratory System. *American Journal of Physical Medicine & Rehabilitation*, 82(10):803–814, 2003.

[29] MJ Fishburn, RJ Marino, and JF Ditun. Atelectasis and Pneumonia in Acute Spinal-Cord Injury. *Archives of Physical Medicine and Rehabilitation*, 71(3):197–200, 1990.

[30] A Hartkopp, H Brønnum-Hansen, AM Seidenschnur, and F Biering-Sorensen. Suicide in a spinal cord injured population: Its relation to functional status. *YAPMR*, 79(11):1356–1361, 1998.

[31] MJ DeVivo, K J Black, J Scott Richards, and SL Stover. Suicide following spinal cord injury. *Spinal Cord*, 29(9):620–627, 1991.

[32] CH Tator. Review of Treatment Trials in Humanspinal Cord Injury: Issues, Difficulties, and Recommendations. *Neurosurgery*, 59(5):957, 2006.

[33] S Knafo and D Choi. Clinical studies in spinal cord injury: moving towards successful trials. *Br J Neurosurg*, 22(1):3–12, 2008.

[34] John C Gensel, Dustin J Donnelly, and Phillip G Popovich. Spinal cord injury therapies in humans: an overview of current clinical trials and their potential effects on intrinsic CNS macrophages. *Expert Opin. Ther. Targets*, pages 1–14, 2011.

[35] RJ Dumont, S Verma, DO Okonkwo, RJ Hurlbert, PT Boulos, DB Ellegala, and AS Dumont. Acute spinal cord injury, part II: contemporary pharmacotherapy. *Clinical neuropharmacology*, 24(5):265, 2001.

[36] DJ Short, WS El Masry, and PW Jones. High dose methylprednisolone in the management of acute spinal cord injury-a systematic review from a clinical perspective. *Spinal Cord*, 38(5):273–286, 2000.

[37] H Hugenholtz. Methylprednisolone for acute spinal cord injury: not a standard of care. *Canadian Medical Association Journal*, 168(9):1145–1146, 2003.

[38] RJ Hurlbert. The role of steroids in acute spinal cord injury: an evidence-based analysis. *Spine*, 26(24S):S39, 2001.

[39] Michael G Fehlings, Nicholas Theodore, James Harrop, Gilles Maurais, Charles Kuntz, Chris I Shaffrey, Brian K Kwon, Jens Chapman, Albert Yee, Allyson Tighe, and Lisa McKerracher. A Phase I/IIa Clinical Trial of a Recombinant Rho Protein Antagonist in Acute Spinal Cord Injury. *J Neurotraum*, 28(5):787–796, 2011.

[40] KE Thomas and LDF Moon. Will stem cell therapies be safe and effective for treating spinal cord injuries? *British Medical Bulletin*, 98(1):127–142, 2011.

[41] Jung Keun Hyun and Hae-Won Kim. Clinical and Experimental Advances in Regeneration of Spinal Cord Injury. *Journal of Tissue Engineering*, 2010:1–20, 2010.

[42] JC Furlan, V Noonan, DW Cadotte, and MG Fehlings. Timing of decompressive surgery of spinal cord after traumatic spinal cord injury:

an evidence-based examination of pre-clinical and clinical studies. *J Neurotraum*, 28(8):1371–1399, 2011.

[43] Leah Y Carreon and John R Dimar. Early Versus Late Stabilization of Spine Injuries. *Spine*, 36(11):E727–E733, 2011.

[44] M P Galea. Spinal cord injury and physical activity: preservation of the body. *Spinal Cord*, 50(5):344–351, 2011.

[45] Kyoung-Tae Kim, Taek-Kyun Nam, Yong-Sook Park, Young-Baeg Kim, and Seung-Won Park. Neuroprotective Effect of Anthocyanin on Experimental Traumatic Spinal Cord Injury. *J Korean Neurosurg Soc*, 49(4):205, 2011.

[46] VR King. Omega-3 Fatty Acids Improve Recovery, whereas Omega-6 Fatty Acids Worsen Outcome, after Spinal Cord Injury in the Adult Rat. *J Neurosci*, 26(17):4672–4680, 2006.

[47] Eric R Kandel, James H Schwartz, and Thomas M Jessell. *Principles of Neuroscience*. McGraw-Hill, New York, NY, 4 edition, 2000.

[48] J Yuan and BA Yankner. Apoptosis in the nervous system. *Nature*, pages 802–809, 2000.

[49] T Misgeld. Death of an axon: studying axon loss in development and disease. *Histochemistry and cell biology*, 124(3):189–196, 2005.

[50] Gina G Turrigiano and Sacha B Nelson. Homeostatic plasticity in the developing nervous system. *Nat Rev Neurosci*, 5(2):97–107, 2004.

[51] JL Gaiarsa, O Caillard, and Y Ben-Ari. Long-term plasticity at GABAergic and glycinergic synapses: mechanisms and functional significance. *Trends in Neurosciences*, 25(11):564–570, 2002.

[52] JA Kleim, JH Freeman, R Bruneau, BC Nolan, NR Cooper, A Zook, and D Walters. Synapse formation is associated with memory storage in the cerebellum. *Proceedings of the National Academy of Sciences*, 99(20):13228, 2002.

[53] JA Kleim, S Barbay, NR Cooper, TM Hogg, CN Reidel, MS Remple, and RJ Nudo. Motor learning-dependent synaptogenesis is localized

to functionally reorganized motor cortex. *Neurobiology of learning and memory*, 77(1):63–77, 2002.

[54] Y Geinisman, RW Berry, JF Disterhoft, JM Power, and EA Van der Zee. Associative learning elicits the formation of multiple-synapse boutons. *The Journal of neuroscience*, 21(15):5568–5573, 2001.

[55] JE Black, KR Isaacs, BJ Anderson, AA Alcantara, and WT Greenough. Learning causes synaptogenesis, whereas motor activity causes angiogenesis, in cerebellar cortex of adult rats. *Proceedings of the National Academy of Sciences*, 87(14):5568, 1990.

[56] Jae K Lee and Binhai Zheng. Role of myelin-associated inhibitors in axonal repair after spinal cord injury. *Exp Neurol*, 235(1):33–42, 2012.

[57] M Li, A Shibata, C Li, PE Braun, L McKerracher, J Roder, SB Kater, and S David. Myelin-associated glycoprotein inhibits neurite/axon growth and causes growth cone collapse. *J Neurosci Res*, 46(4):404–414, 1996.

[58] TA Watkins and BA Barres. Nerve regeneration: regrowth stumped by shared receptor. *Current Biology*, 12(19):R654–R656, 2002.

[59] T GrandPre, SX Li, and SM Strittmatter. Nogo-66 receptor antagonist peptide promotes axonal regeneration. *Nature*, 417(6888):547–551, 2002.

[60] SX Li and SM Strittmatter. Delayed systemic Nogo-66 receptor antagonist promotes recovery from spinal cord injury. *J Neurosci*, 23(10):4219–4227, 2003.

[61] Y Nakamura, Y Fujita, M Ueno, T Takai, and T Yamashita. Paired Immunoglobulin-like Receptor B Knockout Does Not Enhance Axonal Regeneration or Locomotor Recovery after Spinal Cord Injury. *Journal of Biological Chemistry*, 286(3):1876–1883, 2011.

[62] Fang Xie and Binhai Zheng. White matter inhibitors in CNS axon regeneration failure. *Exp Neurol*, 209(2):302–312, 2008.

[63] Marie T Filbin. Myelin-associated inhibitors of axonal regeneration in the adult mammalian CNS. *Nat Rev Neurosci*, 4(9):703–713, 2003.

[64] D Cai, Y Shen, M De Bellard, S Tang, and MT Filbin. Prior exposure

to neurotrophins blocks inhibition of axonal regeneration by MAG and myelin via a cAMP-dependent mechanism. *Neuron*, 22:89–101, 1999.

[65] D Cai, J Qiu, Z Cao, M McAtee, BS Bregman, and MT Filbin. Neuronal cyclic AMP controls the developmental loss in ability of axons to regenerate. *J Neurosci*, 21(13):4731, 2001.

[66] J Qiu, D Cai, H Dai, M McAtee, PN Hoffman, BS Bregman, and MT Filbin. Spinal axon regeneration induced by elevation of cyclic AMP. *Neuron*, 34(6):895–903, 2002.

[67] Damien D Pearse, Francisco C Pereira, Alexander E Marcillo, Margaret L Bates, Yerko A Berrocal, Marie T Filbin, and Mary Bartlett Bunge. cAMP and Schwann cells promote axonal growth and functional recovery after spinal cord injury. *Nat Med*, 10(6):610–616, 2004.

[68] S Neumann, F Bradke, M Tessier-Lavigne, and AI Basbaum. Regeneration of sensory axons within the injured spinal cord induced by intraganglionic cAMP elevation. *Neuron*, 34(6):885–893, 2002.

[69] DH Bhatt, SJ Otto, B Depoister, and JR Fetcho. Cyclic AMP-induced repair of zebrafish spinal circuits. *Science*, 305(5681):254, 2004.

[70] AE Fournier, BT Takizawa, and SM Strittmatter. Rho kinase inhibition enhances axonal regeneration in the injured CNS. *The Journal of neuroscience*, 23(4):1416–1423, 2003.

[71] P Dergham, B Ellezam, C Essagian, H Avedissian, WD Lubell, and L McKerracher. Rho signaling pathway targeted to promote spinal cord repair. *The Journal of neuroscience*, 22(15):6570–6577, 2002.

[72] JS Rudge and J Silver. Inhibition of neurite outgrowth on astroglial scars in vitro. *The Journal of neuroscience*, 10(11):3594–3603, 1990.

[73] RJ McKeon, RC Schreiber, JS Rudge, and J Silver. Reduction of neurite outgrowth in a model of glial scarring following CNS injury is correlated with the expression of inhibitory molecules on reactive astrocytes. *The Journal of neuroscience*, 11(11):3398–3411, 1991.

[74] K Bartus, ND James, KD Bosch, and EJ Bradbury. Chondroitin sulphate proteoglycans: Key modulators of spinal cord and brain plasticity. *Exp Neurol*, 235(1):5–17, 2012.

[75] EJ Bradbury, LDF Moon, RJ Popat, VR King, GS Bennett, PN Patel, JW Fawcett, and SB McMahon. Chondroitinase ABC promotes functional recovery after spinal cord injury. *Nature*, 416(6881):636–640, 2002.

[76] H Lee, R McKeon, and R Bellamkonda. Sustained delivery of thermostabilized chABC enhances axonal sprouting . *Proceedings of the National Academy of Sciences*, 2010.

[77] AW Barritt, M Davies, F Marchand, R Hartley, J Grist, P Yip, SB McMahon, and EJ Bradbury. Chondroitinase ABC promotes sprouting of intact and injured spinal systems after spinal cord injury. *J Neurosci*, 26(42):10856, 2006.

[78] J Silver and JH Miller. Regeneration beyond the glial scar. *Nat Rev Neurosci*, 5(2):146–156, 2004.

[79] A Rolls, R Shechter, and M Schwartz. The bright side of the glial scar in CNS repair. *Nat Rev Neurosci*, 10(3):235–241, 2009.

[80] J R Faulkner. Reactive Astrocytes Protect Tissue and Preserve Function after Spinal Cord Injury. *J Neurosci*, 24(9):2143–2155, 2004.

[81] Christopher Haas, Birgit Neuhuber, Takaya Yamagami, Mahendra Rao, and Itzhak Fischer. Phenotypic analysis of astrocytes derived from glial restricted precursors and their impact on axon regeneration. *Exp Neurol*, 233(2):717–732, 2012.

[82] Angela R Filous, Jared H Miller, Yvette M Coulson-Thomas, Kevin P. Horn, Warren J Alilain, and Jerry Silver. Immature astrocytes promote CNS axonal regeneration when combined with chondroitinase ABC. *Devel Neurobio*, 70(12):826–841, 2010.

[83] NR Saunders, P Kitchener, GW Knott, JG Nicholls, A Potter, and TJ Smith. Development of walking, swimming and neuronal connections after complete spinal cord transection in the neonatal opossum, Monodelphis domestica. *J Neurosci*, 18(1):339–355, 1998.

[84] Kevin Kyungsuk Park, Kai Liu, Yang Hu, Patrice D Smith, Chen Wang, Bin Cai, Bengang Xu, Lauren Connolly, Ioannis Kramvis, Mustafa Sahin, and Zhigang He. Promoting Axon Regeneration in the Adult CNS by Modulation of the PTEN/mTOR Pathway. *Science*, 322(5903):963–966, 2008.

[85] Kai Liu, Yi Lu, Jae K Lee, Ramsey Samara, Rafer Willenberg, Ilse Sears-Kraxberger, Andrea Tedeschi, Kevin Kyungsuk Park, Duo Jin, Bin Cai, Bengang Xu, Lauren Connolly, Oswald Steward, Binhai Zheng, and Zhigang He. PTEN deletion enhances the regenerative ability of adult corticospinal neurons. *Nat Neurosci*, 13(9):1075–U64, 2010.

[86] Dos D Sarbassov, Siraj M Ali, and David M Sabatini. Growing roles for the mTOR pathway. *Current Opinion in Cell Biology*, 17(6):596–603, 2005.

[87] I Sansal. The Biology and Clinical Relevance of the PTEN Tumor Suppressor Pathway. *Journal of Clinical Oncology*, 22(14):2954–2963, 2004.

[88] A Kinkhabwala, M Riley, M Koyama, J Monen, C Satou, Y Kimura, S Higashijima, and J Fetcho. A structural and functional ground plan for neurons in the hindbrain of zebrafish. *Proceedings of the National Academy of Sciences*, 108(3):1164–1169, 2011.

[89] P Carmeliet and M Tessier-Lavigne. Common mechanisms of nerve and blood vessel wiring. *Nature*, 436(7048):193–200, 2005.

[90] Ralf H Adams and Anne Eichmann. Axon Guidance Molecules in Vascular Patterning. *Csh Perspect Biol*, 2(5):a001875, 2010.

[91] C Ruiz de Almodovar, D Lambrechts, M Mazzone, and P Carmeliet. Role and Therapeutic Potential of VEGF in the Nervous System. *Physiol Rev*, 89(2):607–648, 2009.

[92] J Rosenstein and Janette M Krum. New roles for VEGF in nervous tissue–beyond blood vessels. *Exp Neurol*, 187(2):246–253, 2004.

[93] J Widenfalk, A Lipson, M Jubran, C Hofstetter, T Ebendal, Y Cao, and L Olson. Vascular endothelial growth factor improves functional outcome and decreases secondary degeneration in experimental spinal cord contusion injury. *Neuroscience*, 120(4):951–960, 2003.

[94] Hyuk Min Kim, Dong Hoon Hwang, Jong Eun Lee, Seung U Kim, and Byung G Kim. Ex Vivo VEGF Delivery by Neural Stem Cells Enhances Proliferation of Glial Progenitors, Angiogenesis, and Tissue Sparing after Spinal Cord Injury. *Plos One*, 4(3):e4987, 2009.

[95] RL Benton and SR Whittemore. VEGF(165) therapy exacerbates

secondary damage following spinal cord injury. *Neurochem Res*, 28(11):1693–1703, 2003.

[96] CB Patel, DM Cohen, P Ahobila-Vajjula, LM Sundberg, T Chacko, and PA Narayana. Effect of VEGF treatment on the blood-spinal cord barrier permeability in experimental spinal cord injury: dynamic contrast-enhanced magnetic resonance imaging. *J Neurotraum*, 26(7):1005–1016, 2009.

[97] C Dray, G Rougon, and F Debarbieux. Quantitative analysis by in vivo imaging of the dynamics of vascular and axonal networks in injured mouse spinal cord. *Proceedings of the National Academy of Sciences*, 106(23):9459, 2009.

[98] G Courtine, B Song, RR Roy, H Zhong, JE Herrmann, Y Ao, J Qi, VR Edgerton, and MV Sofroniew. Recovery of supraspinal control of stepping via indirect propriospinal relay connections after spinal cord injury. *Nat Med*, 14(1):69–74, 2008.

[99] Thomas Misgeld and Martin Kerschensteiner. In vivo imaging of the diseased nervous system. *Nat Rev Neurosci*, 7(6):449–463, 2006.

[100] O Steward, B Zheng, and M Tessier Lavigne. False resurrections: distinguishing regenerated from spared axons in the injured central nervous system. *J. Comp. Neurol.*, 459(1):1–8, 2003.

[101] M Kerschensteiner, ME Schwab, JW Lichtman, and T Misgeld. In vivo imaging of axonal degeneration and regeneration in the injured spinal cord. *Nat Med*, 11(5):572–577, 2005.

[102] Matthew J Farrar, Ida M Bernstein, Donald H Schlafer, Thomas A Cleland, Joseph R Fetcho, and Chris B Schaffer. Chronic in vivo imaging in the mouse spinal cord using an implanted chamber. *Nat Meth*, 9(3):297–U113, 2012.

[103] Florence M Bareyre, Natalie Garzorz, Claudia Lang, Thomas Misgeld, Hildegard Buening, and Martin Kerschensteiner. In vivo imaging reveals a phase-specific role of STAT3 during central and peripheral nervous system axon regeneration. *Proceedings of the National Academy of Sciences of the United States of America*, 108(15):6282–6287, 2011.

[104] P Dibaj, F Nadrigny, H Steffens, A Scheller, J Hirrlinger, ED Schomburg,

C Neusch, and F Kirchhoff. NO mediates microglial response to acute spinal cord injury under ATP control in vivo. *Glia*, 58(9):1133–1144, 2010.

[105] M Kerschensteiner, E Meinl, and R Hohlfeld. Neuro-immune crosstalk in CNS diseases. *Neuroscience*, 158(3):1122–1132, 2009.

[106] Astrid E Cardona, Erik P Pioro, Margaret E Sasse, Volodymyr Kostenko, Sandra M Cardona, Ineke M Dijkstra, DeRen Huang, Grahame Kidd, Stephen Dombrowski, RanJan Dutta, Jar-Chi Lee, Donald N Cook, Steffen Jung, Sergio A Lira, Dan R Littman, and Richard M Ransohoff. Control of microglial neurotoxicity by the fractalkine receptor. *Nat Neurosci*, 9(7):917–924, 2006.

[107] Francesca Aloisi. Immune function of microglia. *Glia*, 36(2):165–179, 2001.

[108] T Tanaka, M Ueno, and T Yamashita. Engulfment of axon debris by microglia requires p38 MAPK activity. *Journal of Biological Chemistry*, 284(32):21626, 2009.

[109] KA Kigerl, JC Gensel, DP Ankeny, JK Alexander, DJ Donnelly, and PG Popovich. Identification of Two Distinct Macrophage Subsets with Divergent Effects Causing either Neurotoxicity or Regeneration in the Injured Mouse Spinal Cord. *J Neurosci*, 29(43):13435–13444, 2009.

[110] H Wang, Y Fu, P Zickmund, R Shi, and JX Cheng. Coherent anti-Stokes Raman scattering imaging of axonal myelin in live spinal tissues. *Biophys J*, 89(1):581–591, 2005.

[111] Y Fu, TB Huff, HW Wang, H Wang, and JX Cheng. Ex vivo and in vivo imaging of myelin fibers in mouse brain by coherent anti-Stokes Raman scattering microscopy. *Opt Express*, 16(24):19396, 2008.

[112] Terry B Huff, Yunzhou Shi, Wenjing Sun, Wei Wu, Riyi Shi, and Ji-Xin Cheng. Real-Time CARS Imaging Reveals a Calpain-Dependent Pathway for Paranodal Myelin Retraction during High-Frequency Stimulation. *Plos One*, 6(3):e17176, 2011.

[113] Matthew J Farrar, Frank W Wise, Joseph R Fetcho, and Chris B Schaffer. In Vivo Imaging of Myelin in the Vertebrate Central Nervous System Using Third Harmonic Generation Microscopy. *Biophys J*, 100(5):1362–1371, 2011.

[114] MA Kemler, GAM Barendse, M. Van Kleef, HCW De Vet, CPM Rijks, CA Furnee, and FAJM Van den Wildenberg. Spinal cord stimulation in patients with chronic reflex sympathetic dystrophy. *New Engl J Med*, 343(9):618–624, 2000.

[115] Lucie I Bruijn, Timothy M Miller, and Don W Cleveland. Unraveling the mechanisms involved in motor neuron degeneration in ALS. *Annu Rev Neurosci*, 27(1):723–749, 2004.

[116] Payam Dibaj, Heinz Steffens, Jana Zschuentzsch, Frank Kirchhoff, Eike D. Schomburg, and Clemens Neusch. In vivo imaging reveals rapid morphological reactions of astrocytes towards focal lesions in an ALS mouse model. *Neurosci Lett*, 497(2):148–151, 2011.

[117] ME Gurney, HF Pu, AY Chiu, MC Dalcanto, CY Polchow, DD Alexander, J Caliendo, A Hentati, YW Kwon, HX Deng, WJ Chen, P Zhai, RL Sufit, and T Siddique. Motor-Neuron Degeneration in Mice That Express a Human Cu,Zn Superoxide-Dismutase Mutation. *Science*, 264(5166):1772–1775, 1994.

[118] Payam Dibaj, Heinz Steffens, Jana Zschüntzsch, Fabien Nadrigny, Eike D. Schomburg, Frank Kirchhoff, and Clemens Neusch. In Vivo Imaging Reveals Distinct Inflammatory Activity of CNS Microglia versus PNS Macrophages in a Mouse Model for ALS. *Plos One*, 6(3):e17910, 2011.

[119] A M Clement. Wild-Type Nonneuronal Cells Extend Survival of SOD1 Mutant Motor Neurons in ALS Mice. *Science*, 302(5642):113–117, 2003.

[120] P Marinković, MS Reuter, and MS Brill. Axonal transport deficits and degeneration can evolve independently in mouse models of amyotrophic lateral sclerosis. In *Proceedings of the . . .*, 2012.

[121] KA Lukyanov, DM Chudakov, S Lukyanov, and VV Verkhusha. Photoactivatable fluorescent proteins. *Nature Reviews Molecular Cell Biology*, 6(11):885–891, 2005.

CHAPTER 3

NONLINEAR OPTICAL MICROSCOPY AND TECHNIQUES

In this chapter, we will examine the underlying mechanisms of nonlinear microscopy in its many forms. Whereas the previous chapter focused on the biological issues of spinal cord injury, this chapter will be weighted towards the physics of various microscopy techniques. We begin this chapter with a very brief description of what nonlinear optical microscopy achieves in comparison to other imaging modalities and provide some illustrative examples of how this form of microscopy is a powerful tool for the biological sciences and neuroscience in particular. We then move into considering the basic scaling of nonlinear optical signals and how this simple consideration combined with rudimentary beam geometry is sufficient to demonstrate the most valuable aspect of nonlinear microscopy: optical sectioning. From these general considerations, we then discuss the most widely-used form of nonlinear optical microscopy, two-photon excited fluorescence (2PEF), in terms of optimal laser parameters for strongly- and weakly-absorbing dyes. We then consider the processes of second and third harmonic generation (SHG and THG, respectively), and how these techniques share a common platform but a different mechanism than 2PEF. Finally, we round out the chapter with a discussion of optical damage, both in terms of the limits this places on imaging and as a technique for manipulating tissue.

It should also be noted that in this chapter we shall not attempt to merely restate what may be found in fuller treatises, such as the useful texts by Robert Boyd [1] and Jerome Mertz [2]. These texts are highly recommended to the reader for greater understanding of the topics discussed. However, some overlap is unavoidable and we will focus on only the most critical aspects of

these modalities.

3.1 The Significance of Multiphoton Microscopy

Nearly two decades ago, Denk et al. [3] developed nonlinear laser scanning microscopy (NLSM) or multi-photon microscopy (MPM) as an optical imaging modality that allows for micrometer-resolution imaging inside highly scattering tissue. Since that time, MPM has seen considerable use for *in vivo* studies, especially in the neurosciences (for reviews, see [4, 5]), where imaging in the mouse neocortex has reached up to [6] and in excess of [7] 1 mm.

The primary value of MPM is that it achieves *optical sectioning*–that is, the ability to construct a 3-dimensional image by imaging successive, axially-separated planes in isolation from each other–even in the presence of scattering media. Wide-field fluorescence microscopy achieves fluorescence excitation by uniform illumination of the sample, which allows for a large field of view (hence the name) to be imaged simultaneously. This form of microscopy is useful when examining fluorescently-labeled plated cells or fluorescently-stained thin ($\sim$ 10 μm) tissue sections. However, since fluorescence signal is produced everywhere there are fluorophores in the sample, optical sectioning is not possible. In contrast, confocal microscopy achieves optical sectioning by using an aperture to reject all light not originating from the focal volume. Thus, fluorescence is *excited* everywhere within the focused beam, but only *collected* from light originating in the focal plane. By scanning the position of the focus within a given plane, an image may be built up in a point-by-point fashion. Translation of the sample or movement of the focus axially shifts the image plane, allowing for 3-dimensional reconstruction of the specimen. However,

confocal microscopy requires the trajectory of emitted photons to be *ballistic*; that is, to have a return path to the objective devoid of scattering events. In other words, confocal microscopy provides optical sectioning in *transparent* media. In thick tissue, such as the rodent cortex, the assumption of ballistic photon trajectories is quickly lost and signal becomes washed-out.

The great power of MPM and specifically 2PEF is that it allows for optical sectioning regardless of scattering of, and hence, the trajectory of emitted fluorescence[1]. As we shall see in the next section, optical sectioning is achieved by *exciting* fluorescence only in the focal volume. Since we know *a priori* that *any* detected fluorescence could only have arisen within the focal volume, we need only measure the intensity of fluorescent emissions. By way of contrast, recall that in wide-field fluorescence we must simultaneously *measure* position and intensity of fluorescent emissions by creating an image directly, whereas in 2PEF we *know* position and only measure intensity.

The value of 2PEF microscopy should not be understated nor seen as an incremental contribution to biological imaging: it allows for imaging cellular and sub-cellular processes *in vivo* with the same resolution as was previously accessible only to *in vitro* or *in situ*[2] studies. This ability is useful for at least two profound reasons. First, *in vivo* imaging allows for the non-invasive capture of complex dynamic processes invisible to histological analysis. We discussed a number of these studies in the spinal cord in the previous chapter, but a particularly striking example of the relevance of dynamics was seen in the mouse neocortex in a recent paper by Fuhrmann et al. [8]. In this study, Fuhrmann et al. examined the interaction between microglia (labeled with green fluorescent protein (GFP)) and neurons (labeled with yellow fluorescent

[1]It should be noted that scattering will still exponentially diminish the power of the excitation beam, resulting in less generated fluorescence.

[2]For example, brain slice preparations.

protein (YFP)) in a mouse model of Alzheimer's disease. In mice containing the CX_3CR_1 receptor, microglia were observed to swarm affected neurons, induce their death, and subsequently disperse (see Fig. 3.1). Microglial density 100 μm distal to affected neurons did not differ from controls, indicative that uniformly increased microglial proliferation was not a consequence of gene knockout. In contrast, double CX_3CR_1 knockout mice[3] failed to show any of the pathological affects of microglial-mediated neuronal loss. It should be noted that fixed-point histology would only allow for a single panel to be seen in Fig. 3.1, making it difficult or impossible to establish microglia as mediators of neuronal death. Thus, 2PEF allows for the discovery of novel mechanisms–both physiological and pathological–as well as the monitoring of disease progression at the cellular and even sub-cellular level in an unprecedented way.

Second, 2PEF allows for studies of structures and processes *in vivo* for which there simply is not an *in vitro* analog. For example, the availability of calcium indicator fluorophores has extended the value of 2PEF beyond structural imaging to *functional* imaging, enabling an understanding of neuron activity, network structure, and recruitment at the cellular level. Dombeck et al. [9] have demonstrated the power of this technique by imaging calcium activity in awake, active mice. Their central hypothesis was that nature has chosen the most "cost-effective" way of arranging neurons, such that neurons that are correlated in activity are clustered spatially, thereby reducing the length of processes necessary for "wiring". Specifically, Dombeck et al. looked at the distinct behaviors of grooming and running and found that distinct

[3]In this strain of mouse, the CX_3CR_1 receptor protein is replaced (i.e. "knocked out") by a green fluorescent protein. Where mice would normally express the CX_3CR_1 receptor, they now express a fluorescent reporter protein. In mice that are heterozygous for this knockout, a single gene copy of CX_3CR_1 still exists, and the receptor is expressed on the surface of microglia. In double knockouts, microglia are missing the receptor entirely, and will be unable to bind the ligand, fractalkine or CX_3CL_1.

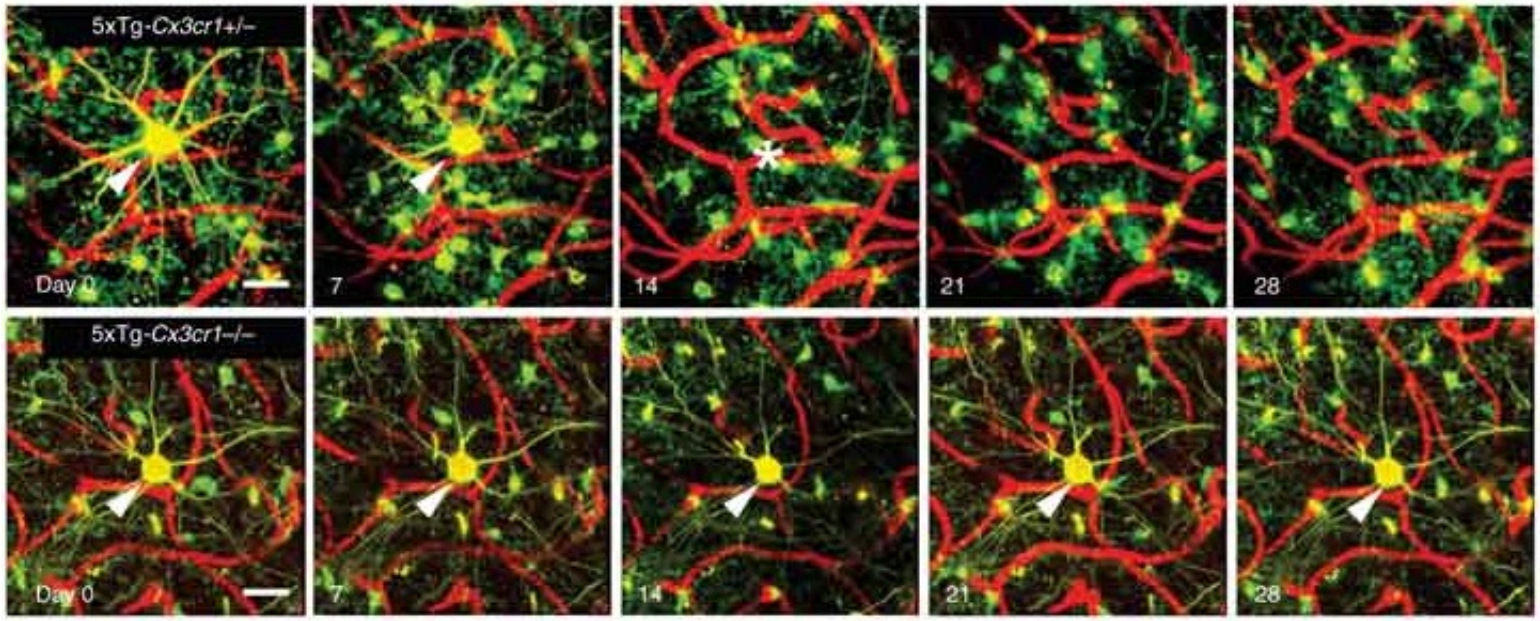

Figure 3.1: MPM shows that CX_3CR_1 receptor mediates microglial-induced neuronal death.
A mouse expressing GFP in microglia with either a single (*top*, +/-) or double (*bottom*, -/-) knockout of the CX_3CR_1 receptor shows that the CX_3CR_1 receptor is responsible for the death of neurons labeled with YFP (*arrows*) in mice over-expressing amyloid beta precursor protein, a model of Alzheimer's disease. Images were taken weekly for 4 weeks. Reprinted by permission from Macmillan Publishers Ltd: *Nature Neuroscience*, Fuhrmann, M. et al. , Microglial Cx3cr1 knockout prevents neuron loss in a mouse model of Alzheimers disease, **13**, 411-13, Copyright 2010.

populations of neurons had strongly correlated firing patterns corresponding to each behavior. Correlated neurons formed distinct clusters, and these clusters were often spatially distinct from one another even when associated with the same behavioral function, which is counterintuitive and opposed the central hypothesis. Yet, *within* each cluster, correlations in neuron activity were strongly linked to neuron spatial separation, with the strongest correlations in activity corresponding to the smallest distance, in agreement with the hypothesis. This finding provides a fundamental insight into the organization of neurons in the mammalian cortex. Moreover, the study explored relations of macroscopic animal behavior to cellular function and spatial organization at the level of individual neurons. 2PEF microscopy is the only technique currently available that can explore these questions on this scale.

Having provided some background on the immense value of MPM, we will now explore the underlying mechanism of these techniques.

3.2 MPM and Optical Sectioning

3.2.1 Nonlinear Optical Signals

By definition, the intensity of light, I_{NL}, produced from a nonlinear process of order[4] m depends on the m^{th} power of the laser intensity, I_L:

$$I_{NL} \propto I_L^m \tag{3.1}$$

[4]We here distinguish the order of the process according to its intensity dependence rather than the order of the nonlinear susceptibility tensor discussed in later sections, e.g. $\chi^{(3)}$ vs. $\chi^{(2)}$. For example, 2PEF is a $\chi^{(3)}$ process, but scales with the square of the laser intensity. We thus consider this to be a second-order process.

For a pulse with a square temporal profile focused to a spot size of area A, the laser intensity is given by:

$$I_L = \frac{E}{A\tau} \tag{3.2}$$

where E is the energy per pulse and τ is the pulse duration. The *nonlinear signal*, S_{NL}, detected at the microscope is then proportional to I_{NL} integrated over the pulse duration (the amount of signal produced throughout the pulse duration), the number of pulses per unit time (the signal produced from all the pulses combined) given by the laser repetition rate, R, and the area of the beam (the total signal produced everywhere in space), which by (3.1) gives:

$$\boxed{S_{NL} \propto \left(\frac{E}{A\tau}\right)^m AR\tau = \frac{E^m}{A^{m-1}\tau^{m-1}}R} \tag{3.3}$$

As we might expect, (3.3) predicts that tight focusing (i.e. using large numerical aperture (NA) lenses) to a small spot, large pulse energies, short pulse durations, and large repetition rates will result in large signal, and hence improved contrast. Alternatively, we may rewrite (3.3) in terms of the average power, given by:

$$\langle P \rangle = ER \tag{3.4}$$

which in turn gives:

$$\boxed{S_{NL} \propto \frac{\langle P \rangle^m}{A^{m-1}(\tau R)^{m-1}}} \tag{3.5}$$

Equation (3.5) is more useful from an experimental viewpoint, as we typically measure average power from a laser with a fixed repetition rate.

3.2.2 Key Focusing Parameters and Resolution

As could be seen above in (3.3) and (3.5), $S_{NL} \propto A^{-(m-1)}$. This fact provides the underlying logic of 2PEF microscopy: signal is only generated at areas of

high intensity, which for a focused Gaussian beam occurs only to an appreciable extent within the confocal volume.

To begin, we first note that all our analysis to date has been for a pulse with a square spatial and temporal profile, while in reality both are Gaussian or Gaussian-like. For our discussion in this section, it will be necessary to consider Gaussian beams. It can be shown that [1] the intensity of a Gaussian beam follows the shape:

$$I_L(r,z) = I_0 \left(\frac{w_0}{w(z)}\right)^2 \exp\left(-\frac{2r^2}{w^2(z)}\right) \tag{3.6}$$

where

$$w(z) = w_0\sqrt{1+(2z/kw_0^2)^2} \tag{3.7}$$

for peak intensity I_0, beam waist w_0, wave vector $k = 2\pi/\lambda$ for wavelength λ, radial coordinate r, and axial coordinate z . In a linear process, such as wide-field fluorescence microscopy, we may integrate (3.6) over the beam area to get the signal[5], $S(z)$:

$$S(z) = \int_0^\infty I(r,z)2\pi r dr = \frac{\pi w_0^2}{2} I_0 \tag{3.8}$$

Thus, for wide-field fluorescence or any linear excitation technique, the signal is independent of the position z (and hence lacks optical sectioning capabilities), as we might have guessed from (3.3).

We now turn our attention to higher order processes. For a process that scales as I_L^m, we have:

$$I_L^m(r,z) = I_0 \left(\frac{w_0}{w(z)}\right)^{2m} \exp\left(-\frac{2mr^2}{w^2(z)}\right) \tag{3.9}$$

Integrating over the area:

$$S_m(z) = \int_0^\infty I(r,z)2\pi r dr = \frac{\pi w_0^2}{2m}\left(\frac{w_0}{w(z)}\right)^{2(m-1)} I_0 \tag{3.10}$$

[5]Of course, the signal will depend on the sample as well. For fluorescence, we would need to multiply by concentration and the absorption cross-section to get the true signal.

or more explicitly

$$S_m(z) = \frac{\pi w_0^2}{2m} \left(\frac{1}{1 + (2z/kw_0^2)^2} \right)^{m-1} I_0 \tag{3.11}$$

As is clear from $S_m(z)$, we now have a signal that depends strongly on the position z, meaning that even if the sample is uniform, signal will be generated preferentially at the focus, giving rise to optical sectioning. The confocal parameter, b, is defined [1] to be:

$$b \equiv kw_0^2 \tag{3.12}$$

which gives the approximate z resolution of the process. For an Airy point spread function (PSF) [2], the beam waist (i.e. diffraction limit) is related to the numerical aperture of the objective by:

$$w_0 = \frac{\lambda}{2\text{NA}} \tag{3.13}$$

A plot of normalized intensity using (3.11) for $m = 2, 3$ is shown in Figure 3.2.

3.2.3 Experimental Setup

Since we know the origin of any nonlinear signal to arise from the focal volume of an objective, we need only move the point of interest and measure the signal, recording the known location and intensity. We might imagine doing this by scanning the sample underneath an objective, but this would result in much slower acquisition than is possible using other techniques. Typically then, the angle of the beam is scanned using galvanometric mirrors or similar devices. Figure 3.3 shows a depiction of the microscope used in our studies. Briefly, femtosecond infrared laser pulses are incident on the scan mirrors,

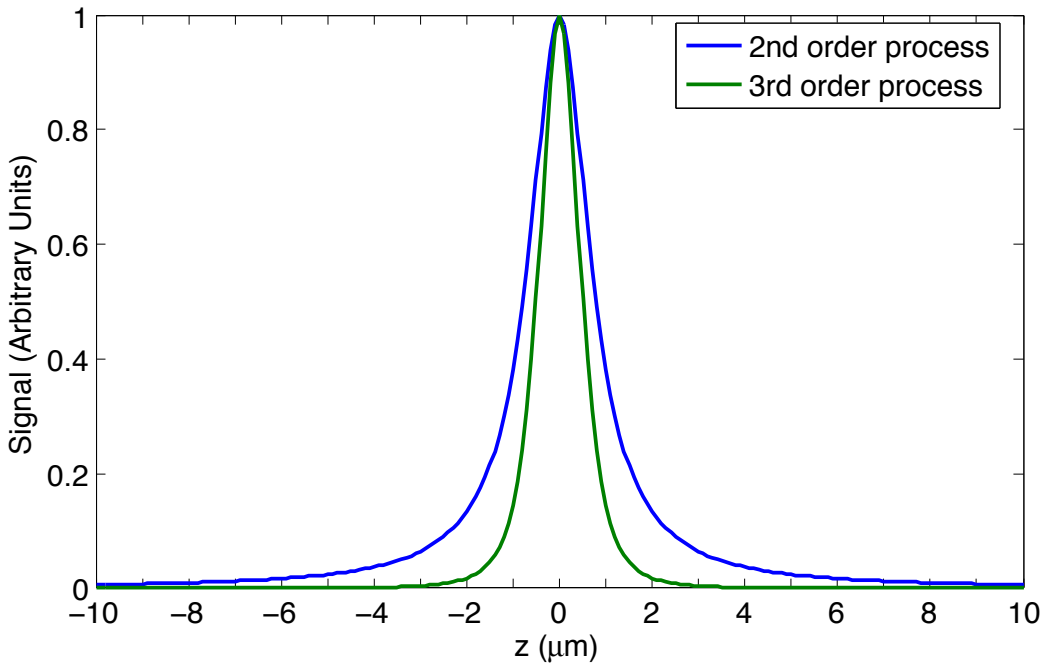

Figure 3.2: Signal as a function of position z for a focused Gaussian beam. For an objective of NA $= 1$, we show the signal intensity profile for a second- (*blue*) and third-order (*green*) process. A linear process is independent of depth.

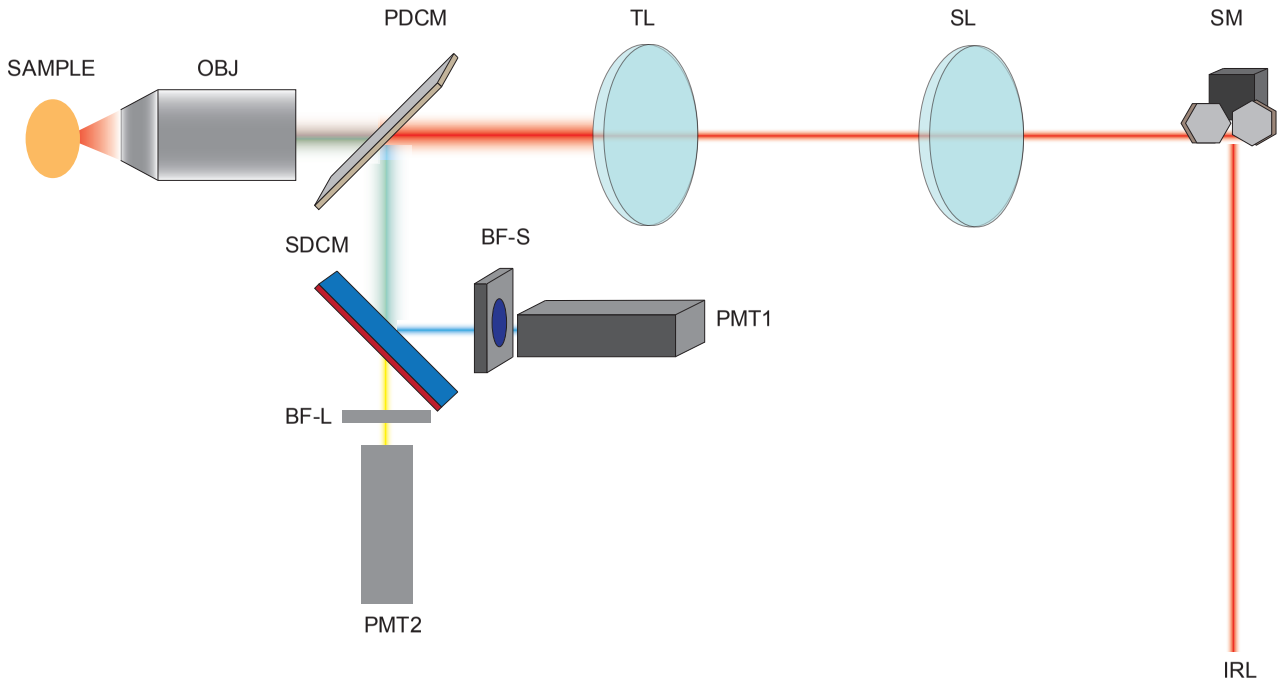

Figure 3.3: Multiphoton microscope setup.
An infrared laser pulse (IRL) is deflected off of rapidly rotating scan mirrors (SM) passing through a tube lens (TL) and a scan lens (SL) which vary the angle of the beam (though not its position) at the back aperture of the objective (OBJ). The generated fluorescence is deflected by the primary dichroic mirror (PDCM) and the light is subsequently split into 2 channels at the secondary dichroic mirror (SDCM). Blocking filters BF-S and BF-L filter the short and long fluorescent wavelengths, respectively. The fluorescent light is detected by photomultiplier tubes (PMT1 and PMT2).

which vary the azimuthal and planar angle of the light. The scan lens/tube lens combination works by forming an image of the scan mirrors at the back aperture of the objective, thus allowing angle to change *without* varying the position. This process assures maximal filling of the back aperture (and so maximizes the effective NA of the objective), while allowing the angle (and thus the xy position in the sample) to vary rapidly. (For a discussion of some of the finer details of under-filling or over-filling the back aperture, see [10]). Translation in z is achieved either by translation of the stage (as in our setup), or by translation of the objective. Faster z-scanning has been achieved by the use of electronically tunable lenses [11], where small changes in current can change the focal length of a lens prior to entry at the back aperture. Alternatively, acoustically tunable gradient index of refraction lenses (TAG lenses) [12, 13] have also been used. Fast scanning in the xy plane as well as in z has been achieved using pairs of acousto-optic deflectors (AODs) [14–16].

3.3 Two-Photon Excited Fluorescence

Since 2PEF was the first modality developed [3], and since the availability of bright exogenous fluorophores and transgenic mice expressing brilliant fluorescent proteins continues to improve and expand, 2PEF has dominated the nonlinear imaging scene. Physically, 2PEF occurs when an electron is promoted to a higher energy state by the absorption of two photons with individual photon energies below the energy gap, but whose sum exceeds it. Subsequent internal conversion and emission of light follows similarly to the more common single-photon excited fluorescence. However, due to the nonlinearity of 2PEF, careful analysis of laser parameters to optimize signal while avoiding saturation

must carefully be determined, which is the subject of this section.

3.3.1 Signal and Saturation

The instantaneous 2PEF power, w_f, produced by excitation from a laser with intensity I_L is often expressed as [2]:

$$w_f = \sigma_{2PEF} I_L^2 \tag{3.14}$$

where σ_{2PEF} is the two-photon excitation fluorescence cross-section[6]. Due to internal conversion, σ_{2PEF} is properly distinguished from the two-photon *absorption* (2PA) cross-section, σ_{2PA}, and is related by:

$$\sigma_{2PEF} = \Phi \sigma_{2PA} \tag{3.15}$$

where Φ is the quantum efficiency which ranges between 0 and 1 and is defined as:

$$\Phi = \frac{2 \times \text{number of photons emitted}}{\text{number of photons absorbed}} \tag{3.16}$$

It is often desirable to talk of power in number of photons rather than the SI equivalent, which can be achieved by expressing intensities in terms of photons by dividing by $h\nu$, where h is Planck's constant and ν is the relevant frequency. This gives the conventional two-photon cross-section in the Göppert-Mayer (GM) unit[7], which is related to the SI equivalent according to [2]:

$$\sigma_{2GM} = \left(\frac{\nu_f}{2\nu}\right) \frac{10^{-58}}{h\nu} \sigma_{2PEF} \tag{3.17}$$

where ν_f and ν are the fluorescence and excitation frequencies, respectively. To see this relation, we first note that the units of σ_{2PEF} are W^{-1}m^4. The total

[6]Technically speaking, σ_{2PEF} is the two-photon excitation fluorescence *action* cross-section, since it depends on intensity and has units W^{-1}m^4. A true cross-section is thus $\sigma_{2PEF} I_L$, which has units of area.

[7]1 GM = 10^{-50} $\text{cm}^4\text{s}/\text{photons}$

number of incident photons is given by dividing by the incident photon energy $h\nu$. These photons are converted to fluorescent photons of frequency ν_f at a rate of one for every two incident photons at frequency ν. The number of fluorescent photons is thus the product of the number of incident photons with the conversion rate. The conversion from m^4 to cm^4 results in an additional factor of 10^{-8}.

For a square pulse of duration τ and energy E, the average fluorescence energy per pulse is simply:

$$\tau w_f = \frac{\sigma_{2PEF} E^2}{\tau A(z)^2} \tag{3.18}$$

where A is the cross-sectional area of the pulse at position z, with $z = 0$ corresponding to the focal plane. For an ensemble of N fluorescent molecules inside the focal volume, V, with concentration C, the total fluorescence is simply $N \times \tau w_f$, which gives:

$$N\tau w_F = CV\tau w_f = CV\frac{\sigma_{2PEF} E^2}{\tau A(z)^2} \tag{3.19}$$

Unlike SHG and THG (discussed in the Section 3.4.1) which do not involve change in the electron populations, 2PEF involves real (as opposed to virtual) electron transitions and relaxations. Consequently, at sufficiently large excitation intensities, it is possible to excite *all* of the dye molecules in the focal volume, such that any further increase in excitation intensity does not produce any change in w_f. Such an occurrence is undesirable as it changes the shape of the point spread function (PSF) to a "top hat" shape, resulting in loss of resolution. Relaxation times, Γ_f^{-1}, are on the order of a few nanoseconds [17], consistent with Fermi's Golden Rule, so molecules certainly cannot relax within a pulse duration. To avoid cumulative saturation, we set an upper bound on pulse repetition rate of approximately $R \ll \Gamma_f \sim 1$ GHz. This limit has been proposed and achieved by Ji et al. [18], and will be examined again later in

this section. It should also be noted that for $\tau \sim 100$ fs $\ll 1$ ns, no molecule is excited twice by the same pulse, so we restrict our considerations to single pulse saturation.

Effective imaging is bounded below by fluorescence detection which requires a minimum of one photon per pixel, which is the product of the expected number of photons per pulse times the pulse repetition rate, R, and the pixel dwell time. As a rough guide, let us assume that we are at the limits of scan speed and this means we need a minimum of 1 photon per pulse. Imaging is bounded above by dye saturation[8]. In the first case, we set the left hand side of (3.19) equal to a single photon energy, and in the second instance, we naïvely set it equal to $Nh\nu_f = CVh\nu_f$ [9]. For $\tau \sim 100$ fs, $A \sim 1\mu$m^2, and typical values for excitation wavelength ($\sim$1 μm) and fluorescence wavelength (500 nm), saturation occurs at energy:

$$\boxed{E \approx 10/\sqrt{\sigma_{2GM}}\ \text{nJ}\cdot\text{GM}^{\frac{1}{2}}} \tag{3.20}$$

Equation (3.20) gives the appropriate energy scale in the nJ range, and the scaling gives 2 orders of magnitude change in σ_{2GM} per order of magnitude change in saturation energy.

This result, however, was based upon a concentration that is uniform for all time. Of course, this is not true since dye molecules that are in the excited state can no longer be excited, and the concentration of molecules in the ground state becomes depleted. In addition, we must take into account two-photon stimulated emission, which will repopulate the ground state.

[8] Or by photodamage, which we shall discuss later in this chapter

[9] This limit assumes a quantum efficiency of unity. It is possible to have all the relevant molecules in an excited state that does not result in fluorescent decay. For example, hemoglobin has a quantum efficiency of 0, but σ_{2PA} as high as 150 GM [19]. Conversely, fluorescein has an efficiency of $\Phi = 0.9$ [20] and at its peak, $\sigma_{2PA} = 37$ GM or $\sigma_{2GM} = 33$ GM [21]. Thus, the validity of the approximation of $\Phi = 1$ is dye dependent, although the correction is not a difficult one to make.

To deal with this complication, we model our molecule as a two-level system with a total of N molecules, with N_g molecules in the ground state and N_e in the excited state. The number of molecules in the ground state is depleted by two-photon absorption and populated by both spontaneous excited state relaxation, occuring at a rate Γ_f^{-1}, and two-photon stimulated emission, proportional to the two-photon stimulated emission cross-section, σ_{2SE}, and the square of the intensity . That is:

$$\frac{dN_g}{dt} = -\sigma_{2GM}\left(\frac{I(t)}{h\nu}\right)^2 N_g + (\Gamma_f + \sigma_{2SE}\left(\frac{I(t)}{h\nu}\right)^2)N_e \tag{3.21}$$

Since we have $N_g(0) = N$ or $N_e(0) = 0$, and since Γ_f is on the order of GHz, compared to the femtosecond duration of $I(t)$, we ignore the spontaneous decay term[10]. After making the substitution, $N_e = N - N_g$, this gives:

$$\frac{dN_g(t)}{dt} = -(\sigma_{2GM} + \sigma_{2SE})\left(\frac{I(t)^2}{(h\nu)^2}\right) N_g + \sigma_{2SE}\left(\frac{I(t)}{h\nu}\right)^2)N \tag{3.22}$$

This is a linear ODE, which for a square pulse can be solved exactly to give:

$$N_g(\tau)/N = [1 - \frac{\sigma_{2SE}}{\sigma_{eff}}]\exp\left(-\sigma_{eff}\frac{(E/h\nu)^2}{A^2\tau}\right) + \frac{\sigma_{2SE}}{\sigma_{eff}} \tag{3.23}$$

where $\sigma_{eff} = \sigma_{2GM} + \sigma_{2SE}$. By consideration of Fermi's Golden Rule, we expect $\sigma_{2GM} = \sigma_{2SE}$, and so we arrive at:

$$\boxed{N_g(\tau)/N = \frac{1}{2}[1 + \exp\left(-2\sigma_{2PEF}\frac{(E)^2}{A^2\tau}\right)]} \tag{3.24}$$

Appreciable saturation occurs when the argument of the exponential in (3.24) is of order unity, which agrees to within a factor of 2 with our naïve estimate. Physically, this requires us to redefine "saturation", since (3.24) gives a decaying exponential with increased pulse energy, rather than a hard cut-off. Moreover,

[10]Put differently, saturation requires the first term in (3.21) to be of order N/τ to excite all molecules in one pulse. Conversely, at the end of the pulse, $N = N_e$, and the second term has order $N\Gamma_f$. Thus, the ratio of the excitation and decay rates amounts to $\Gamma_f^{-1}/\tau \gg 1$.

(3.24) shows us that even the asymptote corresponds to 1/2 the total number of molecules being excited, rather than all the molecules as in our previous estimate. Since a factor of $\sqrt{2}$ is already well within our approximation, we let (3.20) stand as a guideline. For a bright dye ($\sigma_{2GM} = 100$ GM), this happens at pulse energies as low as 1 nJ, while for a dim dye ($\sigma_{2GM} = 0.5$ GM), this happens at approximately 15 nJ. For a typical Ti:Sapphire laser with a repetition rate of around 100 MHz, this corresponds to average powers of 100 mW and 1.4 W for the bright and dim dye, respectively, both of which are well above the average power damage threshold we discuss later. In contrast, for our 1 MHz fiber laser, these shift to average powers of 1 mW and 14 mW for the bright and dim dyes, respectively. Since these are experimentally relevant values at 1 MHz, consideration of saturation cannot be ignored for low repetition rate sources.

We now consider the opposite extreme, where we are signal limited. The focal volume of interest is $V_{2f} = w_0^2 b$ where w_0 is the beam waist at the focus and b is the confocal parameter. Typical values are $w_0 = b = 1\mu$m and concentrations of 10^4 μm^{-3} [11]. Plugging these numbers in as before gives a minimum pulse energy, E_{min}, of:

$$\boxed{E_{min} = \frac{0.1}{\sqrt{\sigma_{2GM}}} \text{ nJ}\cdot\text{GM}^{\frac{1}{2}}} \tag{3.25}$$

or about a factor of 100 away from the saturation point. Trivially, this gives a minimum pulse energy of 0.01 nJ and 0.14 nJ for a bright and dim dye, respectively. Consideration of repetition rate gives average powers of 1 mW and 14 mW at 100 MHz and 0.01 mW and 0.14 mW at 1 MHz for each dye, respectively. If we consider imaging of a weak dye at 100 MHz, a maximum signal of 4 photons per pulse is achieved before the onset of thermal damage

[11] Based on vascular labeling in mice. A 70 000 MW dextran with 4 dye molecules/dextran at 5 % weight solution is injected at 0.1 mL into an animal of average blood volume 1.5 mL, for an average fluorophore concentration on the order of 10^{16} fluorophores/mL or 10^4 fluorphores/μm^3.

at around 60 mW. In contrast, at 1 MHz, pulse energy can be increased until the ablative damage threshold at 30 mW is reached, giving a 200 fold per-pulse increase in signal[12]. Conversely, if both a weak and a strong dye are simultaneously excited, the upper bound is set by the saturation of the strong dye at 1 mW at 1 MHz, limiting the weak dye to a more modest 7-fold signal increase.

Finally, we must consider that the *integrated* signal increases linearly with pulse repetition rate. Thus, by (3.19), the integrated 2PEF power, W_f, is given by:

$$W_f = N\tau w_f \times R = CV\frac{\sigma_{2PEF}E^2}{\tau A(z)^2}R \tag{3.26}$$

or expressed in terms of average power:

$$W_f = CV\frac{\sigma_{2PEF}\langle P\rangle^2}{\tau A(z)^2 R} \tag{3.27}$$

in good agreement with (3.3) and (3.5). Figures 3.4 and 3.5 show a summary of these calculations. In general, curves of constant two-photon power, w_f have slope-1/2 on a log-log plot of E vs R, with increasing two-photon power moving up to the right. Changing σ_{2PEF} on these plots adjusts only the y-intercept. Maximum signal without damage is thus obtained at the intersection of the average power damage threshold and the saturation threshold for a given dye, or the nonlinear damage threshold for a very weak dye. Since harmonic generation (which will be discussed in the next section) is a coherent effect[13] that does not saturate, the only consideration for SHG and THG is given by (3.3), making the point of maximum signal for both SHG and THG occur at the

[12]Damage thresholds and their determination are discussed in Section 3.5

[13]From a density matrix formalism point of view, 2PEF results in changes in diagonal (population) terms because there is a real energy transition for the electron, whereas SHG and THG affect only off-diagonal terms (polarization)

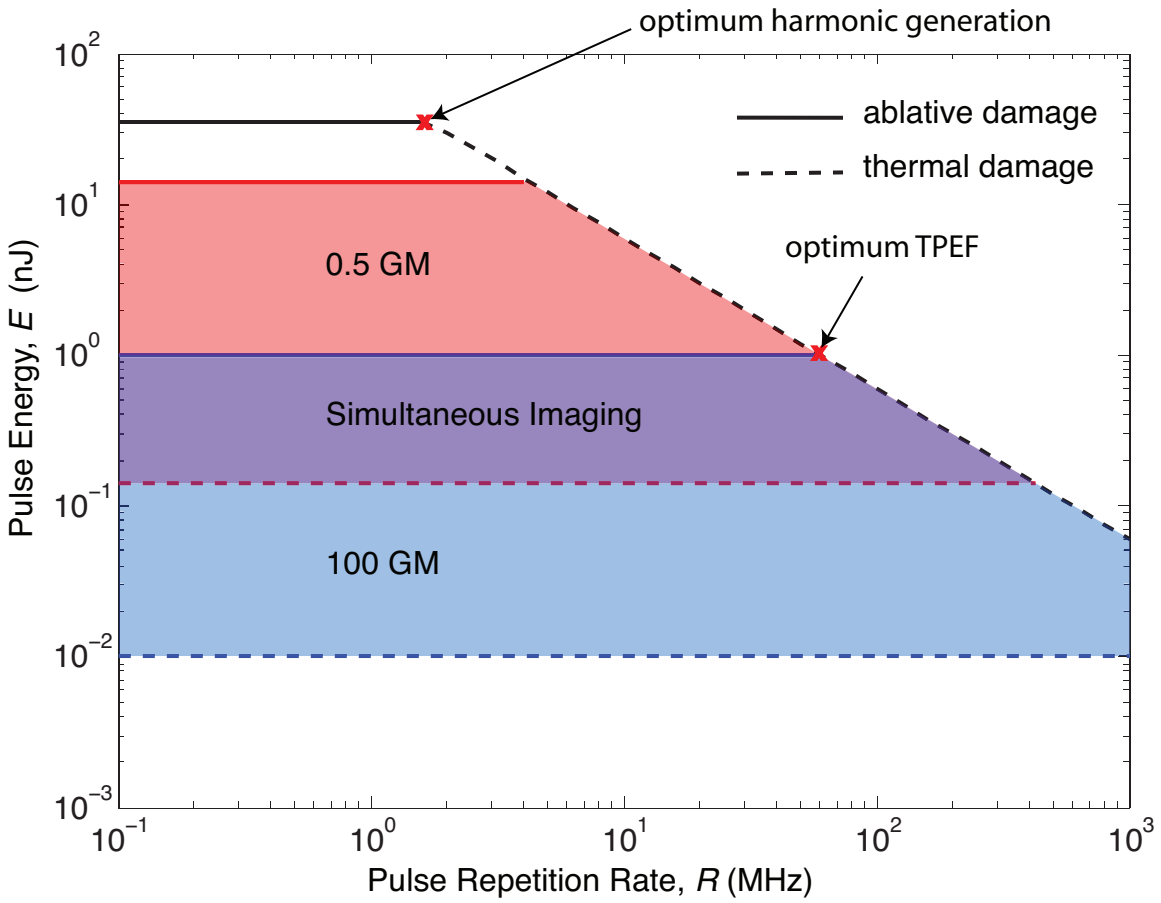

Figure 3.4: Boundary mapping of 2PEF excitation in pulse energy-repetition rate space.
Area outside the damage thresholds limit the regime of possible laser parameters. There is another limit (not shown) at the GHz scale, where the delay between pulses is shorter than the relaxation time of the dye. Results of boundary calculations for a 100 GM dye (*blue*) and a 0.5 GM dye (*red*) are shown, with shaded regions showing the experimentally relevant regimes. Solid lines mark dye saturation levels, dashed lines mark the single-photon-production-per-pulse limit, marking the top and bottom of the regimes, respectively.

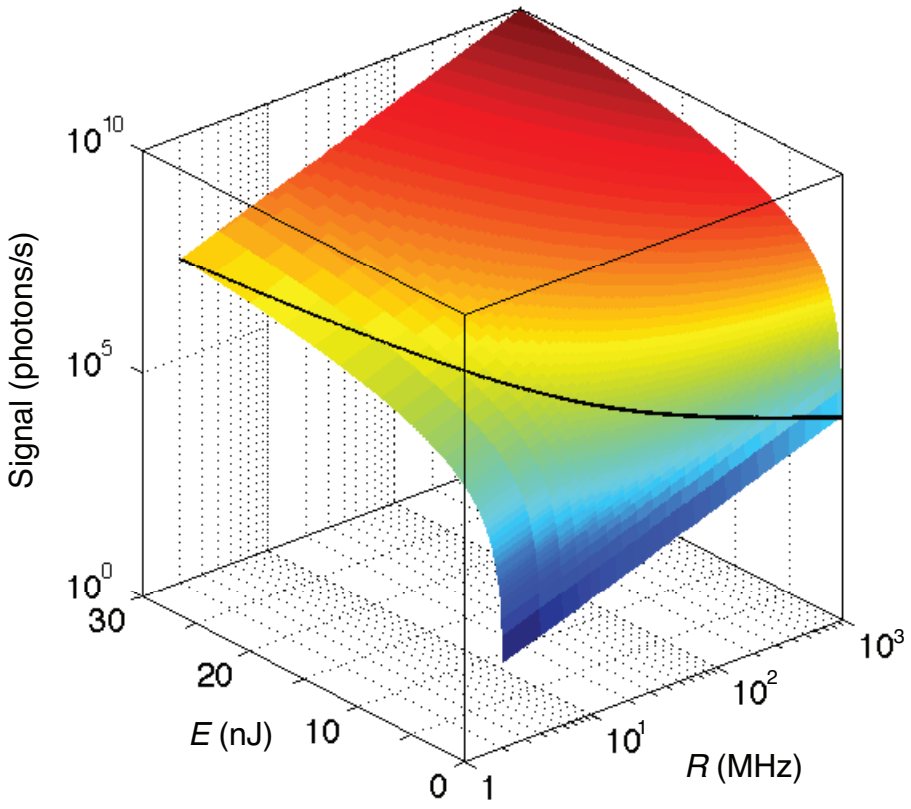

Figure 3.5: 2PEF photon production rate as a function of pulse repetition rate, *R*, and pulse energy, *E* for 100 GM dye.
Signal scales quadratically in *E* and linearly in *R*. The black solid line marks the average power damage threshold.

intersection of the ablative and thermal damage limits[14] (see Figure 3.4). As is evident from Fig. 3.4, simultaneous imaging of dim and bright dyes will pose a challenge, as increasing signal-to-noise for a dim dye may push the bright dye beyond the point of saturation. This concern is not merely theoretical. For example, 2PEF imaging of metabolic activity *in vivo* using intrinsic NADH fluorescence and its relation to microvascular perfusion by FITC (a fluorescein derivative) dextran [22] were simultaneously assessed at 740 nm excitation in the context of cortical spreading depression. At this wavelength, NADH has $\sigma_{2GM} \approx 0.1$ GM [23] while fluorescein has $\sigma_{2GM} \approx 30$ GM [21]. Thus, the high-repetition rate systems of Ji et al. [18] are not necessarily ideal for every process of interest, but would enable faster scanning for bright dyes.

3.4 Harmonic Generation

Harmonic generation (HG), is another nonlinear optical phenomenon. Experimentally, performance of HG imaging is identical to 2PEF, with spectral isolation of the harmonic of interest achieved by spectral selection filters in the same way as for fluorescence emission. In light of the similarities, and since SHG and THG are often generated from contrast arising within the tissue of interest itself, it is tempting to confuse SHG and THG with *endogenous* 2PEF or three-photon excited fluorescence (3PEF). However, this would be a great mistake, since the physical mechanisms are quite different. One key difference between HG and 2PEF is that for HG, the electron never enters an excited state,

[14]To see this limit intuitively, consider that the slope of the thermal damage limit on a log-log plot of E vs. R is -1, while the slopes for lines of constant SHG and THG signal are -1/2 and -1/3, respectively. The intersection of the lines of constant harmonic generation signal with the thermal damage limit is always obtuse, making the intersection with damage limits a unique maximum.

while for 2PEF, it does. To understand this distinction, we must consider non-absorptive material responses to an applied electric field.

3.4.1 Signal Origins

In Section 3.2.1, we found that a simple consideration of the *definition* of nonlinear optical signals was sufficient to explain optical sectioning, and we found that 2PEF followed this analysis closely with the addition of the pre-factor, σ_{2PEF}. However, this analysis is somewhat misleading because we have completely ignored the underlying physics giving rise to such a signal. In reality, nonlinear optical phenomena occur in media that respond to an applied electric field, $\mathbf{E}$, by giving rise to a material polarization or dipole per unit volume, $\mathbf{P}$. This polarization may be written in terms of a Taylor expansion of the electric field:

$$\mathbf{P} = \epsilon_0[\chi^{(1)}\mathbf{E} + \chi^{(2)}\mathbf{E}^2 + \chi^{(3)}\mathbf{E}^3 + \ldots] \tag{3.28}$$

where ϵ_0 is the permittivity of free space[15] and the coefficients, $\chi^{(n)}$, are the n^{th} order susceptibility tensors[16]. Thus, at a given point in the sample, a single monochromatic field of the form

$$E(t) = E_0 \exp(i\omega t) + E_0^* \exp(-i\omega t) = E_0 \exp(i\omega t) + c.c. \tag{3.29}$$

[15]SI units will be used here and throughout as a matter of convention and for ease of comparison with experimentally measured values.

[16]The terms in the expansion (3.28) are properly understood as tensorial products, which we have written in shorthand as "powers" of the electric field. Of course, the electric field is a vector, which cannot be simply "squared" as a scalar. However, since we will be treating the susceptibility tensors as scalars (i.e. working along principal axes in isotropic materials), we will omit their tensorial nature.

where ω is the field frequency, E_0 the field strength, and $c.c.$ denotes complex conjugate will give rise to a material response at frequencies:

$$\chi^{(1)} : \omega \tag{3.30}$$

$$\chi^{(2)} : 2\omega, 0(\text{DC}) \tag{3.31}$$

$$\chi^{(3)} : 3\omega, \omega \tag{3.32}$$

These terms arise straightforwardly from all possible combinations of the given power of the field in each term. However, it is worth noting that in contrast to the considerations in Section 3.2.1, we are now working with *fields*, and not merely *intensities*, which as a general rule means that phase is important. To understand the importance of this aspect, as well as how induced changes in the medium give rise to new output frequencies, we must turn to the nonlinear wave equation.

3.4.2 The Nonlinear Wave Equation

Applying Maxwell's equations to the polarization given in (3.28), along with the slowly varying envelope approximation and assumption of small divergence in $\mathbf{E}$ [1], we easily arrive at the nonlinear wave equation. For an electric field propagating in the z direction of the form:

$$\mathbf{E_j} = \mathbf{A_j}(\mathbf{r}) \exp[i(k_j z - \omega_j t)] + c.c. \tag{3.33}$$

where subscript j denotes the component of the field corresponding to frequency ω_j, the wave equation takes the form:

$$\{\nabla_T^2 \mathbf{A_j} + 2ik_j \frac{\partial \mathbf{A_j}}{\partial z}\} \exp(i[k_j z - \omega_j t]) = \frac{1}{c^2} \frac{\partial^2 (\mathbf{P_{NL,j}}/\epsilon_0)}{\partial t^2} \tag{3.34}$$

where $\nabla_T^2 = \partial^2/\partial x^2 + \partial^2/\partial y^2$ is the transverse Laplacian and $\mathbf{P_{NL,j}}$ is the nonlinear polarization at frequency ω_j. By the requirements of linear independence, we take $\mathbf{P_{NL,j}}$ to have the form:

$$\mathbf{P_{NL,j}} = \mathbf{P_j}(\mathbf{r}) \exp(i[k_j z - \omega_j t]) \tag{3.35}$$

which when inserted into (3.34) yields:

$$\boxed{\{\nabla_T^2 \mathbf{A_j} + 2ik_j \frac{\partial \mathbf{A_j}}{\partial z}\} = -\frac{\omega_j^2}{c^2}(\mathbf{P_j}/\epsilon_0)} \tag{3.36}$$

Equation (3.36) is the nonlinear wave equation. Great insights can be gained in harmonic generation by consideration of this equation in its plane-wave form alone, to which we now turn our attention.

3.4.3 Plane Wave Approximation

The simplest consideration is a homogeneous, isotropic material in the plane wave limit. In this case, the first term in (3.36) vanishes identically. This gives the simple governing equation:

$$\frac{dA_j(z)}{d_z} = i\frac{\omega_j^2}{2k_j c^2} P_j(z)/\epsilon_0 \tag{3.37}$$

Since the work in this thesis is focused on THG (see Chapter 4), we consider a centrosymmetric molecular structure for which $\chi^{(2)} = 0$, though the procedure for second harmonic generation is completely analogous. We thus have by (3.28)[17]:

$$P = \epsilon_0 \chi^{(3)} \{A_1(z) \exp(i[k_1 z - \omega_1 t]) + A_3(z) \exp(i[k_3 z - \omega_3 t]) + c.c.\}^3 \tag{3.38}$$

[17] We drop the notation of the subscript "NL" from hereon in, but it is implicit.

Noting that $\omega_3 = 3\omega_1 \equiv 3\omega$, we collect terms proportional to $\exp(-i3\omega t)$ to get:

$$P_3 = \epsilon_0 \chi^{(3)}[A_1^3 \exp(i3k_1 z) + A_3^2 A_3^* \exp(ik_3 z)] \exp(-i3\omega t) \tag{3.39}$$

In most applications, the pump beam magnitude, $|A_1(z)|$, is considerably larger than the harmonic,$|A_3|$, so we neglect those terms of supralinear order in the third harmonic field, or:

$$P_3 = \epsilon_0 \chi^{(3)}(3\omega; \omega, \omega, \omega) A_1^3 \exp(i[3k_1 z - 3\omega t]) \tag{3.40}$$

But by (3.35), we have:

$$P_3 = P_3(z) \exp(i[k_3 z - 3\omega t]) \tag{3.41}$$

which is true if and only if:

$$P_3(z) = \epsilon_0 \chi^{(3)}(3\omega; \omega, \omega, \omega) A_1^3 \exp(i[3k_1 - k_3]z) = \epsilon_0 \chi^{(3)}(3\omega; \omega, \omega, \omega) A_1^3 \exp(i\Delta k z) \tag{3.42}$$

where

$$\Delta k \equiv 3k_1 - k_3 \tag{3.43}$$

is the wave-vector mismatch[18]. Inserting (3.42) into (3.37) then gives:

$$\frac{dA_3}{dz} = \frac{i(3\omega)^2}{2k_3 c^2} \chi^{(3)}(3\omega; \omega, \omega, \omega) A_1^3 \exp(i\Delta k z) \tag{3.44}$$

Since A_1 also has a nonlinear component and is coupled to A_3 in (3.44), we perform a similar calculation:

$$\frac{dA_1}{dz} = \frac{i\omega^2}{2k_1 c^2}[\chi^{(3)}(\omega; \omega, \omega, -\omega)|A_1|^2 A_1 + 3\chi^{(3)}(\omega; 3\omega, -\omega, -\omega) A_3 A_1^{*2} \exp(-i\Delta k z)] \tag{3.45}$$

where the factor of 3 is a result of the combinatorics of cross terms in (3.38). Since $A_1 \gg A_3$, we ignore the second term to get explicitly:

$$\frac{dA_1}{dz} = \frac{i\omega^2}{2k_1 c^2} \chi^{(3)}(\omega; \omega, \omega, -\omega)|A_1|^2 A_1 \tag{3.46}$$

[18]This is sometimes referred to as the *phase mismatch*, which is a misnomer since the phase is actually the product of the wave-vector mismatch with a length.

For a strong pump and weak harmonic generation, $|A_1|^2 \approx$ constant, and we are left with:

$$A_1(z) = A_1(0) \exp\left(\frac{i\omega^2}{2k_1c^2}\chi^{(3)}(\omega;\omega,\omega,-\omega)|A_1|^2 z\right) \tag{3.47}$$

Substitution of (3.47) into (3.44) gives:

$$\frac{dA_3}{dz} = \frac{i(3\omega)^2}{2k_3c^2}\chi^{(3)}(3\omega;\omega,\omega,\omega)A_1(0)^3 \exp(i\Delta k z) \exp\left(\frac{i3\omega^2}{2k_1c^2}\chi^{(3)}(\omega;\omega,\omega,-\omega)|A_1|^2 z\right) \tag{3.48}$$

Since Δk is a linear effect owing to material dispersion, whereas the second exponential in (3.48) owes to a nonlinear effect, we may ignore the second exponential as contributing a small effect only. Integrating then gives:

$$A_3(z) = \frac{(3\omega)^2}{2k_3c^2}\chi^{(3)}(3\omega;\omega,\omega,\omega)A_1(0)^3 \frac{\exp(i\Delta k z) - 1}{\Delta k} \tag{3.49}$$

where we have assumed that no third harmonic exists prior to entering the material, which we take to be semi-infinite and beginning at $z = 0$ (i.e. $A_3(z = 0) = 0$). Using the link between the field envelope, A, and intensity:

$$I = 2n_\omega \epsilon_0 c|A|^2 \tag{3.50}$$

where n_ω is the index of refraction for frequency ω, we have:

$$\boxed{I_3(z) = \frac{9\omega^2}{16c^4\epsilon_0^2 n_\omega^3 n_{3\omega}}|\chi^{(3)}|^2 \left(\frac{\sin(\Delta k z/2)}{\Delta k/2}\right)^2 I_1^3} \tag{3.51}$$

Figure 3.6 shows the results of the oscillatory nature of (3.51).

It is worth making a few remarks about (3.51). First, we note that our intuition based on (3.1) is correct, in that $I_3 \propto I_1^3$ is verified by explicit calculation. However, we also see the important role of phase in this process, as introduced through the existence of a coherence length, L_{coh} defined by:

$$L_{coh} \equiv \Delta k^{-1} \tag{3.52}$$

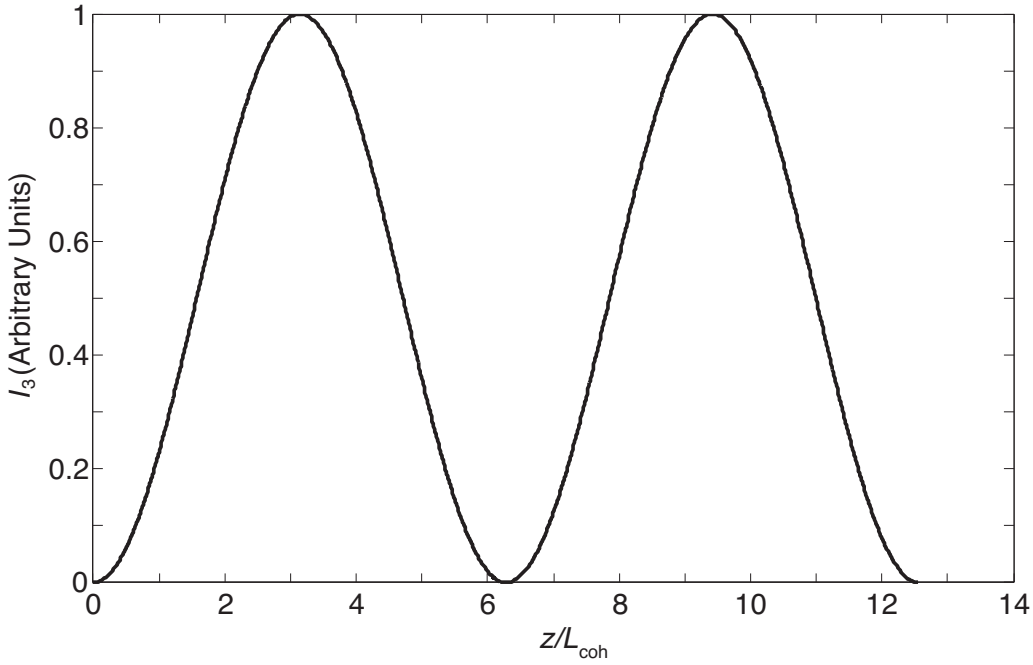

Figure 3.6: Plot of THG intensity as a function of length.
The oscillatory nature of the signal shows the importance of phase in this coherent process. Position is measured in units of coherence length, $L_{coh} = \Delta k^{-1}$.

For $\Delta k \neq 0$, I_3 is an oscillatory function of position, reaching a maximum when $z = (2n+1)\pi L_{coh}$ for integer n, whereas if the exponentials in (3.48) disappear, we have unbounded quadratic growth in z. Thus, unlike the absorptive $\chi^{(3)}$ process[19], THG in a material with a large value of $\chi^{(3)}$ will not necessarily give rise to a large THG signal. This phase dependence is why THG is called a *coherent* process. It is also called a parametric process [1], which means that the electron begins and ends in the same state. In contrast, 2PEF is a non-parametric process since the electron is promoted to a real energy level.

Another property of THG is that it is forward generated, unlike the isotropic emission of fluorescence. This property is also clear from (3.51). For example, for backward generation of TH light (i.e. $k_3 \rightarrow -k_3$), we have that $\Delta k = 3k_1 - k_3 = 3\omega/c(n_\omega - n_{3\omega}) \rightarrow 3\omega/c(n_\omega + n_{3\omega})$, which results in a decrease in L_{coh} (Δk) by approximately 3 orders of magnitude. Paraxial focusing (relevant to microscopy) introduces an additional phase, the Guoy phase [1], which further restricts efficient production to optical interfaces. In addition, our boundary condition for paraxial beams is that $A_3(-\infty) = 0$, with the precise form of A_3 depending on the shape of beam A_1. Since this derivation is shown explicitly in [1] and an example is given in a later chapter on the use of THG for imaging myelin, we shall not repeat the details here.

3.4.4 SHG and THG: Molecular Ordering

Both SHG and THG are coherent, parametric processes, meaning that they both depend on phase and involve wave-vector mismatch. Our intuition from (3.1)

[19]It may seem like the title "two-photon" should suggest a $\chi^{(2)}$ process. However, it is important to keep in mind that a photon corresponds to two powers of the electric field, so that we might equivalently call 2PEF "four-field-excited fluorescence". THG also involves four fields: three at frequency ω and one at frequency 3ω.

serves us well in that SHG scales as the square of the input field. However, SHG and THG are fundamentally different in a number of salient ways. First, SHG can only occur in molecules which lack centrosymmetry, and hence, have $\chi^{(2)} \neq 0$. To see this property of SHG, consider an electron sitting in a potential $V(x)$ which has the Taylor expansion:

$$V(x) \approx ax^2 + bx^3 + cx^4 + \dots \tag{3.53}$$

Centrosymmetry is the requirement that $V(x) = V(-x)$. This requirement is met if and only if $b = 0$. A straight-forward application of perturbation theory in the presence of an electric field will show that the electron will only oscillate (and hence emit) at the second harmonic if $b \neq 0$. In contrast, THG is ubiquitous in both centrosymmetric and non-centrosymmetric media.

Another salient difference between SHG and THG is the dependence on molecular ordering. We shall here follow a toy model proposed by Mertz [2] that is illustrative of this difference. We consider N molecules ordered along the z axis, evenly spaced by lattice parameter, L. Analogous to our consideration of THG in Section 3.4.3, each molecule will emit at the harmonic of interest, with new harmonic light produced in phase with the fundamental at the location of each molecule, but with a relative phase between adjacent atoms due to harmonic wave propagation. However, we will also consider the excitation beam to be polarized along the x axis, and we will assign the m^{th} molecule at position x_m an angle ϕ_m with respect to the x axis. Since the h^{th} harmonic scales with the h^{th} power of the electric field, the harmonic produced at the m^{th} molecule will depend on the component of the electric field along the x axis as $(E_0 \cos(\phi_m))^h$, for field strength E_0. However, by (3.53), we must have that for even harmonics (odd powers of x in (3.53)) that the susceptibility

tensor[20] of order $2h, h = 1, 2, \ldots$ at molecule m, $\chi_m^{(2h)}$, changes sign under the transformation $x \to -x$. Formally,

$$\chi_m^{(2h)} = \begin{cases} sgn(\chi^{(2h)})|\chi^{(2h)}|, & 0 < \phi_m < \pi/2 \\ -sgn(\chi^{(2h)})|\chi^{(2h)}|, & -\pi/2 < \phi_m < 0 \end{cases} \tag{3.54}$$

where sgn denotes the positive or negative sign of $\chi_m^{(2h)}$. In contrast, for even harmonics ($2h + 1, h = 1, 2, \ldots$), (3.53) requires that the sign remains the same, or

$$\chi_m^{(2h+1)} = sgn(\chi^{(2h+1)})|\chi_m^{(2h+1)}|, \ -\pi/2 < \phi < \pi/2 \tag{3.55}$$

The total sum for the harmonic, h, then depends on the sum over all atoms:

$$HG^{(h)} \propto \left| \sum_{m=0}^{N-1} \exp(i\{hk - k_h\}mL) sgn(\chi_m^{(h)}) \cos^h(\phi_m) \right|^2 \tag{3.56}$$

Here, the first term in the sum comes from the phase-mismatch due to dispersion within the medium while the second and third terms owe to the molecular alignment with the field. For a material possessing strong order (i.e. ϕ_m = constant), the last two terms fall out of the expression as a constant and the dispersion phases contribute to a simple geometric series, giving:

$$HG^{(h)} \propto \frac{\sin^2(\Delta k(N+1)L/2)}{\sin^2(\Delta kL/2)} \tag{3.57}$$

where $\Delta k = hk - k_h$. In the limit of large N and small spacing L, this finding is in good agreement with our results in (3.51).

Let us now consider a disordered material, such that ϕ_m is randomly and uniformly distributed over the interval $[-\pi/2, \pi/2]$. To see the effect of molecular alignment, we consider phase-matched conditions (i.e. $hk - k_h = 0$), reducing (3.56) to

$$HG^{(h)} \propto \left| \sum_{m=0}^{N-1} sgn(\chi_m^{(h)}) \cos^h(\phi_m) \right|^2 \tag{3.58}$$

[20] We will work with the case where $\chi^{(h)}$ is real, though it is, in principle, complex

or alternatively,

$$HG^{(h)} \propto N^2 \left|\langle sgn(\chi^{(h)}) \cos^h(\phi)\rangle\right|^2 \tag{3.59}$$

where $\langle \ldots \rangle$ denotes the average over all molecules. Since we have assumed that ϕ_m is uniformly distributed, we may approximate the average as an integral, which gives

$$HG^{(h)} \propto \frac{N^2}{\pi^2} \left| \int_{-\pi/2}^{\pi/2} sgn(\chi^{(h)}) \cos^h(\phi) d\phi \right|^2 \tag{3.60}$$

For even harmonics, (3.54) turns the integrand in (3.60) into an odd function of ϕ, and the integral evaluates to 0, meaning that disorder destroys the harmonic signal. In contrast, for odd harmonics, (3.55) gives an even function as our integrand, and the harmonic remains. For $h = 3$ (i.e. THG), the integral gives

$$THG \propto \left(\frac{4}{3\pi}\right)^2 N^2 \tag{3.61}$$

Thus, SHG and THG differ critically in terms of their dependence on molecular orientation, with THG being more robust to disorder. However, it should be noted that although THG is not destroyed by the random orientation of molecules, the THG signal *is* reduced by more than 50% of its peak value in disordered systems.

While the dearth of asymmetric molecules exhibiting molecular ordering restricts SHG in imaging applications, molecular inversion can be used to create periodically poled materials [24] that switch the sign of $\chi^{(2)}$ on the length-scale of the coherence length, thereby circumventing phase mismatch problems. Moreover, the scarcity of well-ordered, non-centrosymmetric biological molecules makes SHG a highly-specific, dye-free imaging source of image contrast for those non-centrosymmetric molecules which *do* have regular order and orientation, such as collagen [25–27]. Finally, while sources of SHG are less common than THG, $\chi^{(2)} \sim 10^{-11}$ m•V^{-1} (e.g [28]) while $\chi^{(3)} \sim 10^{-22}$

$m^2 \bullet V^{-2}$ (e.g. [29,30]) meaning that SHG will typically give rise to much stronger signals.

3.5 Damage Considerations

We round out this chapter with a discussion of photodamage or photo toxicity, the limits of which we have already mentioned in Section 3.3. By photodamage, we mean injury inflicted on *cells* or *tissue* by the application of light, and so we will exclude the process of photobleaching–the process by which fluorophores are destroyed–from our discussion. Broadly speaking[21], the topic of photodamage can be divided into three categories: thermal damage,nonlinear-absorption-mediated damage, and nonlinear ablation.

3.5.1 Thermal Damage

Since the strength of signal increases with the average power according to (3.5) (although, not indefinitely as we saw in Section 3.3), high-resolution imaging with a large signal-to-noise ratio will tend to favor the use of large average power. However, since fluorescence is based on absorption (and quantum efficiency), equation (3.5) equally governs linear absorption when $m = 1$. The absorbed energy (assuming it is not re-emitted) results in tissue heating, which eventually leads to tissue damage. Straightforwardly from Beer's Law, the

[21]Of course, UV or X-ray mediated damage are also a source of photodamage, technically speaking, and we could add the mutagenic effects of either to the discussion. However, we are interested in *acute* photodamage rather than the long-term health effects of imaging.

power absorbed, P_{abs}, in the focal volume is, to first order:

$$P_{abs} = \alpha b \langle P \rangle \tag{3.62}$$

where α is the extinction coefficient, b is the confocal parameter, and $\langle P \rangle$ is the average laser power, as before. The onset of thermal damage is gradual and difficult to define, since the temperatures at which different proteins denature vary, and the occurrence of damage may not be immediately visible. Experimentally, we have found that *visible* tissue disruption occurred in fixed spinal cord sections at approximately 60 mW using a 10 MHz pulse repetition rate, 300-fs pulse duration, 1040-nm wavelength laser, while we observed tissue damage at approximately 35 mW for a 1 MHz repetition rate laser, with similar wavelength and pulse duration. However, it should be noted that these values will vary with the tissue under consideration and the wavelengths used, since different chromophores will absorb to varying degrees. For example, the absorptivity of hemoglobin can vary as much as 5-fold between 800 nm and 1000 nm, and strongly depends on oxygenation state [31]. Thus, blood-rich tissues such as the liver will have different damage limits than those we have observed. Since thermal damage depends only on average power, as can be seen in (3.62), we should see disparity only if the damage mechanisms differ. As can be seen from (3.4), these damage thresholds correspond to pulse energies of 6 nJ and 35 nJ for the 10 MHz and 1 MHz lasers, respectively. Thus, the higher average power limit corresponds to a lower pulse energy, suggesting that 60 mW *really is* the upper bound on thermal damage, while the 35 nJ pulses correspond to a nonlinear process scaling according to (3.3) with higher values of m, which we shall discuss in Section 3.5.3.

3.5.2 Nonlinear-Absorption-Mediated Damage

The onset of damage in our experiments on fixed tissue was characterized by immediate and visible tissue destruction, either thermal or ablative (see Section 3.5.3). For biological specimens, however, it has been seen that phototoxicity can occur for ranges substantially below this threshold. Hopt et al. have seen phototoxicity after a single scan at 10 mW of average power at 80 MHz pulse repetition rate, assessed by both changes in indicator dye intensity and morphological changes [32]. König et al. [33] have seen that photodamage occurs at 7 mW for 240 fs pulses and follows a scaling of $\langle P \rangle^2/\tau$, which along with wavelength considerations led them to conclude that the damage mechanism is predominantly two-photon absorption (2PA). Koester et al. [34] have confirmed this result and verified that the damage is cumulative, scaling linearly with exposure time. Elsewhere [35], impaired division of cells and interference with cellular metabolism at 6 mW and 150 fs pulses was seen. Tirlapur et al. [36] have seen reactive oxygen species damage, DNA fragmentation, and apoptosis at similar pulse parameters. In each case, pixel dwell times were 10 μs [32], 60 μs and [33, 36] and 80 μs [35] with sub-micron pixel sizes.

In contrast, our own dwell time is approximately 1 μs/pixel, which at 1 MHz gives approximately 1 pulse per pixel, or 80 pulses per pixel with a Ti:Sapph laser at 80 MHz at a magnification of 3 pixels/μm. This amounts to 3 pulses/μm and 240 pulses/μm for the 1 MHz and 80 MHz sources, respectively. In [35] at 80 μs/pixel and approximately 10 pixels/μm , this corresponds to 64000 pulses/μm at 80 MHz. At 6 mW, a cell of area 100 μm^2 would receive a total irradiation dosage of 0.5 mJ/scan. For the same laser parameters, we deliver a mere 2 μJ. This 100-1000 fold increase in pulse delivery may account for

the discrepancy between our observed damage thresholds and those of other groups. In agreement with our observations of thermal damage, Ridsdale et al. [37] have observed good viability below 50 mW while scanning continuously for 7 minutes. All of the above measurements were performed in cultured cells, except for the studies of Koester et al. [34], which examined basal dendrites of layer V neurons in rat neocortical slice preparations.

Since 10 mW is well below our observed damage threshold, we may rule out ablative damage (described in Section 3.5.3) as a mechanism of cell death. Conversely, since 10 mW is also well below thermal damage limits, we rule out linear absorption as well. However, if 2PA followed by chemical reaction is the dominant damage mechanism–as the evidence cited above suggests–then it is reasonable to conclude that cell viability depends on the *cumulative number* of photodamaged molecules, as suggested in [34]. In this case, the number of damaged molecules per scan follows (3.26) for a 1 μm^2 focal spot:

$$\boxed{N_{damaged} \propto \frac{E^2}{\tau} RT} \tag{3.63}$$

where T is the dwell time in s/μm[22]. Expressed in terms of average power, we have by (3.4):

$$\boxed{N_{damaged} \propto \frac{\langle P \rangle^2}{R\tau} T} \tag{3.64}$$

Based on these results, we assumed that damage is significant when a critical number of molecules are destroyed, where this critical number determined by the results of Konig et al. [35]. Based on this data, we calculated the average power using our setup and parameters that would be required to give an equal number of molecules damaged as a function of dwell time using (3.64). The results are shown in Fig. 3.7. For reference, Konig et al. [35] performed 10

[22]More properly, it is given in s/μm^2, since a diffraction limited spot is actually scanned. Instead, we consider dwell time in terms of linear scan rate in one direction so as to keep with convention and simplify calculations.

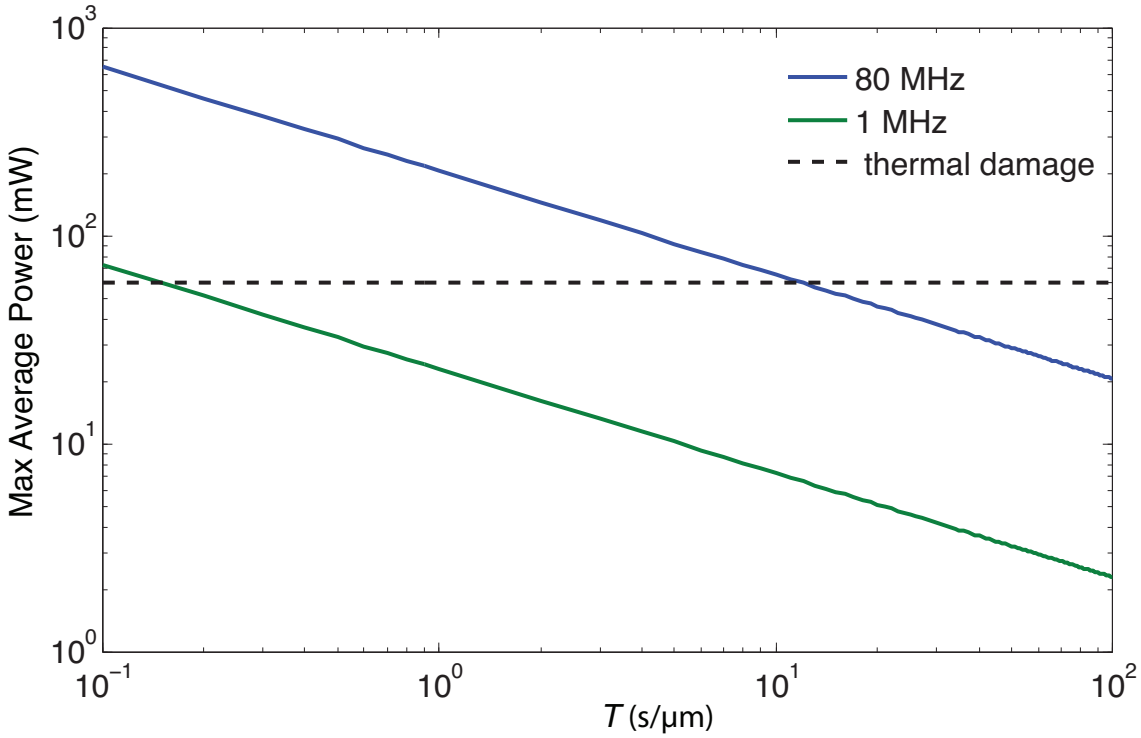

Figure 3.7: Average power required to reach critical two-photon mediated damage as a function of dwell time, T, in one scan.
Shown are results for an 80 MHz (*blue*) and 1 MHz (*green*) excitation source. The average power damage threshold is shown for reference (*dashed line*). By way of reference, our typical dwell time is 10^{-5} s, placing critical 2PA-mediated damage well-beyond the thermal damage limit for either laser system.

scans per cell at a scan rate of 20 s/frame, or a 200 s scan, with a corresponding maximum pulse energy of 0.08 nJ. For our scan rates discussed previously, and a 7 min. (420 s) continuous scan (to match Ridsdale et al. [37]) at the same repetition rate (80 MHz), we calculated the pulse energy required to produce a similar number of damaged molecules, and found this equivalent pulse energy to be

$$E_{equiv} \approx 14 \text{ nJ} \tag{3.65}$$

For an 80 MHz laser source, this corresponds to an average power of 1000 mW, well above average power damage, and consistent with the lack of damage observed by Ridsdale. A similar comparison with the data of Hopt et al. [32], for whom a single scan took 100 ms, an equivalent pulse energy at our scan rates was calculated to be:

$$E_{equiv} \approx 2 \text{ nJ} \tag{3.66}$$

or an average power of approximately 200 mW, again well above damage thresholds. At 1 MHz, the equivalent pulse energies are 1.200 μJ and 53 nJ, respectively, well above ablative thresholds.

In light of the excessive pulse bombardment in previous studies, we find it difficult to draw meaningful conclusions on cell viability as it applies to our present analysis. In our own laboratory setting, longitudinal animal studies have been performed using 20 mW or more at the sample surface from a 1 MHz source without observed pathology. Thus, based on our observations from longitudinal imaging and the absence of meaningful evidence to the contrary, we are justified in assuming that the damage thresholds we have determined from our analysis (or very near to them) are the most relevant to our discussion. Nevertheless, care must be taken in studies requiring extended periods of imaging, since the results of cumulative damage may not present

acutely. For example, three-photon absorption of 800-nm excitation wavelength is equivalent to a single, high-energy, UV photon at 266 nm. Absorption of this energy could lead to DNA breakage and subsequent apoptosis and/or deleterious mutations.

3.5.3 Nonlinear Ablation

Finally, nonlinear ablation is a damage mechanism whereby a hot electron plasma is formed by nonlinear absorption of light in the focal volume of an objective, vaporizing the surrounding medium and resulting in a subsequent shockwave [38]. Just as it is possible to excite an electron from the ground state to an excited state by multi-photon absorption, so it is possible to excite an electron to the point of ionization or at least to the conduction band by multi-photon ionization (MPI) (for a review on atomic MPI, see [39]). However, multi-photon ionization is not the whole picture. A process known as inverse bremsstrahlung absorption (IBA) [39, 40] results in the free electrons absorbing photons non-resonantly from the applied laser field. These "hot" electrons cause impact ionization of the surrounding ions. In turn, these semi-free electrons absorb photons from the laser field, resulting in more impact ionization and so on. The result is an electron "avalanche" or cascade, whence it is sometimes referred to as the "avalanch-breakdown" model [1]. While a complete review of the topic is not possible, an outline of the theory is given in [1]. For those interested in a more comprehensive analysis[23] with an emphasis on the use of this form of damage to induce alterations in tissue, the reader is directed to a review by Vogel and Venugopalan [40]. However, we shall sketch

[23]Nonlinear ablation is its own field of study

an overview of these effects here based on [38, 40].

First, we consider that the density of free electrons, ρ, to be given by the rate equation [38]

$$\frac{d\rho}{dt} = \left(\frac{d\rho}{dt}\right)_{MPI}(\mathbf{E}) + \gamma(\mathbf{E})\rho - g\rho - \eta\rho^2 \tag{3.67}$$

where the first term corresponds to semi-ionized electrons generated by MPI, the second to avalanche ionization at rate γ, the third term to electron diffusion out of the focal volume (and hence no longer subject to the laser field) with coefficient g, and the last term to recombination of electrons in the conduction band with holes left in the valence band, at rate η. Note that both of the first two terms depend on the applied electric field, $\mathbf{E}$, as we have made explicit. Assuming $\rho(t = 0) = 0$, the only electrons available to "seed" the process of avalanche-breakdown are provided by MPI, whereafter the avalanche process can take place. However, due to recombination and diffusion, this process will require a critical plasma density ρ_{cr} to be reached whereupon (3.67) is positive and allows for rapid growth. For femtosecond pulses, this corresponded to $\rho_{cr} \sim 10^{21}$ cm^{-3} in water [38]. However, it is critical to note that unlike thermal damage, (3.67) is predictive of a *threshold* behavior, below which damage is minimal to non-existent.

In looking at (3.3), we may raise the legitimate concern that while imaging may favor a shorter pulse duration, so too would the damage threshold, suggesting a balance between image contrast and damage mechanisms. However, Tien et al. [41] have shown while the damage threshold fluence scales approximately as the square root of the pulse duration above 10 ps, between 10 fs and 1 ps the threshold fluence is nearly constant. This flattening of the trend can be understood by a consideration of the first two terms in (3.67). MPI

depends strongly on the peak power

$$P_p = \frac{E}{\tau} \tag{3.68}$$

to promote electrons into the conduction band. In contrast, the cascade of IBA-associated electrons will depend on how long the pulse continues to accelerate the electrons, and so will result in an increase of electrons via the avalanche mechanism. Since most available laser sources operate with pulses in the range of 50 fs to several hundred fs, it is always advisable to choose the shortest pulse available, since by (3.3) this will give the strongest signal, but will leave the damage threshold unchanged [41].

In addition to the damage resulting from the creation of the plasma itself, the subsequent heating results in the formation of a cavitation bubble. The time- and length-scale of these structures have been studied extensively in water [38, 40, 42, 43]. While these results are interesting in their own right, we shall only mention the occurrence of this effect. This effect is typically how ablative damage is detected when imaging. In our studies, we have seen damage occur at 35 nJ (35 mW) for 300 fs pulses (see Fig. 3.4).

Thus far we have considered laser damage as primarily an undesirable outcome that occurs in the context of trying to achieve higher image contrast. However, nonlinear ablation is actually a desirable effect for targeted manipulation of tissue. Since damage is restricted to the focal volume, damage can be produced below the surface of a structure. For example, Schaffer et al. [44–47] have demonstrated that it is possible to create subsurface changes in glass, including the writing of optical waveguides. This finding is particularly striking since glass is considered transparent at near infrared (NIR) wavelengths with respect to linear absorption, yet is absorbing via nonlinear processes. In a biological context, Nishimura et al. [48] have developed the use of fs laser pulses

for creating targeted models of sub-surface strokes in the brain, which has been used to subsequently study strokes in penetrating arterioles [49] and ascending venules [50], as well as the effects of microhemorrhages on cortical structure [51] and function [52]. We have also used this mechanism for creating minimal spinal cord injuries [53, 54]. Nguyen et al. [55] have also studied its application for creating subsurface cuts in the rodent cortex, with a proposed application to stopping seizure propagation in epilepsy while minimizing collateral damage caused by traditional blade-based surgeries. It has also been studied extensively for corneal surgery [56–58], and remains standard procedure for LASIK surgery. A later chapter in this thesis will examine and review the use of fs laser pulses for transfecting foreign DNA into living cells.

Thus, unlike the other mechanisms of damage, nonlinear ablation provides a useful tool with which to study neuropathology, and is used extensively in three of the following chapters.

REFERENCES

[1] R Boyd. *Nonlinear Optics, 3rd Edition*. Academic Press, 2008.

[2] J Mertz. *Introduction to Optical Microscopy*. Roberts and Company Publishers, Greenwood Village, CO, 1999.

[3] W Denk, J.H. Strickler, and W.W. Webb. Two-photon laser scanning fluorescence microscopy. *Science*, 248(4951):73–76, 1990.

[4] Brian A Wilt, Laurie D Burns, Eric Tatt Wei Ho, Kunal K Ghosh, Eran A Mukamel, and Mark J Schnitzer. Advances in Light Microscopy for Neuroscience. *Annu Rev Neurosci*, 32(1):435–506, 2009.

[5] K Svoboda and R Yasuda. Principles of Two-Photon Excitation Microscopy and Its Applications to Neuroscience. *Neuron*, 50(6):823–839, 2006.

[6] P Theer, MT Hasan, and W Denk. Two-photon imaging to a depth of 1000 m in living brains by use of a Ti: Al¡ sub¿ 2¡/sub¿ O¡ sub¿ 3¡/sub¿ regenerative amplifier. *Opt Lett*, 28(12):1022–1024, 2003.

[7] D Kobat, ME Durst, N Nishimura, AW Wong, CB Schaffer, and C Xu. Deep tissue multiphoton microscopy using longer wavelength excitation. *Opt Express*, 17(16):13354–13364, 2009.

[8] Martin Fuhrmann, Tobias Bittner, Christian K E Jung, Steffen Burgold, Richard M Page, Gerda Mitteregger, Christian Haass, Frank M LaFerla, Hans Kretzschmar, and Jochen Herms. Microglial Cx3cr1 knockout prevents neuron loss in a mouse model of Alzheimer's disease. *Nature Publishing Group*, 13(4):411–413, 2010.

[9] DA Dombeck, MS Graziano, and D W Tank. Functional Clustering of Neurons in Motor Cortex Determined by Cellular Resolution Imaging in Awake Behaving Mice. *J Neurosci*, 29(44):13751–13760, 2009.

[10] Fritjof Helmchen and Winfried Denk. Deep tissue two-photon microscopy. *Nat Meth*, 2(12):932–940, 2005.

[11] BF Grewe, FF Voigt, M Van't Hoff, and F Helmchen. Fast two-layer two-photon imaging of neuronal cell populations using an electrically tunable lens. *Biomedical optics express*, 2(7):2035–2046, 2011.

[12] N Olivier, A. Mermillod-Blondin, C.B. Arnold, and E Beaurepaire. Two-photon microscopy with simultaneous standard and extended depth of field using a tunable acoustic gradient-index lens. *Opt Lett*, 34(11):1684–1686, 2009.

[13] A Mermillod-Blondin, E McLeod, and CB Arnold. High-speed varifocal imaging with a tunable acoustic gradient index of refraction lens. *Opt Lett*, 33(18):2146–2148, 2008.

[14] Gaddum Duemani Reddy, Keith Kelleher, Rudy Fink, and Peter Saggau. Three-dimensional random access multiphoton microscopy for functional imaging of neuronal activity. *Nat Neurosci*, 11(6):713–720, 2008.

[15] R Salomé, Y Kremer, S Dieudonné, J F Léger, O Krichevsky, C Wyart, D Chatenay, and L Bourdieu. Ultrafast random-access scanning in two-photon microscopy using acousto-optic deflectors. *Journal of neuroscience methods*, 154(1-2):161–174, 2006.

[16] Gaddum Duemani Reddy and Peter Saggau. Fast three-dimensional laser scanning scheme using acousto-optic deflectors. *Journal of Biomedical Optics*, 10(6):064038, 2005.

[17] JR Lakowicz, H Szmacinski, K Nowaczyk, KW Berndt, and M Johnson. Fluorescence lifetime imaging. *Analytical biochemistry*, 202(2):316–330, 1992.

[18] N Ji, JC Magee, and E Betzig. High-speed, low-photodamage nonlinear imaging using passive pulse splitters. *Nat Meth*, 5(2):197–202, 2008.

[19] GO Clay, CB Schaffer, and D Kleinfeld. Large two-photon absorptivity of hemoglobin in the infrared range of 780–880 nm. *The Journal of chemical physics*, 126:025102, 2007.

[20] JN Demas and GA Crosby. The measurement of photoluminescence quantum yields. A review. *J. Phys. Chem*, 75(8):991–1024, 1971.

[21] MA Albota, C Xu, and WW Webb. Two-photon fluorescence excitation cross sections of biomolecular probes from 690 to 960 nm. *Applied Optics*, 37(31):7352–7356, 1998.

[22] T Takano, GF Tian, W Peng, N Lou, D Lovatt, AJ Hansen, KA Kasischke, and M Nedergaard. Cortical spreading depression causes and coincides with tissue hypoxia. *Nat Neurosci*, 10(6):754–762, 2007.

[23] WR Zipfel, RM Williams, R Christie, AY Nikitin, BT Hyman, and WW Webb. Live tissue intrinsic emission microscopy using multiphoton-excited native fluorescence and second harmonic generation. *Proceedings of the National Academy of Sciences of the United States of America*, 100(12):7075, 2003.

[24] MM Fejer, GA Magel, DH Jundt, and RL Byer. Quasi-phase-matched second harmonic generation: tuning and tolerances. *Quantum Electronics, IEEE Journal of*, 28(11):2631–2654, 1992.

[25] R. M. Williams, W.R. Zipfel, and W.W. Webb. Second harmonic imaging for collagen structure analysis. *Biophys J*, 82:175A, 2002.

[26] Patrick Stoller, Karen M Reiser, Peter M Celliers, and Alexander M Rubenchik. Polarization-Modulated Second Harmonic Generation in Collagen. *Biophys J*, 82(6):3330–3342, 2002.

[27] RM Williams, WR Zipfel, and WW Webb. Interpreting second-harmonic generation images of collagen I fibrils. *Biophys J*, 88(2):1377–1386, 2005.

[28] MM Choy and RL Byer. Accurate second-order susceptibility measurements of visible and infrared nonlinear crystals. *Physical Review B*, 14(4):1693–1706, 1976.

[29] HS Nalwa. Organic materials for third-order nonlinear optics. *Advanced Materials*, 5(5):341–358, 1993.

[30] V Shcheslavskiy, G Petrov, and VV Yakovlev. Nonlinear optical susceptibility measurements of solutions using third-harmonic generation on the interface. *Appl Phys Lett*, 82:3982, 2003.

[31] WG Zijlstra, A. Buursma, and WP Meeuwsen-Van der Roest. Absorption spectra of human fetal and adult oxyhemoglobin, de-oxyhemoglobin, carboxyhemoglobin, and methemoglobin. *Clinical Chemistry*, 37(9):1633–1638, 1991.

[32] A Hopt and E Neher. Highly nonlinear photodamage in two-photon fluorescence microscopy. *Biophys J*, 80(4):2029–2036, 2001.

[33] K Konig, PTC So, WW Mantulin, and E Gratton. Cellular response to near-infrared femtosecond laser pulses in two-photon microscopes. *Opt Lett*, 22(2):135–136, 1997.

[34] HJ Koester, D Baur, R Uhl, and SW Hell. Ca2+ fluorescence imaging with pico-and femtosecond two-photon excitation: signal and photodamage. *Biophys J*, 77(4):2226–2236, 1999.

[35] K Konig, TW Becker, P Fischer, I Riemann, and KJ Halbhuber. Pulse-length dependence of cellular response to intense near-infrared laser pulses in multiphoton microscopes. *Opt Lett*, 24(2):113–115, 1999.

[36] UK Tirlapur, K Konig, C Peuckert, R Krieg, and KJ Halbhuber. Femtosecond near-infrared laser pulses elicit generation of reactive oxygen species in mammalian cells leading to apoptosis-like death. *Exp Cell Res*, 263(1):88–97, 2001.

[37] JA Ridsdale et al. The viability of cultured cells under two-photon laser scanning microscopy. *Biophys. J.*, 64:A109, 1993.

[38] J Noack and A Vogel. Laser-induced plasma formation in water at nanosecond to femtosecond time scales: calculation of thresholds, absorption coefficients, and energy density. *Quantum Electronics, IEEE Journal of*, 35(8):1156–1167, 1999.

[39] G Mainfray and G Manus. Multiphoton ionization of atoms. *Reports on progress in physics*, 54:1333, 1991.

[40] Alfred Vogel and Vasan Venugopalan. Mechanisms of Pulsed Laser Ablation of Biological Tissues. *Chem. Rev.*, 103(2):577–644, 2003.

[41] AC Tien, S Backus, H Kapteyn, M Murnane, and G Mourou. Short-pulse laser damage in transparent materials as a function of pulse duration. *Phys. Rev. Lett.*, 82(19):3883–3886, 1999.

[42] CB Schaffer, N Nishimura, EN Glezer, AMT Kim, and E Mazur. Dynamics of femtosecond laser-induced breakdown in water from femtoseconds to microseconds. *Opt Express*, 10(3):196–203, 2002.

[43] A Vogel, J Noack, K Nahen, D Theisen, S Busch, U Parlitz, DX Hammer, GD Noojin, BA Rockwell, and R Birngruber. Energy balance of optical breakdown in water at nanosecond to femtosecond time scales. *Applied Physics B: Lasers and Optics*, 68(2):271–280, 1999.

[44] CB Schaffer, A Brodeur, JF García, and E Mazur. Micromachining bulk

glass by use of femtosecond laser pulses with nanojoule energy. *Opt Lett*, 26(2):93–95, 2001.

[45] CB Schaffer and E Mazur. Micromachining using ultrashort pulses from a laser oscillator. *Optics and Photonics News*, 12(4):20–23, 2001.

[46] CB Schaffer, JF Garcia, and E Mazur. Bulk heating of transparent materials using a high-repetition-rate femtosecond laser. *Applied Physics A: Materials Science & Processing*, 76(3):351–354, 2003.

[47] CB Schaffer, AO Jamison, and E Mazur. Morphology of femtosecond laser-induced structural changes in bulk transparent materials. *Appl Phys Lett*, 84:1441, 2004.

[48] N Nishimura, CB Schaffer, B Friedman, PS Tsai, PD Lyden, and D Kleinfeld. Targeted insult to subsurface cortical blood vessels using ultrashort laser pulses: three models of stroke. *Nat Meth*, 3(2):99–108, 2006.

[49] Nozomi Nishimura, Nathanael L Rosidi, Costantino Iadecola, and Chris B Schaffer. Limitations of collateral flow after occlusion of a single cortical penetrating arteriole. *J Cerebr Blood F Met*, 30(12):1914–1927, 2010.

[50] John Nguyen, Nozomi Nishimura, Robert N Fetcho, Costantino Iadecola, and Chris B Schaffer. Occlusion of cortical ascending venules causes blood flow decreases, reversals in flow direction, and vessel dilation in upstream capillaries. *J Cerebr Blood F Met*, 31(11):2243–2254, 2011.

[51] Nathanael L Rosidi, Joan Zhou, Sanket Pattanaik, Peng Wang, Weiyang Jin, Morgan Brophy, William L Olbricht, Nozomi Nishimura, and Chris B Schaffer. Cortical Microhemorrhages Cause Local Inflammation but Do Not Trigger Widespread Dendrite Degeneration. *Plos One*, 6(10):e26612, 2011.

[52] FA Cianchetti, N Nishimura, and CB Schaffer. Stimulus-Evoked Calcium Transients in Somatosensory Cortex are Inhibited After a Nearby Microhemorrhage. *Biomedical Optics*, 2010.

[53] Matthew J Farrar, Frank W Wise, Joseph R Fetcho, and Chris B Schaffer. In Vivo Imaging of Myelin in the Vertebrate Central Nervous System Using Third Harmonic Generation Microscopy. *Biophys J*, 100(5):1362–1371, 2011.

[54] Matthew J Farrar, Ida M Bernstein, Donald H Schlafer, Thomas A Cleland,

Joseph R Fetcho, and Chris B Schaffer. Chronic in vivo imaging in the mouse spinal cord using an implanted chamber. *Nat Meth*, 9(3):297–U113, 2012.

[55] John Nguyen, Jillian Ferdman, Mingrui Zhao, David Huland, Shatha Saqqa, Jan Ma, Nozomi Nishimura, Theodore H Schwartz, and Chris B Schaffer. Sub-surface, micrometer-scale incisions produced in rodent cortex using tightly-focused femtosecond laser pulses. *Lasers Surg. Med.*, 43(5):382–391, 2011.

[56] VV Yakovlev, AH Buist, DN Fittinghoff, and A. Vogel. Applications of Ultrashort-Pulse Lasers in Medicine and Biology (Proceedings Volume), 1998.

[57] H Lubatschowski, G Maatz, A Heisterkamp, U. Hetzel, W Drommer, H Welling, and W Ertmer. Application of ultrashort laser pulses for intrastromal refractive surgery. *Graefe's archive for clinical and experimental ophthalmology*, 238(1):33–39, 2000.

[58] T Juhasz, FH Loesel, RM Kurtz, C Horvath, JF Bille, and G Mourou. Corneal refractive surgery with femtosecond lasers. *Selected Topics in Quantum Electronics, IEEE Journal of*, 5(4):902–910, 1999.

CHAPTER 4

THIRD HARMONIC GENERATION IMAGING OF MYELIN

This chapter contains the manuscript and figures from a study on the use of third harmonic generation as a technique for imaging myelin in the vertebrate central nervous system, with minor additions and formatting changes. Myelin is a critical component of the central nervous system (CNS), and enables long-distance action potential propagation. Many transgenic animals allow specific labeling of cell populations–such as subpopulations of neurons– by introducing a fluorescent reporter gene (such as GFP) with a population-specific promoter. Thus, every time that promoter is activated in the cell, a simultaneous copy of reporter protein is also made, which then diffuses about the cytosol. However, CNS myelin is produced by the multiple windings of the cell membranes of oligodendrocytes, with no cytosol space in between. Thus, while it is possible to label the oligodendroctye cell bodies, labeling myelin itself by exogenous means presents a considerable challenge.

To this end, this work demonstrated that third harmonic generation (THG) presents a dye-free imaging modality for looking at myelin. This work was originally published in March 2011 in Biophysical Journal. This paper is reprinted with permission by Cell Press. The original article may be found under the following citation:

Matthew J. Farrar, Frank W. Wise, Joseph R. Fetcho, and Chris B. Schaffer. In Vivo Imaging of Myelin in the Vertebrate Central Nervous System Using Third Harmonic Generation Microscopy. *Biophys. J.*, **100**, 1362-1371, 2011.

4.1 ABSTRACT

Loss of myelin in the central nervous system (CNS) leads to debilitating neurological deficits. High-resolution optical imaging of myelin in the CNS of animal models is limited by a lack of *in vivo* myelin labeling strategies. We demonstrated that third harmonic generation (THG) microscopy–a coherent, nonlinear, dye-free imaging modality–provides micrometer resolution imaging of myelin in the mouse CNS. In fixed tissue, we found that THG signals arose from white matter tracts and were colocalized with two-photon excited fluorescence (2PEF) from a myelin-specific dye. In vivo, we used simultaneous THG and 2PEF imaging of the mouse spinal cord to resolve myelin sheaths surrounding individual fluorescently-labeled axons, and followed myelin disruption after spinal cord injury. Finally, we suggest optical mechanisms that underlie the myelin specificity of THG. These results establish THG microscopy as an ideal tool for the study of myelin loss and recovery.

4.2 INTRODUCTION

Optical imaging provides nondestructive visualization of dynamic processes in biological systems with subcellular resolution. Conventional, linear optical imaging, however, is limited in depth penetration and suffers a loss in contrast when imaging structures in scattering tissue. Various forms of nonlinear laser scanning microscopy, including two- photon excited fluorescence (2PEF) imaging [1], circumvent these limitations and have enabled, for example, fluorescence-based imaging to a depth of 1 mm in the neocortex of a live mouse with micrometer resolution [2,3].

The fatty myelin sheaths surrounding a subset of axons in the central nervous system (CNS) enable fast conduction of action potentials. Diseases such as multiple sclerosis lead to loss of myelin with consequent deficits in motor function and sensory perception [4]. Substantial imaging of myelin-related pathology has been performed *in vivo* in both human patients and animal models using magnetic resonance imaging (for reviews, see Le Bihan [5] and Bakshi et al. [6]) and positron emission tomography [7–9] but at resolutions of $\sim$200 μm and $\sim$1 mm, respectively, these modalities are insufficient to image the cellular and subcellular structures accessible to optical microscopies. Although protocols exist for labeling myelin in postmortem tissue sections, good exogenous dyes for optical *in vivo* labeling of myelin in animal models are not available, as existing dyes tend to disrupt the lipid structure of myelin. Recent work in transgenic zebrafish has enabled myelin visualization by enhanced green fluorescent protein expression driven by the myelin basic protein promoter [10]. In addition, coherent anti-Stokes Raman scattering (CARS) microscopy has enabled imaging of myelinated fibers without labeling

in live extracted mouse spinal cord [11] and *in vivo* mouse brain [12]. However, the technical challenges associated with this modality have limited its broad adoption as a tool for *in vivo* studies.

Harmonic generation is attractive for *in vivo* imaging because it requires no exogenous dyes or fluorescent proteins. Second-harmonic generation (SHG) has been used to study collagen [13–15], microtubules [16–18], and cell membranes [19–21], among other things. However, SHG is produced only from molecules and structures lacking inversion symmetry and therefore possessing a nonzero $\chi^{(2)}$. This restricts the structures that can be imaged in this modality, providing a tool that images some macromolecular structures with excellent specificity (e.g., collagen), but that cannot image most features of biological interest.

In contrast, third-harmonic generation (THG) is a nonlinear optical process ubiquitous to all molecules in which three photons at the fundamental frequency are up- converted to a photon at the third harmonic with an efficiency proportional to the third-order susceptibility tensor, $\chi^{(3)}(\omega, \omega, \omega; 3\omega)$, and the cube of the intensity of the fundamental beam. Unlike 2PEF, THG is a parametric process that need not have resonances at any of the frequencies involved. Due to the Gouy phase shift associated with focused Gaussian beams [22], THG produced in the focal volume but on either side of the focal plane in the bulk of normally dispersive materials destructively interferes in the far field, resulting in the absence of signal. The presence of an optical interface breaks the symmetry across the focal plane and results in a measurable signal, making THG an interface-sensitive microscopy. THG microscopy has been used to image neurons and their processes [23, 24], lipid bodies in plant seeds and Drosophila embryos [25], plant leaf cells [26], Chara rhizoids [27], zebrafish embryos and larvae [28, 29], cardiomyocytes [30], mouse cartilage

elastin [31], malaria parasites [32], and human cornea [33]. Owing to phase-matching conditions, THG is dominantly generated in the forward direction, making epi-detection possible only after multiple scattering events [34]. Like 2PEF, THG is produced only in the focal volume, making it well suited for imaging in scattering tissues.

In this article, we studied the utility of epi-detected THG as a tool for imaging myelin. We first explored the sources of THG signal in fixed mouse CNS tissue and showed that myelin is the dominant source of image contrast. We then demonstrated *in vivo* imaging of healthy and damaged myelin in the mouse spinal cord using THG. Finally, we explored what optical properties lead to efficient THG production.

4.3 MATERIALS AND METHODS

4.3.1 Ex vivo tissue preparation and imaging

C57BL/6 mice were deeply anesthetized, and perfused through an intracardiac catheter with phosphate-buffered solution (PBS) (Sigma-Aldrich, St. Louis, MO) to clear blood followed by 4% paraformaldehyde (Thermo Fisher Scientific, Waltham, MA) in PBS as a fixative. Some mice expressed yellow fluorescent protein (YFP) in a subset of CNS neurons (C57B/6-thy1- YFPH; Jackson Labs, Bar Harbor, ME). Tissue was then embedded in agarose gel. Mouse brain sections several millimeters thick were cut using a vibratome (Integraslice 7550 PSDS; Campden Instruments, Lafayette, IN) or brain matrix with low-profile histology blades. Spinal cord sections were cut while still in the

vertebral column with a scalpel blade. Tissue was stained in 100:1 dilution of FluoroMyelin Red (FM Red; Invitrogen, Carls- bad, CA) in PBS for a minimum of 8 h. Staining was followed by a washout of minimum 10 h in three changes of PBS. Samples were mounted using 0.5% agarose (Sigma-Aldrich) in PBS for imaging.

Imaging was performed on a locally designed multiphoton microscope and images were taken with a high numerical aperture (NA) 20 water immersion objective lens (NA 14 1.0; Carl Zeiss MicroImaging, Thornwood, NY) or a low NA 4 objective (NA 14 0.28; Olympus America, Center Valley, PA). A 1043-nm wavelength, 300-fs pulse duration, 1-MHz repetition rate fiber laser source (FCPA mJewel D-40; IMRA America, Ann Arbor, MI) was used to generate THG and 2PEF. Comparison images were taken in some samples with a solid-state laser source of higher repetition rate (1028-nm wavelength, 300-fs pulse duration, 10-MHz repetition rate; t-Pulse 500; Amplitude Systemes, Pessac, France). In tissue stained with FM Red, 2PEF and THG images were taken sequentially, with FM Red imaged first, so as not to photo- bleach the FM Red under the higher average powers used for THG imaging. Bandpass filters used for detection were centered at 350 nm for THG, 645 nm for 2PEF of FM Red and Texas Red dextran, and 517 nm for 2PEF of YFP.

Spinal cord sections of homozygous shiverer mice (MBP-shi, Jackson Labs, Bar Harbor, ME)–a strain that is severely myelin-deficient–were compared against controls. Image stacks were taken with the low NA objective at 5-μm increments and $\sim$1-mm maximal depth. Maximum projections were taken to remove any artifacts from sample tilt that might be introduced by averaging. To remove the effects of background pixels, images were traced manually and only pixels interior to the boundary were considered. An image histogram was

computed, and the THG contrast was defined as the full width at half-maximum (FWHM) of the intensity histogram.

4.3.2 In vivo mouse preparation and imaging

Wild-type mice (C57BL/6) or transgenic mice expressing YFP in a subset of pyramidal neurons and dorsal root ganglia (DRG) were used for multimodal imaging. Mice were anesthetized using inhaled isoflurane (5% to induce anesthesia and ∼1.5% to maintain anesthesia during surgery and imaging) on a custom surgery table and a dorsal laminectomy was performed. A rectal thermometer and feedback-controlled heating blanket were used to maintain the animal at 37.5°C. Glycopyrrolate (50 mg/100-g mouse weight) was injected into the thigh muscle to prevent the buildup of fluid in the lungs. Bupivicane, a local anesthetic, was injected at the site of surgical incisions (∼0.1 mL of 0.125%). An incision was made in the skin and the muscle was retracted from the vertebrae spanning T10-T12. The vertebrae were clamped on either side and held in place using custom holders. The lamina of T11 was removed with Vannas scissors, and excess bleeding stopped with the use of gelfoam (Pharmacia & Upjohn, Kalamazoo, MA). Where possible, the dura was left intact. A #0 coverslip was applied over the cord and the interstitial space filled with 0.5% agarose in artificial cerebral spinal fluid. Animals were given 5% (W/V) glucose in saline hourly (1 mL/100-g mouse weight). The blood plasma was fluorescently labeled by intravenous injection of 50 μL of 2.5% (W/V) Texas Red dextran (molecular mass = 70,000 kDa; Invitrogen). The mouse was then transported to the microscopy laboratory and imaging was performed using the same setup as for ex vivo samples. After the imaging sessions, mice were

perfused as described above.

4.3.3 In vivo zebrafish preparation and imaging

Six-day-old larval zebrafish were anesthetized in 0.2% tricaine methanesulphonate (MS-222; Western Chemical International, Scottsdale, CA), and the Mauthner cell was electroporated with 70-kDa Texas-Red dextran in 10% Hanks buffer to fluorescently label the Mauthner axon. Five days later, the animals were again anesthetized and mounted dorsal side up in low melting temperature agarose for *in vivo* imaging on the same setup described above.

4.3.4 Spinal cord microlesioning

Micrometer-scale lesions were produced in the spinal cord by femtosecond laser ablation using ∼100-nJ pulses from a regenerative amplifier (800-nm wavelength, 50-fs pulse duration, 1-kHz repetition rate; Legend model, Coherent Laser, Santa Clara, CA), focused with the 1.0 NA objective into the spinal cord of live, anesthetized mice. Custom software in MATLAB (The MathWorks, Natick, MA) allowed the user to draw a trajectory on a projection of a three-dimensional stack, so as to avoid injuring and rupturing blood vessels, which would obscure imaging. A shutter was then opened and the translation stage followed the trajectory moving at 500 mm/s and disrupting tissue in the focal volume via nonlinear ablation [35], effectively acting as a laser scalpel. The pattern was continued until the desired depth of the cut was reached. The axial extent of the disruption produced by a single laser pass was ∼1-2 μm at the

energies used here and increases with pulse energy. Multiple passes at different depths were used to make a cut several tens of micrometers in depth. To insure an adequate lesion, the same pattern was repeated twice for each cut.

4.3.5 Image processing

Image stacks were median-filtered and the average z-projection computed to show relevant structures. Images taken with the high NA objective were oversampled in z (0.2-μm increments). Frames containing severe motion artifact (largely due to breathing) from *in vivo* imaging sessions were removed and interpolated between.

For tiled images using the low NA objective, a water/air interface was present that was absent when using the high NA water immersion objective. This interface, combined with the field curvature, resulted in images with an inhomogeneous intensity distribution across the field of view. To correct for this effect, images were normalized by the intensity distribution from the surface of the surrounding agarose alone.

4.3.6 Monte Carlo simulation

The method described by Prahl et al. [36] was followed closely. Photon packets were randomly assigned an initial position within the beam waist and corresponding azimuthal angle. Polar angles were assigned randomly for 2PEF simulations, or in a forward propagating arrangement for THG, as described in Appendix B. Detection was achieved for photons that were incident on an

aperture within a fixed acceptance angle, with amplitude dependent on the ratio of path length and absorption length.

All animal procedures were performed with the approval of the Cornell Institutional Animal Care and Use Committee (IACUC) and under the guidance of the Cornell Center for Animal Resources and Education.

4.4 RESULTS

4.4.1 THG image contrast in mouse spinal cord was dominated by myelinated axon tracts

Coronal slices of fixed mouse spinal cord were stained with FluoroMyelin Red (FM Red), a myelin-specific two-photon- excitable dye, and imaged in an epi-detection arrangement. Imaging with a low NA objective showed bright THG from white-matter tracts with only a dim signal from the butterfly-shaped gray matter (Fig. 4.1 a, left), which corresponded well to the pattern of FM Red-stained myelin seen with 2PEF (Fig. 4.1 a, right). High-resolution (high NA) THG imaging showed large signal in regions of dense myelination in the dorsolateral (Fig. 4.1 b, left) and dorsal (Fig. 4.1 c, left) corticospinal tracts. Fine features resolved in the THG images (Fig. 4.1, b and c, left) were similar to those apparent in high-resolution 2PEF images of FM Red-labeled myelin (Fig. 4.1, b and c, right). The dark round holes shown in relief against the strong THG signal (Fig. 4.1, b and c, left) were confirmed to be axons by coregistering THG images with 2PEF images in spinal cord sections from transgenic mice that expressed YFP in a subset of the corticospinal tract axons (see Fig. 4.7 and

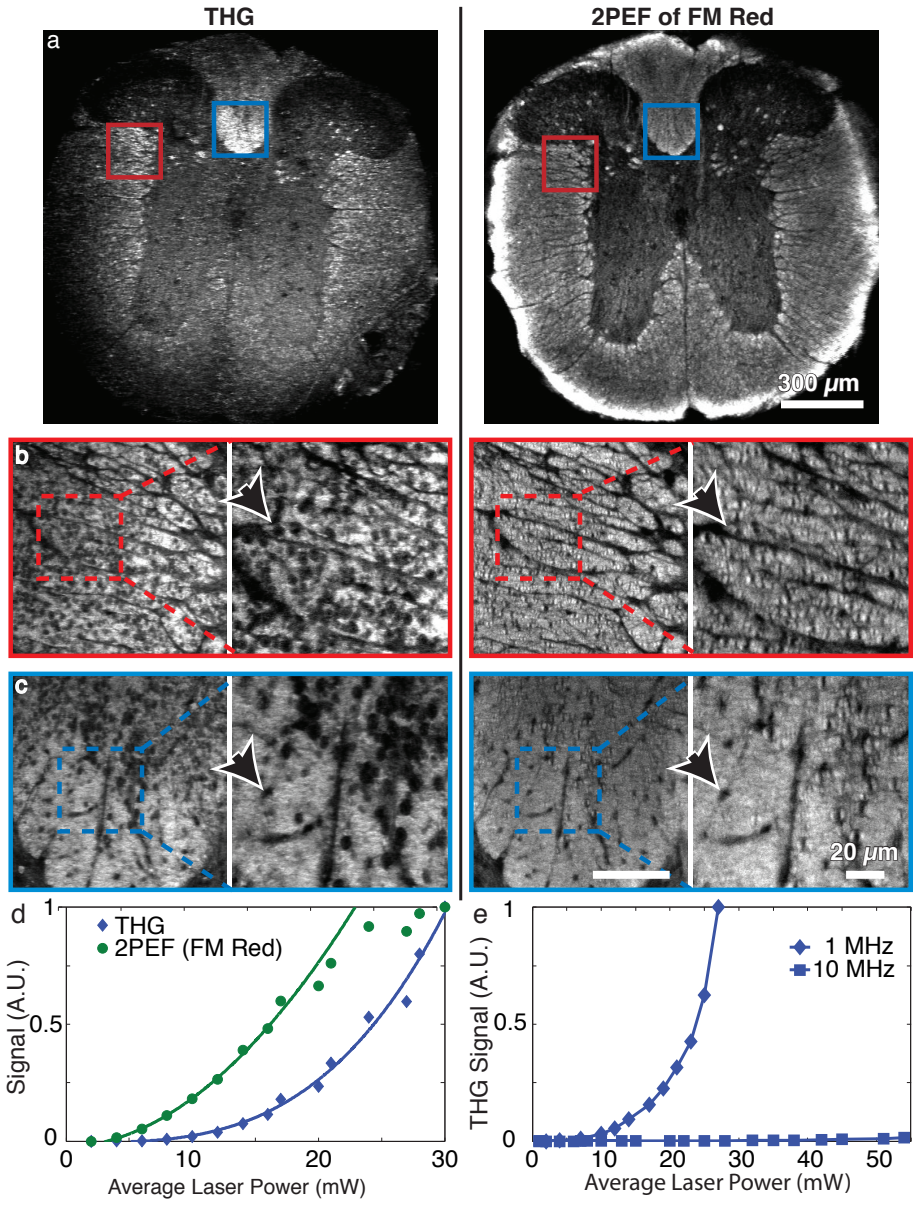

Figure 4.1: Myelinated tracts in mouse spinal cord provided a strong source of THG imaging contrast.

Thick coronal sections of thoracic spinal cord from C57BL/6 mice stained with FM Red dye and imaged using 2PEF and THG. Imaging with a low NA objective showed the gross structure of white-matter tracts (a). Individual axons, seen as holes against a myelin backdrop (arrows), were visible in the dorsal (b) and dorsolateral corticospinal (c) tracts when imaged with a high NA objective. A least-squares power law fit, $S \sim P^b$, of the THG signal, S, from myelinated tissue as a function of average excitation power, P, gave $b = 3.3 \pm 0.3$ and did not saturate like the 2PEF signal (d). THG imaging with a 1-MHz repetition rate source produced significantly more signal intensity than a 10-MHz source with similar wavelength and pulse duration at the same average power (e).

additional text in the Supporting Material). To rule out signal arising from resonant enhancement from either YFP or FM Red, fixed sections of wild-type C57B6/J mice were imaged and showed no difference in THG contrast (data not shown).

The average signal at 350 nm from fixed spinal cord scaled as the cube of the incident laser power (Fig. 4.1 d), with no sign of saturation even above the threshold for sample damage (∼25–30 mW), consistent with THG. In contrast, the 2PEF signal of FM Red scaled as the square of the average power and saturated at high power (Fig. 4.1 d). Using a 10-MHz laser with similar wavelength and pulse duration, we observed much lower THG signal as compared to the 1-MHz laser, for the same average power (Fig. 4.1 e). We were unable to form high-contrast THG images at 10 MHz, whereas this was routinely achieved at 1 MHz. This observation fits with the expected scaling of THG signal (see Discussion).

4.4.2 THG imaging enabled *in vivo* visualization of myelin in mouse and larval zebrafish spinal cord and was combined with 2PEF microscopy for visualization of multiple tissue constituents

The value of THG as an *in vivo* myelin imaging strategy was evaluated in the mouse dorsal thoracic spinal cord. The dorsal lamina of one vertebral body was removed and covered by glass in anesthetized mice that expressed YFP in a subset of dorsal root ganglia (DRG) neurons and had blood vessels labeled with

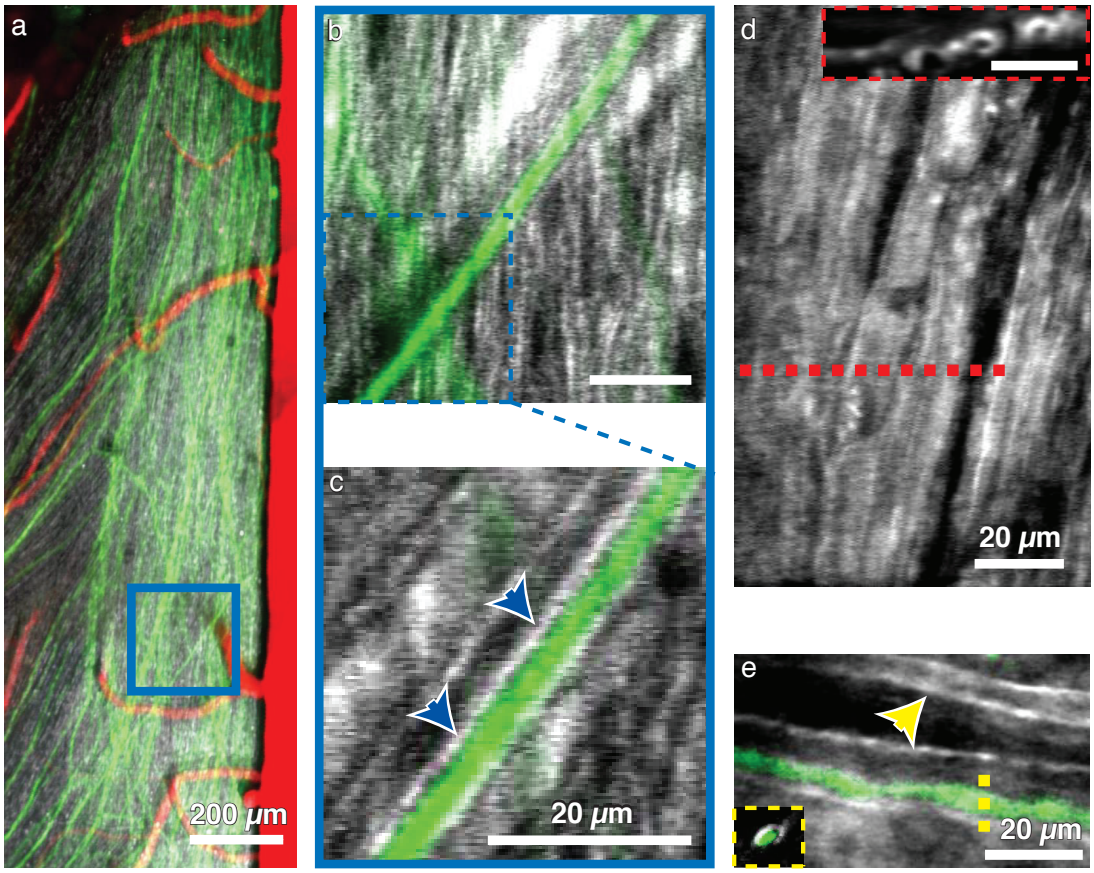

Figure 4.2: *In vivo* THG and 2PEF imaging allowed identification of individual axons and their myelin sheaths in mice and zebrafish.
2PEF imaging of YFP labeled axons (green) and blood vessels labeled by intravascular injection of Texas Red dextran (*red*), together with THG signal (*white*) in the dorsal thoracic spinal cord of a live, anesthetized mouse (a). Small ($\sim$5 μm) z projections allowed for the identification of individual axons (b and c) and their respective myelin sheaths (*blue arrows*). Slicing in the xz plane showed rings of myelin surrounding individual axons (d, *inset*). A Texas Red labeled Mauthner cell axon (e) seen in the dorsal view of 10-day old zebrafish larva showed similar imaging contrast. Myelination on the contralateral Mauthner cell axon was also visible (*yellow arrow*), with the Mauthner axons separated by the notocord.

intravenously injected Texas Red dextran (see Materials and Methods). Blood vessels, notably the large dorsal spine vein at the center of the cord and the branching venules that drain into it, as well as a subset of DRG axons that merge with the dorsal column were visible by 2PEF (Fig. 4.2 a). THG imaging revealed the striated appearance of large numbers of myelinated axons including and running parallel to axons visible from 2PEF of YFP (Fig. 4.2 a). Individual YFP-labeled axons show strong THG from a $\sim$1-μm-thick band immediately adjacent to the 3-μm-diameter axon lumen, in good agreement with published measurements of the g-ratio [37], the ratio of the inner axon diameter to the outer diameter of a myelinated axon, including its myelin sheath (Fig. 4.2, b and c). THG imaging of the most superficial myelinated tracts show distinct circular voids, suggesting axonal lumens, the cylindrical cavities of axons (Fig. 4.2 d, inset). To assess the effectiveness of THG imaging in another common animal model, we electroporated one Mauthner cell in zebrafish larvae with Texas Red dextran and imaged live, immobilized animals. THG imaging showed a myelin sheath encircling the fluorescently labeled axon lumen (Fig. 4.2 e).

4.4.3 In fixed mouse brain, THG contrast was dominated by myelin and was significantly reduced in myelin-deficient shiverer mice compared to wild-type animals

To verify that high-contrast THG signal from myelin was not limited to the spinal cord, we repeated THG imaging and 2PEF microscopy of FM Red in fixed mouse brain tissue (Fig. 4.3). Low NA imaging of both tangential (Fig. 4.3 a) and sagittal (Fig. 4.3 b) sections showed strong correspondence between

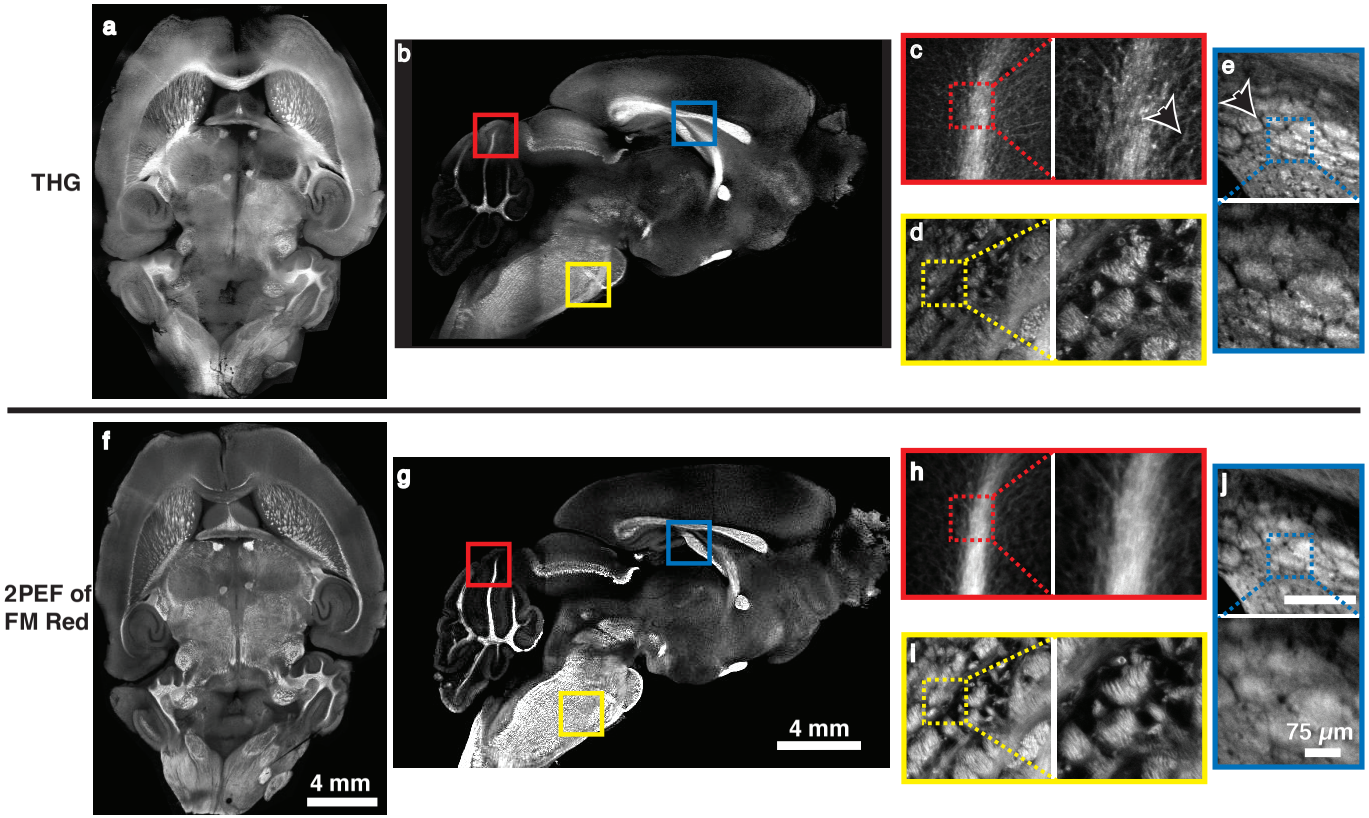

Figure 4.3: CNS myelin was the dominant source of THG contrast in the brain.
Low NA THG imaging of tangential (27 tiled images) (a,f) and sagittal (15 tiled images) (b,g) sections of the mouse brain showed strong overlap between THG and 2PEF images of FM Red labeled myelin. High THG intensities corresponded with known white matter brain regions, such as the mossy fibers in the cerebellar lobes (c, *arrow*,h) the pons and hindbrain (d,i) and axon bundles in the corpus callosum (e, *arrow*,j). High NA images (c-e,h-j) showed correspondence at the micrometer scale between THG images and 2PEF images of FM Red.

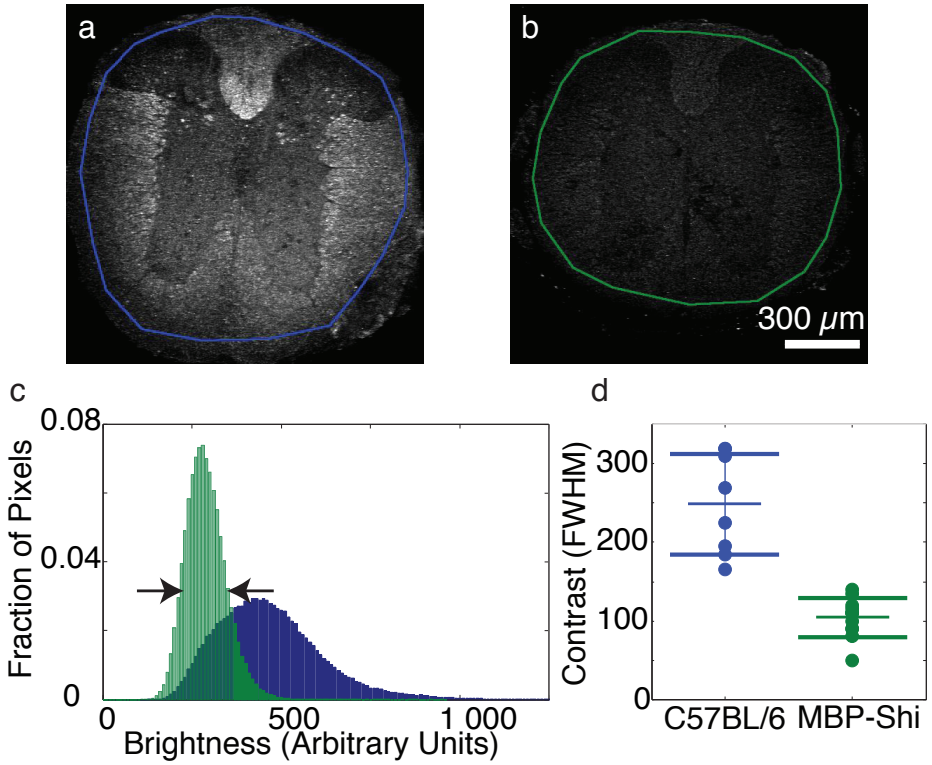

Figure 4.4: Myelin-deficient shiverer mice showed significantly less THG contrast than controls.

Thick coronal sections of thoracic spinal cord from a control mouse (a) and shiverer mouse (b) imaged using a low power objective. The intensity histogram (c) was computed for each section within the traced regions. Contrast was defined as FWHM (*arrows*) of the intensity histogram for control (*blue*) and myelin-deficient (*green*) mice. Control mice (8 sections) showed a higher image contrast as compared to shiverer mice (12 sections, $p \leq 0.05$ ANOVA) (d).

THG and FM Red. High-resolution THG images of densely myelinated regions showed individual myelinated mossy fibers in the cerebellar lobes (Fig. 4.3 c) as well as white matter tracts–dense bundles of myelinated axons–in the corpus callosum and hindbrain (Fig. 4.3, d and e, respectively). As a further verification of myelin as the source of THG contrast, we compared thick tissue sections of spinal cord from control mice (C57B/6-thy1-YFPH, $n = 8$ sections) to myelin-deficient shiverer mice (MBP-shi, $n = 12$ sections), which are homozygous for a mutation of the myelin basic protein gene. This mutation leads to severe hypomyelination in the central nervous system, resulting in tremors and seizure-like behavior [38]. We characterized THG contrast–defined as the FWHM of the intensity histogram–for both strains by comparing low NA images (Fig. 4.4 c). Edges of the sections were omitted by manual tracing (Fig. 4.4, a and b) to remove any artifacts of tissue sectioning. Shiverer mice showed less THG image contrast than controls (Fig. 4.4 d). The THG that was produced in the sections from shiverer mice was largely due to the signal from the tissue/air interface at the top of the sample. Sections from shiverer mice labeled with FM Red (not shown) showed a lack of staining, consistent with this observation. In vivo imaging of the shiverer mice (data not shown) did not show the characteristic striations visible in the wild-type animals (e.g. Fig. Fig. 4.2), individual axons could not be resolved, and THG signal was absent beyond the tissue interface at the dorsal surface of the spinal cord.

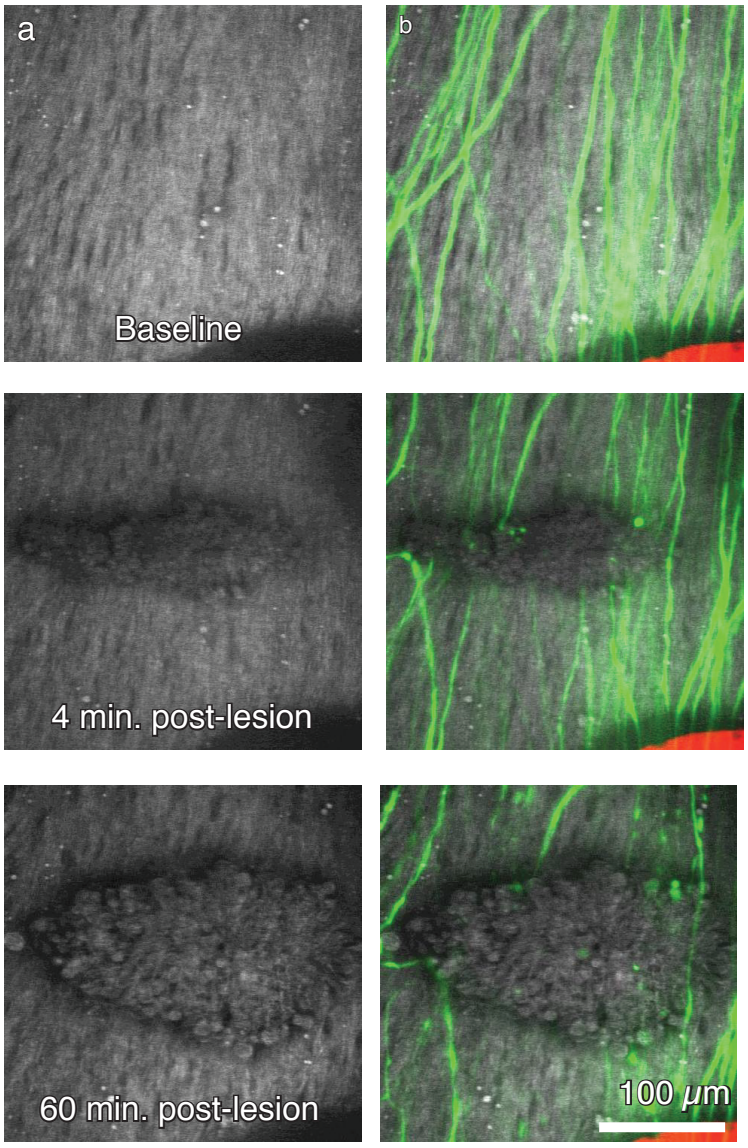

Figure 4.5: Spinal cord microlesions resulted in coordinated myelin and axon degeneration.
A laser lesion produced with femtosecond laser pulses lead to disruption of myelin (*white*) as seen in THG imaging (a). Simultaneous 2PEF imaging of severed axons (*green*) showed spatially and tempo- rally overlapped degeneration of axons and myelin after injury (b). Blood vessels were intentionally spared in creation of these lesions.

4.4.4 Changes in myelin structure after spinal cord injury occurred in regions where axons degenerated

We performed *in vivo* imaging in mice that express YFP in DRG axons before and after spinal cord injury. Spinal cord lesions were created using nonlinear absorption of tightly- focused femtosecond laser pulses from a regenerative amplifier (see Methods). After the microlesion, we performed time-lapsed imaging of THG and 2PEF of YFP-labeled axons up to 1 h after the injury (Fig. 4.5, a–c). Clear alterations in the myelin structure were evident after the lesion and the altered region grew in size over time. We assessed the presence and morphology of YFP-labeled axons within the region of disrupted myelin and found no undamaged axons and few intact proximal or distal axon tips within the region of myelin disruption (five lesions across two animals).

4.4.5 The myelin specificity of THG could be accounted for by the thickness and scattering properties of myelin

One of the distinguishing features of myelin compared to other lipid-water interfaces is that the multimembrane windings of myelin give an overall lipid thickness ranging from hundreds of nanometers to micrometers [37], compared to a typical somatic membrane thickness of only tens of nanometers. We considered THG in the forward generated direction from a biological interface modeled as a slab of dielectric of thickness L surrounded by water. The slab was symmetrically situated about the laser focus at $z = 0$ (Fig. 6 a). Following the analysis of Débarre and Beaurepaire [39], but working in our experimental

limit where, because of tight focusing, the confocal parameter, b, and sample thickness is short compared to the coherence length ($L, b << 2\pi\Delta k^{-1}$, where Δk is the wave vector mismatch), we arrive at (see Appendix A):

$$P_{3\omega} = \alpha P_0^3 \frac{L^2}{(1+(L/b)^2)^2} \left| \frac{\chi_s^{(3)}}{n_{3\omega,s}} - \frac{\chi_2^{(3)}}{n_{3\omega,w}} \right|^2 \tag{4.1}$$

Here, α is a constant dependent on excitation geometry, and $n_{3\omega}$ is the index of refraction at the third harmonic with the subscripts w and s denoting water and slab, respectively. $P_{3\omega}$ and P_0 are the intensities of the third harmonic and fundamental fields, respectively. Equation 1 predicted an approximately quadratic dependence of THG intensity on sample thickness for $L \ll b$ (Fig. 6 b). This result suggests that lipid slabs with the thickness of a cell membrane result in signals up to three-orders-of-magnitude smaller than that of myelin, well below the noise floor of our THG imaging system. This finding is consistent with our observation that the lumen of axons appeared as dark holes against the bright signal from myelin, even though many individual membranes are present in the axon.

Because THG is generated predominantly in the forward direction, epi-detection is possible only after multiple scattering events [34]. In contrast, 2PEF leads to isotropic emission, making epi-detection possible even in the absence of scattering. We used a Monte Carlo simulation to determine collection efficiency of backscattered THG and 2PEF emission as a function of scattering length. We modeled our tissue sample as a semi-infinite slab having uniform scattering and a fixed absorption length of 1 cm. Light was epi-detected after multiple scattering events provided that the light enters the collection aperture of the objective within a fixed acceptance angle (Fig. 6 c, see Appendix B). THG epi-detection efficiency was a decreasing function of scattering length, with detected THG going to zero as scattering length goes to infinity (Fig. 6 d). In

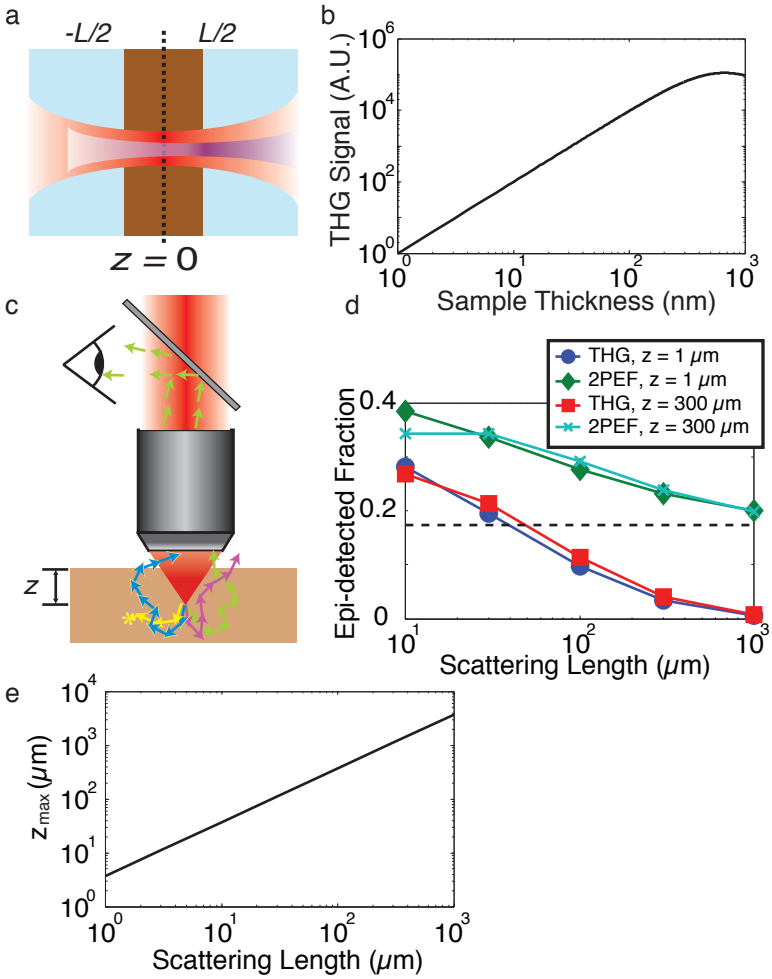

Figure 4.6: The strong THG signal from myelin was due to both the thickness and scattering properties of myelin.
Schematic for analytic calculations, in which a dielectric slab with thickness, L, much smaller than the coherence length, Δk^{-1}, was centered on the laser focus (a). Calculations showed a near-quadratic dependence of THG signal on slab thickness for sample thicknesses $< 1\mu$m (b). Third harmonic is generated in the forward direction and epi-detected only after backscattering (c). The fate of THG photons in a semi-infinite sample were to be absorbed (*yellow*), escape but not enter the objective (*mauve*), escape and hit the lens at an angle above the NA (*cyan*), or enter the objective with the acceptance angle and be detected (*green*). Monte Carlo simulations (d) for forward-generated THG and isotropically emitted fluorescence (i.e., 2PEF) originating from the focal volume gave the epi-detected fraction of light as a function of scattering length. (Dashed line) Asymptotic value of the 2PEF collection efficiency for infinite scattering length (ballistic photons only), while the efficiency tended to zero for THG. The maximum depth, z_{max}, at which high signal/noise THG imaging can be performed using a 1-W laser source to maintain the necessary 25 mW at the focus decreased linearly with scattering length (e).

contrast, the 2PEF signal tended to the ballistic photon limit with increased scattering length (marked by the dashed line in Fig. 6 d). Both THG and 2PEF showed little dependence of collection efficiency on how deep within the sample the light is generated, assuming constant excitation.

From *in vivo* 2PEF image stacks of YFP-labeled axons in the white-matter tracts, we measured the 2PEF signal attenuation length at 1043-nm wavelength, which has been shown to be dominated by scattering [3]. We fitted the exponential decay of signal as a function of depth (using constant power excitation and assuming a constant fluorophore density) and found that the white matter of the mouse spinal cord has a 2PEF signal attenuation length of $\sim$20–30 μm at 1043 nm.

We did not consider resonance effects in our analysis of the myelin signal.

4.5 DISCUSSION

4.5.1 THG enables visualization of CNS myelin *in vivo* and in fixed tissue and can be implemented on existing multiphoton microscopes

We demonstrated the ability to image CNS myelin in mice both *in vivo* (Fig. 4.2) and *ex vivo* (Figs. 1 and 3) using THG microscopy. This technique is well suited for the study of mouse models of demyelination, due to multiple sclerosis or after spinal injury (Fig. 4.5), because it opens the door to longitudinal imaging without the complication or artifacts of repeated labeling. Our demonstration

of THG imaging of myelinated axons in zebrafish (Fig. 4.2 e) suggests this technique could be combined with high-throughput drug testing in simple animal models [40]. CARS microscopy has also been shown to be an effective probe of myelination *in vivo* [11, 12]. However, this technique requires spatial and temporal overlap of 2-ps laser pulses at different wavelengths [41], a technical challenge that limits the widespread use of this modality compared to 2PEF and harmonic generation imaging.

In CARS microscopy, the myelin specificity is due to the chemical properties of myelin, namely the high density of carbon-hydrogen bonds. In contrast, our analysis suggests that the myelin specificity of THG arises predominantly from the geometrical properties of myelin. One potential advantage of THG for myelin imaging is that this method can be readily performed on existing multiphoton microscopes with the simple addition of a suitable–albeit nonstandard–femtosecond laser source and the correct detection filters, making broad adoption of this technique straightforward. Also, the laser parameters appropriate for THG are well suited for 2PEF and SHG imaging (e.g., Fig. 4.2), enabling straightforward multimodal microscopy, where the different contrast mechanisms provide complementary information [42]. For example, 2PEF, SHG, and THG multimodal microscopy has been used to monitor subcellular details in the cell division cycles during zebrafish embryogenesis [43].

4.5.2 THG is a broadly applicable, dye-free imaging modality

THG is ubiquitous to all molecules, but the efficiency of THG production is both geometry- and molecule-specific, as shown in Eq. 4.1. Our analysis suggests that the presence of a significant optical interface–both in geometric extent

and in optical properties–is both necessary and sufficient for efficient THG. Consistent with this understanding, our work has shown that myelin in the CNS can be imaged with THG, while previous researchers have shown that lipid droplets of several hundred nanometers to several micrometers [39], malaria hemazoin pigments between 0.2 and 10 μm [32], and red blood cells [44, 45], can all be imaged using THG. Additionally, we anticipate that THG may be an effective tool for visualizing myelinated nerves in the peripheral nervous system, such as the cavernous nerves running along the prostate.

4.5.3 Available excitation power and sample damage thresholds limit THG signal, suggesting that optimized laser parameters are essential

One drawback for THG imaging is that although collection efficiency is improved by short scattering length samples, the maximum depth at which measurable excitation can be achieved is severely limited. Assuming a 1-W laser source and the experimentally observed $\sim$15–20 mW required for 300-fs pulses at 1 MHz pulse repetition rate to generate reasonable THG signal/noise (still weak compared to 2PEF of fluorescently-labeled blood vessels and axons), the maximum depth that can be imaged falls off quickly with increasing scattering length (Fig. 6 e) due to the attenuation of excitation light by scattering. For the $\sim$ 20-μm scattering length of the spinal cord white matter, we predict a maximal imaging depth of 70 μ m (Fig. 6 e), and we experimentally achieved $\sim$ 50 μm. The maximum laser energy and power that can be used is set by sample damage. With the 1 MHz repetition rate laser, we observed immediate

sample damage at average power of ∼25–30 mW (25–30 nJ per pulse), likely due to nonlinear ablative processes. By way of comparison, we took images in the same sample using a 300-fs, 1028-nm source with a 10-MHz pulse train. For the 10-MHz laser system, we observed immediate sample damage at average powers of ∼50–55 mW (5–5.5 nJ per pulse), likely due to thermal effects. In either regime, photochemical-mediated damage may also contribute. One means of extending the depth limitations and/or improving the signal/noise of THG imaging, while remaining below damage thresholds, is to optimize laser parameters. THG signal depends on the inverse squares of both the repetition rate, R, and pulse duration, τ, and the cube of the average power, $< P >$:

$$THG \sim \langle P \rangle^3 / (R\tau)^2 \tag{4.2}$$

The observed disparity in THG signal (Fig. 4.1 e) between images obtained with 10-MHz and 1-MHz repetition rate laser sources is consistent with this scaling. Because ablative damage threshold varies little with pulse duration below 10 ps [46], it is always desirable to have the shortest pulse possible, with a pulse duration of 15 fs at the focus of a large NA objective possible when dispersion is carefully managed and a broad bandwidth source is used [47]. In addition, because the THG signal does not saturate, the maximum signal that can be obtained comes at the intersection of the ablative and average power damage thresholds. Thus, for a maximum pulse energy of 20 nJ (below ablative damage threshold) and a maximum average power of 50 mW (below thermal damage threshold), the optimum pulse repetition rate is 2.5 MHz. Our laser source operates at 1 MHz and emits 300-fs pulses, suggesting a signal improvement of ∼1000 is possible with an optimal laser source. In previous studies [24–33] in which THG imaging was performed in high-collection-efficiency forward detection systems, the use of suboptimal sources was not the limiting factor on

image contrast. However, as we have demonstrated by in vivo imaging of CNS myelin, the reduced collection efficiency inherent in epi-detected THG strongly suggests that the use of lower repetition rate sources (e.g., Fig. 4.1 e) may lead to significant contrast improvement, consistent with Eq. 4.2. In contrast, 2PEF microscopy–where the signal scales as the square of the average power and only inversely with the repetition rate– may benefit from the higher scan speeds possible when higher repetition rates and bright fluorophores are used [48]. However, the optimum laser repetition rate will depend on the balance between efficient signal production and dye saturation determined by the two-photon cross-section of all the labels present. It is therefore imperative to select laser sources that optimize signal from the nonlinear process of interest.

4.5.4 THG microscopy provides the capability for in vivo studies of demyelinating diseases

We imaged acute changes in myelin structure after spinal cord injury (Fig. 4.5). Our observation of axon degeneration involving a brief period of inaction followed by rapid fragmentation is consistent with the acute axonal degeneration observed in previous studies [49]. Our comparison of THG images of myelin and 2PEF images of axons after laser-based spinal cord transections suggests that acute myelin degeneration spatially and temporally overlaps with acute axonal degeneration.

4.6 CONCLUSIONS

We have demonstrated that THG provides a dye-free optical imaging modality for visualizing CNS myelin in two animal models. We have also seen that this source of contrast was significantly improved by the use of a high peak-power, low repetition-rate laser source, suggesting that these laser parameters may be more suitable for imaging weak nonlinear signals. We anticipate that these findings will be of use to both the neuroscience community and present what we believe to be new guidance for the development of laser sources for nonlinear microscopy.

4.7 APPENDIX A: CALCULATION OF THG SIGNAL FROM A DIELECTRIC SLAB

We begin with the expression for the THG from a dielectric slab of thickness L, centered at the laser focus (z 14 0), immersed in water (Fig. 6) given by Débarre and Beaurepaire [39],

$$\begin{aligned} E_{3\omega} =& iC(\vec{R})E_0^3 \left\{ \frac{\chi_s^{(3)}}{n_{3\omega,s}} (t_{sw}^{3\omega} t_{ws}^{\omega}) \int_{-L/2}^{L/2} dz \frac{\exp(i\Delta k_s(z+L/2))}{(1+i2z/b)^2} + \right. \\ & \frac{\chi_w^{(3)}}{n_{3\omega,w}} \left[(t_{sw}^{3\omega} t_{ws}^{3\omega}) \int_{-\infty}^{-L/2} dz \frac{\exp(i\Delta k_w(z+L/2))}{(1+i2z/b)^2} + \right. \\ & \left. \left. (t_{sw}^{\omega} t_{ws}^{\omega})^3 \int_{L/2}^{+\infty} dz \frac{\exp(i\Delta k_w(z-L/2))}{(1+i2z/b)^2} \right] \right\} \end{aligned} \tag{4.3}$$

where $\chi^(3)$ is the third-order nonlinear susceptibility tensor, $n_{3\omega}$ is the index of refraction at the third harmonic, Δk is the wavevector mismatch, b is the confocal parameter, t_ω is the transmission coefficient at frequency ω, and $C(\vec{R})$

is a factor that depends only on the radial geometry of the beam. Subscripts w and s denote water and slab, respectively. The difference in the arguments of the exponential in each integral arises due to requirements of the continuity of the electric field at a boundary. We neglect transmission coefficients, which are almost one in most cases of interest. This yields the expression for the third harmonic field

$$E_{3\omega} = iC(\vec{R})E_0^3 \left\{ \frac{\chi_w^{(3)}}{n_{3\omega,w}} \int_{-\infty}^{-L/2} dz \frac{\exp(i\Delta k_w(z+L/2))}{(1+i2z/b)^2} + \right. \\ \frac{\chi_s^{(3)}}{n_{3\omega,s}} \int_{-L/2}^{L/2} dz \frac{\exp(i\Delta k_s(z+L/2))}{(1+i2z/b)^2} + \\ \left. \frac{\chi_w^{(3)}}{n_{3\omega,w}} \exp(i\Delta k_s L) \int_{+L/2}^{+\infty} dz \frac{\exp(i\Delta k_w(z-L/2))}{(1+i2z/b)^2} \right\} \tag{4.4}$$

For the tight focusing geometry used for high-resolution imaging here, the coherence length, $2\pi\Delta k^{-1}$, is much greater than both the confocal parameter, b, and the sample size, L. If we consider that the Lorentzian term is significant only when $z \ll b$, then we may ignore the exponential phases. Each integral reduces to the form

$$\int_\alpha^\beta \frac{dz}{(1+i2z/b)^2} = \frac{\beta-\alpha}{(1+i2\beta/b)(1+i2\alpha/b)} \tag{4.5}$$

which when inserted into Eq. 4.4 gives

$$E_{3\omega} = iC(\vec{R})E_0^3 \frac{L}{(1+(L/b)^2)^2} \left[\frac{\chi_s^{(3)}}{n_{3\omega,s}} - \frac{\chi_w^{(3)}}{n_{3\omega,w}} \right] \tag{4.6}$$

Finally, squaring this and integrating over all radial coordinates yields the final expression

$$P_{3\omega} = \alpha P_0^3 \frac{L^2}{(1+(L/b)^2)^2} \left| \frac{\chi_s^{(3)}}{n_{3\omega,s}} - \frac{\chi_w^{(3)}}{n_{3\omega,w}} \right|^2 \tag{4.7}$$

where α represents the integration over radial coordinates, and $P_{3\omega}$ and P_0 are the intensities of the third harmonic and fundamental fields, respectively.

4.8 APPENDIX B: DESCRIPTION OF THE MONTE CARLO SIMULATION

We determined the fraction of THG or 2PEF light that is detected by an epi-oriented microscope objective using Monte Carlo simulation. We modeled our collection optics as corresponding to a 3-mm aperture with an acceptance angle of 49°. We modeled our excitation optics as corresponding to an objective with NA = 1.0 and working distance of 1.8 mm. Each photon had one of four fates:

1. It is absorbed in the sample (yellow in Fig. 6 c), or

2. It misses the aperture entirely (mauve in Fig. 6 c), or

3. It arrives at the aperture with an angle larger than the acceptance angle (cyan in Fig. 6 c), or

4. It arrives within the aperture below the acceptance angle and is detected (green in Fig. 6 c) with an intensity dependent on its path length in comparison to the sample absorption length.

We set the absorption length in our simulation to be 1 cm, in between the absorption of the hemoglobin in the blood and water. An anisotropy factor of $g = 0.96$ was used. For each set of conditions (depth and scattering length), the fate of 10^6 photons was determined.

The simulated THG was a forward propagating beam matching the properties of fundamental focused through a 1.0 NA objective but having a beam waist of $1/\sqrt{3}$ the size of the fundamental and correspondingly narrower distribution of polar angles. Azimuthal angles were chosen at random from a uniform distribution. For 2PEF simulations, both azimuthal angles and polar angles were chosen at random from a uniform distribution.

4.9 ACKNOWLEDGMENTS

We thank Francesca Minale for help with the zebrafish imaging experiments, Chris Xu and Alan Arai for critically reading this manuscript, and IMRA America Inc. for the loan of its FCPA mJewel D-400 laser.
We thank the National Institutes of Health (grant No. RO1 EB002019 to C.B.S. and F.W.W., and grant No. DP1 OD006411 to J.R.F.) and the National Science and Research Council of Canada (to M.J.F.) for financial support.

4.10 Supplementary Text

The appearance of holes in THG images of white matter tracts in the spinal cord was due to the presence of axons. Transgenic mice expressing YFP in a subset of pyramidal neurons and DRGs were perfused and the spinal cord was sectioned. THG and 2PEF imaging were performed simultaneously. Some of the holes in the THG image of myelin are seen to correspond to fluorescently labeled axon tips (Fig. 4.7), suggesting that the holes in the myelin seen in Fig. 4.1b and 1c are axons viewed on axis.

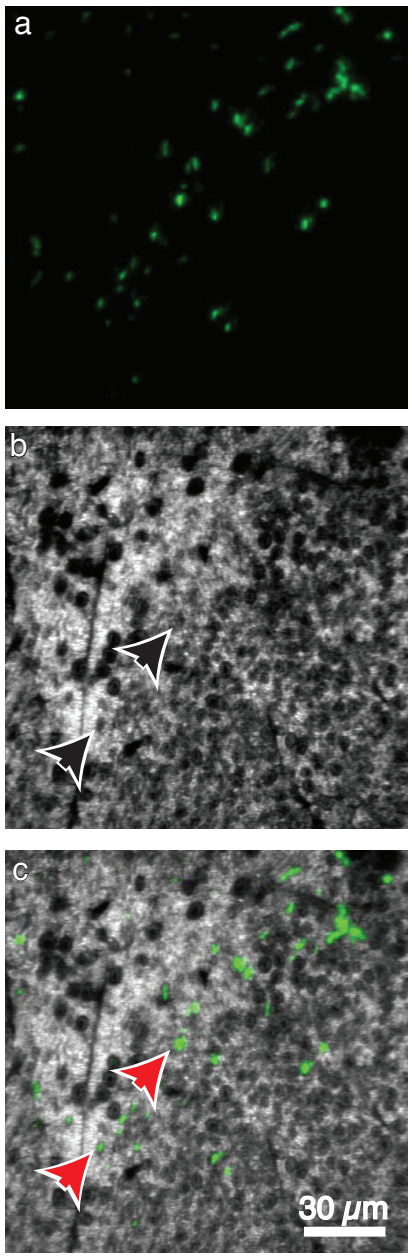

Figure 4.7: Apparent holes in THG images of the dorsal corticospinal tract were axons seen on-axis.
Fixed sections of spinal cord from mice expressing YFP in a subset of pyramidal neurons and DRG neurons were imaged using 2PEF and THG simultaneously. The axons (a) were seen on-axis perpendicular to the cut, and appear as dark holes (black arrows) in the THG image (b). Overlaying the images revealed some axons (red arrows) in the myelin relief (c), indicating that the holes were axons or axon bundles. Because this is a 2D-projection, not all axons have a corresponding visible hole.

REFERENCES

[1] W Denk, JH Strickler, and WW Webb. Two-photon laser scanning fluorescence microscopy. *Science*, 248(4951):73–76, 1990.

[2] P Theer, MT Hasan, and W Denk. Two-photon imaging to a depth of 1000 μm in living brains by use of a Ti: Al_2O_3 regenerative amplifier. *Opt Lett*, 28(12):1022–1024, 2003.

[3] Demirhan Kobat, Michael E Durst, Nozomi Nishimura, Angela W Wong, Chris B Schaffer, and Chris Xu. Deep tissue multiphoton microscopy using longer wavelength excitation. *Opt Express*, 17(16):13354–13364, 2009.

[4] Robin J M Franklin and Mark R Kotter. The biology of CNS remyelination. *J Neurol*, 255(S1):19–25, 2008.

[5] Denis Le Bihan. Looking into the functional architecture of the brain with diffusion MRI. *Nat Rev Neurosci*, 4(6):469–480, 2003.

[6] R Bakshi, AJ Thompson, MA Rocca, D Pelletier, V Dousset, F Barkhof, M Inglese, CRG Guttmann, MA Horsfield, and M Filippi. MRI in multiple sclerosis: current status and future prospects. *The Lancet Neurology*, 7(7):615–625, 2008.

[7] CG Radu, CJ Shu, SM Shelly, ME Phelps, and ON Witte. Positron emission tomography with computed tomography imaging of neuroinflammation in experimental autoimmune encephalomyelitis. *Proceedings of the National Academy of Sciences*, 104(6):1937, 2007.

[8] B Stankoff, Y Wang, M Bottlaender, MS Aigrot, F Dolle, C Wu, D Feinstein, GF Huang, F Semah, and CA Mathis. Imaging of CNS myelin by positron-emission tomography. *Proceedings of the National Academy of Sciences*, 103(24):9304, 2006.

[9] Y Wang, C Wu, AV Caprariello, E Somoza, W Zhu, C Wang, and RH Miller. In vivo quantification of myelin changes in the vertebrate nervous system. *J Neurosci*, 29(46):14663, 2009.

[10] Seung-Hyun Jung, Suhyun Kim, Ah-Young Chung, Hyun-Taek Kim, Ju-Hoon So, Jaeho Ryu, Hae-Chul Park, and Cheol-Hee Kim. Visualization of myelination in GFP-transgenic zebrafish. *Dev. Dyn.*, 239(2):592–597, 2010.

[11] H Wang, Y Fu, P Zickmund, R Shi, and JX Cheng. Coherent anti-Stokes Raman scattering imaging of axonal myelin in live spinal tissues. *Biophys J*, 89(1):581–591, 2005.

[12] Y Fu, T.B. Huff, H.W. Wang, H Wang, and J.X. Cheng. Ex vivo and in vivo imaging of myelin fibers in mouse brain by coherent anti-Stokes Raman scattering microscopy. *Opt Express*, 16(24):19396, 2008.

[13] Patrick Stoller, Karen M Reiser, Peter M Celliers, and Alexander M Rubenchik. Polarization-Modulated Second Harmonic Generation in Collagen. *Biophys J*, 82(6):3330–3342, 2002.

[14] RM Williams, WR Zipfel, and WW Webb. Second harmonic imaging for collagen structure analysis. *Biophys J*, 82:175A, 2002.

[15] RM Williams, WR Zipfel, and WW Webb. Interpreting second-harmonic generation images of collagen I fibrils. *Biophys J*, 88(2):1377–1386, 2005.

[16] W Mohler, AC Millard, and PJ Campagnola. Second harmonic generation imaging of endogenous structural proteins. *Methods*, 29(1):97–109, 2003.

[17] AC Kwan, DA Dombeck, and WW Webb. Polarized microtubule arrays in apical dendrites and axons. *Proceedings of the National Academy of Sciences*, 105(32):11370, 2008.

[18] William H Stoothoff, Brian J Bacskai, and Bradley T Hyman. Monitoring tau-tubulin interactions utilizing second harmonic generation in living neurons. *Journal of Biomedical Optics*, 13(6):064039, 2008.

[19] Paul J Campagnola, Mei-de Wei, Aaron Lewis, and Leslie M Loew. High-Resolution Nonlinear Optical Imaging of Live Cells by Second Harmonic Generation. *Biophys J*, 77(6):3341–3349, 1999.

[20] Andrew C Millard, Lei Jin, Mei-de Wei, Joseph P Wuskell, Aaron Lewis, and Leslie M Loew. Sensitivity of Second Harmonic Generation from Styryl Dyes to Transmembrane Potential. *Biophys J*, 86(2):1169–1176, 2004.

[21] L Moreaux, O Sandre, M Blanchard-Desce, and J Mertz. Membrane imaging by simultaneous second-harmonic generation and two-photon microscopy. *Opt Lett*, 25(5):320–322, 2000.

[22] R Boyd. *Nonlinear Optics, 3rd Edition*. Academic Press, 2008.

[23] D Yelin and Y Silberberg. Laser scanning third-harmonic-generation microscopy in biology. *Opt Express*, 5(8):169–175, 1999.

[24] EJ Gualda, G Filippidis, M Mari, G Voglis, M Vlachos, C Fotakis, and N Tavernarakis. In vivo imaging of neurodegeneration in Caenorhabditis elegans by third harmonic generation microscopy. *Journal of Microscopy*, 232(2):270–275, 2008.

[25] D Débarre, W Supatto, AM Pena, A Fabre, T Tordjmann, L Combettes, MC Schanne-Klein, and E Beaurepaire. Imaging lipid bodies in cells and tissues using third-harmonic generation microscopy. *Nat Meth*, 3(1):47–53, 2005.

[26] M Müller, I Squier, KR Wilson, and GI Brakenhoff. 3D microscopy of transparent objects using third-harmonic generation. *Journal of Microscopy*, 191:266–274, 1998.

[27] J Squier, M Müller, G Brakenhoff, and KR Wilson. Third harmonic generation microscopy. *Opt Express*, 3:315–324, 1998.

[28] SW Chu, SY Chen, TH Tsai, TM Liu, CY Lin, HJ Tsai, and CK Sun. In vivo developmental biology study using noninvasive multi-harmonic generation microscopy. *Opt Express*, 11:3093–3099, 2003.

[29] CK Sun, SW Chu, SY Chen, TH Tsai, TM Liu, CY Lin, and HJ Tsai. Higher harmonic generation microscopy for developmental biology. *Journal of structural biology*, 147(1):19–30, 2004.

[30] V Barzda, C Greenhalgh, JA der Au, S Elmore, JHGM van Beek, and J Squier. Visualization of mitochondria in cardiomyocytes by simultaneous harmonic generation and fluorescence microscopy. *Appl Phys Lett*, 79(24):4045–4047, 2001.

[31] CK Sun, CH Yu, SP Tai, CT Kung, IJ Wang, HC Yu, HJ Huang, WJ Lee, and YF Chan. In vivo and ex vivo imaging of intra-tissue elastic fibers using third-harmonic-generation microscopy. *Opt Express*, 15:11167–11177, 2007.

[32] JM Bélisle, S Costantino, ML Leimanis, MJ Bellemare, D Scott Bohle, E Georges, and PW Wiseman. Sensitive detection of malaria infection by third harmonic generation imaging. *Biophys J*, 94(4):L26–L28, 2008.

[33] N Olivier, F Aptel, K Plamann, MC Schanne-Klein, and E Beaurepaire.

Harmonic microscopy of isotropic and anisotropic microstructure of the human cornea. *Opt Express*, 18:5028–5040, 2010.

[34] D Débarre, N Olivier, and E Beaurepaire. Signal epidetection in third-harmonic generation microscopy of turbid media. *Opt Express*, 15(14):8913–8924, 2007.

[35] N Nishimura, CB Schaffer, B Friedman, PS Tsai, PD Lyden, and D Kleinfeld. Targeted insult to subsurface cortical blood vessels using ultrashort laser pulses: three models of stroke. *Nat Meth*, 3(2):99–108, 2006.

[36] SA Prahl, M Keijzer, SL Jacques, and AJ Welch. A Monte Carlo model of light propagation in tissue. *Dosimetry of Laser Radiation in Medicine and Biology*, 5:102–11, 1989.

[37] DL Sherman and PJ Brophy. Mechanisms of axon ensheathment and myelin growth. *Nat Rev Neurosci*, 6(9):683–690, 2005.

[38] GF Chernoff. Shiverer: an autosomal recessive mutant mouse with myelin deficiency. *Journal of Heredity*, 72(2):128–128, 1981.

[39] D Débarre and E Beaurepaire. Quantitative characterization of biological liquids for third-harmonic generation microscopy. *Biophys J*, 92(2):603–612, 2007.

[40] CE Buckley, P Goldsmith, and RJM Franklin. Zebrafish myelination: a transparent model for remyelination? *Disease Models and Mechanisms*, 1(4-5):221–228, 2008.

[41] A Zumbusch, GR Holtom, and XS Xie. Three-dimensional vibrational imaging by coherent anti-Stokes Raman scattering. *Phys. Rev. Lett.*, 82(20):4142–4145, 1999.

[42] H Chen, H Wang, MN Slipchenko, YK Jung, Y Shi, J Zhu, KK Buhman, and JX Cheng. A multimodal platform for nonlinear optical microscopy and microspectroscopy. *Opt Express*, 17:1282–1290, 2009.

[43] N Olivier, MA Luengo-Oroz, L Duloquin, E Faure, T Savy, I Veilleux, X Solinas, D Debarre, P Bourgine, and A Santos. Cell Lineage Reconstruction of Early Zebrafish Embryos Using Label-Free Nonlinear Microscopy. *Science*, 329(5994):967, 2010.

[44] AC Millard, PW Wiseman, DN Fittinghoff, KR Wilson, JA Squier, and M Muller. Third-harmonic generation microscopy by use of a compact, femtosecond fiber laser source. *Applied Optics*, 38(36):7393–7397, 1999.

[45] GO Clay, AC Millard, CB Schaffer, J Aus-der Au, PS Tsai, JA Squier, and D Kleinfeld. Spectroscopy of third-harmonic generation: evidence for resonances in model compounds and ligated hemoglobin. *Journal of the Optical Society of America B*, 23(5):932–950, 2006.

[46] AC Tien, S Backus, H Kapteyn, M Murnane, and G Mourou. Short-pulse laser damage in transparent materials as a function of pulse duration. *Phys. Rev. Lett.*, 82(19):3883–3886, 1999.

[47] M Müller, J Squier, R Wolleschensky, U Simon, and GJ Brakenhoff. Dispersion pre-compensation of 15 femtosecond optical pulses for high-numerical-aperture objectives. *Journal of Microscopy*, 191(2):141–150, 1998.

[48] N Ji, JC Magee, and E Betzig. High-speed, low-photodamage nonlinear imaging using passive pulse splitters. *Nat Meth*, 5(2):197–202, 2008.

[49] M Kerschensteiner, ME Schwab, JW Lichtman, and T Misgeld. In vivo imaging of axonal degeneration and regeneration in the injured spinal cord. *Nat Med*, 11(5):572–577, 2005.

CHAPTER 5

A CHRONIC SPINAL CHAMBER FOR LONGITUDINAL OPTICAL STUDIES OF THE MOUSE SPINAL CORD

In this chapter, we address one of the needs cited in Chapter 3, namely, the need for repeated, time-lapsed *in vivo* microscopy in the spinal cord, analogous to studies in the brain. Prior to our work, time-lapsed optical imaging in the spinal cord was limited to protocols requiring invasive surgery prior to every imaging session, placing limits on the number (and thus frequency) of measurements that can be made, as well as risking complications with each opening. We addressed this need and these limitations by engineering a spinal cord chamber that allows for a nearly arbitrary number of imaging sessions[1] without the need for repeated surgeries.

Specifically, the device had to surmount 3 challenges. First, the vertebral column undergoes routine motion and has important structural properties, and so the device must add stability to the area surrounding exposed vertebrae to compensate for any loss of mechanical integrity due to removal of the dorsal laminae. Second, the vertebral column is surrounded by and attached to soft tissue, which makes gluing to the bone or surrounding tissue all but impossible[2]. Thus, our chamber had to be secured to the vertebral column without its primary mode of attachment using glues. Lastly, the chamber had to be able to be stabilized externally during imaging for the removal of motion artifact.

Having met these requirements, we have demonstrated the usefulness of this technique for longitudinal *in vivo* imaging in both healthy and injured mouse

[1]The limits being the ability of the animal to withstand repeated bouts of anesthesia, and, of course, the inherent limitations of the experimenter himself/herself.

[2]Unlike the cranium, where gluing is routine.

spinal cords. We are hopeful that this protocol will prove a useful platform for unambiguously evaluating therapeutic strategies, thereby expediting the discovery of efficacious treatments. This work was originally published as an online advanced publication in January 2012 in Nature Methods, with the print version being released in March 2012. This article is here reprinted with minor modifications with the permission of Nature Publishing Group. The original article may be found under the following citation: Matthew J. Farrar, Ida M. Bernstein, Donald H. Schlafer, Thomas A. Cleland, Joseph R. Fetcho, and Chris B. Schaffer. Chronic *in vivo* imaging in the mouse spinal cord using an implanted chamber. *Nature Methods*, **3**, 297-302, 2012.

5.1 ABSTRACT

Understanding and treatment of spinal cord pathology is limited in part by a lack of time-lapse *in vivo* imaging strategies at the cellular level. We developed a chronically implanted spinal chamber and surgical procedure suitable for time-lapse *in vivo* multiphoton microscopy of mouse spinal cord without the need for repeat surgical procedures. We routinely imaged mice repeatedly for more than 5 weeks postoperatively with up to ten separate imaging sessions and observed neither motor-function deficit nor neuropathology in the spinal cord as a result of chamber implantation. Using this chamber we quantified microglia and afferent axon dynamics after a laser-induced spinal cord lesion and observed massive microglia infiltration within 1 d along with a heterogeneous dieback of axon stumps. By enabling chronic imaging studies over timescales ranging from minutes to months, our method offers an ideal platform for understanding cellular dynamics in response to injury and therapeutic interventions.

5.2 INTRODUCTION

In vivo optical imaging in the live mouse cortex has been achieved at depths of more than 1 mm with sub-micrometer resolution using nonlinear microscopy coupled with cranial window preparations [1]. This imaging approach has particular value for the study of neuropathology. For example, longitudinal studies (time-lapse imaging of the same region in the same animal over multiple days) in mouse models have relied on two-photon excited fluorescence (2PEF) microscopy to study the appearance and evolution of amyloid-β plaques in Alzheimers disease [2–4], the rate and extent of amyloid-β clearance in response to antibody therapy [5], the diapedesis of circulating cancer cells and formation of metastatic tumors [6] as well as the long-term effects of occlusion and reperfusion of cerebral blood vessels [7]. In all cases, a surgical protocol enabling repeated optical access to the relevant tissue is a prerequisite to longitudinal studies. Existing protocols include an open-skull protocol [8] for a cranial window in which a small portion of the mouse skull is replaced with glass, thinned-skull preparations [9] and a recently described glass-reinforced, thinned-skull preparation [10].

Chronic optical imaging could offer comparable experimental advantages to the study of the spinal cord, including studies of spinal cord injury (SCI), spinal tumors, syringeomyelia, myelitis and spinal cord ischemia. For example, time-lapse *in vivo* studies of axon trajectories after SCI would enable unambiguous identification of spared, injured and regenerating axons and provide an ideal platform for evaluating therapies aimed at spurring axon growth. This approach has been demonstrated *in vivo* in zebrafish [11], where injured axons as well as axons that regenerated in response to therapy have been imaged

over several days after SCI. Others have performed time-lapse fluorescence imaging in the spinal cord of mice expressing enhanced GFP (EGFP) in a subset of dorsal root ganglia (DRG) neurons for up to 72 h after SCI [12]. However, this imaging requires artificial ventilation and the suppression of breathing during image acquisition, limiting the timescale of cellular dynamics accessible. Similarly, 2PEF imaging in the spinal cord of mice expressing GFP in microglia has been demonstrated [13] with up to two imaging sessions in the same mouse separated by several days. Heavy sedation, whole- body suspension and local clamping are used to reduce remaining motion artifacts resulting from breathing and heartbeat. Similar techniques have been used to study microglia dynamics after a laser-induced microinjury [14], calcium signaling of dorsal horn neurons [15], the effects of peripheral nerve lesioning on sprouting of severed DRG axons [16] and experimental autoimmune encephalomyelitis [17]. Finally, imaging at as long as 4 months after SCI with as many as six imaging sessions in one subject has been achieved without interfering with animal breathing during imaging [18].

In all of these studies, obtaining images on days after the initial surgery is possible only by repeated surgical opening of the animal for each imaging session. Repeat surgeries increase the risk of infection, add a potentially confounding source of inflammation, cause tissue damage, cause additional pain and distress to the animal and severely limit the number of imaging time points possible. However, unlike the cranium, the relevant portions of the spine routinely flex and are close to the heart and lungs, requiring any chronic preparation to maintain the mechanical stability of the spine and minimize motion artifacts during imaging.

To provide a surgical preparation that enables repeated optical imaging of

the mouse spinal cord without requiring repeated surgeries, we developed an implantable spinal chamber that provides continuous optical access to the mouse spinal cord. Using this chamber, we performed 2PEF imaging in transgenic mice expressing fluorescent proteins in microglia and afferent axons, and found axon morphology to be stable over 8 weeks of imaging. Standard tests of locomotor function did not show deficits in mice with the implant as compared to control mice. Postmortem histology did not show evidence of damage to the spinal cord from the surgery but revealed increases in microglia numbers in the dorsal portion of the spinal cord, consistent with mild inflammation. Finally, we imaged blood vessels, afferent axons and microglia after laser-induced microlesioning of the spinal cord using 2PEF microscopy and quantified microglial infiltration and axon dieback dynamics on time scales spanning four orders of magnitude. We found that the increase in microglial density at the lesion site was fastest within the first 24 h after injury. Axon dieback rates were highly heterogeneous among axons, were fastest immediately after injury and slowed over 5 weeks after SCI.

5.3 RESULTS

5.3.1 The imaging chamber

The chamber consisted of two metal bars that attach to the spine together with a top plate that attaches to the bars and holds a glass window (Fig. 5.1a). The implantation procedure entailed retracting muscles and scraping clean the dorsal laminae over the imaging site, then fusing three vertebrae by clamping

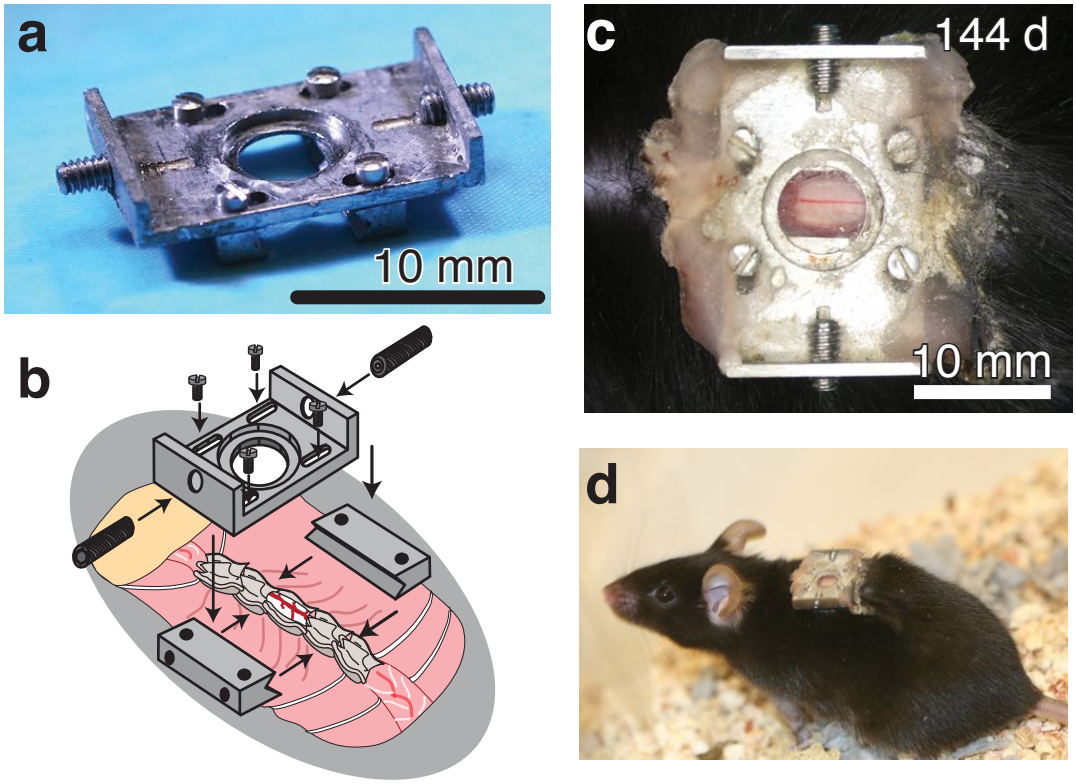

Figure 5.1: An imaging chamber for longitudinal optical access to mouse spinal cord without the need for repeated surgeries.
(a) Photograph of the imaging chamber. (b) Schema showing the implantation of the imaging chamber in mice at the T11–T12 vertebra, just below the dorsal fat pad (*taupe*). (c) Photograph showing the spinal cord imaged through the implanted chamber 144 d after the surgery. (d) Photograph of a mouse with an implanted chamber (same mouse as in c).

them on either side with small metal bars (Fig. 5.1b) held magnetically on fixed posts and finally performing a dorsal laminectomy with vanna scissors. We trimmed the lateral edges of the bone as close to the metal bars as possible and sealed the bone using a combination of cyanoacrylate and dental acrylic. We maintained clamping pressure as the chamber assembly was completed by bolting a top plate onto the metal bars, applying a silicone elastomer over the spinal cord, sealing the chamber with a glass coverslip on top and with additional glue around the edges, and finally gluing the skin to the base of the top plate (Supplementary Fig. 5.6, Supplementary Protocol and Online Methods). During 2PEF imaging, we reduced motion artifacts by securing the mouse to tapped holding posts twisted onto the set screws in the exposed wings of the top plate, thereby stabilizing the spine and elevating the mouse off of the surgical table (Supplementary Fig. 5.7) to permit free expansion of the chest cavity during inspiration. Mechanical drawings for custom parts are available in Supplementary Notes 1–6. The chamber enabled continuous optical access to the spinal cord (Fig. 5.1c) without repeat surgeries. Mice behaved normally over the weeks after surgery, with no signs of lordosis or kyphosis (Fig. 5.1d). Micro-computed tomography imaging of a mouse 6 d after implantation confirmed alignment of the spine and revealed no signs of vertebral damage (Supplementary Video 1[3]).

5.3.2 Long-term imaging of spinal cord axons and blood vessels

We implanted our chamber in transgenic mice expressing enhanced YFP (EYFP) in afferent axons from a subset of DRG neurons. We imaged mice at up to eight

[3]All supplementary videos are available online through www.nature.com/nmeth/

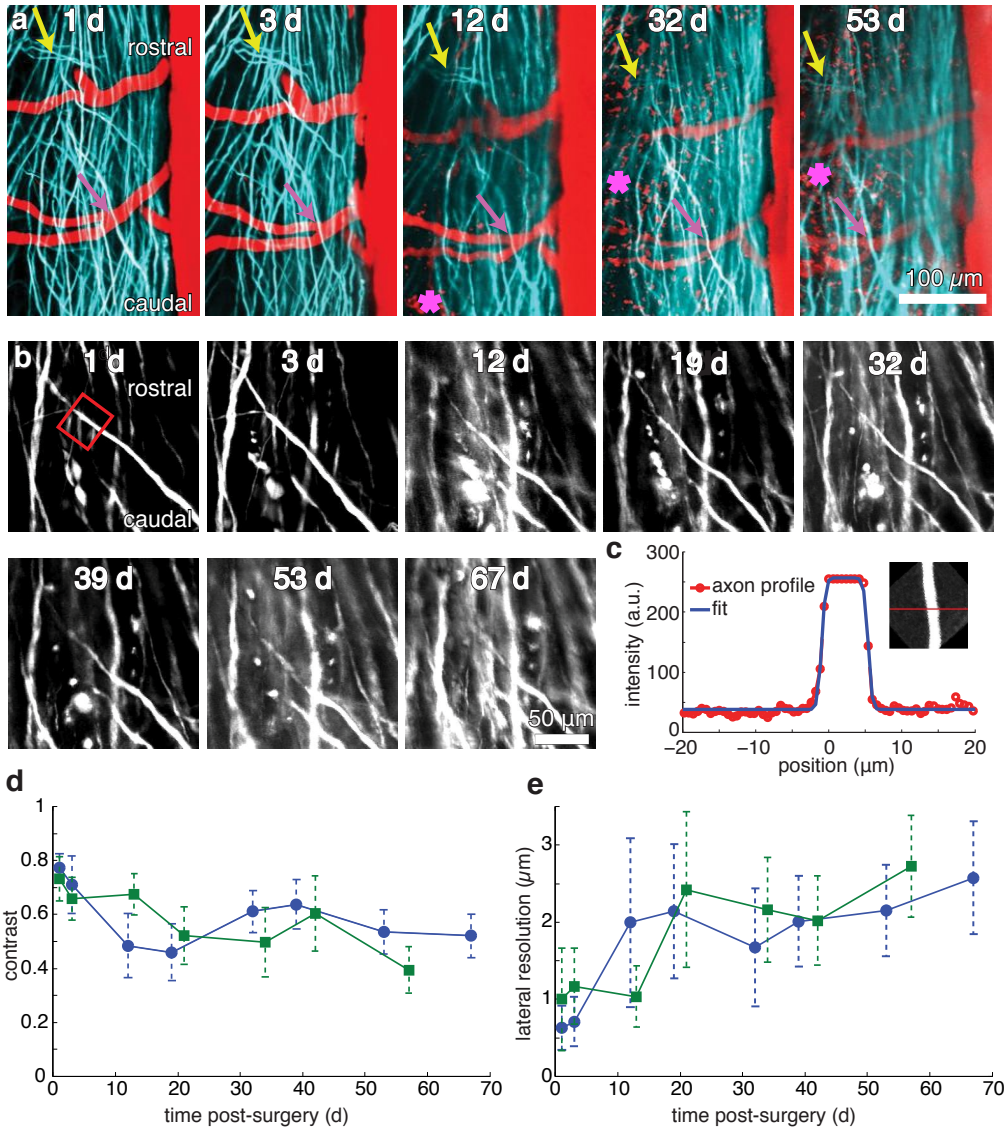

Figure 5.2: Longitudinal 2PEF imaging of axons and blood vessels over many weeks after surgery.

(a) Projections of 2PEF image stacks of afferent axons expressing EYFP (*teal*) and blood vessels labeled with intravenously injected Texas Red dextran (*red*) taken over 9 weeks after chamber implantation. Asterisks indicate the location of red autofluorescence from invading, likely inflammatory, cells located above the spinal cord at later time points. Arrows denote landmark features of the axons that were visible at all time points. (b) High-resolution 2PEF imaging of EYFP-expressing axons from the same region as in a. (c) Profile and fit (Methods, Equation (5.3)) across maximum intensity projections of selected axon segments shown in the boxed region in b and in the inset; scale bar, 30 μm). A.u., arbitrary units. (d,e) Image contrast (d) and lateral spatial resolution (e) as functions of time after surgery from the fits for all axon segments for two mice (separate curves for each mouse, 10 axons measured at each time point for each mouse). Error bars, s.d.

separate times as long as 67 d postoperatively, revealing that axon morphologies and numbers of axons were stable (Fig. 5.2a). We used blood vessels labeled with Texas Red dextran and obvious features of the axons to navigate to the same region of interest across different imaging sessions. At some time points, blood vessels had increased or decreased diameter compared to baseline but with stable morphology. Image contrast visibly diminished over time, which we quantified by fitting projections of axon segments to a simple model (Fig. 5.2b,c and Online Methods). We found a decrease in image contrast and a loss of lateral resolution over time (Fig. 5.2d,e), with the greatest change occurring over the first 14 d owing to the formation of a fibrous growth over the surface of the spinal cord. The duration over which we could resolve individual axons expressing fluorescent proteins using 2PEF imaging varied between as few as 5 d and as many as 140 d (Supplementary Fig. 5.8). We found that in mice that had only minimal fibrosis 1–2 weeks after surgery, axons could routinely be resolved up to more than 5 weeks. We could image for more than 5 weeks in $\sim 50\%$ of the mice with implants. At all time points, in mice in which fibrous tissue growth was minimal, imaging depth was limited to 30–50 μm by the short scattering length of myelin [19]. In cases in which fibrous growth was dense, we could not resolve axons at any depth. In some mice, we observed a myelin-poor region between adjacent dorsal roots that enabled imaging up to depths of 300 μm, well into the dorsal horn (Supplementary Fig. 5.9).

5.3.3 Locomotor function was preserved after implantation

We used two behavioral assays to assess the impact of the implant on motor function. We first tested mice for gait abnormalities during normal movement

[20]. Mice with inked paws ran the length of a narrow enclosure, after which we analyzed the patterns of their footprints to measure base of support (lateral distance between hindlimb placement), stride length and running speed for mice with spinal chamber implants as well as sham controls (shaved and anesthetized but not receiving surgery; three mice per group). We found no remarkable differences in gait attributable to the implant at any time point (Supplementary Fig. 5.5). In the second assay, we assessed spontaneous activity, rearing behaviors and movement speed by video-monitored open-field testing. We determined the cumulative time spent immobile, grooming, rearing and speed distributions from *post hoc* video analysis. Grooming time in mice with implants was significantly higher on days 1–3 after surgery than in sham controls, but this difference did not persist over time ($P = 0.0069$; $n = 3$ mice per group). We observed no differences in immobility or rearing times. We derived nominal top speeds from speed distributions as the average speed above the 75th percentile. Although we observed a slight reduction in top ambulatory speed in mice with implants, as compared to sham controls, it was not statistically significant (Supplementary Fig. 5.5). Finally, mice with implants did not exhibit any difficulty in grooming hindquarters or climbing (Supplementary Video 2).

5.3.4 Inflammation but no focal trauma to the spinal cord

We performed histological analysis using mice expressing EGFP in microglia (CX3CR1-GFP) or in astrocytes (GFAP-GFP) or via standard hematoxylin and eosin staining (Fig. 5.3a–c).

We implanted the spinal chamber in the transgenic mice and perfused them

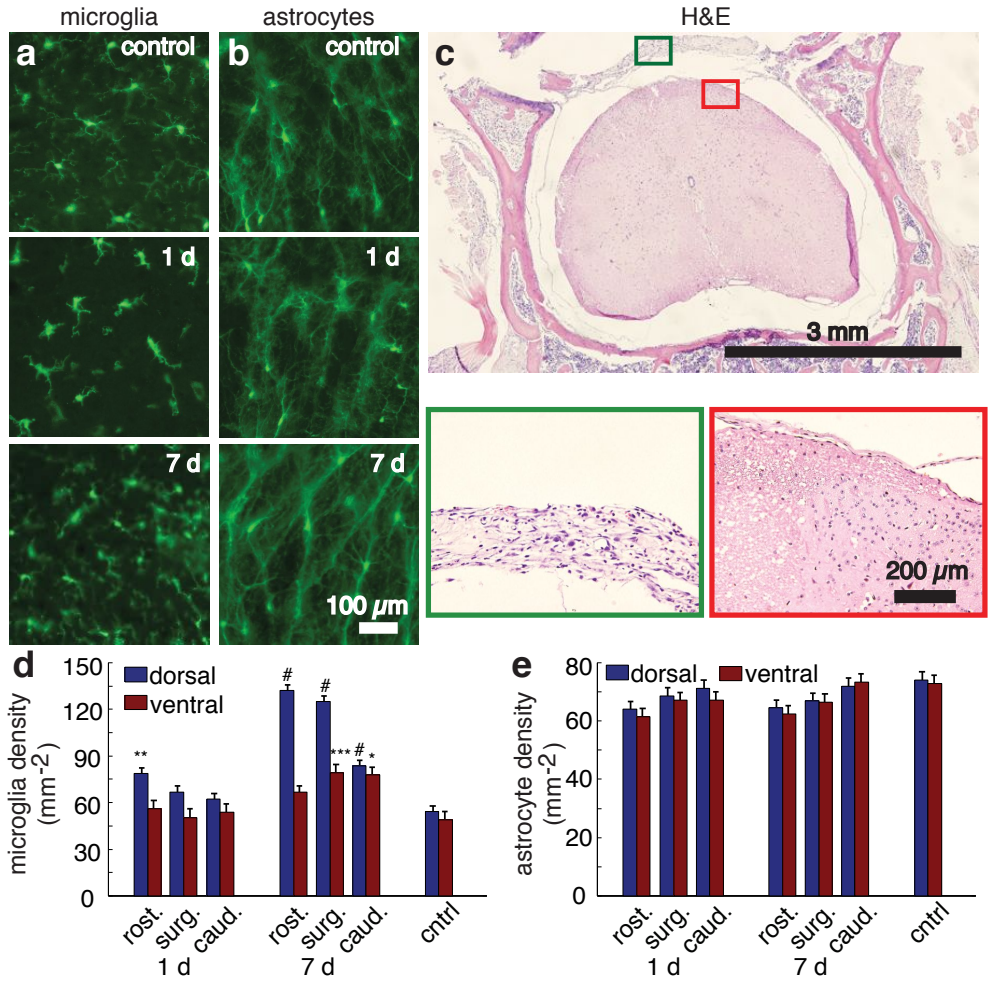

Figure 5.3: Histological analysis of reactive microglia and astrocytes, and tissue morphology after chamber implantation.
(a,b) Wide-field fluorescence images of 30-μm-thick coronal tissue sections from the laminectomy site 1 d and 1 week after implantation and in non-surgical controls for mice expressing EGFP in microglia (a) or astrocytes (b). (c) Hematoxylin and eosin–stained tissue section taken 7 d after implantation. Magnifications of the left and right boxed regions show the fibrous connective tissue that covered the dorsal aspect of the spinal cord under the implant and the neural tissue, respectively. (d,e) Microglia (d) and astrocyte (e) densites in spinal cord sections 1 and 7 d after implantation for sections one vertebra rostral to the surgical site (rost.), at the surgical site (surg.) and one vertebra caudal to the surgical site (caud.) and in controls ($*P = 0.012; **P = 0.0010; ***P = 0.0098; \#P < 0.0001; n \geq 15$ measurements per segment per time point; 3 mice per time point). Error bars, s.e.m.

for histology analysis 1 d and 1 week after surgery. We used mice that did not undergo surgery as controls (three mice per group). In mice that received implants, we analyzed sections from the site of laminectomy as well as the immediately rostral and caudal vertebrae. Both 1 d and 1 week after surgery, microglia in sections under the surgical site showed a more condensed structure with fewer processes compared to controls, but we observed no ameboid structures indicative of phagocytic microglia [21] (Fig. 5.3a). Microglia densities (Fig. 5.3d) in the dorsal aspect of the rostral segment of the spinal cord 1 d after surgery and in the dorsal aspect of all segments 1 week after surgery were elevated compared to controls. Astrocytes showed no obvious changes in morphology or cell density (Fig. 5.3b,e) across all groups.

For standard histopathology studies, we killed and perfused mice 1 d, 1 week and 1 month postoperatively (two mice per group). In all cases, control regions showed normal tissue in nerves, bone, muscle and spinal cord. Mild dermatitis was present at the skin-implant junction in all mice. Focal meningitis at the caudal edge of the window occurred in one mouse in the 1-week group. We observed no signs of meningitis or disruption of neural tissue in the other mice (Fig. 5.3c) or in other regions of the mouse exhibiting focal meningitis. Neutrophils were absent in spinal cord tissue of all mice at all time points. The fibrous tissue (Fig. 5.3c) over the dorsal surface of the cord progressively thickened over time and was the limiting factor to the duration of imaging. We observed indications of muscle injury including myositis, myodegeneration and myoregeneration along with epidural neutrophilic fascitis at the site of implantation at the 1-d and 1-week time points. Reactive bone growth and fibroplasia occurred at the lateral edges of the window at the 1-month time point. The silicone elastomer showed no signs of cellular infiltration.

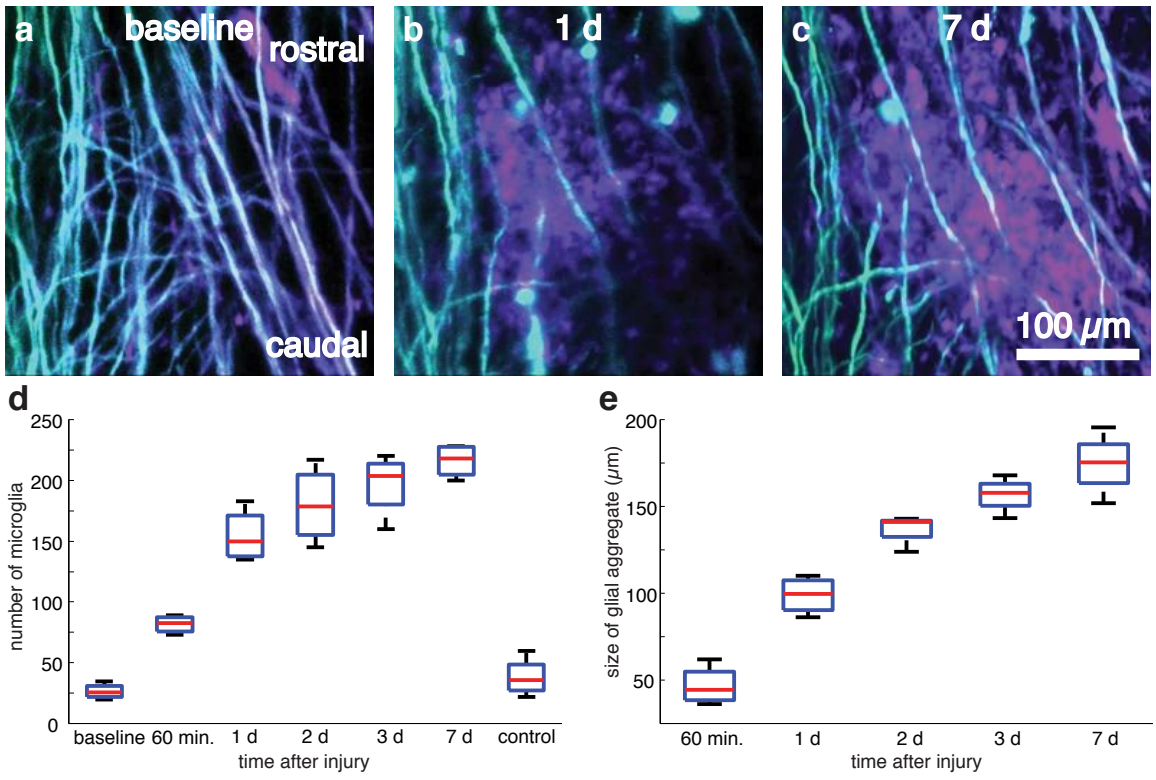

Figure 5.4: Imaging and quantification of microglial scar formation at the site of a laser-induced SCI.
(a,b) Projections of 2PEF image stacks of EYFP-labeled axons (*teal*) and EGFP- labeled microglia (*mauve*) before (a), 1 d (b) and 1 week (c) after producing a 200-μm-long laser-induced microlesion in the spinal cord. (d,e) Boxplots of the number of microglia (d) and the microglial scar size (e) in the 300-μm field of view over time (four lesions in two mice). Horizontal red lines denote the median, blue boxes bound the 25th and 75th percentiles of the data, and the whiskers denote non- outlier extrema (defined as outside the box by less than 1.5 times the interquartile range).

5.3.5 Numbers of microglia increased over 7 d after SCI.

We used double-transgenic mice expressing EYFP in a subset of DRG axons and EGFP in microglia to evaluate the dynamics of microglial scar formation after a $\sim 200\ \mu$m-long, 35-μm-deep laser-induced transection injury to the dorsal column produced using tightly focused femtosecond laser pulses (Fig. 5.4a–c; four lesions in two mice). We intentionally spared blood vessels in the creation of the lesion. Microglial cell counts increased dramatically during the first day and continued to increase more slowly over the following 6 d (Fig. 5.4d). The spatial extent of the densely packed microglial scar increased steadily over 7 d (Fig. 5.4e).

5.3.6 2PEF imaging of axon dieback after SCI.

We evaluated axonal response to injury in nine laser lesions in five mice expressing EYFP in DRG afferent axons (Fig. 5.5a). We imaged two mice for 5 weeks after injury (four lesions). We collected several image stacks at the lesion site at different times after SCI (Supplementary Video 3). We used characteristic features of spared axons to define a common point of origin across different imaging sessions (Fig. 5.5b). We used manual tracking both from three-dimensional (3D) stacks and 2D projections to determine the distance of individual axon tips from the lesion along the rostral-caudal direction (Fig. 5.5b,c). Owing to axon density and insufficient spatial extent of the image stacks, we could not distinguish ascending axons from descending branches of the DRG neurons. Owing to a loss of image contrast immediately after injury, tracing was possible for most but not all axons (95 of 107 axons traced) on acute

timescales (0–2 h). The average response of axons was to die back from the lesion site, but the extent and rate of axon dieback was highly heterogeneous (Fig. 5.5b,c). Some axons exhibited the rapid acute axonal degeneration that has been previously described [12]. Other axons persisted near the lesion site for several days or even weeks, with some mounting an abortive growth response (Fig. 5.5b,c). Axon tip morphology (Fig. 5.5b) also varied from day to day. The average dieback speed of the axons (defined as the change in an axon tips axial position between successive imaging sessions divided by the elapsed time, with growth phases excluded) declined by nearly three orders of magnitude over the 5 weeks after injury (Fig. 5.5d).

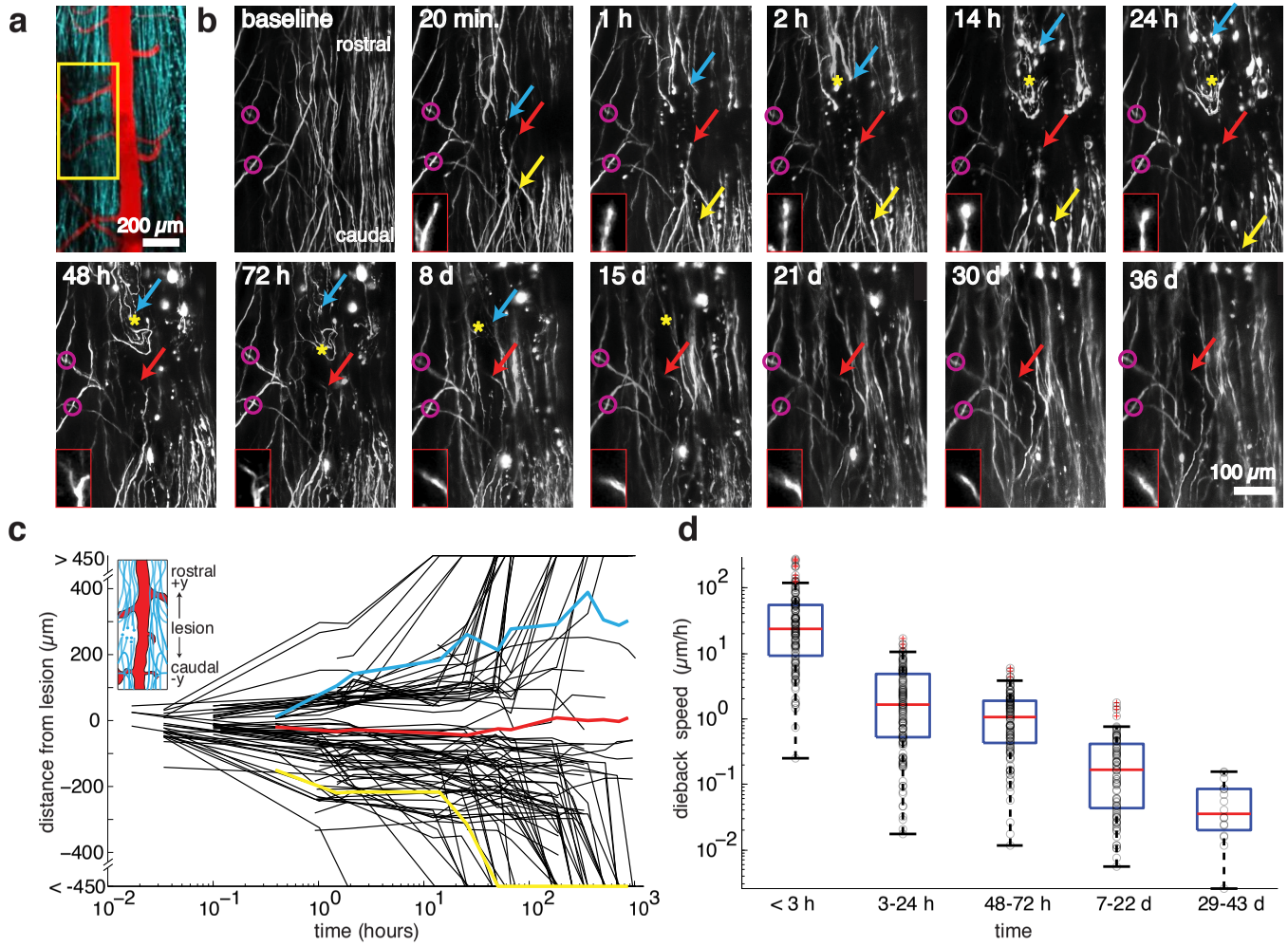

Figure 5.5: 2PEF imaging and quantification of axon dieback after a laser-induced SCI.

Figure 5.5: 2PEF imaging and quantification of axon dieback after a laser-induced SCI. (a) Projection of a 2PEF image stack from mice expressing EYFP (*teal*) in a subset of DRG neurons with the vasculature labeled with Texas Red dextran (*red*). (b) Projections of 2PEF image stacks of EYFP-expressing axons shown in the boxed region in (a) before and at indicated times after a lesion produced by translating high-energy, tightly focused femtosecond laser pulses through the cord. Mauve circles indicate easily recognizable patterns in spared axons that were identified at all time points and provide a point of origin. Yellow arrows, axon that exhibited rapid degeneration; blue arrows, axon that died back more slowly; red arrows, axon that persisted near the lesion site and made an ultimately aborted growth response (the morphology of this axon's tip is shown in the insets; scale bar in inset, 10 μm); and *, location of early sprouting responses that did not persist over time. (c) Position of axon endings over time after the lesion, with positive and negative values corresponding to positions rostral and caudal to the lesion site, respectively (see schematic in inset) (107 individual axon trajectories over nine lesions in five mice). Axon trajectories in color correspond to the locations marked by respectively colored arrows in b. (d) Speed of axon-tip dieback for axons remaining in the field of view over time after the lesion. Black circles denote measurements of dieback speed from individual axon tips, horizontal red lines represent the median, the blue boxes bound the 25th to 75th percentage of the data, and the whiskers extend 1.5 times the interquartile range beyond the boxes. Points outside the whiskers were considered outliers and have a red cross through them. Because axons died back beyond the imaging field over time, the dieback speed at early times includes data from 100 axons, and the last time point includes data for only 16 axons.

5.4 DISCUSSION

Our study of microglial invasion after laser-induced SCI revealed that although the number and spatial extent of microglia continued to increase over time, the largest fractional change occurred within the first 24 h after injury, consistent with previous studies [14]. Microglia are known to phagocytose growth-inhibitory axon debris [22] in white-matter tracts [23], suggesting that the chronic, gradual recruitment of microglia may be related to the progressive degeneration of the axons involved. Thus, imaging of microglia infiltration and the clearance of axon debris will be critical for developing optimal therapeutic strategies to manipulate the microglial response.

One of the key challenges in studies of regenerative strategies for SCI is the establishment of an optimal therapeutic time window [24–26]. Although the delay of treatment has been discussed at length with respect to the glial scar [25], our observation of heterogeneity in axon dieback, instances of early but transient sprouting and decrease in dieback rate at longer timescales may suggest an optimal therapeutic window based on axon dynamics. Our axon-by-axon characterization of axon dieback rates agreed with previous studies of acute [12] and longer-term [27,28] measurements but revealed details of this transition and allowed classification of subpopulations of axons by response: $\sim 15\%$ were stable (remained within 400 μm of the lesion for at least 4 weeks), $\sim 15\%$ rapidly disintegrated (died back beyond the field of view within the first day) and $\sim 70\%$ progressively degenerated over the first month. Such dynamic data are inaccessible to postmortem histology or analysis of gross lesion size. In future studies we will attempt to correlate these classes of heterogeneity in axon dieback with heterogeneity in regenerative responses to therapy.

Previous studies [12,13,16,18] have demonstrated time-lapse imaging of the spinal cord via repeated surgical opening of the skin above the spinal cord. Because of the inherent stresses and risks of repeated surgeries or restrictions placed by the Institutional Animal Care and Use Committee, the number of times these procedures may be performed places severe limitations on longitudinal studies. For example, in

one long-term longitudinal study, only six imaging sessions were possible in 4 months [18]. To effectively study disease dynamics and especially response to therapeutic agents, imaging must span a sufficiently long period of time to establish therapeutic limits with an imaging frequency that enables capture of transient responses. The chamber we developed requires only a single surgery and grants continuous optical access, with the frequency of imaging being limited only by the ability of the mouse to endure multiple rounds of anesthesia. We imaged immediately after SCI up to 2 h after injury, then every 12 h for 1 d, then daily for 3 d and finally weekly for 5 weeks, for a total of 13 imaging time points after SCI.

We observed microglia at the surgical site to have higher densities and fewer processes 1 week after surgery compared to control mice, suggesting an activated but not phagocytic phenotype [21]. This result is consistent with an analogous study that considered [29] inflammatory responses under cranial windows , and care will need to be taken when using our spinal cord window in studies sensitive to even mild inflammatory responses. However, we observed that even a minimal laser injury to the spinal cord results in an order of magnitude increase in microglia density near the injury, including microglia showing phagocytic ameboid morphologies. This increase far exceeds the less than twofold increase in microglia density owing to the surgery, suggesting that our chamber does not substantially confound studies in which microglial responses are more drastic.

When combined with 2PEF imaging of transgenic mice expressing fluorescent proteins in axons, microglia, astrocytes, oligodendrocytes, endothelial cells and immune cells and with nonlinear microscopy techniques to visualize myelin (such as third harmonic generation [19]), the spinal chamber described here is an ideal tool for longitudinal studies of healthy and diseased-state spinal cord, including pathologies such as multiple sclerosis, implanted spinal cord tumors or the establishment of meningitis after bacterial challenge. As our chamber does not lead to motor deficits, functional loss or recovery may be straightforwardly correlated with cellular images.

5.5 METHODS

5.5.1 Surgical procedure

We anesthetized mice under 5% isoflurane on a custom-built surgery table (Supplementary Fig. 5.7) and then maintained on $\sim 1.5\%$ isoflurane in 100% oxygen. We injected 0.05 mg of glycopyrrolate (an anticholinergic) per 100-g mouse intramuscularly. We also injected 1 mL per 100-g mouse of 5% (w/v) glucose in normal saline subcutaneously hourly. We used a rectal thermometer and feedback-controlled heating blanket to maintain body temperature at 37.5°C. We shaved the dorsal surface above the thoracic spine and applied three alternating washes each of 70% (v/v) ethanol and iodine to the skin to reduce the likelihood of infection. We gave a subcutaneous injection of 0.1 mL of 0.125% (v/v) bupivicaine at the site of skin incision.

We made a small incision in the skin at the T11–T13 level of the mouses spine and held back the skin with retractors. We made an incision three vertebrae long on either side of T12 and scraped the bone clean on the top and the sides. We severed tendons attached to the three vertebrae using surgical scissors. We trimmed all incongruous tissue to reduce necrosis. We used sterile cotton applicators to control bleeding. We clamped the three vertebrae by magnetic stainless steel bars with a notched groove and held under pressure on 30-mm stainless steel posts with a three-pronged plug, consisting of two pins to prevent rotation and a central magnet to hold the bar. We removed the dorsal lamina of T12 using vanna scissors, and used sterile gel foam (Pharmacia & Upjohn Co.) or cotton applicators along with sterile saline to control bleeding and keep blood off the surface of the cord. We trimmed the lateral edges of the bone back as close as possible to the edges of the bars and the surface of the bone sealed with dental acrylic and cyanoacrylate. Where possible, we left the dura intact.

Keeping the cord irrigated with normal saline, we positioned a top plate and screws inserted into the metal bars. We injected Kwik-Sil silicone elastomer (World Precision

Instruments) into the space between the cord and the top plate and sealed the chamber with a 5-mm diameter coverslip. We used cyanoacrylate glue and dental acrylic to seal the chamber at the rostral and caudal vertebrae. With pressure maintained by the screws, we removed the three-pronged steel posts. We pulled the skin to the edge of the implant and secured it with cyanoacrylate glue and dental acrylic. We inserted set screws into the wings of the top plate. An illustration of the procedure with accompanying photographs is available in Supplementary Figure 1. We again injected bupivicaine (0.1 mL, 0.125%) around the edge of the implant. During recovery, we placed the mouse on a heated surface and administered ketoprofen (5 mg $kg^{-1}d^{-1}$) and dexamethasone (0.2 mg kg^{-1} d^{-1}) every 24 h for 72 h. A step-by-step description of how to perform the procedure, with suggested solutions to common problems, is available in the Supplementary Protocol. We performed all surgery under a stereomicroscope (Leica MZ12.5).

All animal procedures performed were approved by the Cornell Institutional Animal Care and Use Committee and were performed under the guidance of the Cornell Center for Animal Resources and Education.

5.5.2 Mice

For imaging, we used mice of the YFP-H line (Jackson Labs), which express EYFP in a subset of pyramidal neurons and dorsal root ganglia. In addition we used CX_3CR1-GFP mice (Jackson Labs), which express EGFP in microglia. We also used crosses between the YFP-H and CX_3CR1-GFP lines. For histopathological analysis, we used mice of the YFP-H line and mice of the Emx-1-cre (Jackson Labs) lines. We used CX_3CR1-GFP mice and GFAP-GFP (Jackson labs), which express GFP in astrocytes, to study reactive gliosis in microglia and astrocytes, respectively.

In all cases, mice were of both sexes and 3–12 months in age when the device was implanted, and they were heterozygous for each transgene. Mice were group-

housed before chamber implantation and were singly housed in rat-size cages after implantation to minimize the risk of the mouse bumping the implanted chamber against the cage lid.

5.5.3 Histology

We deeply anesthetized mice and perfused them transcardially with phosphate buffered saline (PBS; pH 7.4) (SigmaAldrich) to clear the blood, followed by fixation with 4% (w/v) paraformaldehyde (PFA) (ThermoFisher Scientific) in PBS.For gliosis studies in GFAP-GFP and CX_3CR1-GFP mice, we immersed whole spines in PFA for 1 d after perfusion followed by removal of the spinal cord from the vertebral canal by microsurgical dissection. We immersed dissected spinal cords in 30% (w/v) sucrose in PBS until saturated. We froze spinal cords in optimal cutting temperature (OCT) compound (Tissue-Tek) and cut sections at a nominal thickness of 30 μm on a Microm HM550 cryotome (ThermoFisher Scientific). We took sections at the rostral and caudal edges of the implant, under the glass and control regions located one vertebrae in the rostral and caudal direction from the edges of the implant. We examined tissues under an Olympus BX41 wide-field fluorescence microscope.

For hematoxylin and eosin staining–based histopathology studies, we examined whole fixed mice for gross pathology, and gently freed and removed the skin surrounding the chambers. We separated the chambers from their attachment to the subjacent vertebral bodies starting at one end by gentle dorsal traction. Once freed from the vertebral bodies, we carefully separated the chambers from subjacent soft tissues (epaxial muscle and connective tissues). We removed any material (mostly injected silicone) that had adhered to the ventral surface of the glass windows using a scalpel and reserved it for staining. After removing ribs and organs from the vertebral column, we collected 3-mm crosssections of the vertebral column, including surrounding muscle, from 1 cm rostral, 1 cm caudal and directly below the center

of the window by making cuts perpendicular to the vertebral column using a broad tissue blade. We inserted tissues into cassettes and immersed them again in PFA. We decalcified tissues by rinsing tissue cassettes under running water for 15 min, followed by placement in a vacuum jar containing equal volumes of 20% (w/v) sodium citrate dihydrate and 50% (v/v) formic acid. Tissues were held under vacuum at room temperature (20–25°C) with constant stirring using a magnet for ∼24 h. After this procedure, we rinsed tissues under running water for 10 min and put in a solution of 70% (v/v) ethyl alcohol. We then embedded tissues in paraffin wax using an automated tissue processor (Tissue-Tek VIP), sectioned (4-μm thick sections) them and stained them with hematoxylin and eosin using an automated stainer (Shandon Varistain 24-4; Thermo Scientific). We sealed slides with a coverslip and examined them using an Olympus BX40 microscope.

5.5.4 2PEF microscopy

To image (or reimage) the spinal cord, we anesthetized mice with isoflurane and placed them on the custom surgery table described previously for the laminectomy procedure. Mice also received glycopyrrolate and glucose as described above. We used tapped 30-mm posts secured in an optical post holder to screw finger-tight onto the set screws of the wings of the top plate of the implant to locally immobilize the spine (Supplementary Fig. 5.6g). We elevated mice slightly by the implant to allow room for chest expansion and contraction during breathing. After imaging, we twisted off the posts and the mouse was allowed to recover on a heated surface.

We performed imaging using a custom-designed multiphoton microscope with a 20X water-immersion objective lens (numerical aperture (NA) = 1.0; Carl Zeiss MicroImaging), a 40X water-immersion objective (NA = 0.8; Olympus) or a 4X objective (NA = 0.28; Olympus). We performed 2PEF imaging using 1,043-nm wavelength, 1-MHz, 300-fs pulses from a fiber laser (FCPA μJewel D-400; IMRA) and/or 920-nm, 87-

MHz, 100-fs pulses from a Ti:sapphire laser oscillator (MIRA HP; Coherent). We used emission filters at 645/65 nm (center wavelength/bandwidth), 550/50 nm and 517/65 nm (Chroma Technology) to isolate fluorescence from Texas Red dextran, YFP and GFP, respectively (see Supplementary Note 7 for individual image details).

5.5.5 Spinal cord lesioning

We made lesions measuring 100–300 μm long, 5–10 μm wide and 30–40 μm deep in the dorsal spinal cord by femtosecond laser ablation using ~100-nJ pulses from a regenerative amplifier (800-nm wavelength, 50-fs pulse duration, 1-kHz repetition rate; Legend, Coherent). We used custom software in Matlab (MathWorks) to define a 2D trajectory by tracing a pattern on a z-dimension projection of a 3D image stack. To minimize the loss of image contrast caused by excessive bleeding, we intentionally avoided cutting blood vessels where possible. To execute the pattern, the mouse was translated at 500 μm s^{-1} along the traced trajectory in the x-y plane while a shutter controlling the femtosecond pulses was opened, producing a cut ~2–3 μm deep. The mouse was then translated by 1 μm in the z direction, and the cut pattern was repeated. This procedure was iterated until a cut depth of 30–40 μm was achieved. The shutter was closed during translation in the z dimension. When deemed necessary, we repeated the cut to ensure complete transection of axons. Because the damage was mediated by an electron-ion plasma formed by nonlinear optical absorption and there was very little thermal energy deposited, the damage was largely confined to the focal volume.

5.5.6 Image processing

We computed image projections by taking the standard deviation (s.d.) along the z axis of three-dimensional image stacks. For contrast and resolution measurements,

we used maximum pixel intensity projections of isolated axon segments. As we oversampled image stacks, we manually removed frames with large motion artifacts resulting from breathing without loss of information. Owing to the high density of microglia observed after SCI, there was ambiguity in distinguishing cell bodies from densely packed processes. We manually identified microglia cell bodies as fluorescent ameboid structures with visible boundaries, traced them and counted them in 2D projections using custom Matlab software. We defined microglia scar size as the mean square radius in manual traces of the boundary of the largest contiguous aggregate of microglia. For axon tracing, we Fourier filtered high-resolution (0.59 μm pixel^{-1}.) 3D image stacks, took the s.d. projection and stitched the images together using PanaVue stitching software. We used spared axons that were stable over the duration of the experiments to define a common point of origin among imaging sessions. We marked axon endings and tracked them using custom software in Matlab. We resolved ambiguities by examining trajectories in the 3D stacks.

In double-transgenic mice expressing YFP in axons and GFP in microglia, we used emission filters with 517/65 nm and 550/50 nm (center wavelength/bandwidth) with 920-nm excitation for 2PEF imaging. We linearly unmixed images in custom software written in Matlab. Briefly, we manually selected image features corresponding to axons (YFP) or microglia (GFP) in both imaging channels and generated a mixing matrix. We then solved for the inverse matrix and calculated the resultant unmixed images containing separate fluorescent species.

5.5.7 Contrast and resolution fitting

. To characterize the contrast and resolution, we first used ImageJ to isolate axon segments of $\sim$40–50 μm in length from image stacks of the same region across multiple days. We performed subsequent analysis in Matlab. We computed the maximum projection along the z axis and median-filtered the resulting image with a 1-pixel filter

radius. To orient the segment so that the axis ran parallel to the y axis, we used a radon transform to find the angle of orientation and rotated the image accordingly.

As we considered the maximum intensity projection across the axon volume, the intensity profile is equal to the value of the intensity profile taken immediately through the center of the axon, where, to good approximation, the excited fluorescence in the axon is approximately constant in the x direction. For an axon of radius R, and displaced from the origin by an amount δ, the fluorophore concentration profile, C, in a single scan at the center is

$$C(x) = C_0 \left(\theta(x + R + \delta) - \theta(x - R + \delta)\right) \tag{5.1}$$

where C_0 is the axonal fluorophore concentration and $\theta(x)$ is the Heaviside step function. For a Gaussian beam with intensity profile

$$I(x) = I_0 \exp\left(-\frac{x^2}{2a^2}\right) \tag{5.2}$$

where I_0 is tthe peak laser intensity and a is a measure of the beam waist, the image intensity, F(x), is given by the convolution of equations (5.1) and (5.2) with the addition of a background noise floor, B

$$F(x) = A\left(\text{erf}\left(\frac{x + R + \delta}{\sqrt{2}a}\right) - \text{erf}\left(\frac{x - R + \delta}{\sqrt{2}a}\right)\right) + B \tag{5.3}$$

where

$$A = \sqrt{\frac{\pi}{2}} a I_0 C_0 \tag{5.4}$$

We fit equations (5.3) to each line of the axon profile (Fig. 5.2c) and averaged the results. Failure to converge by nonlinear least-squares fitting or an R^2 value less than 0.85 was used to exclude data points. We defined contrast as

$$\frac{F(-\delta) - B}{F(-\delta) + B} \tag{5.5}$$

which ranges between 0 (no contrast) and 1 (noiseless contrast), where $F(-\delta)$ is the intensity peak in the axon. We took resolution as the parameter a.

5.5.8 Behavioral assays

We subjected mice to open-field and runway assays. We first made measurements 1 d before implantation of an imaging window, followed by measurements each day for the first 7 d and a final time point at 14 d after implantation. We made all measurements at the same time of day to avoid circadian variability. We tested mice that were shaved and anesthetized, but not operated on, simultaneously as sham controls.

We constructed analysis of footprints from the runway assay in which mice with inked paws traversed the length of a Plexiglass enclosure (76 cm long $\times$ 8 cm wide $\times$ 20 cm high) to enter a dark goal box at the end of the runway. We placed mice on an inked pad in a 15-cm-long staging area separated from the main runway by a sliding insert. We placed paper tape on the floor of the runway to collect ink pawprints. Removal of the insert marked the beginning of the trial. All trials were video-recorded from above. We performed three trials at each time point, and took footprint measurements from 5 consecutive steps in each trial. We then returned mice to their home cage between trials to minimize the effects of fatigue. Mice received 10–14 d of behavioral training before surgery. During training, we encouraged mice to traverse the length of the runway without pausing, receiving prompting from the experimenter where necessary. We deemed training complete when mice traversed the length of the runway without pausing or prompting. We assessed hindlimb base of support as the lateral distance between hindlimbs and stride length as the distance between the central pads of two consecutive hindlimb prints on the left or right. We determined average speed by dividing the runway length by the total time of the trial, as determined by the video clock.

We assessed rearing, grooming, mobility and top ambulatory speeds in open-field measurements. We placed mice in the center of a Plexiglass enclosure (46 cm long $\times$ 46 cm wide $\times$ 47 cm high) with black sides and a white base. We recorded mice from above for 5 min under red-light illumination. Video tracking analysis was performed based on the videos using ANY-maze software (Stoelting Company) and Matlab. We

defined rearing as any period during which the mouse lifted both of its forelimbs off the ground simultaneously. We defined grooming as any period during which the animal licked its fur or moved its forelimbs over the head. Top speeds were determined as the mean of the speeds greater than the 75th percentile.

5.5.9 Statistical analysis

We compared grooming time, time spent immobile, rearing time, base of support, stride length and average speed using the analysis of variance (ANOVA) test. Where the null hypothesis was rejected, we performed post hoc analyses using Tukeys honestly significant difference for pairwise comparisons. We compared top speeds of mice receiving surgery and sham treatments each day using a Mann-Whitney U test.

We compared microglia and astrocyte densities using ANOVA. Where the null hypothesis was rejected, we performed *post hoc* analyses using Tukeys honestly significant difference on mean to compare groups.

We performed statistical tests in Kaelidograph (Synergy) and Matlab. We set the criterion for significance in all cases to be $\alpha = 0.05$

5.6 ACKNOWLEDGMENTS

We thank the US National Institutes of Health (DP OD006411 to J.R.F. and R01 EB002019 to C.B.S.) and the National Science and Research Council of Canada (to M.J.F.) for financial support, IMRA America, Inc. for the loan of their FCPA μJewel D-400 laser, J. Siebert for critically reading this manuscript, N. Ellis for his assistance in the machine shop and M. Riccio for his assistance with the MicroCT imaging.

5.7 SUPPLEMENTARY MATERIALS

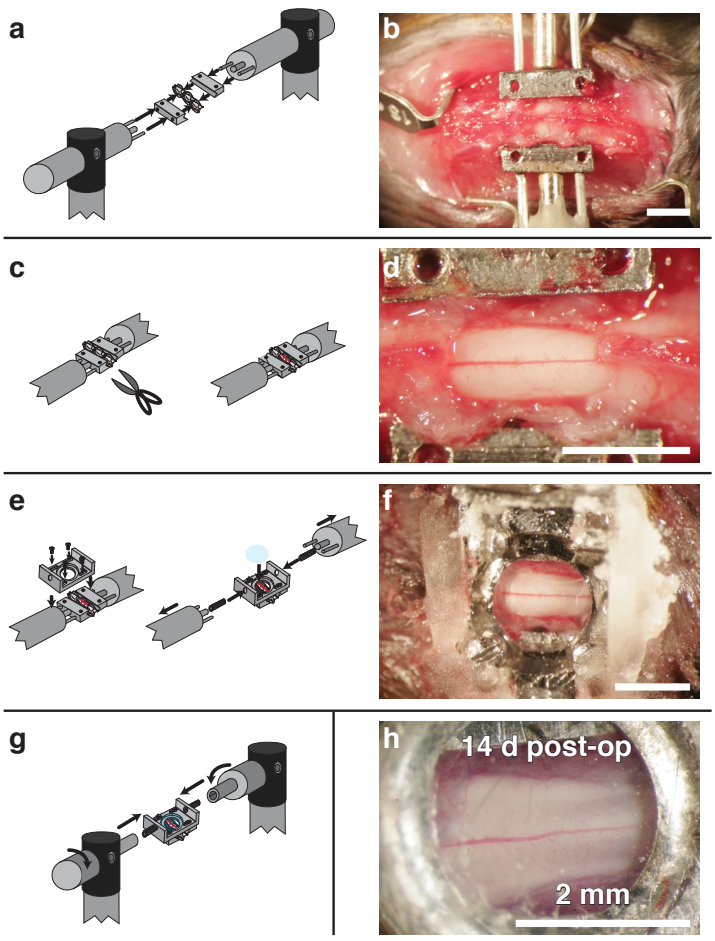

Figure 5.6: A metallic spinal chamber implant was mounted via a custom delivery system onto the vertebral column and provided long-term optical access to the spinal cord.
The exposed vertebrae (T10–T12) were clamped by notched metal bars attached to holder posts (a,b) after soft muscle had been retracted. Vanna scissors were used to complete a dorsal laminectomy (c,d) on the central vertebra (T11). A top plate was secured using four screws, maintaining the clamping pressure (e). Silicone elastomer was placed over the cord and the chamber was sealed with glass, while set screws were inserted into the wings of the top plate (e,f). Holder posts were removed (e) and the skin was sealed using a combination of cyanoacrylate adhesive and dental acrylic cement (f). To image, mice were anesthetized and the spine was locally immobilized by securing the implant to holder posts via the set screws (g). Optical access was possible for several weeks or more (h).

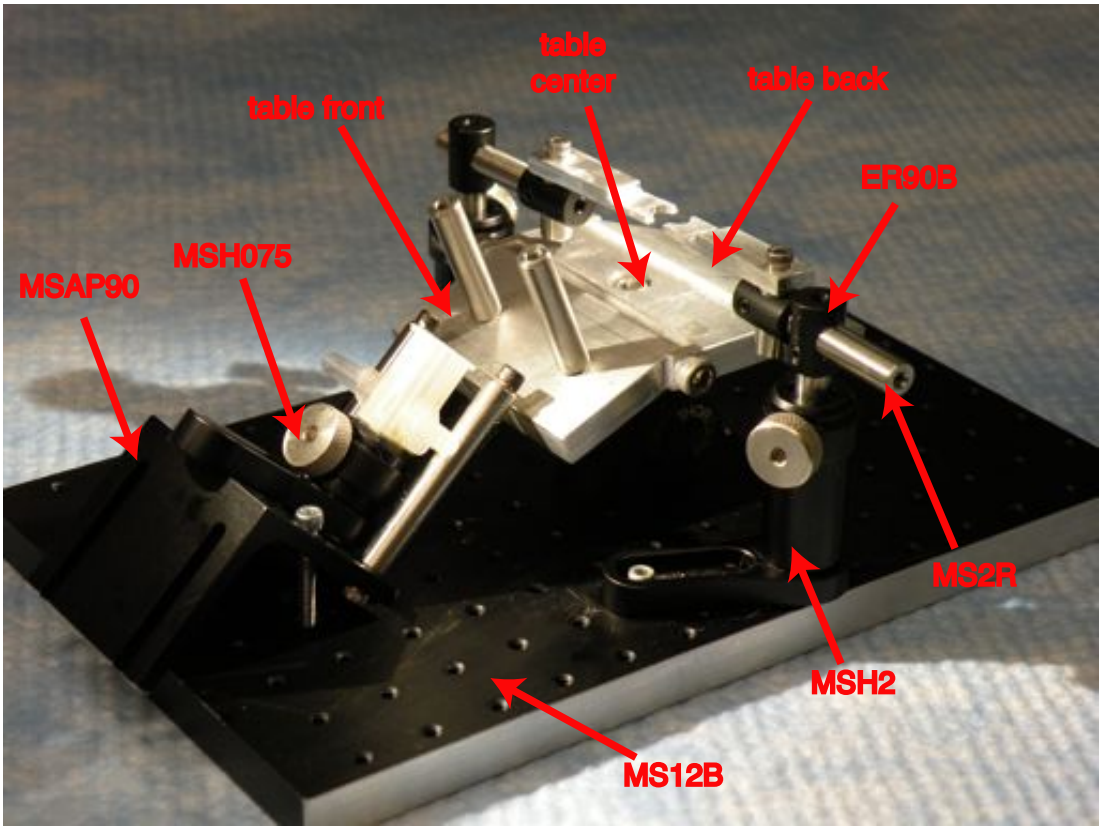

Figure 5.7: A custom surgery table allows for both surgery and imaging procedures. A procedure table –composed of rotary wings and a center part–designed for surgery and imaging is readily built with relatively inexpensive optics parts. Parts as labeled are available from Thor Labs under the following part numbers: ϕ6 mm posts (MS2R) and post- holders (MSH2), right-angle post adapters (ER90B), post-holder for nose-cone (MSH075), angle bracket (MSAP90), ϕ1/2" post (TR2) and post-holder (PH1.5) (below the surgery table), and breadboard (MS12B). The posts that screw to the set screws in the top plate of the imaging chamber, as illustrated in Fig. 5.1g, mount to the ER90B right-angle adaptors. Shown mounted here is a vertebral clamp for acute imaging where a chronic chamber is not required. Optionally, posts can be added to the table front to prevent sliding during surgery.

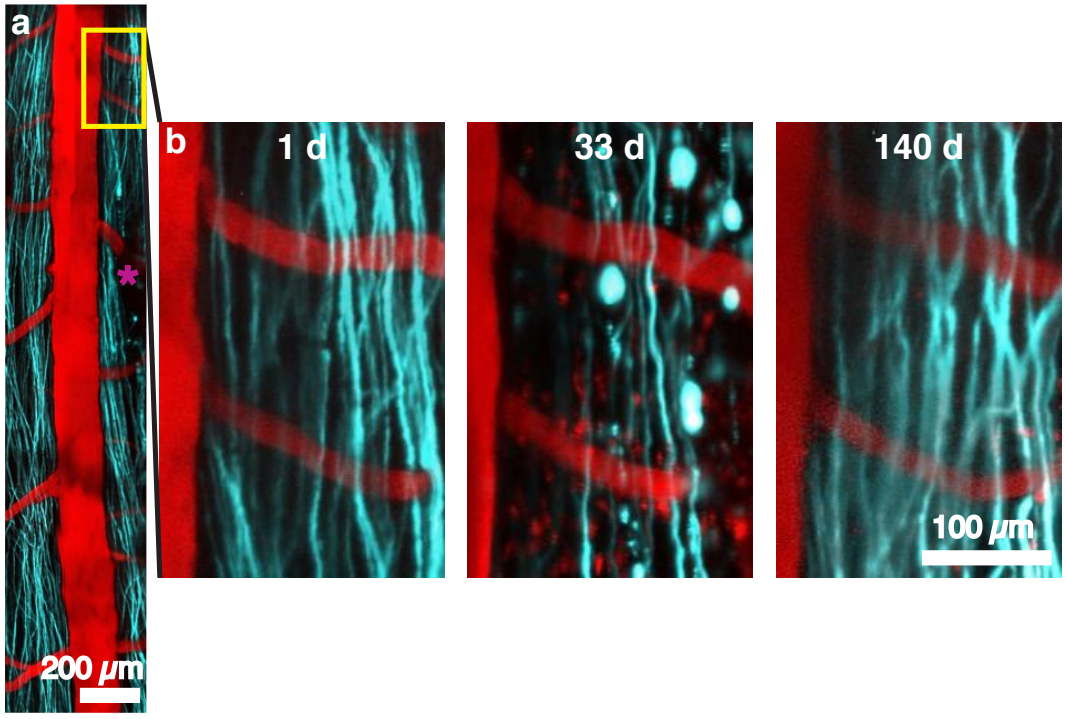

Figure 5.8: Imaging with individual axonal resolution is possible out to as many as 140 days post-surgery.
In one animal considered, multiple imaging sessions were possible out to as long as 140 days. An injury induced during surgery was evident one day after the surgery (a, *mauve asterisk*) and a region rostral to the injury (a, *yellow box*) remained sufficiently clear so as to image individual axons. Axonal degeneration progressed rostrally over time (b), with little change on one day post-surgery, severe degeneration in the selected region by day 33, and only spared axons present at day 140.

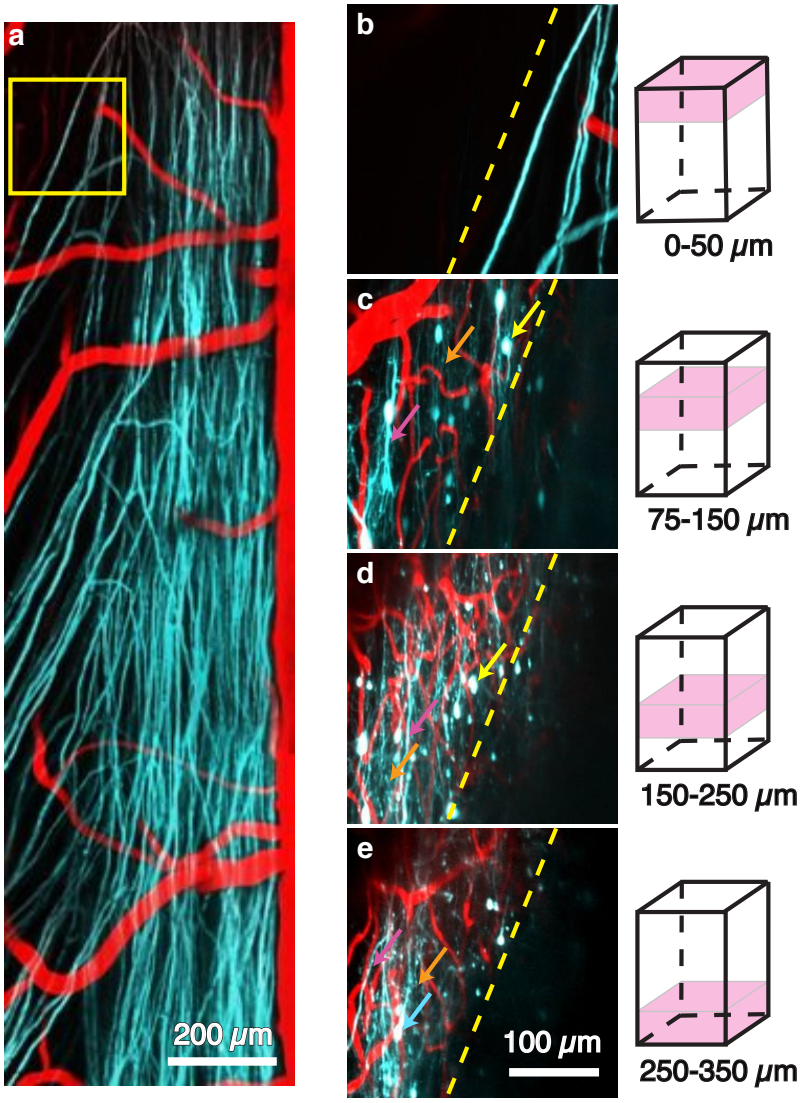

Figure 5.9: Anatomically myelin-poor regions of the spinal cord enable deep- tissue imaging.
Regions of the dorsolateral spinal cord between dorsal roots (a, *yellow box*) exhibit regions deficient of densely myelinated axons (YFP, *teal*). In these regions, imaging of neuron cell bodies (*yellow arrows*), dendrites (*orange arrows*), axons (*mauve arrows*), and vasculature (Texas Red dextran, *red*) in the dorsal horn is possible up to several hundred micrometers below the surface (b-e). Image projections are taken at and over the depths given by the illustrations (*right*). The dotted line marks the stark change in contrast between areas underlying myelinated superficial axons and regions of sparse axon density.

Supplementary Note 1

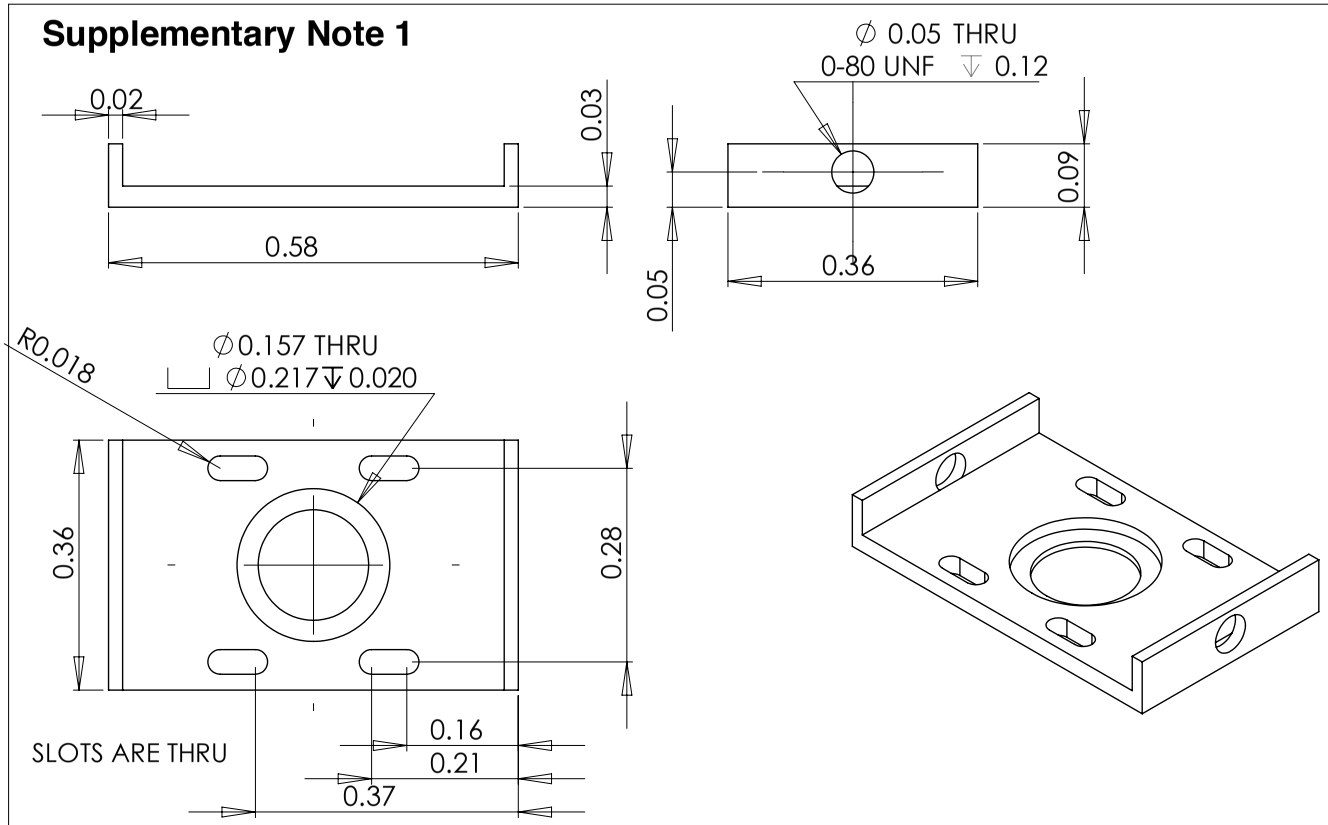

SCALE 5:1

PART: CHAMBER TOP PLATE
QUANTITY: 1
MATERIAL: 316 STAINLESS STEEL

Supplementary Note 2

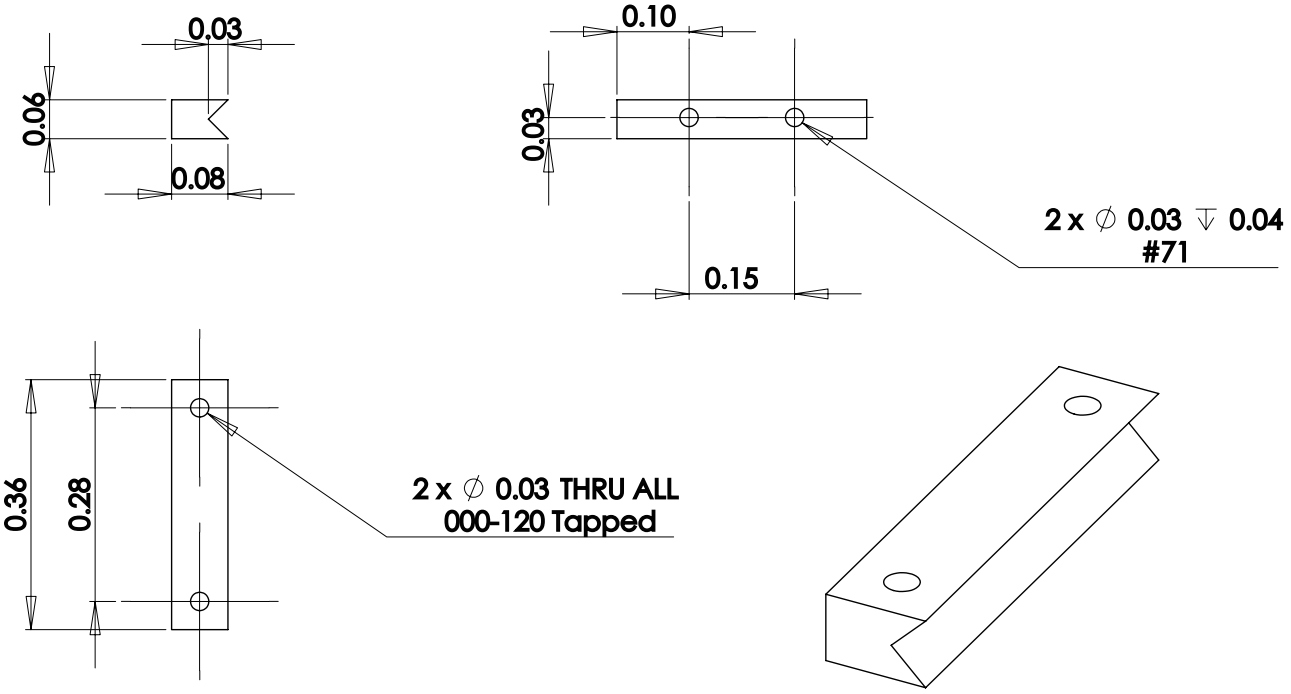

SCALE: 5:1

PART: CHAMBER SIDE BAR
QUANTITY: 2
MATERIAL: MAGNETIC STAINLESS STEEL (E.G. 430)

Supplementary Note 3

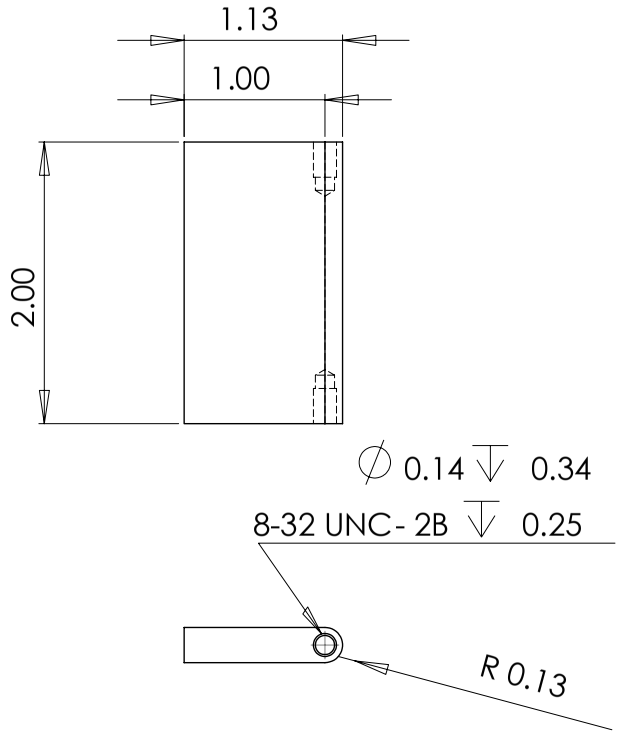

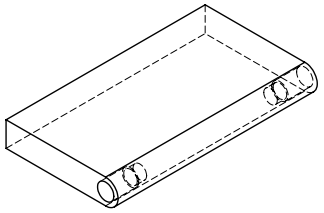

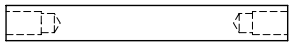

SCALE: 1:1

PART: TABLE FRONT/BACK
QUANTITY: 2
MATERIAL: ALUMINUM

REV

Supplementary Note 4

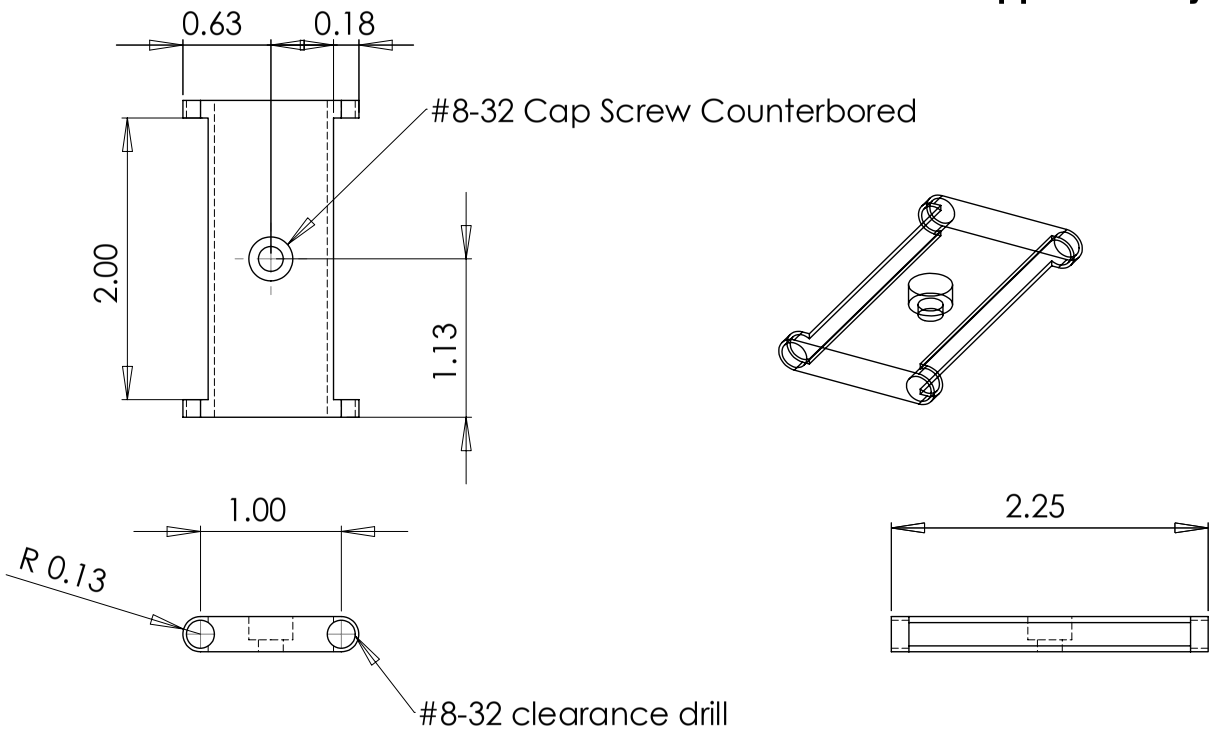

SCALE: 1:1

PART: TABLE CENTER
QUANTITY: 1
MATERIAL: ALUMINUM

Supplementary Note 5

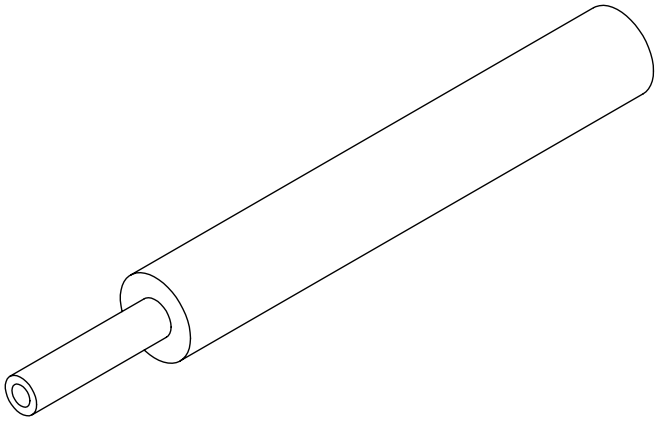

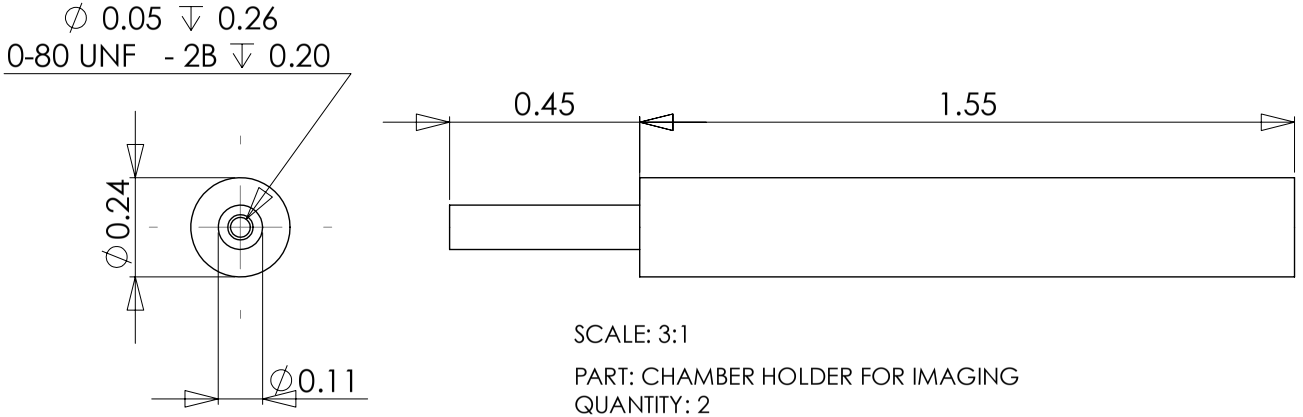

SCALE: 3:1

PART: CHAMBER HOLDER FOR IMAGING
QUANTITY: 2
MATERIAL: MODIFIED THOR LABS POST (STAINLESS STEEL)

Supplementary Note 6

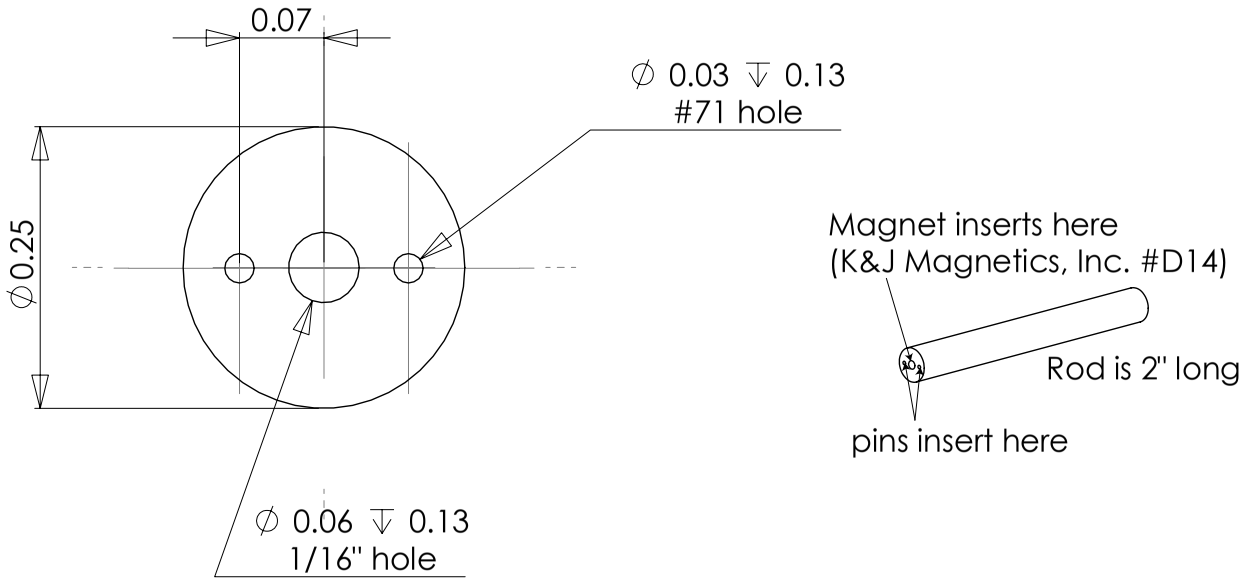

SCALE: 8:1

PART: BAR HOLDER FOR SURGERY
QUANTITY: 2
MATERIAL: MODIFIED THOR LABS POST (STAINLESS STEEL)

Supplementary Protocol

1. A mouse is anesthetized on 5 % isoflurane mixed with 100 % oxygen in an induction chamber.
2. Once initial anesthesia has been achieved, the isoflurane is reduced to ~1.5-2 % for the duration of the procedure.
3. The mouse receives glycopyrrolate (0.05 mg per 100-g mouse), an anticholinergic, via intramuscular injection into the hindlimbs.
4. The mouse is transferred to a shaving/washing station away from the sterile surgery field where the relevant portions are shaved and receive three alternating washes of iodine and 70 % ethanol applied by cotton applicator.
5. The mouse receives 0.1 mL of 0.125 % bupivicaine, a local anesthetic, subcutaneously near the peak of the thoracic curvature. Between the ears or anywhere distal to the surgery site, 1 mL per 100-g mouse of 5 % glucose in saline, 0.25 mL per 100-g mouse of 0.5 mg/mL ketoprofen, and 0.2 mL per 100-g mouse of 0.1 mg/mL dexamethasone are administered by subcutaneous injection.
6. The mouse is transferred to custom spinal surgery table (Supplementary Fig. 3) with a feedback-controlled heating blanket overlaid with sterile drapes. All surgical tools should be sterilized by autoclaving or other suitable sterilization technique.
7. A small (~1 cm incision) is made with a #10 scalpel in the skin near the thoracic arch, and fascia connecting the skin to the underlying muscle is gentle pulled away using forceps.
8. Retractors are use to hold back the skin, creating an approimately ~1” x 1.5” exposed field.

9. After finding T11, T10 is firmly grasped through the muscle using forceps, and a scalpel is used in combination with a bone scraper to remove the muscle overlying T10-T12. Sterile cotton applicators are used to control bleeding as well as to gently remove tissue adhered to the bone.
10. Using curved scissors and forceps, tendons are severed from the transverse processes of vertebrae T10-T12.
11. Tissue lateral to the vertebral column is severed and retracted from the bone deep and wide enough to allow insertion of the side bars, but taking care not to injure the dorsal roots. Bleeding is controlled with sterile cotton applicators. Critical Step: To avoid necrosis, tissue must be trimmed smooth, especially along the transverse process of the vertebrae.
12. Side bars are delivered on custom 3-pronged post-holders (bar holder) and fuse the 3 vertebrae by clamping. The compression is held by tightening set screws on the right-angle post adapter.
13. Critical Step: It is essential that all soft tissue be effectively removed from T11. This can be achieved by drying the bone with cotton applicators and/or by applying a modest amount of cyanoacrylate glue and removing it after hardening, effectively providing a means of tissue debridement.
14. Vanna scissors are inserted just into the epidural space on either lateral aspect of the dorsal lamina of T11. If the bone is sufficiently dry, the initial cut should cause the bone to crack along its length.
15. The process is repeated for the contralateral side, and any rostral or caudal soft tissue is gently cut away while pulling the dorsal lamina away from the spinal cord with forceps.

Bleeding is controlled at the edges of the laminectomy using sterile cotton applicators. Blood is cleared from the spinal cord by flushing the exposed cord with artificial cerebrospinal fluid (ACSF). Critical Step: During the removal of the bone, part of the periosteum may detach and cover the spinal cord. This tissue should be delicately removed with a dural hook or small needle. Care should be taken to distinguish the periosteum from the dura mater.

16. Once the initial lamina is removed, carefully trim back the bone on the transverse processes to more fully expose the spinal cord. The surface of the bone may be sealed by carefully applying dental cement to both the bone surface and the side bars.

17. Once bleeding has been controlled and the spinal cord cleanly exposed, the top plate is positioned on top of the side bars and centered over the laminectomy.

18. Four #000-120 screws can then be partially inserted, starting with diagonally opposite slots. Once the final position is satisfactorily achieved, these screws may be tightened.

19. Kwik Sil elastomer is injected into the laminectomy site, taking care to avoid air bubbles.

20. Immediately after injection, a #0 cover slip is inserted to seal the laminectomy, gently applying pressure to squeeze the silicone into the rest of the chamber.

21. Approximately 10-20 minutes should be given to allow the silicone to set.

22. The silicone and chamber are sealed at the rostral and caudal edges by applying small amounts of dental acrylic and/or superglue to the chamber, silicone, and the exposed bone of T10 and T12.

23. The set screws on the right-angle adapters are loosened and the custom-delivery system is gently removed from the side bars.

24. Retractors are removed, and the skin is pulled up around the edges of the implant and secured with cyanoacrylate glue.
25. #0-80 set screws are inserted into the wings of the top plate.
26. Dental acrylic is applied on top of the skin at the edges of the implant and used to fill the slots in the top plate, providing a good seal on the chamber.
27. A second injection of 0.1 mL of 0.125 % bupivicaine is administered around the implant and the animal is transferred to a clean cage on a heat pad to recover.

Step-by-Step Imaging Procedure

1. The mouse is anesthetized on 5 % isoflurane mixed with 100 % oxygen in an induction chamber.
2. Once anesthesia has been achieved, the isoflurane is be reduced to ~1.5-2 % for the duration of imaging.
3. The mouse receives glycopyrrolate (0.05 mg per 100-g mouse), an anticholinergic, via intramuscular injection into the hindlimbs.
4. The mouse is transferred to the custom surgery table (Supplementary Figure 3) with a feedback-controlled heating pad.
5. Tapped posts (chamber holders) are inserted into the right-angle adapter and twisted onto the set screws on the wings of the chamber.
6. Set screws on the right-angle adapter are tightened to prevent the chamber from moving during imaging.

7. The posts are raised in the post-holders to elevate the thorax from the surgery table, thereby allowing for free expansion of the chest upon inspiration without introducing motion artifact. Set screws on the post-holders prevent up-down motion of the posts.
8. Vasculature is labeled by intravascular injection of a fluorescent dextran by retro-orbital injection. Briefly, a syringe is inserted under the eyeball with the bevel towards the nasal septum while dye is slowly ejected.
9. Multiphoton microscopy is performed for up to several hours.
10. The tapped posts (chamber holders) are unscrewed and the mouse is allowed to recover.

Trouble Shooting

Problem	Possible Reason	Solution
1. Chamber detaches from spinal cord post-surgically	• insufficient clamping pressure • insufficient gluing	• ensure appropriate pressure applied and that set screws in right-angle adapters are tight • apply glues more liberally at the rostral and caudal edges of the implant
2. Profuse bleeding in peripheral tissue during surgery.	• severing of major artery	• cauterize bleed with electro- or thermal cautery • apply pressure to bleed until stopped with cotton applicator
3. Air bubbles in silicone under window.	• air in mixer tip • air entering through edges of chamber	• ensure that air has been evacuated from the mixer tip prior to filling chamber • apply glues more liberally at the edge of the chamber to prevent silicone from pulling away from tissue • ensure that silicone has opportunity to set prior to disturbing the chamber
4. Blood in window post-surgery.	• bleeding in peripheral tissue entering under silicone • bleeding from vertebral body • bleeding from the spinal cord itself	• determine the source of bleeding by removing the silicone, and if necessary, replace it. • apply glues more liberally at the rostral and caudal edges of the implant to seal out any peripheral fluid from entering • ensure that the bone has stopped bleeding before applying silicone • carefully applying a thin layer of superglue to the bone can help reduce bone bleeds

Problem	Possible Reason	Solution
5. Rapid (few days) loss of image contrast	• fibrous tissue growth	• trim back more of transverse processes and seal with dental acrylic • reduce space for fibrous tissue to grow by minimizing the space between the glass and spinal cord by appropriate leveling of the implant
6. Motion artifact complicates imaging.	• chamber is loose • chamber is not securely held • mouse is insufficiently elevated • spinal cord moving within vertebral column	• ensure appropriate pressure is applied and that set screws in right-angle adapters are tight • apply glues more liberally at the rostral and caudal edges of the implant • ensure all set screws are tightly fastened • elevate mouse so that chest can expand freely upon inspiration

Supplementary Note 7: Equipment and Settings

Image(s): Figure 1a,d
Acquisition device: Canon DS12601 Digital Camera
Lens: Canon Macro Lens (EF 100 mm)
Photo Processing: image brightening, uniform linear contrast adjustment

Image(s): Figure 1c
Acquisition device: Canon DS12601 Digital Camera
Lens: Leica MZ12.5 Stereomicroscope
Photo Processing: image brightening, uniform linear contrast adjustment

Image(s): Figure 2a
Objective Lens: Zeiss 20x water immersion (NA = 1.0)
Original bit depth: 16 bit/color
Fluorphore(s): YFP, Texas Red
Excitation Wavelength: 1040 nm
Bandpass Emisssion Filters: 517/65 nm, 645/65
Dichroic: 600-nm long-pass
x-y resolution: 1.11 µm/pix
z increment: 1 µm/frame
z-projection type: standard deviation
Filtering: none

Image(s): Figure 2b
Objective Lens: Zeiss 20x water immersion (NA = 1.0)
Original bit depth: 16 bit
Excitation Wavelength: 1040 nm
Fluorphore(s): YFP
Bandpass Emisssion Filters: 517/65 nm
Dichroic: 600-nm long-pass

x-y resolution: 0.59 µm/pix
z increment: 0.5 µm/frame
z-projection type: standard deviation
Filtering: bandpass filtering (0-80 pixel)

Image(s): Figure 3a,b,c (insets)
Microscope: Olympus BX41
Objective Lens: Olympus UPlan Fl 20x/0.5
Original bit depth: 8 bit
Excitation Source: Halogen lamp
Bandpass Emisssion Filters: standard GFP filter cube
Field of View: 880 µm
Image processing: image cropping

Image(s): Figure 3c
Microscope: Olympus BX41
Objective Lens: Olympus UPlan Fl 4x/0.13
Original bit depth: 8 bit
Type: Bright field image
Field of View: 4.2 mm/panel
Image processing: image stitching (4 panels), image cropping

Image(s): Figure 4a-c
Objective Lens: Zeiss 20x water immersion (NA = 1.0)
Original bit depth: 16 bit/color
Fluorphore(s): YFP, GFP
Excitation Wavelength: 920 nm and 1040 nm
Bandpass Emisssion Filters: 517/65 nm, 550/50
Dichroic: 560-nm long-pass
x-y resolution: 0.59 µm/pix
z increment: 1 µm/frame

z-projection type: average
Filtering: linear unmixing

Image(s): Figure 5a
Objective Lens: Olympus 4x (NA = 0.28)
Original bit depth: 16 bit/color
Fluorphore(s): YFP, Texas Red
Excitation Wavelength: 1040 nm
Bandpass Emisssion Filters: 517/65 nm, 645/65
Dichroic: 600-nm long-pass
x-y resolution: 2.78 µm/pix
z increment: 5 µm/frame
z-projection type: standard deviation
Filtering: linear unmixing, image stitching (3 panels)

Image(s): Figure 5b
Objective Lens: Zeiss 20x water immersion (NA = 1.0)
Original bit depth: 16 bit
Fluorphore(s): YFP
Excitation Wavelength: 1040 nm
Bandpass Emisssion Filters: 517/65 nm, 645/65
Dichroic: 600-nm long-pass
x-y resolution: 0.59 µm/pix
z increment: 1 µm/frame
z-projection type: standard deviation
Filtering: bandpass filtering (0-80 pixel)

Image(s): Supplmentary Figure 1b,d,f,h
Acquisition device: Canon DS12601 Digital Camera
Lens: Leica MZ12.5 Stereomicroscope
Photo Processing: image brightening, uniform linear contrast adjustment

Image(s): Supplementary Figure 2
Acquisition device: Nikon P80 Digital Camera
Photo Processing: image brightening, uniform linear contrast adjustment

Image(s): Supplementary Figure 3
Objective Lens: Olympus 40x water immersion (NA = 0.8)
Original bit depth: 16 bit/color
Fluorphore(s): YFP, Texas Red
Excitation Wavelength: 1040 nm
Bandpass Emisssion Filters: 517/65 nm, 645/65
Dichroic: 600-nm long-pass
x-y resolution: 0.59 µm/pix
z increment: 1 µm/frame
z-projection type: standard deviation
Filtering: none

Image(s): Supplementary Figure 4
Objective Lens: Olympus 40x water immersion (NA = 0.8)
Original bit depth: 16 bit/color
Fluorphore(s): YFP, Texas Red
Excitation Wavelength: 1040 nm
Bandpass Emisssion Filters: 517/65 nm, 645/65
Dichroic: 600-nm long-pass
x-y resolution: 0.59 µm/pix
z increment: 0.5 µm/frame
z-projection type: standard deviation
Filtering: none

REFERENCES

[1] D Kobat, ME Durst, N Nishimura, AW Wong, CB Schaffer, and C Xu. Deep tissue multiphoton microscopy using longer wavelength excitation. *Opt Express*, 17(16):13354–13364, 2009.

[2] RH Christie, BJ Bacskai, WR Zipfel, RM Williams, ST Kajdasz, WW Webb, and BT Hyman. Growth arrest of individual senile plaques in a model of Alzheimer's disease observed by in vivo multiphoton microscopy. *J Neurosci*, 21(3):858–864, 2001.

[3] Ping Yan, Adam W Bero, John R Cirrito, Qingli Xiao, Xiaoyan Hu, Yan Wang, Ernesto Gonzales, David M Holtzman, and Jin-Moo Lee. Characterizing the Appearance and Growth of Amyloid Plaques in APP/PS1 Mice. *J Neurosci*, 29(34):10706–10714, 2009.

[4] Melanie Meyer-Luehmann, Tara L Spires-Jones, Claudia Prada, Monica Garcia-Alloza, Alix de Calignon, Anete Rozkalne, Jessica Koenigsknecht-Talboo, David M Holtzman, Brian J Bacskai, and Bradley T Hyman. Rapid appearance and local toxicity of amyloid-beta plaques in a mouse model of Alzheimer's disease. *Nature*, 451(7179):720–U5, 2008.

[5] CM Prada, M Garcia-Alloza, RA Betensky, SX Zhang-Nunes, SM Greenberg, BJ Bacskai, and MP Frosch. Antibody-Mediated Clearance of Amyloid-beta Peptide from Cerebral Amyloid Angiopathy Revealed by Quantitative In Vivo Imaging. *J Neurosci*, 27(8):1973, 2007.

[6] Yvonne Kienast, Louisa von Baumgarten, Martin Fuhrmann, Wolfgang E F Klinkert, Roland Goldbrunner, Jochen Herms, and Frank Winkler. Real-time imaging reveals the single steps of brain metastasis formation. *Nat Med*, 16(1):116–U157, 2010.

[7] Carson K Lam, Taehwan Yoo, Bennett Hiner, Zhiqiang Liu, and Jaime Grutzendler. Embolus extravasation is an alternative mechanism for cerebral microvascular recanalization. *Nature*, 465(7297):478–482, 2010.

[8] A Holtmaat, T Bonhoeffer, DK Chow, J Chuckowree, V De Paola, SB Hofer, M Hübener, T Keck, G Knott, and WCA Lee. Long-term, high-resolution imaging in the mouse neocortex through a chronic cranial window. *Nat Protoc*, 4(8):1128–1144, 2009.

[9] G Yang, F Pan, CN Parkhurst, J Grutzendler, and WB Gan. Thinned-skull cranial window technique for long-term imaging of the cortex in live mice. *Nat Protoc*, 5(2):201–208, 2010.

[10] Patrick J Drew, Andy Y Shih, Jonathan D Driscoll, Per Magne Knutsen, Pablo Blinder, Dimitrios Davalos, Katerina Akassoglou, Philbert S Tsai, and David Kleinfeld. Chronic optical access through a polished and reinforced thinned skull. *Nat Meth*, 7(12):981–U60, 2010.

[11] DH Bhatt, SJ Otto, B Depoister, and JR Fetcho. Cyclic AMP-induced repair of zebrafish spinal circuits. *Science*, 305(5681):254, 2004.

[12] M Kerschensteiner, ME Schwab, JW Lichtman, and T Misgeld. In vivo imaging of axonal degeneration and regeneration in the injured spinal cord. *Nat Med*, 11(5):572–577, 2005.

[13] D Davalos, JK Lee, WB Smith, B Brinkman, MH Ellisman, B Zheng, and K Akassoglou. Stable in vivo imaging of densely populated glia, axons and blood vessels in the mouse spinal cord using two-photon microscopy. *Journal of neuroscience methods*, 169(1):1–7, 2008.

[14] P Dibaj, F Nadrigny, H Steffens, A Scheller, J Hirrlinger, ED Schomburg, C Neusch, and F Kirchhoff. NO mediates microglial response to acute spinal cord injury under ATP control in vivo. *Glia*, 58(9):1133–1144, 2010.

[15] Helge C Johannssen and Fritjof Helmchen. In vivo Ca2+imaging of dorsal horn neuronal populations in mouse spinal cord. *J Physiol-London*, 588(18):3397–3402, 2010.

[16] B Ylera, A Ertürk, F Hellal, F Nadrigny, A Hurtado, S Tahirovic, M Oudega, F Kirchhoff, and F Bradke. Chronically CNS-injured adult sensory neurons gain regenerative competence upon a lesion of their peripheral axon. *Current Biology*, 19(11):930–936, 2009.

[17] Jiyun V Kim, Ning Jiang, Carlos E Tadokoro, Liping Liu, Richard M Ransohoff, Juan J Lafaille, and Michael L Dustin. Two-photon laser scanning microscopy imaging of intact spinal cord and cerebral cortex reveals requirement for CXCR6 and neuroinflammation in immune cell infiltration of cortical injury sites. *J Immunol Methods*, 352(1-2):89–100, 2010.

[18] C Dray, G Rougon, and F Debarbieux. Quantitative analysis by in vivo imaging of the dynamics of vascular and axonal networks in injured mouse spinal cord. *Proceedings of the National Academy of Sciences*, 106(23):9459, 2009.

[19] Matthew J Farrar, Frank W Wise, Joseph R Fetcho, and Chris B Schaffer. In Vivo Imaging of Myelin in the Vertebrate Central Nervous System Using Third Harmonic Generation Microscopy. *Biophys J*, 100(5):1362–1371, 2011.

[20] JN Crawley. *Whats Wrong with My Mouse? Behavioral Phenotyping of Transgenic and Knockout Mice*. Wiley-Liss, New York, 2000.

[21] WJ Streit, SA Walter, and NA Pennell. Reactive microgliosis. *Progress in neurobiology*, 57(6):563–581, 1999.

[22] T Tanaka, M Ueno, and T Yamashita. Engulfment of axon debris by microglia requires p38 MAPK activity. *Journal of Biological Chemistry*, 284(32):21626, 2009.

[23] H Aldskogius and EN Kozlova. Central neuron-glial and glial-glial interactions following axon injury. *Progress in neurobiology*, 55(1):1–26, 1998.

[24] G García-Alías, R Lin, SF Akrimi, D Story, EJ Bradbury, and JW Fawcett. Therapeutic time window for the application of chondroitinase ABC after spinal cord injury. *Exp Neurol*, 210(2):331–338, 2008.

[25] A Rolls, R Shechter, and M Schwartz. The bright side of the glial scar in CNS repair. *Nat Rev Neurosci*, 10(3):235–241, 2009.

[26] CH Tator. Review of Treatment Trials in Humanspinal Cord Injury: Issues, Difficulties, and Recommendations. *Neurosurgery*, 59(5):957, 2006.

[27] Gamal I Seif, Hiroshi Nomura, and Charles H Tator. Retrograde axonal degeneration ("Dieback") in the corticospinal tract after transection injury of the rat spinal cord: A Confocal Microscopy study. *J Neurotraum*, 24(9):1513–1528, 2007.

[28] Kevin P Horn, Sarah A Busch, Alicia L Hawthorne, Nico van Rooijen, and Jerry Silver. Another barrier to regeneration in the CNS: Activated macrophages induce extensive retraction of dystrophic axons through direct physical interactions. *J Neurosci*, 28(38):9330–9341, 2008.

[29] Hua-Tai Xu, Feng Pan, Guang Yang, and Wen-Biao Gan. Choice of cranial window type for in vivo imaging affects dendritic spine turnover in the cortex. *Nat Neurosci*, 10(5):549–551, 2007.

CHAPTER 6

THE MOUSE POSTERIOR SPINAL VENOUS SYSTEM AND CHANGES IN FLOW AFTER POSTERIOR SPINAL VEIN OCCLUSION

In this section, we describe a work in progress on the mouse spinal vasculature. This project was worked on with two students under my supervision, Jonathan Rubin and Darcy Diago, whose hard work and insights have led to the development of this project. Jonathan Rubin adopted a ferric (III) chloride technique for inducing vascular clots, and applied this method to the posterior spinal vein (PSV) of the mouse spinal cord. This technique allowed us to create a point occlusion in the PSV without causing collateral damage to surrounding vessels or tissue. In effect, we were able to study the changes in blood flow resulting purely from disruption in flow and in the absence of larger-scale trauma.

Darcy Diago adopted a tissue clearing technique, allowing us to characterize the posterior spinal vasculature up to a depth of approximately 700 μm from the posterior surface, including the PSV and posterior spinal arteries. Given that the short scattering length of myelin limits *in vivo* imaging or imaging without clearing to less than 100 μm, this technique presents a considerable advantage to mapping the spinal cord microvasculature. Darcy has also mapped the spinal vasculature by manual tracing and classification. My contributions to this work include project definition and scope, mentorship and experimental oversight, the performance of *in vivo* measurements (along with Jonathan Rubin), the development of our simple model, and manuscript preparation. While this chapter is written in the style of a paper, its results and conclusions should nevertheless be considered tentative, especially with respect to our observation of hemorrhaging. We aim to publish this work in the near future under the title (or similar):

Farrar, MJ, Diago, DM, Rubin, JD and Schaffer, CB. The Mouse Posterior Spinal Venous System and Changes in Flow After Posterior Spinal Vein Occlusion.

6.1 ABSTRACT

The availability of transgenic mouse models has made the mouse an increasingly popular model for studying spinal cord injury (SCI). Essential to understanding the injury and post-injury environment of SCI is a knowledge of the vascular architecture of the spinal cord. Unlike larger animals, fewer studies of the spinal cord vasculature have been performed in mice, with most of these studies focusing on the arterial supply of the spinal cord. We have mapped the mouse posterior spinal cord vasculature in the lower thoracic (T9-T13), with an emphasis on the veinous drainage. We have examined this vasculature at the large scale of the posterior spinal vein (PSV) down to the capillary and arteriole levels up to 700 μm below the posterior surface of the mouse spinal cord. Among our findings, we discovered that the PSV contains large branches exiting the spinal cord, shunting blood back to the heart. In addition, we have developed a model of atraumatic occlusion of the PSV and measured flow into the PSV at baseline and following PSV occlusion. We observed that the change in flow was highly dependent on the location of the clot with respect to the large branches. In some cases, changes in pressure were severe enough to result in the formation of a distal hemorrhage. We have developed a simple model to explain our results.

6.2 INTRODUCTION

Spinal cord injury (SCI) remains one of the most debilitating neurological diseases, affecting an estimated 265,000 persons in the U.S.A. alone [1]. In addition to the immediate tissue disruption caused by trauma, considerable secondary injury results from vascular disruptions, including hemorrhage, ischemia and edema [2–4]. Besides traumatic SCI, spontaneous SC infarct [5–11] is a clinically observed ischemic condition leading to paralysis, and is particularly difficult to diagnose [12, 13]. While the majority of these cases are on the arterial side, venous infarcts have also been observed [14, 15]. A complete understanding of the ischemic susceptibility of the SC to SCI and infarct, requires a detailed understanding of the SC microvascular architecture.

To this end, previous studies have used the corrosion cast technique to study the anatomy of the spinal cord vasculature in humans [16, 17], rabbits [18], cats [19], pigs [20, 21], and rats [22–24]. However, the growing availability of transgenic mouse strains makes the mouse spinal vasculature of particular interest, yet vascular architecture of the mouse remains much less explored. While magnetic resonance imaging (MRI) techniques have been used for comparative angiography between mice and rats, anatomical focus has largely been at the level of arterial supply [25]. Moreover, although these studies have brought anatomical understanding to the SC in different species, they did not attempt a graph-theoretic analysis of the microvascular network.

In addition to vascular architecture, spinal cord blood flow (SCBF) has been measured [26–33] in healthy and diseased states. In all but one case [33], these studies determined blood flow as an average over some region and did not consider flow at the level of individual vessels. Miyazaki et al. [33], have measured blood flow and diameters of individual capillaries in the anterior horn of the lumbar spinal cord in wild type mouse and a transgenic mouse model of familial amyotrophic lateral sclerosis (fALS). Nevertheless, SCBF at the level of individual pre-capillary arterioles and post-capillary venules remains largely unexplored.

In contrast to the spinal cord, detailed 2-D surface maps [34] and 3-D volume maps

[35, 36] of microvascular in the rodent neocortex have been made and the connection of topology to transport made by targeted vessel occlusion. In addition, detailed blood flow studies of the rodent cortex have examined changes in flow as a result of neural activation [37–39], and after clot formation in penetrating arterioles [40] and ascending venules [41] as models of ischemic small stroke [42].

We have adopted a method of tissue clearing [43] combined with a fluorescent intraluminal vessel fill to study the mouse SC microvasculature, with a focus on the posterior vasculature in the lower thoracic spinal cord. Using 2-photon excited fluorescence (2PEF) microscopy, we performed *ex vivo* imaging of these tissues and created 3-dimensional images of the vascular architecture. By tracing these images, we created a topological map of the SC vasculature and measured key network properties of the posterior SC. At the large scale, we identified large branches in the PSV which exit the spinal cord, "shunting" blood back to the heart.

In addition to vascular mapping, we have developed a model of atraumatic occlusion of the posterior spinal vein (PSV) using a ferric (III) chloride thrombosis model [44]. Using this technique along with 2PEF *in vivo* imaging of the posterior mouse SC, we measured diameter and flow velocity in pre-PSV feeder venules before and after PSV occlusion. We observed resultant changes in flow, with increased, decreased and unchanged flows after occlusion. Comparison with our vascular maps revealed that feeder venule flow disruption by occlusion of the PSV varied strongly with proximity to the large shunts, with the most pronounced effects occurring for clots close to these shunts. In some cases, this pressure redistribution resulted in hemorrhaging distal to the site of occlusion. We developed a simple resistance-flow model in conjunction with our vascular maps to address these observations.

6.3 Methods

6.3.1 Mouse Surgery and Clot Formation

We performed surgery on mice of a C57B6/J background using the setup and methods described previously [45]. In a few cases, mice heterozygous for EmxCre were used. Briefly, mice were anesthetized using a 5 % isofluorane/oxygen mixture, which was reduced to 1-2 % after induction of anesthesia. Mice received 50 μg glycopyrrolate per 100-g mouse intramuscularly and 0.1 mL 5% W/V glucose hourly throughout both surgery and imaging. Surgery was performed on a custom table, and a rectal thermometer monitored temperature on a feedback-controlled heating pad set to 37.5 °C. Skin and muscles were retracted and a double posterior laminectomy was performed at T11-T12 using spring scissors. Warm 1% agarose (Sigma-Aldrich) solution was applied to the spinal cord and a #0 coverslip (Electron Microscopy Sciences) laid on top. After the gel set, the coverslip was removed and the agarose near the cut site was carefully cut away. A small patch of dura over the PSV was removed, and the coverslip reapplied. Gel foam (Pharmacia & Upjohn) and 0.9% W/V saline were applied over the exposed spinal cord.

To initiate a clot, we adopted a ferric(III) chloride ($FeCl_3$) technique [44]. Briefly, the coverslip was removed and dry gel foam and cotton swabs were used to reduce fluid over the PSV locally. A glass micropipette filled with 5% W/V $FeCl_3$ was gently touched to the exposed PSV, depositing a small droplet by capillary action. A clot was seen to form within 10-20 minutes of exposure by cessation at the point of application (i.e. a "white clot"). The area was subsequently flooded with saline to remove the $FeCl_3$ and excess fluid was removed.

6.3.2 *Ex Vivo* Tissue Preparation

Mice were deeply anesthetized using sodium pentobarbital. After the absence of reflex in response to foot or tail pinch stimulus, animals were perfused transcardially with 1x phosphate-buffered solution (PBS; pH = 7.4; Sigma-Aldrich) prior to perfusion with 4% W/V paraformaldehyde (Thermo-Fischer Scientific) in PBS. In mice where *ex vivo* fluorescence imaging of blood vessels was performed, these solutions were warmed to at least 37.5 °C prior to perfusion and followed by perfusion with 1% low-melting-point agarose (Sigma-Aldrich) mixed with 5% W/V lysine fixable Texas Red dextran (MW = 70 000; Invitrogen) [35]. Mice were then rapidly cooled using crushed ice until agarose had set.

To determine gross PSV architecture, we injected 2 mL India ink following perfusion.

6.3.3 Gross Angiography and Tissue Staining

To determine the region of the clot with respect to large veinous drains, whole spines were removed from the lower lumbar to lower cervical regions, and successive posterior laminectomies were performed. Wide-field fluorescent images were taken *in situ* on a fluorescent microscope (Examiner D1; Carl Zeiss), and the location of the clot and shunts was carefully marked.

For ink fills, a similar procedure was followed, except that the posterior processes were removed from the foramen magnum to the caudal equina. Bright-field illumination was used in place of fluorescence microscopy.

To determine the location of any hemorrhages relative to the clot location, an approximately 1-cm segment of the spinal cord centered on the clot site was excised from the vertebral canal. This segment was then cut in half at the clot site, yielding a rostral segment 0.5 cm above the clot and a caudal segment 0.5 cm below the clot.

Segments were marked for correct orientation by injecting a small amount of Evans blue to the segment side opposite the clot. Segments were stained with diaminobenzidine (DAB) Peroxidase Substrate Kit (Vector Labs) for 15 minutes. Segments were then transferred to 60% sucrose for at least 24 hours prior to sectioning. Each segment was cut into 40 μm sections on a cryotome (Microm HM550; Thermo-Fisher Scientific) after embedding in optimal cutting temperature (OCT; Tissue-Tek) compound. If a hemorrhage was visible to the unaided eye during the sectioning process, sections were saved and the axial distance was determined by the number of slices taken from the clot site.

6.3.4 Tissue Clearing

We followed the clearing procedure described by Dodt et al. [43] closely. All spinal cords perfused with lysine-fixable-Texas-Red-dextran-labeled agarose were extracted on ice and immediately placed in 4% paraformaldehyde fixative for one day at 4C. We then removed the spinal cords from vertebrae T9 through T13 and placed them in fixative again for one hour at room temperature (20-25C). We rinsed all tissues 2 times in 1x PBS, and stored them in PBS for one day at 4C. Spinal cords were dehydrated by successive incubation in ethanol (30%, 50%, 70%, 80%, 96%, and twice in 100% for one day each) at room temperature. The tissues were then rinsed and left in 95% hexane (Sigma-Aldrich) for one hour. Tissues were finally transferred to a solution of 1:2 benzyl alcohol/benzlbenzoate, which was the final clearing solution in which the tissue was stored and imaged. Since dye diffuses out of the gel and leaves the vessels over time, a balance between duration of tissue clearing and fluorophore concentration must be optimized. We found that after four days we could achieve imaging depths over 500 μm with robust vessel labeling.

6.3.5 2PEF Imaging and Blood Vessel Measurements

Following surgery, mice were transported to the microscopy laboratory where we performed 2PEF imaging on a custom microscope. Mice were injected retroorbitally with 2.5 % W/V Texas Red dextran (MW = 70,000 kDa; Invitrogen) A low numerical aperture (NA) objective (NA = 0.28; Olympus America) was used to take a large ($\sim$ 3 mm) field of view image of the vasculature.

To measure blood vessel diameters and flow speeds, we used a large NA objective (NA = 1.0; Carl Zeiss). After focusing on the vessel of interest in the xy plane, the animal was translated axially in z in increments of $1 - 2$ μm while simultaneously recording images. Average vessel diameter was determined using custom Matlab software, in which vessel boundaries were manually traced from the maximum intensity projection of the image sequences.

To measure flow speeds, we used the 2PEF line-scan method described previously [37]. The center of the vessel was estimated by eye, and after centering the vessel in the xy plane and rotating the scan pattern such that the vessel was oriented along the x axis, a single line was repeatedly raster-scanned over time. Since red blood cells (RBCs) exclude the fluorescently labeled plasma, they appear as dark regions against a bright background on the scan. Scans are repeated at constant intervals, generating a 2-D image with time as the y axis. The slope of these lines was then calculated using a radon-transform algorithm [46], giving the average speed in the vessel center. The volumetric flow, Q, was determined according to

$$Q = \frac{1}{2}\pi r^2 v_{max} \tag{6.1}$$

where r is the vessel radius and v_{max} is the RBC speed at the center of the vessel (see Section 6.7.1).

Ex vivo imaging was performed using the same objectives. We found that we could obtain imaging depths between 550-750 μm from the posterior surface of the intact spinal cord using the clearing procedure described. During imaging, samples were housed in an imaging chamber filled with 1:2 benzylalcohol/benzybenzoate

clearing solution. Since the clearing solution dissolved polystyrene petri dishes, we constructed a custom imaging chamber. The imaging chamber consisted of a glass-bottom petri dish edged with Kwik-Sil Elastomer (World Precision Instruments) and topped with a cover slide. This construction also prevented the spinal cord from moving during imaging.

6.3.6 Determination of Pressure Changes After an Occlusion

To determine the pressure drop across the measured feeder venules, we fit the function:

$$Q(a, b; r) = \frac{a}{1 + br^4} \tag{6.2}$$

to the measured values of flow and vessel radii before and after occlusion. Here, the parameter $a \propto \Delta P$, for pressure drop ΔP (see Section 6.7.1). The parameter b is a constant depending only on resistances upstream of the feeder venules.

To allow for greater stability when fitting, we first fit (6.2) to the baseline data and determined the most likely value of b by nonlinear least squares fitting. Baseline data was then re-fit with b fixed at this value, making a the only free parameter. Post-occlusion data were also fit with b fixed at this value.

6.3.7 Vessel Tracing and Classification

We obtained 3D reconstructions of the spinal cord tissues from z-stacks 550-750 μm in depth with overlapping regions of interest. A custom image stitching software was used to create a 3D composite stack of the microvasculature environment in each tissue. We used custom tracing software to manually delineate and label each vessel. Principal arteries and veins were classified using: stereotypical location (e.g. posterior arteries), orientation, branching pattern, and vessel width; capillaries were identified by having

the smallest diameter and the highest branching number. Lines and nodes denoted vessels and branching points, respectively.

Networks were analyzed as an adjacency matrix. Degree was determined as the mean of non-zero rows larger than unity. Geodesics were determined using Dijkstra's algorithm implemented in Matlab.

6.4 RESULTS

6.4.1 Multiple imaging modalities reveal posterior spinal cord vasculature

To study the gross anatomy of the PSV, we injected 2 mL India ink to the mouse vasculature following perfusion with paraformaldehyde (Fig. 6.1a). We then exposed the posterior aspect of the spinal cord from the base of the medulla oblongata to the cauda equina. We observed ($n = 3$ mice) that the large posterior spinal vein traverses the entire length of the spinal cord and branched and exited the spinal cord at four locations. These "shunts" were seen at distances of 5.1 ± 2 mm (cervical), 22.3 ± 7 mm (mid to lower thoracic), 34.5 ± 10 mm (lower thoracic upper lumbar), and 47.4 ± 4 mm (lumbar), relative to the bifurcation point at the medulla oblongata, with the two caudal-most shunts being the most pronounced.

Since we were most interested in the thoracic region, we considered the middle thoracic shunts both *in vivo* and using *ex vivo* fluorescently-labeled agarose vessel fills (Fig. 6.1b), as in [35]. From *ex vivo* sections (including ink fills), we measured the distance between shunts to be 10.3 ± 9 mm (n = 11 mice), containing $N = 115 \pm 30$ feeder venules ($n = 4$ mice), or a density of 11.6 $\pm$ 2 vessels•mm^{-1} ($n = 4$ mice).

From *in vivo* measurements, we observed a mean feeder venule-diameter 24.8 ± 9 μm ($n = 187$ vessels in 9 mice; error is $\pm$ S.D.) and a mean PSV diameter of 146 $\pm$ 40 μm

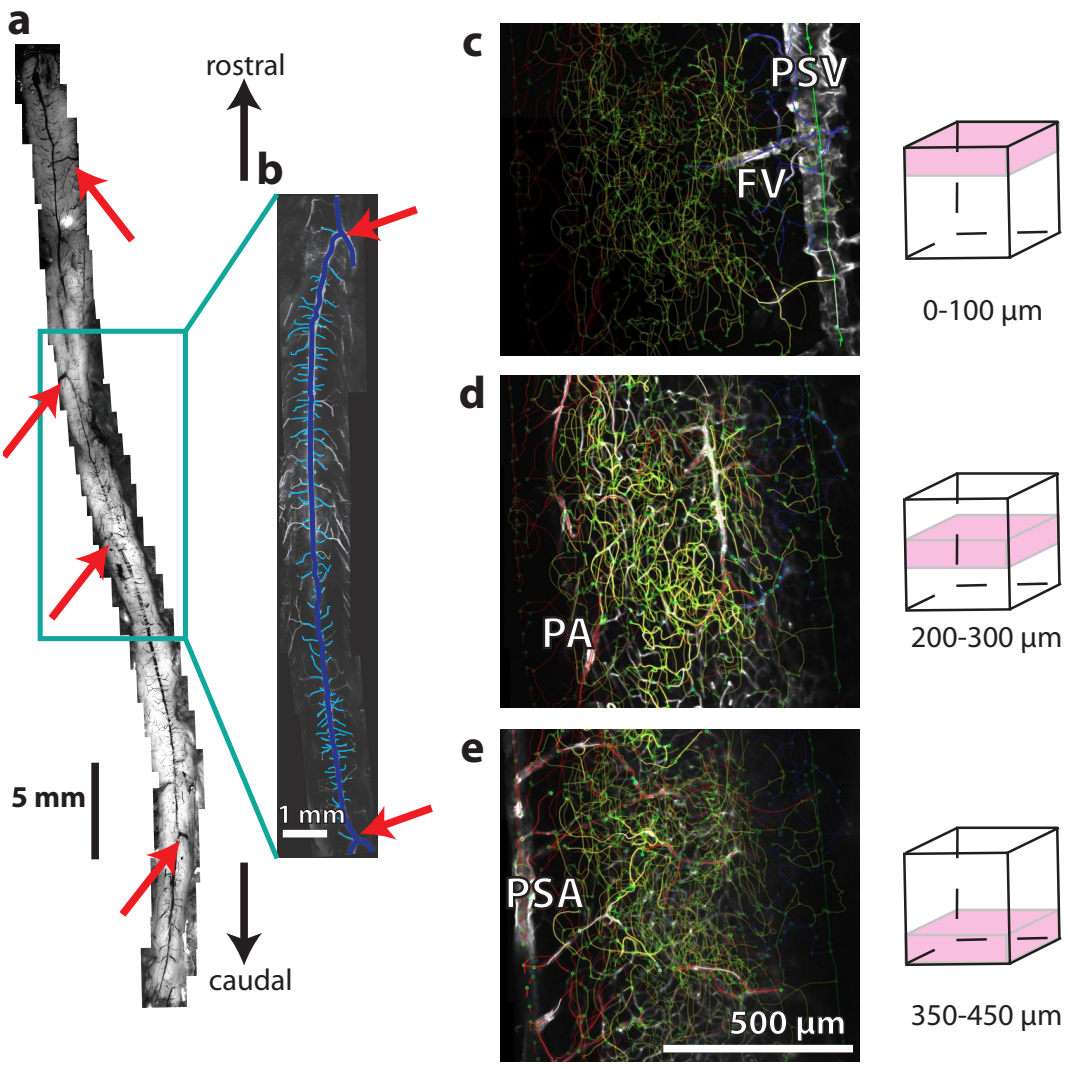

Figure 6.1: Mapping of the dorsal spinal vasculature.
Ink perfused vasculature in the exposed whole spine (a) reveals that the PSV extends the full length of the SC and is relieved by large shunts (*arrows*) along its length. We focused on the mid-thoracic to upper-lumbar region of the SC (*teal box*). In other mice, agarose mixed with lysine-fixable Texas Red was perfused into mice to fluorescently label vessel lumens (b), allowing for quantitative measurements of PSV (*navy*) length and the number of feeder venules (*cyan*) between shunts (*arrows*). Quantitative vessel mapping from 3-D image stacks (c-e) was used to trace vascular path and map connectivity. Vessels were classified as posterior spinal arteries (PA; *red*), penetrating arterioles (PA; *red*), feeder venules (FV; *blue*), PSV (*green*), or capillaries (*yellow*). Nodes were marked by green circles. Images (c-e) are representative slices of different depths from the dorsal surface of the SC.

reduce the degree[3].

6.4.2 A Clot in the PSV Results in Diverse Upstream Flow Changes

Optical access for *in vivo* optical imaging of the mouse SC was obtained by performing a double posterior laminectomy at T11-T12 (Fig. 6.2a). We measured vessel diameter and v_{max} in approximately 20 vessels caudal to the clot both at baseline and following an induced clot. Vessel diameter was determined by taking small ($\sim 10 - 50\mu$m) 2PEF image z-stacks encompassing the diameter of the vessel. The maximum projection (Fig. 6.2b) was computed and the average vessel diameter determined by manual tracing. A line scan (see Methods) was taken at the center of the vessel (Fig. 6.2b, *red line*), creating a 2-D image of that line vs. time (Fig. 6.2c). This approach allowed for a straightforward measurement of maximum RBC flow speed, v_{max}. Volumetric blood flow was computed according to (6.1). In one mouse, we measured line scans of the PSV on either side of the rostral shunt and saw that blood flowed into the shunt from both sides, corresponding to flow in opposite directions (see Section 6.8, Fig.6.7). After baseline flows were measured, a point occlusion in the PSV was generated by application of $FeCl_3$ to the exposed PSV (Fig. 6.2d). The PSV was observed under a stereomicroscope until clot formation was observed. After clot formation, flows were remeasured. Approximately 30 min. elapsed between the end of baseline measurements and the beginning of post-clot measurements. Control experiments received saline rather than $FeCl_3$, and 30 min. was allowed to elapse before vessels were remeasured. Tracings of the venules feeding into the PSV (6.2e,f) were used to map vessel flow speeds at baseline (Fig. 6.2e) and after occlusion ((Fig. 6.2f).

We induced clots at a variety of locations with respect to adjacent pairs of

[3]For example, a hexagonal lattice (honeycomb) network has a degree of 3 at all interior nodes, but a degree of only 2 for some of the nodes on the boundary of the network.

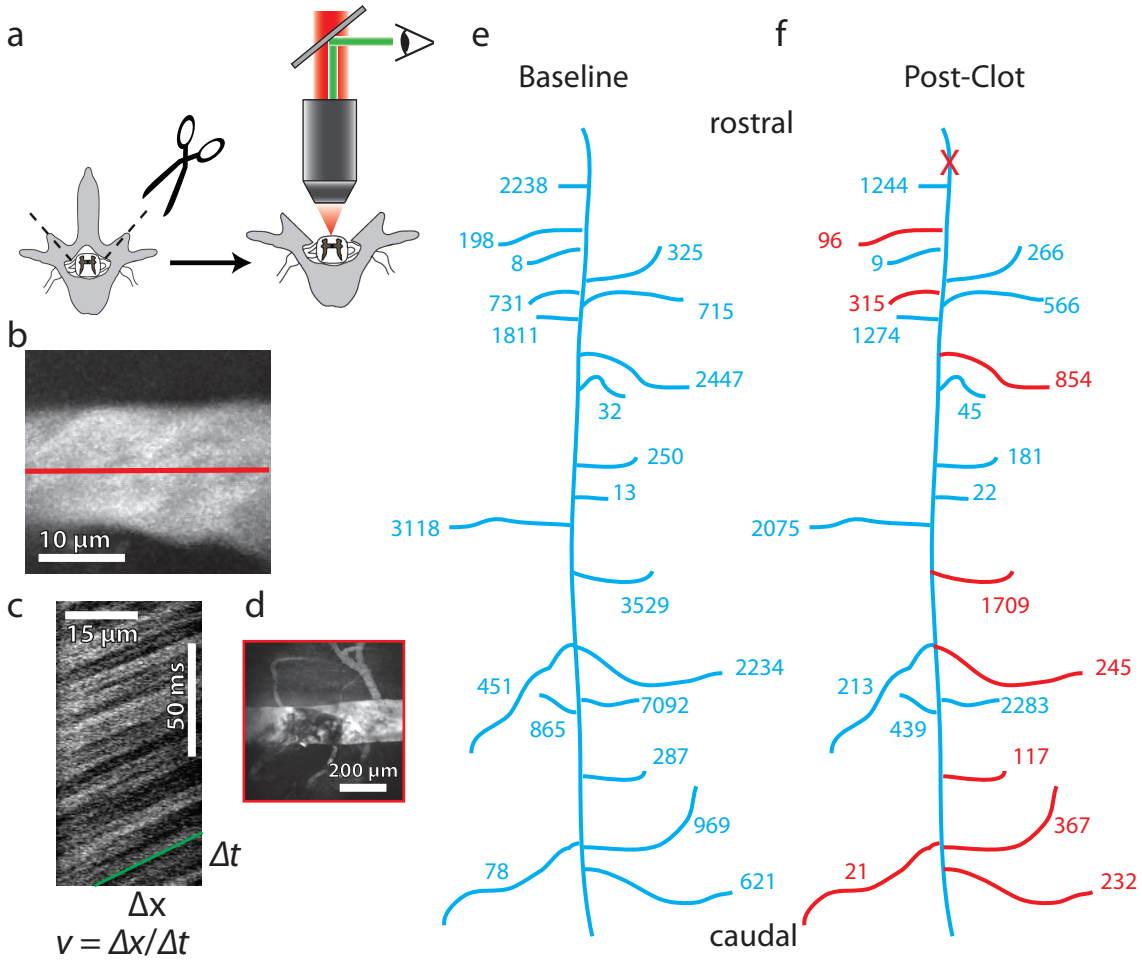

Figure 6.2: ***In vivo*** **2PEF imaging allowed for blood flow measurements in the primary feeder venules of the PSV.**
A posterior laminectomy allowed for optical access to the spinal cord, which was subsequently imaged by 2PEF microscopy (a). Small image stacks centered on feeder venule segments were taken and maximum intensity projections of image stacks were used to measure diameters (b). Repeated raster scanning of a line in the center of the vessel (b; *red line*) was used to generate a flow profile (c), the slope of which gives the speed. $FeCl_3$ was used to create a clot in the PSV (d). To visualize flow changes, we created flow maps before (e) and after (f) clot formation. Vessels experiencing a more than 2-fold decrease in flow are highlighted in red. An "X" marks the clot location. Units of flow are $\mu m^3/ms$.

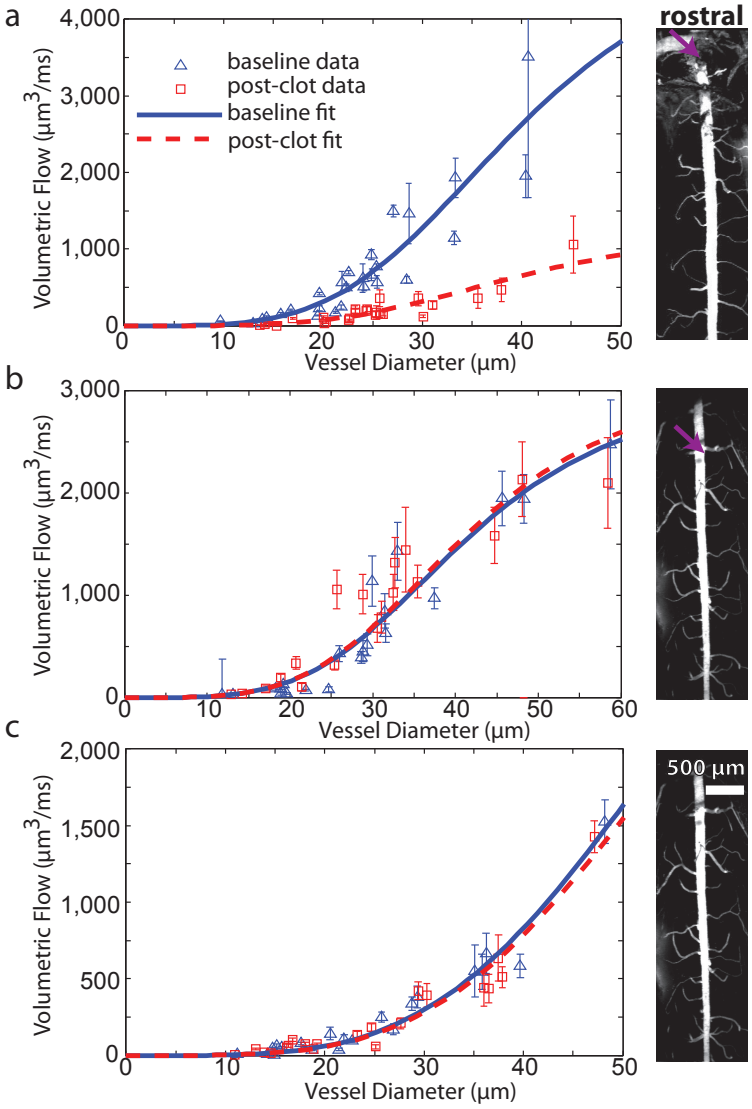

Figure 6.3: Clot location determines changes in upstream flow.
We measured blood flow speeds and diameters in the first 20 feeder venules (a-c) caudal to the clot site at baseline (*blue triangles*) and after a clot (*red squares*). The parameter a (proportional to the pressure drop across the feeder venules) was determined by fitting (6.2) to baseline (*solid blue line*) and post-clot (*dashed red line*) measurements. Representative data and fits are shown for a clot near the rostral shunt (a), medial to the shunts (∼4 mm from the rostral branch) (b), and sham clot samples (c). Images show the clot location in the PSV (*arrows*).

PSV shunts, and measured resulting changes in flow in 20 upstream feeder venules. To determine the pressure drop across feeder venules, we computed the volumetric flow Q, and plotted this as a function of vessel diameter, $2r$ (Fig. 6.3a-c). The pressure drop was determined by fitting (6.2) to the data. If shunt location was not visible within the laminectomy site, the animal was perfused with lysine-fixable Texas Red-labeled agarose and the distance of the clot from the shunts was determined by *ex vivo* imaging (data not shown). For a clot formed just below the rostral shunt, we found a severe decrease in the flow in upstream feeder venules (Fig. 6.3a). In contrast, very little change was seen for a clot produced towards the middle of the shunts (Fig. 6.3b; $\sim$ 4mm from the rostral shunt). A sham control measurement showed no changes in flow (Fig. 6.3c). Combining results across mice, we considered the pressure drop across feeder venules before and after clot as a function of clot location with respect to the location of the shunts (Fig. 6.4a). We normalized the clot location by the total distance between adjacent shunts, choosing our convention such that the caudal shunt corresponded to 0 and the rostral shunt to correspond to 1. The largest differences were observed for clots nearest the shunts. Sham control experiments showed no change ($\Delta P_{clot}/\Delta P_{baseline} = 0.95 \pm 0.04$; $n = 3$ mice; error is $\pm$ S.D.).

6.4.3 A Simple Flow-Resistance Model Predicts A Variety of Upstream Flow Changes

To understand why change in flow depended on clot location, we developed a network flow model (see Section 6.7.2) to simulate baseline and post-clot flows and pressure drops as a function of clot location, using the length convention described above. We considered a model of 100 feeder venules between PSV shunts, with branch number "0" corresponding to the branch nearest the caudal shunt and branch number "100" corresponding to the branch closest to the rostral shunt. In our model, baseline

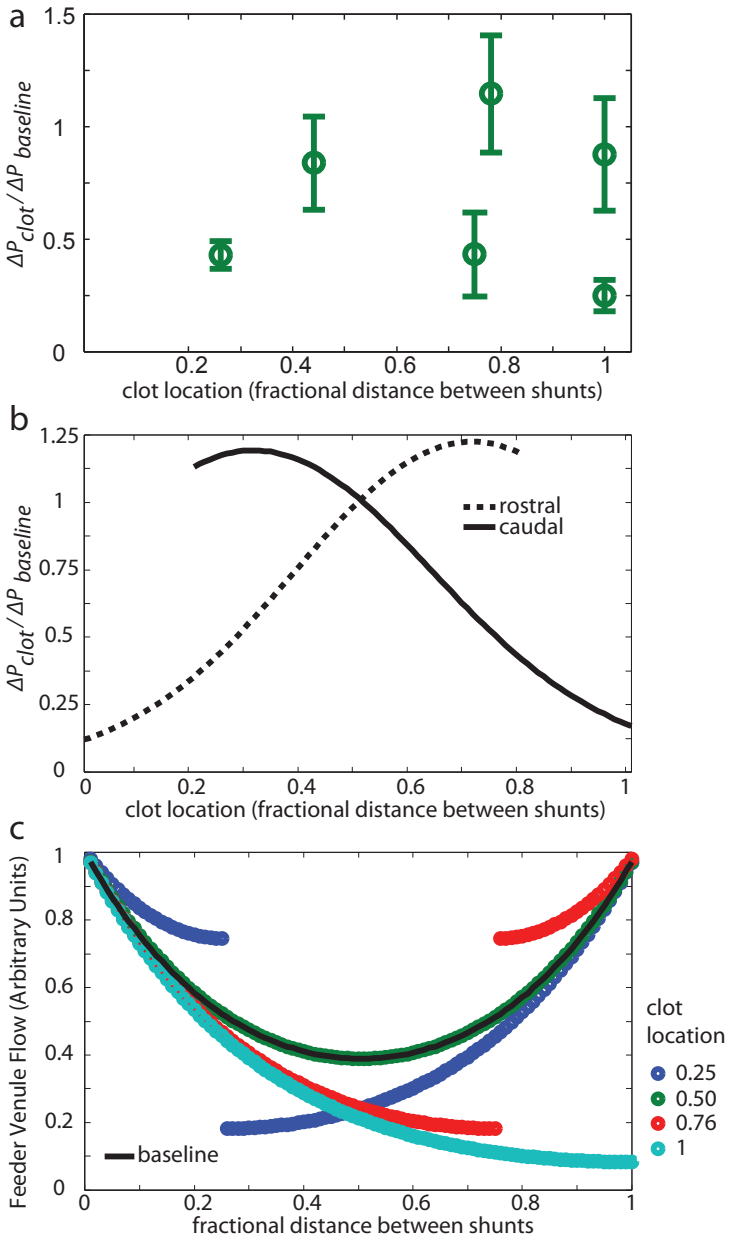

Figure 6.4: A simple model predicted that changes in flow depend strongly on clot location.

We observed that the largest changes in pressure drop across feeder venules occurred for clots nearest the PSV shunts (a). Error bars are from 95% confidence intervals in fit parameters. Clot location was specified as fractional distance between adjacent shunts, with 0 corresponding to the caudal shunt and 1 to the rostral shunt. To compare with measured values, we simulated the average pressure drop ratio, $\Delta P_{clot}/\Delta P_{baseline}$, across the first 20 caudal (*solid line*) and rostral (*dashed line*) feeder venules as a function of clot location (b). Flow in individual feeder venules (c) before (*black line*) and after clot (*colored circles* were also considered for a variety of clot locations.

conditions resulted in flow bifurcation in the PSV at the mid-point between the two shunts, with flow converging towards the shunts in either direction (data not shown). Baseline flow in the feeder venules followed a parabolic trend (Fig. 6.4b; *solid line*). We calculated the change in flow as a function of length along the PSV (i.e. in each feeder venule) for several clot locations (Fig. 6.4c). Clots were simulated by setting the resistance for that segment of the PSV equal to infinity. Simulations showed that clots formed in the center of the PSV had no effect on feeder venule flow, as that is a predicted point of bifurcation in the direction of PSV blood flow. In contrast, simulated clots towards the rostral (caudal) shunt resulted in a decrease (increase) in feeder venule flow caudal to the occlusion site. The reverse trend was observed in flow rostral to the occlusion site.

Our model contained only unitless flows and constant resistances, making the pressure drop across vessels the only point of comparison between theory and experiment. The pressure drop, ΔP, was determined experimentally by fitting volumetric flow as a function of diameter (Fig. 6.3). The fit parameter, a, is directly proportional to ΔP, such that $a_{clot}/a_{baseline} = \Delta P_{clot}/\Delta P_{baseline}$. Using the simulated data, we calculated the average pressure drop ratio directly in the first 20 vessels caudal to the clot (Fig. 6.4b). We similarly calculated the same measure for the first 20 vessels rostral to the clot for reference. The resultant changes in pressure caudal to the clot followed the opposite trend of flow changes rostral to the clot, and vice versa. Comparison of experimental data (Fig. 6.4a) with simulated data (Fig. 6.4b; *solid line*) showed agreement for clots near the rostral shunt and midpoint, but the simulated data did not agree with the decrease in pressure drop seen for a more caudally located clot.

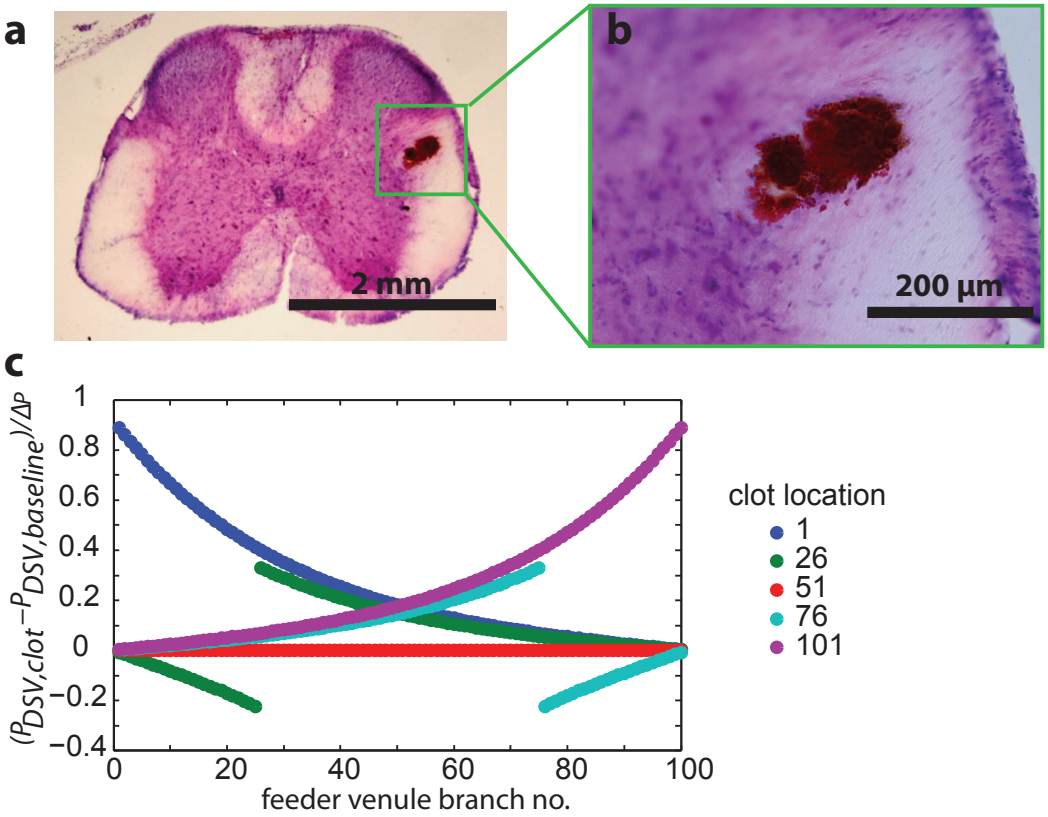

Figure 6.5: Occlusion of the PSV can lead to a hemorrhage distal to the clot site. We observed hemorrhages distal to the clot at the boundary of the gray and white matter (a). These clots were typically several hundred micrometers (linear dimension) in size (b). We used our flow model to simulate the difference between the baseline and post-occlusion pressures in the PSV along the PSV length (c). We considered a variety of clot locations (*colored circles*). Pressures were normalized by the pressure difference between the distant pressure source and the shunt pressure, $\Delta P = P - P_{ground}$ (see Section 6.7.2).

6.4.4 Occlusion of the PSV Can Lead to Distal Upstream Hemorrhaging

To study the acute effects of PSV occlusion, we examined the mouse SC for blood products near the clot site histologically. Following clot formation and/or 2PEF imaging, mice were euthanized and perfused intracardially with paraformadelhyde. Tissue was stained for red blood cells using a DAB staining protocol. Strikingly, we observed hemorrhages within the SC but distal in approximately 1/3 of mice (11 out of n=30 mice; 1 of $n = 6$ control mice). Sections which showed a hemorrhage (Fig. 6.5a,b) were identified during the sectioning process. Hemorrhages were observed at the boundaries of the gray/white matter. From our vessel tracing, this location corresponded to either at pre-capillary arterioles or post-capillary venules.

In some mice (3 of $n = 30$ mice in clot experiments; 1 of $n = 6$ in control mice), we observed hemorrhages that were atypical in both location, size (an order of magnitude larger in area compared to the majority of hemorrhages), or both. These data were excluded in a blinded study of histological slices and were believed to be artifacts of the surgical procedure.

To understand this result, we considered the difference between the baseline and post-occlusion pressures along the PSV for a variety of clot locations (Fig. 6.5c). We normalized this change in pressure by the network pressure drop between distant arterioles and PSV shunts, $\Delta P = P - P_{ground}$ (see Section 6.7.2). Analogous to our predictions for flow, we found that a large pressure change in the PSV occurred for clots close to the large shunts, while a mid-point clot resulted in no pressure re-distribution. As for flow, the largest changes in PSV pressure were seen at feeder venule nodes closest to the clot.

6.5 DISCUSSION

6.5.1 The mouse PSV has stereotyped topology but highly variable geometry

We observed the mouse spinal cord to be supplied by three arteries and drained by two veins, with the ASA and PSV being the largest of the arteries and veins, respectively. This architecture is analogous to the human SC [17], further supporting mice as a valuable model for studies of SC pathology. However, while we consistently observed large shunts along the length of the PSV, the location of these shunts varied considerably, occurring in different segments across animals. This observation is consistent with the high degree of variability in spinal vasculature more generally. In a survey of the literature [48], the number of anterior and posterior radicular arteries in humans was reported as varying between 2-17 and 11-25, respectively. The largest and most stereotyped of these anterior radicular arteries is the artery of Adamkiewicz, the location of which varied as much as by 11 segments, between T6 and L4 [48]. The high degree of variability has caused some [49] to question the very existence of this artery in rats. In humans, the variability of the veinous system is reportedly higher than the arterial side [50]. Thus, the variability we observe in shunt location and the inadequacy of our model to account for all of the observed behavior in changes in flow direction after occlusion are in agreement with current knowledge of SC vascular anatomy.

6.5.2 The mouse SC is susceptible to Ischemic Injury of Veinous Origin

Our present study showed that occlusion of the PSV near large shunts can result in more than a 70% change in pressure across upstream feeder venules, suggestive of significant flow impediment and upstream ischemia on acute timescales. In addition, the potential for hemorrhage that we have observed may suggest further pathology, such as those arising from neurotoxic blood products [51]. In contrast to the middle cerebral artery network in the brain which has a mean vessel/node ratio of 1.5 [36], the mouse SC capillary network has a ratio of approximately unity, meaning that alternate routes of perfusion following occlusion of an upstream (or downstream) vessel are extremely limited. This limitation may make the mouse SC more susceptible to ischemic injury. In line with this observation, longitudinal studies [52, 53] of PSV occlusion in rats have shown atrophy of the posterior columns, reactive gliosis, macrophage infiltration, and onset of paraplegia. Interestingly, in a study examining the results of PSV ligation [53], variability in pathological SC "softening" was attributed to unknown veinous anastomoses. This attribution fits well with our model and measurements which described the relationship between these anastomoses and flow redistribution within the SC following PSV occlusion.

In contrast, a study in rhesus monkeys [54] demonstrated that large-scale occlusion (as many as 9 vertebral segments) of the PSV did not result in clinical pathology, although demyelination was observed in posterior columns. Dilation of the ASV was seen to compensate for PSV occlusion. Care must therefore be taken when applying murine models of veinous SC ischemic injury to humans or other animal models, despite anatomical similarities.

In addition, the use of vascular endothelial growth factor (VEGF) has had a controversial role in pre-clinical animal studies of SCI, with a robust finding that exogenous injection of VEGF [55], viral induction of VEGF expression [56], or

transplantation of VEGF-expressing neural stem cells (NSCs) [57] led to increased number of vessels within 7-10 days post-SCI, increased gliogenesis, increased spared tissue, less axon disintegration, and improved behavioral outcomes. While the majority of these VEGF-mediated effects–with the exception of increased vascularity–are believed to be the result of VEGF on neural and glial targets directly [58, 59], a systematic graph theoretical study of capillary connectivity analogous to the one we have performed is pertinent to understanding therapeutic mechanism. Similar connectivity studies would be of value in age-related studies of vascularity, as a decrease in capillary and central artery density with age has been observed in rats [22].

6.5.3 The PSV serves as a potentially bi-direction drain for the mouse spinal cord

Our toy model and observation of the variability of blood flow rearrangement with respect to clot location after PSV occlusion suggest that the PSV has or has the potential for bidirectional flow between adjacent shunts. At a minimum, our observation of bidirectional flow at the rostral shunt confirms that flow within the PSV as a whole is not unidirectional. This observation is consistent with the partial flow theory of SCBF [2], which accounts for bidirectional flow and even flow reversals in the spinal cord under physiological conditions. In the brain, basal and stimulus-induced fluctuations in blood flow have been observed [37–39], owing to neurovascular coupling. Like the brain, the SC is auto-regulatory in blood pressure [27], and functional MRI studies of the SC [60–62] have revealed similar changes in activity-dependent perfusion.With respect to network topology, recent modeling [63] has revealed that the optimal structure of a transport network depends not only on steady-state flow, but also on fluctuating sources. These findings suggest that the bidirectional nature of PSV blood flow is part of a larger optimization strategy for fluctuating arteriole pressures.

6.5.4 Future studies

Our present findings on flow disruption are encouraging, but lack statistical power. The same can be said of the observation of post-occlusion hemorrhaging, especially since we have not yet been able to rule out the possibility of hemorrhaging induced by the invasive surgery procedure required for access to the dorsal SC. Additional experiments along the same lines will help improve the strength of these conclusions. In addition, it is our intention to explore nano computer tomography (nanoCT) studies of hemorrhaging. By injecting iodine intravascularly immediately prior to clotting, we will be able to deduce the origins and 3-dimensional size of hemorrhage more precisely than using present post-mortem histological techniques.

Similarly, our 3-dimensional tracing/mapping of the dorsal SC vasculature is incomplete, spanning only a few feeder venules on one side of the spinal cord. A more complete mapping will allow for greater network characterization, especially at the level of larger vessels.

Finally, our minimalist mathematical description of the PSV allowed for an understanding of the observed variety in upstream feeder venule flow to PSV occlusion. While satisfying Occam's razor, the ability of our model to capture the true nature of flow in the PSV could be improved upon by allowing for physiologically relevant fluctuations in pressure and the replacement of fixed feeder venule resistances with a distribution of resistances provided by *in vivo* imaging data.

6.6 ACKNOWLEDGMENTS

We would like to thank the National Institutes of Health (C.B.S. Grant No. R01 EB002019), the National Science and Engineering Research Council (NSERC) of Canada (to M.J.F.), and the Cornell Biology Scholars program (J.D.R. and D.M.D.) for financial support.

6.7 APPENDIX A: THEORY

6.7.1 Vessel speeds fitting function

Experimentally, we were able to measure only the flows in the primary feeder branches of the PSV (*cyan* branches in Fig. 6.6b,c). Flows at the center of the PSV were too fast for 2PEF line-scan measurements, and the physiological burden of anesthesia places time constraints on further upstream measurements. We thus measured the blood velocity in the center of the primary feeder venules and their diameters close to the PSV.

For Poiseuille flow [64] in a tube, we have the relation:

$$Q = -\frac{\pi r^4}{8\eta l}\Delta P \tag{6.3}$$

where r is the radius of the vessel under consideration, η is the fluid viscosity, l is the tube length, and ΔP is the pressure drop across the tube. From the form of (6.3), we can identify resistance as:

$$R \equiv \frac{8\eta l}{\pi r^4} \tag{6.4}$$

whereupon we have a simple resistance-flow relation:

$$Q = -\frac{\Delta P}{R} \tag{6.5}$$

We also have that the flow profile takes the form [64]:

$$v(\rho) = -\frac{\Delta P}{4\eta l}(r^2 - \rho^2) \tag{6.6}$$

for radial coordinate ρ. Comparing this expression to (6.3), we have

$$Q = \frac{\pi r^2}{2} v_{max} \tag{6.7}$$

where $v_{max} \equiv v(\rho = 0)$ is the velocity at the center of the vein.

Since we know from our vascular maps that the veins are isolated from each other by a large resistance, we treat them as causally isolated. Moreover, we know that both the posterior spinal artery and the posterior lateral arteries supply the mouse

spinal cord, with the ascending venules providing a common drain. Therefore, we considered the feeder venules to be attached to a common pressure source dropped across a resistive load, R_∞, of capillaries, arterioles and feeder venules prior to reaching the feeder venules as has been done in similar modeling in the brain [65]. Each feeder venule was then assumed to have a composite resistance (Fig. 6.6a) given by:

$$R = R(r) + R_\infty \tag{6.8}$$

where $R(r)$ has the form of (6.4) and all venules were taken to have approximately equal length l. Inserting (6.8) into our basic flow relation given by (6.5) and substituting (6.4) for $R(r)$ we have

$$Q = \frac{\Delta P}{\frac{8\eta l}{\pi r^4} + R_\infty} \tag{6.9}$$

We therefore have a fitting function to the experimental data of the form

$$Q(a, b; r) = \frac{a}{1 + br^4} \tag{6.10}$$

where we have the interpretation

$$a = \frac{\Delta P}{R_\infty} \tag{6.11}$$

$$b = \frac{8\eta l}{R_\infty \pi} \tag{6.12}$$

6.7.2 Flow Network

Network Model

We considered a segment of the PSV containing N feeder venules flowing into the PSV. We devised a numbering scheme such that the nodes corresponding to the pressure sources of the feeder venules are denoted by even indices, P_{2j}, for $j = 1, \ldots, N$. The beginning source node for the PSV is denoted as P_0 and the final sink as P_{2N+1}. The nodes which link feeder venules to the PSV were thus at pressures P_{2j-1} for

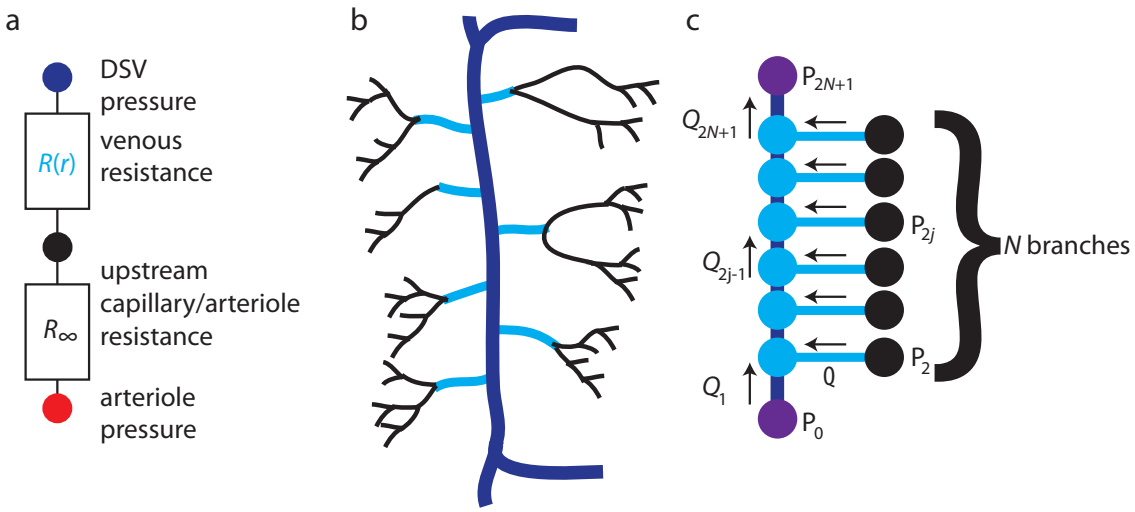

Figure 6.6: Flow in the mouse PSV was modeled by a simple resistance-flow network. To fit the experimental data, we considered the feeder venules to derive their pressure from a common distant artery source, dropped across a radially-dependent resistance in the feeder venule and an upstream average (constant) resistance, R_∞ (a). To characterize the venous system (b), we considered the PSV (b;*blue*) to be fed by feeder venules (b; *cyan*), which in turn are fed by upstream venules, capillaries, arterioles and arteries (b; *black*). Periodic "shunts" were observed leaving the spinal cord (a;*arrows*, b (*top,bottom*). We modeled the system as consisting of N feeder venules feeding into the PSV with shunts at either end (c).

$j = 1, \ldots, N$ (see Fig. 6.6c).

By our convention, we took the the volumetric flow rates, Q_j, to be towards the PSV in the feeder venules and considered this direction to be positive (i.e. $Q_{2j} > 0$ when flows were directed towards the PSV). Similarly, we took the flows between adjacent segments of the PSV to be positive when flowing caudal to rostral (i.e. $Q_{2j-1} > 0$ when flows were from bottom to top in Fig. 6.6c). We modeled our system by specifying the end-point pressures, P_0, P_{N+1}, P_{2j} and resistances, and solved for the resultant flow. To simulate an occlusion, we set the target edge of the network to have infinite resistance, but assumed that end-point pressures remain fixed. At each point, we assumed the relation

$$P_n - P_m = Q_{nm} R_{nm} \tag{6.13}$$

for nodes n, m with resistance R_{nm} between them and resultant flow, Q_{nm}. To simplify notation, we denoted all flows in the feeder venules by the feeder venule node (i.e. Q_{2j} corresponds to the flow out of node P_{2j} to the PSV). We followed a similar convention for PSV nodes (see Fig. 6.6c).

Conservation of flow at each junction gave

$$Q_{2j} + Q_{2j-1} = Q_{2j+1}, j = 1, .., N \tag{6.14}$$

Summing (6.14) over all values of j gave the conservation for the network:

$$\sum_{j=1}^{N} Q_{2j} = Q_{2N+1} - Q_1 \tag{6.15}$$

Similarly, computing pressure drops between any feeder venule and node 0 gave

$$P_{2j} - Q_{2j} R_{2j} + \sum_{n=1}^{j} Q_{2n-1} R_{2n-1} = P_0 \tag{6.16}$$

At this point, the system was completely determined up to the specification of model parameters and/or the addition of some assumptions about our system.

Initial Parameters and Assumptions

From (6.4), we see that $R \propto r^{-4}$. From a larger scale anatomical perspective, we know that the region where we image is bounded by large branches leaving the PSV, effectively shunting blood flow from the PSV back to the heart. We considered these "shunts" to be the analog of electrical grounding wires, and so we set $P_0 = P_{2N+1} = P_{ground}$[4]. Also, based on *ex vivo* experimental data (see Section 6.4.1), we considered $N = 100$ feeder venules in between these large shunts.

To simplify analysis, we considered the feeder venules to have equal resistance (i.e. $R_{2j} \equiv R_{fv}$, $j = 1, 2, \ldots, N$). We use (6.4) to obtain the relative resistances of the feeder branches to the PSV resistance:

$$R_{2j-1} \equiv R_{PSV} = \left(\frac{r_{fv}}{r_{PSV}}\right)^4 R_{fv} \approx 10^{-3} R_{fv}, j = 1, 2, \ldots, N+1 \tag{6.17}$$

where we have used experimental measurements (see Section 6.4.1) for the respective radii.

Finally, we considered the feeder venules to be attached to a distant source of arteriole pressure (i.e. the lateral spinal arteries and/or the posterior spinal artery) which is reduced after passing through a resistive network of branching arterioles, capillaries, and upstream venules with magnitude R_∞ [65](Fig. 6.6a), arriving at the feeder venules with an approximately uniform pressure, P.

Using our assumptions above, we rewrite (6.16) as:

$$R_{fv} Q_{2j} - \sum_{n=1}^{j} R_{2n-1} Q_{2n-1} = P - P_{ground} = \Delta P, j = 1, 2, \ldots, N \tag{6.18}$$

where

$$\Delta P \equiv P - P_{ground}. \tag{6.19}$$

and recall that $R_{2n-1} = R_{PSV} = 10^{-3} R_{2j}$, $n = 1, 2, \ldots, N+1$ prior to the clot formation. Combining (6.18) with (6.14), we have $2N$ equations for $2N+1$ unknown flows. Taking

[4]Recall that we could at least one pressure in our circuit to an arbitrary value, since only pressure differences will matter.

one final loop at the rostral end gave the final needed equation.

$$R_{fv}Q_{2N} + R_{2N+1}Q_{2N+1} = \Delta P \tag{6.20}$$

Since we only compared *relative* changes in flow experimentally, we simplified our model by turning our equations into dimensionless flows. Takinge our unit of flow such that

$$\frac{\Delta P}{R_{fv}} \equiv 1 \tag{6.21}$$

then dividing (6.18) and (6.20) by R_{fv} and (6.14) by $\Delta P/R_{fv}$ gave:

$$Q_{2j} - 10^{-3}\sum_{n=1}^{j} Q_{2n-1} = 1, j = 1, 2, ..N \tag{6.22a}$$

$$Q_{2N} + 10^{-3}Q_{2N+1} = 1 \tag{6.22b}$$

$$Q_{2j} + Q_{2j-1} - Q_{2j+1} = 0, j = 1, .., N \tag{6.22c}$$

where we have invoked (6.17) as well.

The only free parameter left in our model was the clot location, which we denoted by X and could occur along any of the edges in the PSV. The sparse flow matrix given by (6.22) was easily solved by reduction to row-reduced echelon form, giving the flow solution. To simulate the results of the clot, we set $R_X \to \infty$ and $Q_{2N+1} = 0$ and solved for the flows once again, assuming that the end-point pressures (i.e. ΔP) remain fixed. Since the pressure drop between the feeder venules and the PSV are linearly related to the flows with unit proportionality in our model, we reported the relative changes in pressure drops.

6.8 APPENDIX B: SUPPLEMENTARY FIGURE

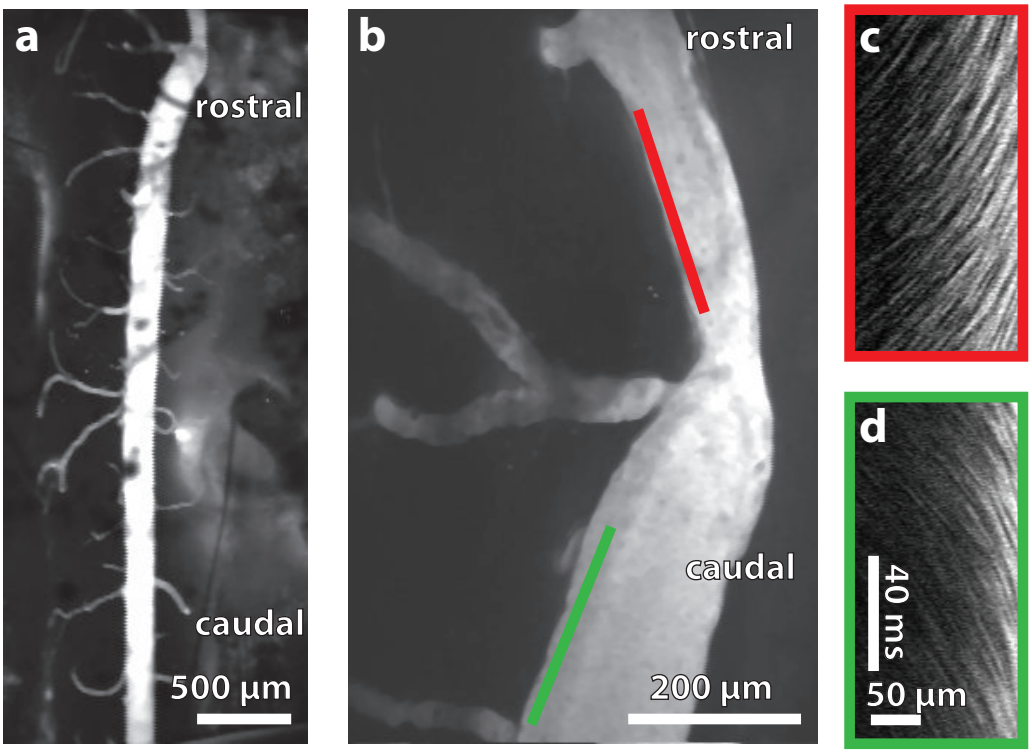

Figure 6.7: Flow into PSV shunts is bidirectional.
A segment of the PSV (a) containing a large veinous shunt (a *top*; b) was seen to have bidirectional flow into the shunt. The shunt was partially obscured by surrounding bone. Blood flow in the PSV rostral and caudal to the shunt (b) was too fast to measure quantitatively, so line scans caudal (*green line*) and rostral (*red line*) of the PSV was taken at the luminal wall of the PSV where the flow is slower to measure direction only. Line scans on either segment were performed in the same direction, caudal to rostral.The slope of the line scan in the rostral segment (c) was seen to flow in a rostral-caudal direction (negative slope), while the slope of the line can in the caudal segment (d) was seen to flow in the caudal-rostral direction (positive slope).

6.9 APPENDIX C: SIMULATION CODE

```
function [Q DP] = clot_simulation(varargin)
%%This code simulates the dorsal spinal vein (DSV) occlusion in a mouse.
%%The model assumes 100 side-branches, with equal side branch pressure
%%sources and large pressure sinks spanning the DSV.  Theory for this model
%%is found in the Theory section of the manuscript.


%Initialization of Model Parameters
N=100; %number of nodes
P0 = 0; %end pressure
PF = P0; %final endpoint pressure
P = 1; %sidebranch pressures
RDSV = 1e-3; %DSV segmental resistance
R = 1; %side branch resistance
target = []; %vessel to clot ("X" in the theory)

if nargin %If a target is specified as an argument, use it
    target = cell2mat(varargin(1));
end

%Initialize Resistances
R(2:2:2*N) = R;
R(1:2:2*N+1) = RDSV;


%Solve for Resultant Flow

for clot = 0:1 %Before and After clot

    %Pre-allocate memory for flow matrix
    FlowMat(1:2*N+1, 1:2*N+2)=0;

    %Conservation of Flow Block: Q(2j) +Q(2j-1) - Q(2j+1) = 0
    for j=1:N
        FlowMat(j,2*j)=1;
        FlowMat(j,2*j-1)=1;
        FlowMat(j,2*j+1)=-1;
    end

    %Pressure Drop Loop: R(2j)Q(2j) - sum R(2j-1) Q(2j-1) = P-P0
    for j=1:N
        for n=1:j
        FlowMat(j+N,2*n-1) = -R(2*n-1);
        end
        FlowMat(j+N,2*j) = R(2*j);
        FlowMat(j+N,2*N+2)= P-P0;
    end

    %Pressure Drop Loop: R(2N)Q(2N)+R(2N+1)Q(2N+1) = P-PF
    FlowMat(2*N+1,2*N)= R(2*N);
    FlowMat(2*N+1,2*N+1)=R(2*N+1);
    FlowMat(2*N+1,2*N+2) = P-PF;


    %Solve for the flows by reducing to row-reduced echelon form
    temp = rref(FlowMat);
```

```
    %store results as a column (1 = before clot, 2 = after clot)
    Q(clot+1,:) = temp(:,2*N+2);

    %Cause clot in target vessel
    if ~clot
        if isempty(target) %if no target specified as input
        target = str2num(cell2mat(inputdlg('Which Vessel Number do you wish↙
to clot?'))); %target DSV edge to clot
        R(target) = 1e4; %Set value to very large number (effective↙
infinity)
        end
    end
end

%Calculates the pressure drops across the side branches
DP(:,1) = Q(1,2:2:2*N).*R(2:2:2*N);
DP(:,2) = Q(2,2:2:2*N).*R(2:2:2*N);
```

REFERENCES

[1] S.C.I. Facts. Figures at a Glance. Birmingham, AL: National Spinal Cord Injury Statistical Center; 2011. 2011.

[2] AEM Mautes, MR Weinzierl, F Donovan, and LJ Noble. Vascular events after spinal cord injury: contribution to secondary pathogenesis. *Physical therapy*, 80(7):673–687, 2000.

[3] Janelle M Fassbender, Scott R Whittemore, and Theo Hagg. Targeting Microvasculature for Neuroprotection after SCI. *Neurotherapeutics*, 8(2):240–251, 2011.

[4] Michelle T L Ng, Anthea T Stammers, and Brian K Kwon. Vascular Disruption and the Role of Angiogenic Proteins After Spinal Cord Injury. *Transl. Stroke Res.*, 2(4):474–491, 2011.

[5] Stefan Weidauer, Michael Nichtweiss, Heinrich Lanfermann, and Friedhelm Zanella. Spinal cord infarction: MR imaging and clinical features in 16 cases. *Neuroradiology*, 44(10):851–857, 2002.

[6] H Hirono, A Yamadori, M Komiyama, H Yakura, and T Yausui. Mri of Spontaneous Spinal-Cord Infarction - Serial Changes in Gadolinium-Dtpa Enhancement. *Neuroradiology*, 34(2):95–97, 1992.

[7] Jan Thöne, Andreas Hohaus, Andreas Bickel, and Frank Erbguth. Severe spinal cord ischemia subsequent to fibrocartilaginous embolism. *Journal of the Neurological Sciences*, 263(1-2):211–213, 2007.

[8] Konstantinos Spengos, Georgios Tsivgoulis, Panagiotis Toulas, Sofia Sameli, Sofia Vassilopoulou, Nikolaos Zakopoulos, and Konstantinos Sfagos. Spinal cord stroke in a ballet dancer. *Journal of the Neurological Sciences*, 244(1-2):159–161, 2006.

[9] Jay J Han, Teresa L Massagli, and Kenneth M Jaffe. Fibrocartilaginous embolism—an uncommon cause of spinal cord infarction: a case report and review of the literature. *Archives of Physical Medicine and Rehabilitation*, 85(1):153–157, 2004.

[10] Jan Thöne, Andreas Hohaus, Andreas Bickel, and Frank Erbguth. Severe spinal cord ischemia subsequent to fibrocartilaginous embolism. *Journal of the Neurological Sciences*, 263(1-2):211–213, 2007.

[11] L Tosi, G Rigoli, and A Beltramello. Fibrocartilaginous embolism of the spinal cord: a clinical and pathogenetic reconsideration. *Journal of Neurology, Neurosurgery & Psychiatry*, 60(1):55–60, 1996.

[12] J Novy, A Carruzzo, P Maeder, and J Bogousslavsky. Spinal cord ischemia: clinical and imaging patterns, pathogenesis, and outcomes in 27 patients. *Archives of neurology*, 63(8):1113, 2006.

[13] J Faig, O Busse, and R Salbeck. Vertebral body infarction as a confirmatory sign of spinal cord ischemic stroke: report of three cases and review of the literature. *Stroke*, 29(1):239, 1998.

[14] RC Kim, HR Smith, ML Henbest, and BH Choi. Nonhemorrhagic Venous Infarction of the Spinal-Cord. *Ann Neurol.*, 15(4):379–385, 1984.

[15] M Niino, T Isu, and K Tashiro. Nonhemorrhagic venous infarction of the spinal cord without spinal vascular malformation. *J Neurol*, 246(9):852–854, 1999.

[16] F Schweighofer, F Anderhuber, C Zolss, JM Passler, HP Hofer, and R Wildburer. Blood supply to the cervical spinal cord and possible therapeutic consequences in cervical spinal cord injuries. *Unfallchirurg*, 96(3):134–137, 1993.

[17] ZA Zhang, H Nonaka, and T Hatori. The microvasculature of the spinal cord in the human adult. In *Neuropathology*, pages 32–42. Toho Univ,Sch Med,Dept Pathol 1,Tokyo 143,Japan, 1997.

[18] D Mazensky, J Radonak, J Danko, E Petrovova, and M Frankovicova. Anatomical study of blood supply to the spinal cord in the rabbit. *Spinal Cord*, 49(4):525–528, 2010.

[19] Y Naka, T Itakura, K Nakai, K Nakakita, H Imai, T Okuno, I Kamei, and N Komai. Microangioarchitecture of the feline spinal cord: Three-dimensional observation of blood vessel corrosion casts by scanning electron microscopy. *J Neurosurg*, 66(3):447–452, 1987.

[20] Justus T Strauch, Alexander Lauten, Ning Zhang, Thorsten Wahlers, and Randall B Griepp. Anatomy of Spinal Cord Blood Supply in the Pig. *The Annals of Thoracic Surgery*, 83(6):2130–2134, 2007.

[21] Christian D Etz MD PhD, Fabian A Kari MD, Christoph S Mueller MD, Daniel Silovitz MS, Robert M Brenner MS, Hung-Mo Lin PhD, and Randall B Griepp MD. The collateral network concept: A reassessment of the anatomy of spinal cord perfusion. *The Journal of Thoracic and Cardiovascular Surgery*, 141(4):1020–1028, 2011.

[22] Ming-Guo Qiu and Xing-Hong Zhu. Aging Changes of the Angioarchitecture and Arterial Morphology of the Spinal Cord in Rats. *Gerontology*, 50(6):360–365, 2004.

[23] I Koyanagi, CH Tator, and PJ Lea. Three-dimensional analysis of the vascular

system in the rat spinal cord with scanning electron microscopy of vascular corrosion casts. Part 2: Acute spinal cord injury. *Neurosurgery*, 33(2):285, 1993.

[24] I Koyanagi, CH Tator, and PJ Lea. Three-dimensional analysis of the vascular system in the rat spinal cord with scanning electron microscopy of vascular corrosion casts. Part 1: Normal spinal cord. *Neurosurgery*, 33(2):277, 1993.

[25] M Bilgen and B Al-Hafez. Comparison of spinal vasculature in mouse and rat: investigations using MR angiography. *Neuroanatomy*, 5:12–18, 2006.

[26] G Crosby. Local spinal cord blood flow and glucose utilization during spinal anesthesia with bupivacaine in conscious rats. *Anesthesiology*, 63(1):55, 1985.

[27] R Hickey, MS Albin, L Bunegin, and J Gelineau. Autoregulation of spinal cord blood flow: is the cord a microcosm of the brain? *Stroke*, 17(6):1183–1189, 1986.

[28] MG Fehlings, CH Tator, and RD Linden. The relationships among the severity of spinal cord injury, motor and somatosensory evoked potentials and spinal cord blood flow. *Electroencephalography and Clinical Neurophysiology/Evoked Potentials Section*, 74(4):241–259, 1989.

[29] PW Hitchon, LJ Mouw, TN Rogge, JC Torner, and AK Miller. Response of spinal cord blood flow to the nitric oxide inhibitor nitroarginine. *Neurosurgery*, 39(4):795, 1996.

[30] GD Carlson, KE Warden, JM Barbeau, E Bahniuk, KL Kutina-Nelson, CL Biro, HH Bohlman, and JC LaManna. Viscoelastic relaxation and regional blood flow response to spinal cord compression and decompression. *Spine*, 22(12):1285, 1997.

[31] Maryana Simonovich, Efrat Barbiro-Michaely, and Avraham Mayevsky. Real-Time Monitoring of Mitochondrial NADH and Microcirculatory Blood Flow in the Spinal Cord. *Spine*, 33(23):2495–2502, 2008.

[32] Guillaume Duhamel, Virginie Callot, Patrick Decherchi, Yann Le Fur, Tanguy Marqueste, Patrick J Cozzone, and Frank Kober. Mouse lumbar and cervical spinal cord blood flow measurements by arterial spin labeling: Sensitivity optimization and first application. *Magn. Reson. Med.*, 62(2):430–439, 2009.

[33] Kazunori Miyazaki, Kazuto Masamoto, Nobutoshi Morimoto, Tomoko Kurata, Takahumi Mimoto, Takayuki Obata, Iwao Kanno, and Koji Abe. Early and progressive impairment of spinal blood flow–glucose metabolism coupling in motor neuron degeneration of ALS model mice. *J Cerebr Blood F Met*, 32(3):456–467, 2011.

[34] Chris B Schaffer, Beth Friedman, Nozomi Nishimura, Lee F Schroeder, Philbert S Tsai, Ford F Ebner, Patrick D Lyden, and David Kleinfeld. Two-Photon Imaging of

Cortical Surface Microvessels Reveals a Robust Redistribution in Blood Flow after Vascular Occlusion. *Plos Biol*, 4(2):e22, 2006.

[35] PS Tsai, JP Kaufhold, P Blinder, B Friedman, PJ Drew, HJ Karten, PD Lyden, and D Kleinfeld. Correlations of Neuronal and Microvascular Densities in Murine Cortex Revealed by Direct Counting and Colocalization of Nuclei and Vessels. *J Neurosci*, 29(46):14553–14570, 2009.

[36] P Blinder, AY Shih, C Rafie, and D Kleinfeld. Topological basis for the robust distribution of blood to rodent neocortex. *Proceedings of the National Academy of Sciences*, 107(28):12670–12675, 2010.

[37] D Kleinfeld, PP Mitra, F Helmchen, and W Denk. Fluctuations and stimulus-induced changes in blood flow observed in individual capillaries in layers 2 through 4 of rat neocortex. *Proceedings of the National Academy of Sciences of the United States of America*, 95(26):15741–15746, 1998.

[38] E Chaigneau, P Tiret, J Lecoq, M Ducros, T Knopfel, and S Charpak. The Relationship between Blood Flow and Neuronal Activity in the Rodent Olfactory Bulb. *J Neurosci*, 27(24):6452–6460, 2007.

[39] Gabor C Petzold and Venkatesh N Murthy. Role of Astrocytes in Neurovascular Coupling. *Neuron*, 71(5):782–797, 2011.

[40] Nozomi Nishimura, Nathanael L Rosidi, Costantino Iadecola, and Chris B Schaffer. Limitations of collateral flow after occlusion of a single cortical penetrating arteriole. *J Cerebr Blood F Met*, 30(12):1914–1927, 2010.

[41] J Nguyen, N Nishimura, RN Fetcho, C Iadecola, and CB Schaffer. Occlusion of cortical ascending venules causes blood flow decreases, reversals in flow direction, and vessel dilation in upstream capillaries. *J Cerebr Blood F Met*, 31(11):2243–2254, 2011.

[42] Nozomi Nishimura, Chris B Schaffer, Beth Friedman, Philbert S Tsai, Patrick D Lyden, and David Kleinfeld. Targeted insult to subsurface cortical blood vessels using ultrashort laser pulses: three models of stroke. *Nat Meth*, 3(2):99–108, 2006.

[43] HU Dodt, U Leischner, A Schierloh, N Jährling, CP Mauch, K Deininger, JM Deussing, M Eder, W Zieglgänsberger, and K Becker. Ultramicroscopy: three-dimensional visualization of neuronal networks in the whole mouse brain. *Nat Meth*, 4(4):331–336, 2007.

[44] KD Kurz, BW Main, and GE Sandusky. Rat Model of Arterial Thrombosis Induced by Ferric-Chloride. *Thromb Res*, 60(4):269–280, 1990.

[45] Matthew J Farrar, Frank W Wise, Joseph R Fetcho, and Chris B Schaffer. In Vivo Imaging of Myelin in the Vertebrate Central Nervous System Using Third Harmonic Generation Microscopy. *Biophys J*, 100(5):1362–1371, 2011.

[46] T P Santisakultarm, N R Cornelius, N Nishimura, A I Schafer, R T Silver, P C Doerschuk, W L Olbricht, and C.B. Schaffer. In vivo two-photon excited fluorescence microscopy reveals cardiac- and respiration-dependent pulsatile blood flow in cortical blood vessels in mice. *AJP: Heart and Circulatory Physiology*, 302(7):H1367–H1377, 2012.

[47] MEJ Newman. The structure and function of complex networks. *SIAM review*, 45(2):167–256, 2003.

[48] B Brockstein, L Johns, and BL Gewertz. Blood supply to the spinal cord: anatomic and physiologic correlations. *Annals of vascular surgery*, 8(4):394–399, 1994.

[49] WI Schievink, W Luyendijk, and JA Los. Does the artery of Adamkiewicz exist in the albino rat? *J Anat*, 161:95, 1988.

[50] A Santillan, V Nacarino, E Greenberg, HA Riina, Y P Gobin, and A Patsalides. Vascular anatomy of the spinal cord. *Journal of NeuroInterventional Surgery*, 4(1):67–74, 2011.

[51] S Fujimoto, H Katsuki, M Ohnishi, M Takagi, T Kume, and A Akaike. Plasminogen potentiates thrombin cytotoxicity and contributes to pathology of intracerebral hemorrhage in rats. *J Cereb Blood Flow Metab*, 28(3):506–515, 2008.

[52] A Martinez-Arizala, RJ MORA, PW MADSEN, BA GREEN, and N Hayashi. Dorsal spinal venous occlusion in the rat. *J Neurotraum*, 12(2):199–208, 1995.

[53] Z Zhang, H Nonaka, T Nagayama, T Hatori, F Ihara, L Zhang, and M Akima. Circulatory disturbance of rat spinal cord induced by occluding ligation of the dorsal spinal vein. *Acta neuropathologica*, 102(4):335–338, 2001.

[54] JL DOPPMAN, M GIRTON, and MA POPOVSKY. Acute Occlusion of the Posterior Spinal Vein - Experimental-Study in Monkeys. *J Neurosurg*, 51(2):201–205, 1979.

[55] J Widenfalk, A Lipson, M Jubran, C Hofstetter, T Ebendal, Y Cao, and L Olson. Vascular endothelial growth factor improves functional outcome and decreases secondary degeneration in experimental spinal cord contusion injury. *Neuroscience*, 120(4):951–960, 2003.

[56] Yang Liu, Sarah Figley, S Kaye Spratt, Gary Lee, Dale Ando, Richard Surosky, and Michael G Fehlings. An engineered transcription factor which activates VEGF-A enhances recovery after spinal cord injury. *Neurobiol Dis*, 37(2):384–393, 2010.

[57] Hyuk Min Kim, Dong Hoon Hwang, Jong Eun Lee, Seung U Kim, and Byung G Kim. Ex Vivo VEGF Delivery by Neural Stem Cells Enhances Proliferation of Glial Progenitors, Angiogenesis, and Tissue Sparing after Spinal Cord Injury. *Plos One*, 4(3):e4987, 2009.

[58] C Ruiz de Almodovar, D Lambrechts, M Mazzone, and P Carmeliet. Role and Therapeutic Potential of VEGF in the Nervous System. *Physiol Rev*, 89(2):607–648, 2009.

[59] J Rosenstein. New roles for VEGF in nervous tissue–beyond blood vessels. *Exp Neurol*, 187(2):246–253, 2004.

[60] S Madi, AE Flanders, S Vinitski, GJ Herbison, and J Nissanov. Functional MR imaging of the human cervical spinal cord. *American journal of neuroradiology*, 22(9):1768–1774, 2001.

[61] Giovanni Giulietti, Federico Giove, Girolamo Garreffa, Claudio Colonnese, Silvia Mangia, and Bruno Maraviglia. Characterization of the functional response in the human spinal cord: Impulse-response function and linearity. *NeuroImage*, 42(2):626–634, 2008.

[62] PW Stroman and LN Ryner. Functional MRI of motor and sensory activation in the human spinal cord. *Magnetic resonance imaging*, 19(1):27–32, 2001.

[63] F Corson. Fluctuations and redundancy in optimal transport networks. *Phys. Rev. Lett.*, 104(4):48703, 2010.

[64] YC Fung. *Biomechanics: Circulation*. Springer, New York, NY, 2 edition, 1996.

[65] S Lorthois, F Cassot, and F Lauwers. Simulation study of brain blood flow regulation by intra-cortical arterioles in an anatomically accurate large human vascular network. Part II: Flow variations induced by global or localized modifications of arteriolar diameters. *NeuroImage*, 54(4):2840–2853, 2011.

CHAPTER 7

NONLINEAR OPTICAL REFLECTION MICROSCOPY (NORM) AS A TECHNIQUE FOR VISUALIZING OPTICAL INTERFACES

In this section, we present preliminary data and the underlying theory of a microscopy technique that was developed as part of my admission to candidacy exam. In essence, this technique changes the amount of reflected light at an interface by modulating the intensity-dependent indices of refraction in both media. At the time of writing, experiments have been limited to proof-of-principle experiments, and we have not yet developed NORM into a true microscopy. Our largest challenge at present is the elimination of off-interface signal, which we hope to eliminate by tighter focusing of both the pump and pulse beams. Provided that this endeavor is successful, evaluation for imaging biological specimens will be determined in fixed tissue. Extending these studies to *in vivo* imaging and upgrading to a mirror-scanning microscopy will be essential later developments for multi-modal imaging with established techniques of 2-photon excited fluorescence and harmonic generation.

7.1 ABSTRACT

Multi-photon microscopy has made possible the imaging of *in vivo* dynamics at the micrometer scale deep inside scattering tissue. However, contrast generated by the creation of new wavelengths results in spectral overlap between different species of interest, limiting the number of tissue constituents that can be imaged simultaneously. We present both theory and data on nonlinear optical reflection microscopy (NORM), a technique that allows for non-specific mapping optical interfaces. This modality can provide contextual information to labeled structures without adding multiple imaging channels or contrast agents. The technique uses lock-in amplification to measure small changes in the reflectance of a probe beam induced by modulation of the intensity-dependent index of refraction, n_2, from a strong pump beam. Current experiments consist of axial scans of polymeric materials, which are expected to have large values of n_2. Present challenges and future experiments are discussed.

7.2 INTRODUCTION

The advent of nonlinear laser scanning microscopy (NLSM) by Denk et al. [1] made sub-micrometer optical image generation possible even deep in scattering tissue. Mechanisms of contrast for NLSM in biological tissue include 2-photon excited fluorescence (2PEF) [1] [2], second harmonic generation (SHG) [3–6], third harmonic generation (THG) [7–10], and coherent anti-Stokes Raman spectroscopy (CARS) [11]. All have been employed for biological imaging by generating new wavelengths via nonlinear processes which take place only at high intensities. These high intensities are achieved by ultrashort pulses and tight focusing, with the signal being generated appreciably only at the focus of the objective. Since the origin of the novel wavelength is known a priori, light simply has to be collected as opposed to imaged, which eliminates image blurring by scattering. By raster scanning the focus, an image can be effectively built up in point-by-point fashion.

In addition to techniques that generate new wavelengths, it is also possible to measure intensity changes relative to some baseline. For example, envelope modulation and the quadratic dependence of two-photon absorption (TPA) on laser intensity has been exploited to harmonically deplete the incident laser pulse train [12]. A similar technique [13] was used in a two color TPA modulation approach. This technique has been used to distinguish melanomas from benign nevi [14] and to image changes in blood oxygenation [15]. Photo-thermal lensing has also been used as a pump-probe technique to visualize optical chromophores, such as red blood cells [16].

Moreover, the nonlinearity (and thus, optical sectioning) does not have to arise from higher-order susceptibility tensors as in the techniques above, but can arise from a product of linear effects, as in pump-probe spectroscopy. Excited state absorption [13] uses linear absorption of a pump beam to excite chromophores into a higher energy level. Chromophores in this excited state–but not the in the ground state–absorb probe light, resulting in a depletion of probe light. Conversely, stimulated emission microscopy [17] [18]uses a pump beam to achieve population inversion in

chromophores, which then return to the ground state when stimulated by a probe beam. In all cases the change in transmitted probe intensity was determined by lock-in amplification.

Pump-probe spectroscopies based on self-phase modulation (SPM) have been exploited in spectroscopy measurements by transmission modulation [19–21]. However, it should be noted that these measurements are not based on interface dynamics, but from phase modulations in the bulk. SPM has also been used as a source of contrast by the filling of a spectral hole in a shaped pulse [22, 23]. Nonlinear reflection modification has been studied theoretically [24]and experimentally [25–28] as an optical switching technique by modulating the index of refraction at the angle giving rise to (linear) total internal reflection. Hysteresis effects in the intensity were also predicted/observed [24–28].

In spite of these advances, no nonlinear analog of differential interference contrast (DIC) imaging has yet been developed to visualize the big picture context surrounding structures of interest labeled fluorescently or imaged using other means of nonlinear contrast. This deficit potentially results in the omission of important aspects of the tissue environment. We have developed a pump-probe microscopy technique that uses the intensity-dependent index of refraction to modulate the total indices of refraction–and thus the coefficient of reflection–at an optical interface. We have called this imaging modality Nonlinear Optical Reflection Microscopy (NORM). We here present an experimental schematic, theoretical background, and supporting data. Also, we have demonstrated proof of principle based on expected dependences on pump power, polarization angle, temporal delay.

Our discussion includes key challenges at present and a discussion and strategies to overcome these drawbacks.

7.3 THEORY

7.3.1 Cross-phase modulation and the intensity-dependent index of refraction

We consider our analysis in the plane wave limit of the nonlinear wave equation, which is sufficient to describe our system. In this limit, the wave equation reduces to:

$$\frac{dA_j(z)}{dz} = i\frac{\omega_j^2}{2k_j c^2} P_j(z)/\epsilon_0 \tag{7.1}$$

where subscript j indexes the frequency and we have the forms

$$E_j = A_j(z)\exp[i(k_j z - \omega_j t)] + c.c. \tag{7.2}$$

$$P_{NL,j} = P_j(z)\exp[i(k_j z - \omega_j t)] + c.c. \tag{7.3}$$

for the electric field and nonlinear polarization, respectively. The abbreviation "$c.c.$" denotes "complex conjugate". Here, ω denotes angular frequency, k is the wave vector, c is the speed of light, and ϵ_0 is permittivity of free space. We have already assumed that the electric field envelope, $A_j(z)$, is a slowly varying function of z compared to the phase in (7.2). Since we will consider two frequencies in a pump-probe experiment, we will index the pump with $j = 1$ and the probe with $j = 2$. The polarization is related to the electric field by

$$\mathbf{P_{NL}} = \epsilon_0 \sum_{m\geq 2} \chi^{(m)} : \mathbf{E}^m \tag{7.4}$$

where $\chi^{(m)}$ is the m^{th}-order electric susceptibility tensor and colon denotes tensorial product. While the tensor product is the most general form, we shall assume we are working in a principle direction for an isotropic material, and treat $\chi^{(m)}$ as a scalar.

We work in the Rayleigh-Debye [29] limit of (7.1) and (7.4), where we consider the mixing of fields at all frequencies algebraically and use these values in the right hand side of (7.1). For centrosymmetric molecules (which comprise the majority

of molecules) $\chi^{(2)}$ vanishes, making $\chi^{(3)}$ terms the lowest-order nonlinear effect to consider. For dual input beams of ω_1 and ω_2, we have:

$$P_1 = \epsilon_0 \chi^{(3)} \left[6|A_2|^2 + 3|A_1|^2\right] A_1 \tag{7.5}$$

$$P_2 = \epsilon_0 \chi^{(3)} \left[6|A_1|^2 + 3|A_2|^2\right] A_2 \tag{7.6}$$

We neglect all other four-wave mixing terms due to phase mismatch. In the limit of a strong pump and a weak probe (i.e. $|A_1| \gg |A_2|$), we are left with

$$P_1 = 3\epsilon_0 \chi^{(3)} |A_1|^2 A_1 \tag{7.7}$$

$$P_2 = 6\epsilon_0 \chi^{(3)} |A_1|^2 A_2 \tag{7.8}$$

These terms correspond to self-phase modulation (7.7) and cross-phase modulation (7.8). Since we are interested in the effect on the probe beam, we will concentrate on (7.8).

If we insert (7.8) back into (7.1), we have the differential equation

$$\frac{dA_2(z)}{dz} = i \frac{3\omega_2^2}{k_2 c^2} \chi^{(3)} |A_1|^2 A_2 \tag{7.9}$$

In the limit of a strong pump, $|A_1|^2 \approx$ constant, and (7.9) integrates directly to give:

$$A_2(z) = A_2(0) \exp(i3 \frac{\omega_2}{n_{\omega_2} c} \chi^{(3)} |A_1|^2 z) \tag{7.10}$$

where we have used that $k_2 = n_{\omega_2} \omega_2 / c$ for index of refraction, n_{ω_2}. We have assumed bounds of $(0, z)$ on our integral, though in principle these depend on boundary conditions specified by the geometry of interest. We convert between field amplitude and intensity using $I = 2 n_\omega \epsilon_0 c |A|^2$, leaving us with:

$$A_2(z) = A_2(0) \exp\left(i \frac{\omega_2}{c} \left[\frac{3\chi^{(3)}}{2 n_{\omega_1} n_{\omega_2} \epsilon_0 c} \right] I_1 z \right) \tag{7.11}$$

The form of (7.11) gives rise to the definition:

$$n_2 \equiv \frac{3\chi^{(3)}}{2 n_{\omega_1} n_{\omega_2} \epsilon_0 c} \tag{7.12}$$

such that the oscillating electric field has the structure given by (7.11) and (7.2):

$$E_2 = A_2(0) \exp\left\{ i \left[\frac{(n_{\omega_2} + n_2 I_1)\omega_2}{c} z - \omega_2 t \right] \right\} \tag{7.13}$$

Thus, the effect of cross-phase modulation is an intensity dependent index of refraction $n_2 I_1$.

7.3.2 Reflection from a dielectric interface

Consider a dielectric slab with combined index N_2 existing on $0 < z < L$ and surrounded by a medium of index N_1, as shown in Fig. 7.1b. We denote the reflection and transmission coefficients *from* medium 1 *to* medium 2 by r_{12} and t_{12}, respectively. If we denote the signal (reflected) field as E_S then by considering the diagram in Figure 7.1b we arrive at:

$$E_S = E_2\{r_{12}(\theta) + t_{12}(\theta)t_{21}(\phi)r_{21}(\phi)\sum_{m=0}^{\infty}[r_{21}^2(\phi)\cos(\Phi(L,\phi))]^m\} \tag{7.14}$$

where the first term represents the initial reflection and the summation accounts for internal reflections. The angles θ and ϕ are an incidence/refraction angle pair related by Snell's Law:

$$\mathcal{N}_1 \sin\theta = \mathcal{N}_2 \sin\phi \tag{7.15}$$

and

$$\Phi(L,\phi) = \frac{2\omega_2}{c}\int_0^L \frac{\mathcal{N}_2(z)dz}{\cos\phi} \tag{7.16}$$

is the phase acquired by internal reflections. As before, we take the probe beam to be much weaker than the pump beam, such that:

$$\mathcal{N}_2(z) = n_{0,2} + n_{2,2}I_1 \tag{7.17}$$

$\mathcal{N}_1$ is defined analogously.

The sum in (7.14) is a geometric series and is easily evaluated:

$$\sum_{m=0}^{\infty}[r_{21}^2(\phi)\cos(\Phi(L,\phi))]^m = \frac{1}{1 - r_{21}^2(\phi)\cos(\Phi(L,\phi))} \tag{7.18}$$

which in turn gives our governing equation:

$$E_S = E_2\{r_{12}(\theta) + \frac{t_{12}(\theta)t_{21}(\phi)r_{21}(\phi)}{1 - r_{21}^2(\phi)\cos(\Phi(L,\phi))}\} \tag{7.19}$$

The Fresnel equations describe the index of refraction of light on a dielectric surface for both s and p polarizations, and may be found in any standard optics text. Using these equations we eliminate refraction angle ϕ in the phase integral to get:

$$\Phi(L,\theta) = \frac{2\omega_2}{c}\int_0^L \frac{\mathcal{N}(z)\mathcal{N}_2(z)dz}{\sqrt{\mathcal{N}^2(z)-\sin^2\theta}} \tag{7.20}$$

where

$$\mathcal{N} \equiv \frac{\mathcal{N}_2}{\mathcal{N}_1} \tag{7.21}$$

For most biological interfaces of interest, the interface thickness $L \ll b$ for confocal parameter b, and so the intensity and therefore the indices of refraction are approximately constant over the region of interest. In this case, the integral evaluates trivially to give:

$$\Phi(L,\theta) = \frac{2\omega_2 L\mathcal{N}\mathcal{N}_2}{c\sqrt{\mathcal{N}^2-\sin^2\theta}} \tag{7.22}$$

7.3.3 The semi-infinite slab approximation

For epi-detection microscopy, normal incidence (i.e. $\theta = 0$) is the most relevant consideration. Moreover, we will consider a semi-infinite slab, such that material 1 exists everywhere for $z < 0$ and material 2 exists everywhere for $z > 0$. In this case, internal reflections in (7.14) do not contribute to the signal, and only the first reflection matters. For normal incidence, the reflectivity coefficient, r, is given by:

$$r = \left(\frac{1-\mathcal{N}}{1+\mathcal{N}}\right) \tag{7.23}$$

where we now write N explicitly as:

$$\mathcal{N} = \frac{n_{0,2}+n_{2,2}I_1}{n_{0,1}+n_{2,1}I_1} \tag{7.24}$$

where the first subscript denotes the linear (n_0) or intensity-dependent (n_2) index of refraction, and the second subscript denotes the medium. We now consider some pertinent special cases.

Linear index mismatch

It is convenient to define the variables:

$$\Delta n_2 \equiv n_{2,1} - n_{2,2} \tag{7.25a}$$

$$\sigma n_2 \equiv n_{2,1} + n_{2,2} \tag{7.25b}$$

$$\Delta n_0 = n_{0,1} - n_{0,2} \tag{7.25c}$$

$$\sigma n_0 = n_{0,1} + n_{0,2} \tag{7.25d}$$

By the definitions of $\mathcal{N}_{1,2}$, we have:

$$r = \frac{1-\mathcal{N}}{1+\mathcal{N}} = \frac{\Delta n_0 + \Delta n_2 I_1}{\sigma n_0 + \sigma n_2 I_1} \tag{7.26}$$

Keeping only terms at most linear in the intensity-dependent indices (since $n_2 I_1 \ll n_0$) of refraction we have:

$$E_S = E_2 \left\{ \left(\frac{\Delta n_0}{\sigma n_0} \right) \left[1 + \left(\frac{\Delta n_2}{\Delta n_0} - \frac{\sigma n_2}{\sigma n_0} \right) I_1 \right] \right\} \tag{7.27}$$

Squaring (7.27) to get the intensity and keeping only terms linear in the intensity-dependent index of refraction as before we arrive at the signal intensity:

$$I_S(I_1) = \left(\frac{\Delta n_0}{\sigma n_0} \right)^2 \left[1 + 2 \left(\frac{\Delta n_2}{\Delta n_0} - \frac{\sigma n_2}{\sigma n_0} \right) I_1 \right] I_2 \tag{7.28}$$

which has a modulation depth:

$$\frac{\Delta I_S}{I_S(I_1 = 0)} \equiv \Delta R = 2 \left(\frac{\Delta n_2}{\Delta n_0} - \frac{\sigma n_2}{\sigma n_0} \right) I_1 \tag{7.29}$$

where ΔR is the change in reflectivity. As expected, we have a quadratic nonlinear signal by virtue of the fact that the (7.28) scales as the product of the pump and probe, $I_1 I_2$.

Linear index matching

A second interesting case is for linear index matching ($n_{0,1} = n_{0,2} \equiv n_0$) without intensity-dependent index matching ($n_{1,2} \neq n_{2,2}$). In this case, similar analysis gives

$$I_S = \left(\frac{\Delta n_2}{2 n_0} \right)^2 I_1^2 I_2 \tag{7.30}$$

There are two interesting points about (7.30). First, the signal is in reference to a null-point: in the absence of the pump, no reflected signal exists (i.e. $I_S(I_1 = 0) = 0$), unlike the linear index-mismatched case, where a strong carrier signal is weakly modulated. Second, the scaling is now a cubic effect in terms of intensities, receiving two intensity powers from the pump and one from the probe. However, since the lowest order of this effect is in $(\Delta n_2)^2$, we anticipate this effect to be very small.

7.3.4 Finite thickness slabs

For biological specimens of interest, we are typically concerned with interfaces similar in thickness to cell membranes (∼10 nanometers). Still assuming normal incidence, we return to the full form of (7.14) for normal incidence. In this limit, and for wavelengths between ~ 500 nm-1 μm, the signal to lowest order in Φ becomes

$$I_S = I_S^{(0)} \frac{(1-\mathcal{N})^4 \Phi^4}{64\mathcal{N}^2} \tag{7.31}$$

where superscript 0 denotes the estimates without accounting for internal reflections (i.e the semi-infinite slab approximation). Using (7.22) with $\theta = 0$, we have:

$$I_s = I_S^{(0)} \frac{(1-\mathcal{N})^4 (k_2 L)^4}{4\mathcal{N}^2} \tag{7.32}$$

Cell membranes are on the order of 10 nm, while the probe light has a 520-nm wavelength, giving $k_2 L \approx 0.1$. For the first medium of water ($n_{0,1} = 1.33$) and the second medium a cell membrane ($n_{0,2} \sim 1.48$ [30]), we have $\mathcal{N} \approx 1.1$. This contribution gives a back-of-the-envelope estimate of

$$I_s \approx 10^{-9} I_S^{(0)} \tag{7.33}$$

Thus, in samples where internal reflection terms cannot be ignored, we anticipate a much weaker signal with a strong dependence on sample thickness. Moreover, since n_2 varies widely with dielectric (1.9×10^{-20} m^2/W [31]for water; 1.54×10^{-19} m^2/W for fused silica [20]; n_2 of $-2.42 \times l0^{-12}$ m^2/W for polystyrene (PS) [32]), the extent of modulation will depend critically on the materials at the interface.

7.3.5 Polarization dependence

In addition, it should be noted that while signal depends on pump and probe *intensity*, we have suppressed the tensorial nature of (7.4). In reality, the index of refraction will be modulated in the direction(s) determined by the pump polarization and the third-order electric susceptibility tensor, $\chi^{(3)}$. For an isotropic material with no off-diagonal tensor terms, maximum signal is obtained when the pump and probe polarizations are aligned and signal is destroyed when they are orthogonal.

7.4 METHODS

Our experimental setup was as shown in Fig. 7.1a. Briefly, a low-repetition rate (1 MHz) 1040-nm laser source with 300-fs pulses (FCPA μJewel; IMRA America) was split into two arms. The first arm was frequency doubled in a lithium triborate (LBO) crystal (Newlight Photonics) to 520 nm light, which was used as the probe light. Any unconverted fundamental was filtered using an interference filter (517-nm bandpass filter; Chroma Technology). The second (pump) arm passed through a delay arm and was modulated by an optical chopper at 6.4 kHz. To control power, a half-waveplate mounted on a rotation mount was used to rotate the polarization of the light prior to passing through a polarizing beamsplitter. A second half-wave plate was placed in the pump path to allow for polarization rotation with respect to the probe. Pairs of lenses were used to form telescopes to resize each beam. The two arms were recombined at a dichroic mirror and incident on the back aperture of the microscope objective. Beams were overlapped spatially. Temporal alignment was achieved using the delay line produced by a pair of mirrors on a translation stage (Fig. 7.1a; MM). Reflected light was epi-detected by a 50:50 non-polarizing beamsplitter and a photodiode. Pump light was filtered by a blocking filter (Schott BG39; Thor Labs). Modulation of the reflected probe beam was measured by lock-in amplification (SRS530; Stanford Research Systems) of

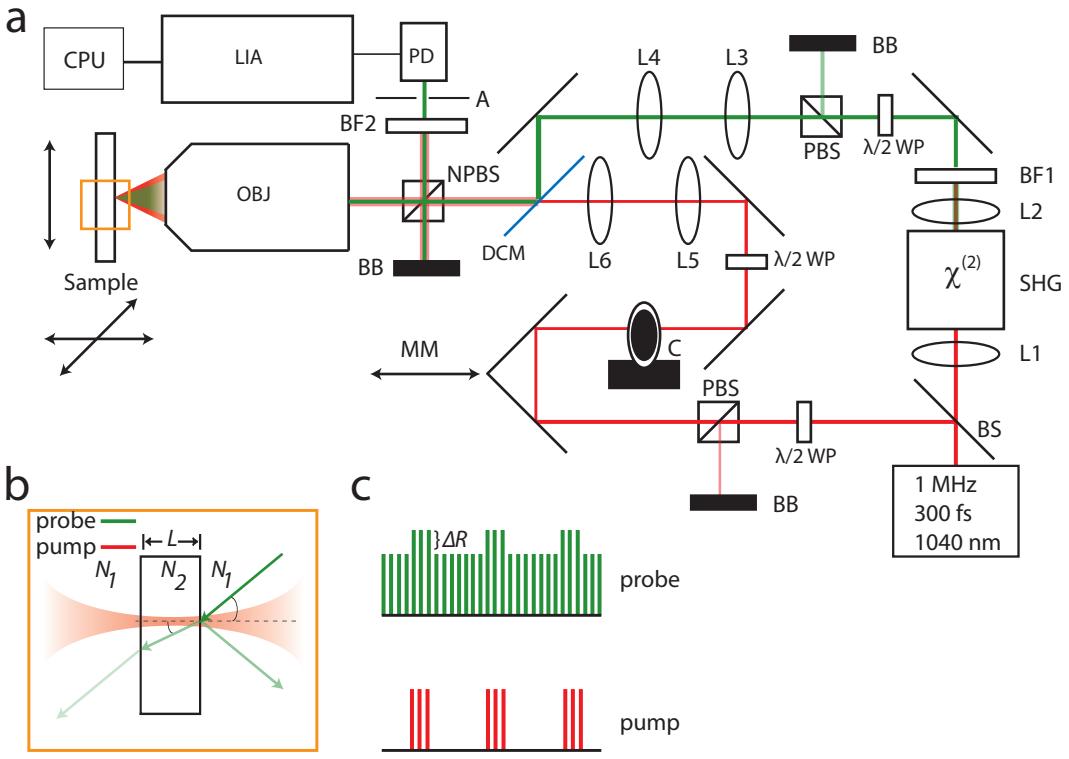

Figure 7.1: Figure 1: A nonlinear optical reflection microscopy (NORM) setup. (a) A fiber laser source (1 MHz pulse repetition rate; 300-fs pulses, 1040-nm central wavelength) is split into two arms by a 50:50 beamsplitter (BS). Lens L1 focuses light into the frequency doubling crystal ($\chi^{(2)}$) where second harmonic generation (SHG) results in 520-nm light (green) being produced. L2 is used to collimate the resulting light. Fundamental wavelength (red) is filtered by blocking filter (BF1). The pump arm passed through a delay stage with movable mirrors (MM). A chopper (C) modulated the pump at 6.4 kHz. Half-waveplates ($\lambda/2$ WP) and polarizing beamsplitters (PBS) were used for power control of both the pump and probe arms. Rejected light was removed by beam blocks (BB). A second half-waveplate was used to rotate the pump polarization. Telescopes (L3 and L4; L5 and L6) were used to resize the the pump and probe beams, which were combined at the dichroic mirror (DCM) and focused onto the sample through a microscope objective (OBJ). The sample was placed on a computerized three-dimensional translation stage. A non-polarizing beamsplitter (NPBS) reflected the return light onto a photodiode (PD). Pump light was filtered by blocking filters (BF2). Off-axis light was blocked by an aperture (A). The photodiode signal was amplified using a lock-in amplifier (LIA) with the chopping frequency from the chopper as a reference, and the lock-in output was read using a computer (CPU). (b) Pump light modulates the indices of refraction at an interface of a dielectric slab of thickness L and index N2 surrounded by a medium of index N1, leading to a change in reflectivity at the interface, ΔR, (c), which provides optical contrast.

the photodiode signal at the chopper frequency and the lock-in output was digitized using a custom script in Matlab (Mathworks Inc.). The sample was placed on a three-dimensional translation stage (GTS30V and ILS-100; Newport Corporation) also controlled by the Matlab script. To date, we have only performed scans in the axial direction.

The pump changed the indices of refraction at interfaces (Fig. 7.1b) by cross-phase modulation (i.e. the intensity-dependent index of refraction). A differential change in the reflectivity of the interface (c) resulted in a modulation of the probe light. The transmitted light is oppositely modulated, but non-ballistic trajectories from back-scattered transmission were blocked by an aperture (Fig. 7.1a). Fig. 7.1c shows a positive modulation for illustrative purposes, but the sign of modulation depends on the optical properties of the two materials.

We performed axial scans of dielectrics with a lock-in integrating constant of 100 ms and no signal averaging. Stage speed and sampling rate were chosen to allow approximately 10 points/m. We used a sample of 1-mm thick polyethylene terephthalate (PETG) with a water-immersion lens (40x, NA = 0.8; Olympus America). We also performed experiments on 800 μm thick PS (data not shown).

7.5 RESULTS

PETG has an index of refraction of [33] 1.567, but we were unable to find a measured value of n_2 in the literature. PS (data not shown) has an index of refraction of 1.589 [33] and an estimated value between $n_2 = -9.3 \times 10^{-13}$ [34] and n_2 of -2.42×10^{-12} m^2/W [32]. Water has an index of refraction of 1.33 and 1.9×10^{-20} m^2/W [31]. We thus anticipated both a strong modulation from the PETG or PS and a strong carrier signal from linear index mismatch. Axial scans (Fig. 7.2a) showed a sharp peak in the NORM signal at the interface of water/PETG. We observed a second broad peak inside the PETG, presumably due to an off-axis nonlinear Kerr effect. We used a weakly-focused

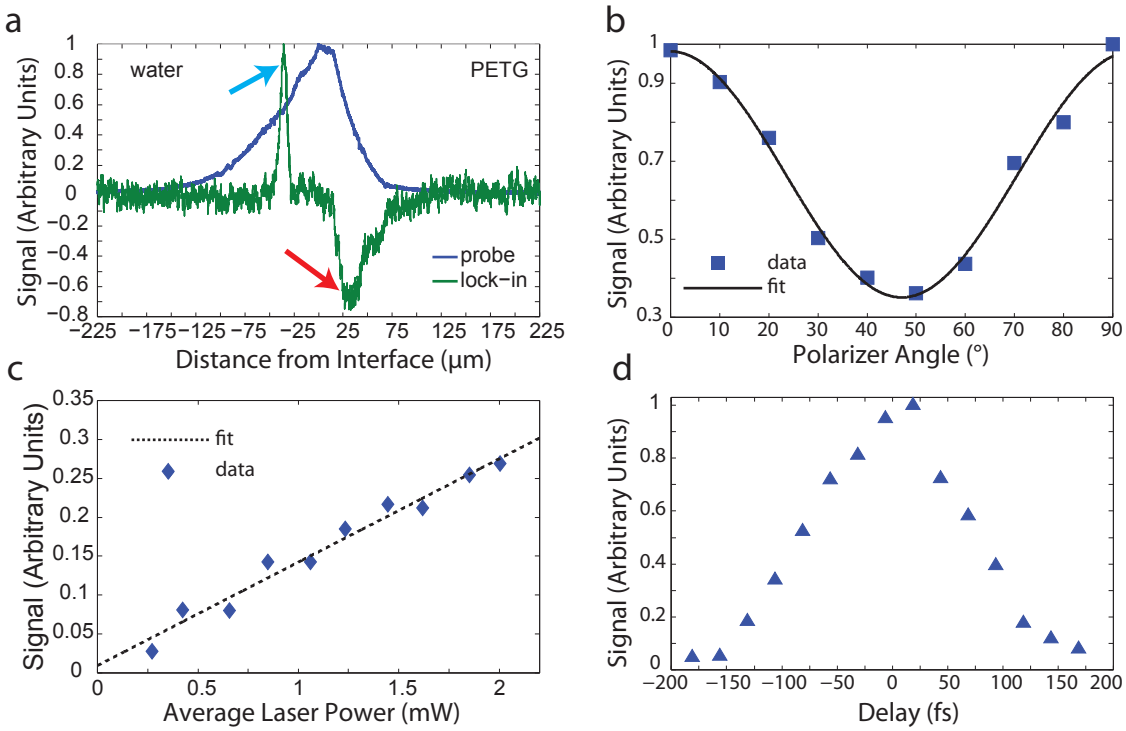

Figure 7.2: Axial scan measurements showed hallmarks of NORM.
(a) An axial scan showed interface sensitivity. The scan revealed weak-focusing of the probe beam (blue). A sharp peak (*cyan arrow*) in the lock-in signal (*green*) is believed to have arisen due to NORM while a broader pulse of opposite modulation (*red arrow*) is believed to have arisen from out-of-focus Kerr effects. (b) Signal varied sinusoidally as a function of the polarizer angle. Polarization of the pump with respect to the probe is twice the polarizer angle. (c) Signal varied linearly with pump power. (d) Signal strongly depended on temporal overlap, with a full width of approximately 300 fs.

probe pulse to facilitate ease of axial alignment. That the probe was weakly focused was readily seen from the raw reflectance (probe) trace for the interface (Fig. 7.2a; *blue trace*). Since the objective had NA = 0.8 ,we anticipated resolution on the order of 0.3 μm, whereas the full-width-at-half-maximum of the probe trace was approximately 60 μ. This weak focusing was achieved by the use of a narrow beam, under-filling the back aperture of the objective and reducing the effective NA.

Axial scans were performed for a variety of polarizer angles of the pump (Fig. 7.2b). For a perfect polarizer, the polarization of the pump will rotate 90° every time the polarizer rotates 45°. Since polarization is unique only in the range 0° to 90°, for an isotropic material the signal is then expected to oscillate with a period of 90° in the polarizer angle. Signal was determined from the axial scan as the peak in the lock-in signal. After normalizing the data, a cosine was fit to the data with a period of $94 \pm 7^\circ$, in good agreement with the theoretical prediction of 90°. Incomplete extinction of NORM signal at 45° was likely due to inefficiency in the polarizer and/or local anisotropy in the material of interest.

Analogously, we measured signal peaks from axial scans as a function of pump power (Fig. 7.2c). A linear fit was confirmed with $R^2 = 0.97$. Probe power was not scanned due to the proximity of the minimum probe power required for efficient signal to the damage threshold for PETG. No signal was observed when either the pump or probe was blocked.

Finally, signal peaks were determined from axial scans with varying temporal offsets produced by a delay line (Fig. 7.2d). Temporal increments were measured from 1/4 turns of a 50-μm/turn fine adjustment dial. A full width of approximately 300 fs was observed, in good agreement with 300-fs pulse duration of the laser.

7.6 DISCUSSION

Our data showed four hallmarks expected by the theoretical description of NORM: interface sensitivity, polarization dependence, linear power scaling, and temporal sensitivity in the 100-fs range.

Since NORM is an interface microscopy, we anticipated significant signal only at an interface where the change in index of refraction results in a robust reflected carrier signal. However, this observation alone is not sufficient to rule out other interface-sensitive processes, such as interference between interface-SHG and the probe.

The linear power scaling of the signal with pump laser intensity ruled out effects such as interface-SHG or any higher-order effects, since these depend on higher powers of the pump laser power. However, the interface sensitivity and scaling do not eliminate thermal effects, such as photothermal lensing [16] which could possess both features.

However, the dependence of the signal on both polarization and its temporal sensitivity ruled out such a process. First, absorptive processes are largely independent of polarization, whereas the observed signal was strongly polarization dependent. Second, absorptive effects last at least as long as electron relaxation times (typically on the order of nanoseconds [35]), while thermal effects depend on the thermal diffusion coefficient (typically on the order of microseconds). Thus, the observation of a 300-fs window during which signal is efficiency generated is exactly what is expected for a parametric process.

The sum of these four findings is strongly indicative of NORM. However, Fig. 7.2a contains an unfortunate, broad, off-interface signal. This effect had the same power scaling and polarization dependence as the narrower peak (data not shown), suggesting that it is a Kerr effect. Since this microscopy is technically challenging, we used narrow beams to under-fill the back aperture of the objective, thereby creating weaker focusing in the sample. This allowed for easier axial and planar alignment of the two beams. However, as our observation shows, this compromise introduced artifacts which would complicate any kind of imaging. Future experiments will use tightly focused pump and

probe beams to eliminate effects away from an interface.

Finally, with this correction made, it will be important to assess the value of NORM for imaging biological interfaces by using all three dimensions of translation. Initially, we will evaluate NORM as a stage-scanning microscopy. However, since this significantly reduces the speed of image acquisition, we will upgrade the system to a mirror-scanning protocol than can be performed simultaneously with other NLSM modalities. We are optimistic in our assessment of NORM as an *in vivo* DIC analog.

7.7 ACKNOWLEDGMENTS

We would like to thank IMRA America Inc. for the loan of its FCPA mJewel D-400 laser and LBO crystal system. We thank the National Institutes of Health (grant No. RO1 EB002019 to C.B.S.) and the National Science and Research Council of Canada (to M.J.F.) for financial support.

REFERENCES

[1] W Denk, JH Strickler, and WW Webb. Two-photon laser scanning fluorescence microscopy. *Science*, 248(4951):73–76, 1990.

[2] C Xu, W Zipfel, JB Shear, RM Williams, and WW Webb. Multiphoton fluorescence excitation: new spectral windows for biological nonlinear microscopy. *Proceedings of the National Academy of Sciences of the United States of America*, 93(20):10763, 1996.

[3] Paul J Campagnola, Mei-de Wei, Aaron Lewis, and Leslie M Loew. High-Resolution Nonlinear Optical Imaging of Live Cells by Second Harmonic Generation. *Biophys J*, 77(6):3341–3349, 1999.

[4] L Moreaux, O Sandre, M Blanchard-Desce, and J Mertz. Membrane imaging by simultaneous second-harmonic generation and two-photon microscopy. *Opt Lett*, 25(5):320–322, 2000.

[5] Paul J Campagnola, Andrew C Millard, Mark Terasaki, Pamela E Hoppe, Christian J Malone, and William A Mohler. Three-Dimensional High-Resolution Second-Harmonic Generation Imaging of Endogenous Structural Proteins in Biological Tissues. *Biophys J*, 82(1):493–508, 2002.

[6] G Cox, E Kable, A Jones, I Fraser, F Manconi, and MD Gorrell. 3-dimensional imaging of collagen using second harmonic generation. *Journal of structural biology*, 141(1):53–62, 2003.

[7] Y Barad, H Eisenberg, M Horowitz, and Y Silberberg. Nonlinear scanning laser microscopy by third harmonic generation. *Appl Phys Lett*, 70(8):922–924, 1997.

[8] M Muller, I Squier, KR Wilson, and GI Brakenhoff. 3D microscopy of transparent objects using third-harmonic generation. *Journal of Microscopy*, 191:266–274, 1998.

[9] J Squier, M Muller, G Brakenhoff, and KR Wilson. Third harmonic generation microscopy. *Opt Express*, 3:315–324, 1998.

[10] D Yelin and Y Silberberg. Laser scanning third-harmonic-generation microscopy in biology. *Opt Express*, 5(8):169–175, 1999.

[11] A Zumbusch, GR Holtom, and XS Xie. Three-dimensional vibrational imaging by coherent anti-Stokes Raman scattering. *Phys. Rev. Lett.*, 82(20):4142–4145, 1999.

[12] P Tian and WS Warren. Ultrafast measurement of two-photon absorption by loss modulation. *Opt Lett*, 27(18):1634–1636, 2002.

[13] D Fu, T Ye, TE Matthews, G Yurtsever, and WS Warren. Two-color, two-photon, and excited-state absorption microscopy. *Journal of Biomedical Optics*, 12:054004, 2007.

[14] TE Matthews, IR Piletic, MA Selim, MJ Simpson, and WS Warren. Pump-Probe Imaging Differentiates Melanoma from Melanocytic Nevi. *Science Translational Medicine*, 3(71):71ra15–71ra15, 2011.

[15] Dan Fu, Tong Ye, Thomas E. Matthews, Benny J. Chen, Gunay Yurtserver, and Warren S. Warren. High-resolution in vivo imaging of blood vessels without labeling. *Opt Lett*, 32(18):2641–2643, 2007.

[16] Sijia Lu, Wei Min, Shasha Chong, Gary R Holtom, and Sunney Xie. Label-free imaging of heme proteins with two-photon excited photothermal lens microscopy. *Appl Phys Lett*, 96(11):113701, 2010.

[17] C Y Dong, P T So, T French, and E Gratton. Fluorescence lifetime imaging by asynchronous pump-probe microscopy. *Biophys J*, 69(6):2234–2242, 1995.

[18] W Min, S Lu, S Chong, R Roy, GR Holtom, and XS Xie. Imaging chromophores with undetectable fluorescence by stimulated emission microscopy. *Nature*, 461(7267):1105–1109, 2009.

[19] L Luo, L Chen, ZR Qiu, XY Yu, DC Dai, JY Zhou, and J Kuhl. Measurement of femtosecond resonant nonlinear refraction in Nd: YVO by degenerate pump-probe spectroscopy. *Journal of Applied Physics*, 89:8342, 2001.

[20] I Kang, T Krauss, and F Wise. Sensitive measurement of nonlinear refraction and two-photon absorption by spectrally resolved two-beam coupling. *Opt Lett*, 22(14):1077–1079, 1997.

[21] JK Wang, TL Chiu, CH Chi, and CK Sun. Nonlinear refraction and absorption measurements with chirped femtosecond laser pulses: experiments and simulations. *Journal of the Optical Society of America B*, 16(4):651–661, 1999.

[22] Martin C Fischer, Henry C Liu, Ivan R Piletic, Yasmin Escobedo-Lozoya, Ryohei Yasuda, and Warren S Warren. Self-phase modulation signatures of neuronal activity. *Opt Lett*, 33(3):219–221, 2008.

[23] MC Fischer, T Ye, G Yurtsever, A Miller, M Ciocca, W Wagner, and WS Warren. Two-photon absorption and self-phase modulation measurements with shaped femtosecond laser pulses. *Opt Lett*, 30(12):1551–1553, 2005.

[24] AE Kaplan. Hysteresis reflection and refraction by a nonlinear boundary—a new class of effects in nonlinear optics. *JETP Lett*, 24(114):3.10, 1976.

[25] IC Khoo. Optical-thermal induced total internal reflection-to-transmission switching at a glass-liquid crystal interface. *Appl Phys Lett*, 40:645, 1982.

[26] RR Michael and CM Lawson. Nonlinear transmission and reflection at a dielectric-carbon microparticle suspension interface. *Opt Lett*, 17(15):1055–1057, 1992.

[27] GB Altshuller, VS Ermolaev, KI Krylov, MA Makarov, and LI Pavlov. Nonlinear reflection of picosecond pulses from a galss-liquid interface. *Optics Communications*, 56(2):131–135, 1985.

[28] PW Smith, JP Hermann, WJ Tomlinson, and PJ Maloney. Optical bistability at a nonlinear interface. *Appl Phys Lett*, 35:846, 1979.

[29] Jerome Mertz. *Introduction to optical microscopy*. Roberts & Company Publishers, Greenwood Village, CO, 2009.

[30] J. Beuthan, O. Minet, J. Helfmann, M. Herrig, and G. Müller. The spatial variation of the refractive index in biological cells. *Physics in Medicine and Biology*, 41:369, 1996.

[31] ZW Wilkes, S Varma, YH Chen, HM Milchberg, TG Jones, and A Ting. Direct measurements of the nonlinear index of refraction of water at 815 and 407 nm using single-shot supercontinuum spectral interferometry. *Appl Phys Lett*, 94(21):211102, 2009.

[32] S Nicola, AE Kaplan, and S Martellucci. Stable hysteretic reflection of light at a nonlinear interface. *Applied Physics B: ...*, 1989.

[33] Marvin Weber. *Handbook of Optical Materials*. CRC Press LLC, 2003.

[34] CR Mendonca, MM Costa, J Giacometti, FD Nunes, and SC Zilio. Nonlinear refractive indices of polystyrene films doped with azobenzene dye Disperse Red 1. *Electron Lett*, 34(1):116–117, 1998.

[35] JR Lakowicz, H Szmacinski, K Nowaczyk, KW Berndt, and M Johnson. Fluorescence lifetime imaging. *Analytical biochemistry*, 202(2):316–330, 1992.

CHAPTER 8

OPTOPORATION AND GENETIC MANIPULATION OF CELLS USING FEMTOSECOND LASER PULSES

In this chapter, we will report on our work on an optical technique for transfecting cells in a targeted manner. The introduction of a foreign gene–ranging from simple reporter genes, such as a fluorescent protein, to gene knockdown by siRNA vectors–is one of the most powerful tools available to molecular biology. However, chemically-induced membrane permeability techniques, such as the use of Lipofectamine™, do not allow for cellular targeting, and so are limited in their use to whole populations of plated cells. While other techniques, such as single-cell electroporation allow for cellular targeting, *in vivo* application of these techniques requires the insertion of probes into the tissue of interest and requires considerable technical prowess, as cellular targeting may require the reaching a single neuron with a micropipette tip after penetrating layers of overlying tissue! This challenge severely limits the number of cells that may be targeted, since each cell requires a separate insertion.

Optoporation–the process of creating an optically-induced transient pore in the cell membrane–circumvents both these limitations. Because there are no probes to be inserted (past the injection of plasmid into the extracellular matrix), cellular targeting may be performed in a "point-and-shoot" fashion by co-aligning imaging and ablation lasers. Moreover, because there are no probes to insert, targeting of multiple cells can easily be achieved on experimental time scales.

The experiments in this chapter were completed by Andrew Davis, a former undergraduate student in the lab. I assisted in this project by developing a mathematical model and aiding in quantitative data analysis, as well as providing guidance with respect to experiments and the scope of the paper. Other experimental and intellectual contributions were provided by Dr. Nozomi Nishimura, Dr. Moonsoo Jin, and of course, Dr. Chris Schaffer. The manuscript was jointly written by Andrew Davis, Chris Schaffer, and myself. We aim to publish a revised version of this

manuscript in the near future under the title (or similar):

Davis, AD Farrar, MJ, Nishumura, N, Jin, M and Schaffer, CB. Optoporation and genetic manipulation of cells using femtosecond laser pulses, 2012.

8.1 ABSTRACT

Femtosecond laser optoporation has emerged as a powerful approach to introduce membrane-impermeable exogenous molecules into targeted cells, and has been used extensively to transfect individual cells in culture. Despite this utility, only a narrow range of potential laser regimes for optoporation have been explored. In addition, the dynamics of the laser-produced membrane pores and the effect of pore behavior on cell viability and transfection efficiency remains poorly elucidated. We quantified the formation and resealing of transient pores in cultured cells after irradiation by tightly-focused femtosecond laser pulses in two distinct irradiation regimes: millions of low-energy pulses and two higher energy pulses. Acute pore resealing was found to be a reliable indicator of long-term cell viability in both regimes. Laser energies where cells could be reliably permeabilized and survive, and where targeted cells could be transfected, were determined for both irradiation regimes. We further quantified the pore radius and pore duration produced as a function of incident laser energy. These data showed that pore size was the governing factor in cell viability, regardless of which laser irradiation regime was used to produce the pore. Surprisingly, we found that for cells that successfully resealed, larger pores tended to reseal more quickly than smaller pores, essentially ruling out a passive resealing mechanism. These data provide a quantitative understanding of the formation of membrane pores after femtosecond irradiation and the dependence of the pore behavior on laser parameters

8.2 INTRODUCTION

Femtosecond laser optoporation has emerged as a powerful technique for introducing foreign genetic material into targeted cells and has been applied to a variety of cell types, *in vitro*. Previous studies [1–5] have optoporated cells using high-repetition rate trains ($\sim$80 MHz) of low energy ($\sim$1 nJ) near infrared (800 nm) laser pulses that were focused at high numerical aperture ($\sim$1.4 NA) onto the membrane of targeted cells for short durations ($\sim$40 ms). In this regime, nonlinear absorption of laser energy in the focal volume is thought to lead to the production of a low-density electron plasma that causes disruption of chemical bonds, release of free electrons, and the production of thermoelastic stress waves [6]. Over many pulses, these effects cumulatively cause a transient disruption of the cell membrane that has been used to allow exogenous dyes [2, 3], macromolecules [7], gold nanoparticles [5], or DNA plasmid [1–4] to enter the cell. In an appreciable fraction of optoporated cells, the pore in the cell membrane reseals, leaving the cell intact and healthy [8].

The possibility of translating femtosecond laser optoporation from an *in vitro* to an *in vivo* setting offers great potential as a technique for studying the pathogenesis of complex diseases in model organisms and for exploring genetic regulation of cell fate and behavior. Few existing approaches for *in vivo* transfection offer the possibility of physically targeting individual cells. For *in vivo* optoporation deep inside tissue, the laser energy will have to be increased to make up for scattering losses and deliver sufficient intensity to the focal volume to drive nonlinear absorption. However, thermal damage thresholds bound the average laser power that can be used, suggesting that lower-repetition rate laser sources, or even single pulses, may have an advantage for *in vivo* optoporation applications. The mechanism for membrane damage and pore formation, however, will likely be different when cumulative effects between successive pulses are no longer a factor [6]. For irradiation with a small number of pulses at low repetition rate, higher pulse energies will likely be necessary and will result in the formation of a high-density plasma at the laser focus through multiphoton

and avalanche ionization, leading to ablative damage and vaporization of material in the focal volume [9]. Such an ablative mechanism has previously been used to damage blood vessels in the brain of rodents as a means to model ischemic [10, 11] and hemorrhagic [11, 12] microstrokes. This ablative mechanism has not, however, been explored for cell optoporation and transfection, and optimal parameters in this irradiation regime need to be determined *in vitro* in order to establish the feasibility for future *in vivo* work. In addition, a more quantitative understanding of the membrane pore size that is produced for different laser parameters and the influence of pore size and dynamics on subsequent cell viability and transfection efficiency would be of great benefit to the field. Finally, although expression of exogenous DNA after optoporation has been extensively studied, the mechanisms for DNA plasmid entry have not been explicitly considered and may not be as simple as diffusion through the laser-created pore.

In this article, we explored femtosecond optoporation in cultured cells across two different laser irradiation regimes: irradiation with millions of low energy pulses, as has been used extensively in previous work, and irradiation with two higher energy pulses. By monitoring efflux of a small intracellular dye after optoporation and later measuring cell viability, we determined acute resealing of membrane pores to be a reliable indicator of long-term cell viability. We measured pore formation and cell viability as a function of laser energy for both irradiation regimes and found optimal parameters for cell-targeted DNA transfection and demonstrated $\sim$30% transfection efficiencies for both irradiation regimes. We estimated the size of the laser-produced pore from our data on dye efflux and found that pore size was the determining factor in cell viability for both low-energy, high repetition-rate pulse trains and higher-energy, isolated pulses. Surprisingly, we found that large membrane pores closed faster than small ones in cells that resealed, suggesting that active cell resealing mechanisms are likely. Finally, we found that fluorescently-labeled DNA plasmid accumulates over time on the cell membrane after optoporation with two higher energy pulses, suggesting the possibility of a novel mechanism beyond diffusion for plasmid entry into the cell. This

work builds a quantitative understanding of pore creation after optoporation across two laser irradiation regimes and sets the stage for future *in vivo* optoporation of targeted cells using low repetition rate lasers.

8.3 METHODS

8.3.1 Cell culture

Optoporation experiments were performed using adherent chinese hamster ovarian (CHO) cells that were grown to a sub-confluent monolayer in 35-mm glass-bottomed culture dishes coated with poly-d-lysine (MatTek Corporation, Ashland, MA) and placed in a humidified incubator with 5% CO2 / 95% air at 37° C. Growth media solutions were made using advanced Dulbeccos modified eagle medium (D-MEM) with 10% fetal bovine serum (Atlanta Biologicals, Lawrenceville, GA), 1% GlutaMAX^{TM} solution (Invitrogen, Carlsbad, CA), 1% Penicillin-Streptomycin (Invitrogen, Carlsbad, CA), and 50 μg/mL Gentamicin (Invitrogen, Carlsbad, CA). During optoporation and imaging experiments, the cells were placed in media consisting of D-MEM, 1% sodium pyruvate (Invitrogen), 1% GlutaMAX^{TM} solution, 1% Penicillin-Streptomycin, and 50 μg/mL Gentamicin. Imaging cells in this solution was necessary to avoid optical absorption of emitted fluorescence in the normal growth media by the pH indicator.

8.3.2 Two-photon excited fluorescence microscopy

CHO cells were imaged using a custom-built two-photon excited fluorescence (2PEF) microscope with two simultaneous fluorescent detection channels. Images were acquired using a Ti:Sapphire laser (MIRA-HP; Coherent, Inc., Santa Clara, CA) with 100-fs pulse duration, a central wavelength at 800-850 nm, and a repetition rate of 76

MHz. A 20X-magnification, 1.0-numerical aperture (NA) water-immersion microscope objective (Zeiss, Thornwood, NY) was used for all imaging. Fluorescence emission from green fluorescent molecules (green fluorescent protein (GFP), calcein-AM, fluorescein) was collected through a 517-nm bandpass filter with 65-nm bandwidth, while a 645-nm bandpass filter with a 70-nm bandwidth was used for red-emitting dyes (ethidium bromide, CellTrace™ calcein red-orange AM). Image series were acquired during optoporation and three-dimensional image stacks with 0.5-μm spacing in the axial direction were attained at baseline and after optoporation. Image processing and analysis were performed using ImageJ and custom scripts written in MATLAB (MathWorks: Natick, MA).

8.3.3 Cell membrane disruption using femtosecond laser systems

Targeted membrane disruption was performed using two laser systems. The first was a low repetition rate, high pulse energy Ti:Sapphire regenerative amplifier with 100-fs pulse duration, 1-kHz repetition rate, and 800-nm central wavelength (Legend-USP; Coherent, Inc., Santa Clara, CA). A polarizing beamsplitter cube was used to introduce this beam into the 2PEF microscope so that the pulses were focused at the center of the imaging field and in the 2PEF imaging plane, enabling real-time monitoring of optoporation dynamics. Laser energy incident on the cells was controlled by neutral density filters, and a fast mechanical shutter limited the number of pulses incident on each cell to two pulses. We also optoporated cells using pulses from the 76-MHz laser used for 2PEF imaging. The laser beam from the Ti:Sapphire oscillator was split so that one beam could be used for 2PEF imaging, while the second was aligned, as above, to focus at the center of the imaging field and in the imaging plane. Laser energy was varied using a half-waveplate/polarizing beamsplitter pair, and exposure time was

controlled to be 50 ms, corresponding to 3.8×10^6 pulses, with a mechanical shutter. In both cases, a mechanical stage with sub-micrometer motion control in three dimensions (Newport, Irvine, CA) enabled precise targeting of the laser focus to the edge of the plasma membrane of the cell.

8.3.4 CHO cell labeling with calcein dyes

We labeled CHO cells for 2PEF imaging using calcein-AM or CellTrace™ calcein red-orange AM (Invitrogen, Carlsbad, CA). Initially, calcein dyes are nonfluorescent due to an ester-bond attached group that both quenches fluorescence and makes the dye cell membrane permeable. Once inside functional cells, the intracellular esterases cleave the quenching group, producing a hydrophilic, membrane-impermeable fluorescent label in the cytoplasm of the cell. We added 5 μL of a 1 mg/mL Calcein-AM or CellTrace™ calcein red-orange AM dissolved in dimethyl sulfoxide (DMSO) to 10 mL of phosphate buffered saline (PBS). The growth media was siphoned and 2 mL of dye solution was added to each culture dish and incubated at room temperature for 45 minutes. For each assay, Calcein-AM or CellTrace™ calcein red-orange AM was chosen so this cytoplasm-labeling dye could be excited simultaneously with and the fluorescence emissions spectrally separated from other fluorescent species used in the assay (e.g., ethidium bromide or GFP).

8.3.5 Monitoring efflux of calcein dye after optoporation

The dependence of optoporation efficiency on laser parameters was evaluated by monitoring efflux of calcein dye from the cell after laser irradiation of the membrane. For calcein-AM, we used an 850-nm wavelength for 2PEF imaging. Dye efflux was quantified from images using custom scripts in MATLAB (MathWorks: Natick, MA). To

determine the fluorescence intensity as a function of time, which is directly proportional to dye concentration inside the cell, we outlined the targeted cell by hard thresholding to create a mask and calculated the average fluorescence intensity of the pixels within this mask over time. The mean background pixel intensity was subtracted off all data points. The baseline fluorescence was determined from the average across several frames taken before cell targeting. We established a detection threshold for dye efflux based on the fluctuations in fluorescence of controls cells (N = 83). Irradiated cells with a decrease in fluorescence intensity of more than twice the standard deviation of the fluctuations in control cells were defined as permeabilized.

8.3.6 Assessing cell viability after optoporation

To determine cell viability, cells were restained with 4-μM calcein-AM and 4-μM ethidium bromide (EtBr) 90 min after optoporation and were reimaged. Cells that exhibited increased fluorescence after calcein-AM restaining and exluded the membrane-impermeable, nucleic acid binding EtBr were interpreted to have intact plasma membranes that had resealed after optoporation and to have active intracellular enzymes and thus be alive and functional.

8.3.7 Measurement of volume change after optoporation

To assess changes in cell volume after optoporation, CHO cells were transfected with GFP and 2PEF image stacks were taken before and after optoporaiton. GFP-labeled cells were used instead of calcein-AM-labeled cells in order to minimize efflux of cytoplasmic fluorescent molecules after optoporation. Cells were transfected with pAAVeGFP via Lipofectamine^{TM} 2000 24 hours prior to optoporation. Approximately 2 μg of DNA plasmid was added to 750 μL OPTI-MEM (Invitrogen, Carlsbad, CA)

and 5 μL Lipofectamine solution was added to 750 μL OPTI-MEM in a separate tube. The two tubes were then combined, mixed gently, and incubated at room temperature for 20 min before the solution was added to the cells. Three-dimensional (3-D) 2PEF image stacks, with 0.5 μm spacing between sections, were attained at baseline, 30 s, and 5 min after membrane irradiation. Volume analysis was performed using Volocity Imaging Software (PerkinElmer, Waltham, MA). The cell of interest was selected by hard thresholding and the cell volume was reconstructed from the 3-D image stack. Images of the volume projections were created using OsiriX Imaging Software. Volume measurements were made in cells where a hole was produced and the membrane resealed, and volume changes of non-targeted, control cells were assessed at the same time points.

8.3.8 Movement of labeled DNA plasmid after optoporation

In order to track DNA plasmid behavior after optoporation, we monitored the movement of fluorescently-labeled DNA plasmids in the extracellular solution after cell membrane irradiation. We used 20 μg/ml LabelIT® Plasmid Delivery Control (Mirus Bio, Madison, WI) labeled with fluorescein ($\sim$1 fluorescein molecule for every 20-60 bp of DNA plasmid). The 2.7-kb plasmid was not capable of protein expression due to the locations of fluorescein binding. Fluorescein-labeled plasmid was imaged using 800-nm excitation. The cells were labeled with CellTrace™ calcein red-orange. The 2PEF imaging laser intensity had to be increased in order to image the labeled plasmid, causing some photobleaching of the calcein red-orange dye. We quantified the intensity of labeled plasmid on the targeted patch of the plasma membrane after optoporation by monitoring the average fluorescence intensity over time. Two control experiments were performed. In the first control, localized increases in signal after optoporation due to, for example, autofluorescence were examined at the location of membrane irradiation in the absence of labeled plasmid. In the second control, labeled plasmid

accumulation in non-targeted cells was measured to establish a detection threshold for plasmid accumulation at the membrane of targeted cells.

8.3.9 Transgene expression

In order to transfect single cells using laser-based optoporation, DNA plasmids were prepared from transfected Escherichia coli cells using a Midiprep DNA Purification System (Qiagen, Valencia, CA). A 4.7-kb pAAVeGFP plasmid that coded for GFP was dissolved in clear growth media solution at a concentration of 10 μg/ml and applied to cell culture plates for the duration of the optoporation session. CellTrace^{TM} calcein red-orange AM was used to label the CHO cells, and 800-nm excitation was used for 2PEF imaging. We used femtosecond laser ablation to place distinguishing marks in the polystyrene culture dish underneath the targeted cells to facilitate later identification of specific cells. After each optoporation session, the plasmid solution was siphoned, normal growth media was applied, and the cells were stored in a humidified incubator at 37° C. Cells were imaged again using either 2PEF or wide-field fluorescence microscopy 24 and 48 hours after optoporation to monitor expression of GFP. To rule out double-counting of successfully transfected cells due to cell division, targeted cells were separated by at least 100 μm. Two cells expressing GFP in close proximity (e.g., less than 20 μm apart) 48 hours after irradiation were considered a single transfection event followed by cell division. To ensure the plasmid was functional, a Lipofectamine transfection reagent was used as a positive control. Negative controls were performed by leaving a solution containing plasmid and clear growth media in a cell culture dish for the length of the optoporation session without targeting the cells.

8.3.10 Statistics

Statistical comparisons were made using a two-tailed Fishers exact test (Figs. 1h and 5h). Results were considered significant when $p < 0.05$. All error bars shown in bar graphs (Figs. 1h, 2a-d, 3d, 5h, and 6f) represent 95% confidence intervals and were calculated using a binomial distribution. The boxplots (Figs. 1i and j, 3b and c, and 4d) display the 25thto 75th percentile (box), the median (red line), and data within 1.5 times the interquartile range from the 25th and 75th percentile (whiskers). Outliers were defined as points that fell outside the range denoted by the whiskers and are identified with a red "+" through the datapoint. Means were calculated without statistical outliers and are indicated by an orange "x" on the box plots. All means and standard deviations reported in the paper do not include statistical outliers.

8.4 RESULTS

8.4.1 Imaging dye efflux allowed quantification of pore creation and cell viability after optoporation

In order to identify optimal laser parameters for membrane pore creation, we tightly focused femtosecond laser pulses on the membrane of CHO cells labeled with calcein-AM and monitored the efflux of dye over time using 2PEF (Fig. 8.1a-c). We used two different exposure conditions: either two pulses from a 1-kHz repetition rate pulse train with pulse energies between 9 and 26 nJ (amplifier, see Fig. 8.1a-c), or 3.8×10^6 pulses from a 76-MHz pulse train with pulse energies between 0.4 and 1.3 nJ (oscillator). For both exposure conditions, cells that were permeablized exhibited an exponential decrease in fluorescence intensity immediately after targeting, indicative of pore creation (Fig. 8.1g). The fluorescence intensity then either stabilized, indicating

resealing of the pore, or continued to decrease, suggesting the laser-created pore did not reseal (Fig. 8.1g). Non-targeted cells served as controls and exhibited stable fluorescence intensity over time.

Ninety minutes after targeting, cells were stained with additional calcein-AM and with EtBr, then re-imaged and scored for cell viability (Fig. 8.1d). EtBr uptake and unchanged calcein-AM fluorescence (Fig. 8.1e) indicated cell death, while EtBr exclusion and increased calcein-AM fluorescence (Fig. 8.1f) suggested both an intact plasma membrane and functional esterase activity inside the cell, indicating a viable cell. All cells that were negative for EtBr also exhibited an increase in calcein-AM fluorescence. For both of the laser exposure conditions, over 90% of cells that resealed acutely were viable at 90 min (Fig. 8.1h). The total amount of dye efflux was higher for cells killed by permeabilization as compared to cells that survived for both amplifier (Fig. 8.1i) and oscillator (Fig. 8.1j) irradiation. However, permeabilized cells that remained viable after amplifier irradiation showed greater dye efflux, on average, than permeabilized, viable cells irradiated with the oscillator, and cells killed by amplifier irradiation showed much more dye efflux than those killed by oscillator irradiation (Fig. 8.1i and j). Because we found such a strong relationship between acute membrane resealing and cell viability at 90 min (Fig. 8.1h, $p = 1.0 \times 10^{-13}$ for amplifier, $p = 3.2 \times 10^{-10}$ for oscillator, Fishers exact test), we considered cells that resealed acutely as viable in all subsequent analyses.

The threshold for membrane permeabilization with amplifier irradiation was 9.5 nJ and the percentage of permeabilized cells increased to 100% at the highest energies used, although cell viability decreased sharply for pulse energies higher than 14 nJ (Fig. 8.2a). For the oscillator pulses, our threshold for permeabilization of 0.65 nJ agreed well with previous reports [2,3]. The percentage of permeabilized cells increased more gradually with increasing energy for the oscillator pulses as compared to the amplifier irradiation, while cell viability decreased significantly only at the highest pulse energies used (Fig. 8.2b). The fraction of cells that are successfully permeabilized and remain viable reached a maximum of 45% for 12 nJ pulse energy for the amplifier irradiation

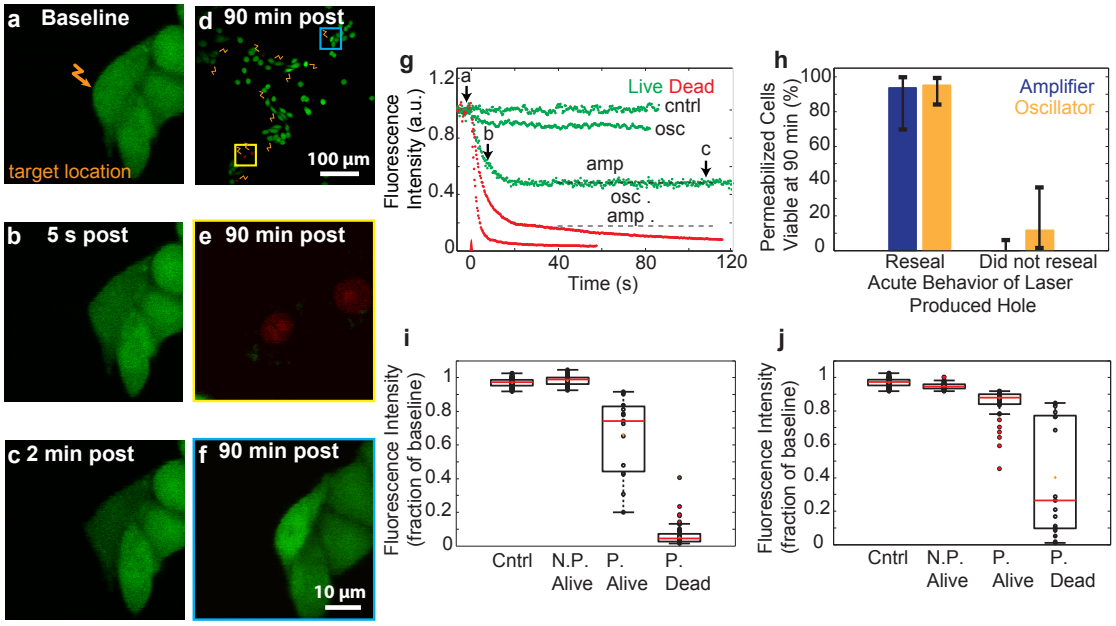

Figure 8.1: Pore formation and cell viability after femtosecond laser irradiation. CHO cells were irradiated with femtosecond pulses (2 pulses; 14 nJ) at the plasma membrane (a, *arrow*) and calcein fluorescence intensity (*green*) was monitored over time (b,c). Multiple spatially separated cells were irradiated (d, *arrows*). Application of calcein-AM and EtBr (*red*) 90 minutes after optoporation produced EtBr-labeled nuclei in dead cells (e). Live cells showed no EtBr labeling and exhibited an increase in calcein fluorescence (f). Fluorescence intensity was monitored as a function of time (g) for cells targeted with either the amplifier (amp; 2 pulses, 1 kHz) or oscillator (osc; 3.8×10^6 pulses, 1 MHz) sources at various energies. Cells with final intensities approaching the noise floor had failed to reseal (red), while cells with stabilized, constant intensity had regained membrane integrity (*green*). The labeled arrows along the green trace representing amplifier optoporation correspond to the fluorescence intensity at timepoints of the images in (*a-c*). Cell viability at 90 min. for holes that did and did not reseal acutely, for optoporation with each laser source (h). Fluorescence intensity after optoporation expressed as a fraction of baseline intensity was compared against cell permeabilization (permeabilized, P.; not-permeabilized, N.P.) and viability for cells irradiated with the amplifier (i) the oscillator (j). Cells with an intensity drop of two standard deviations below baseline intensity were considered permeabilized.

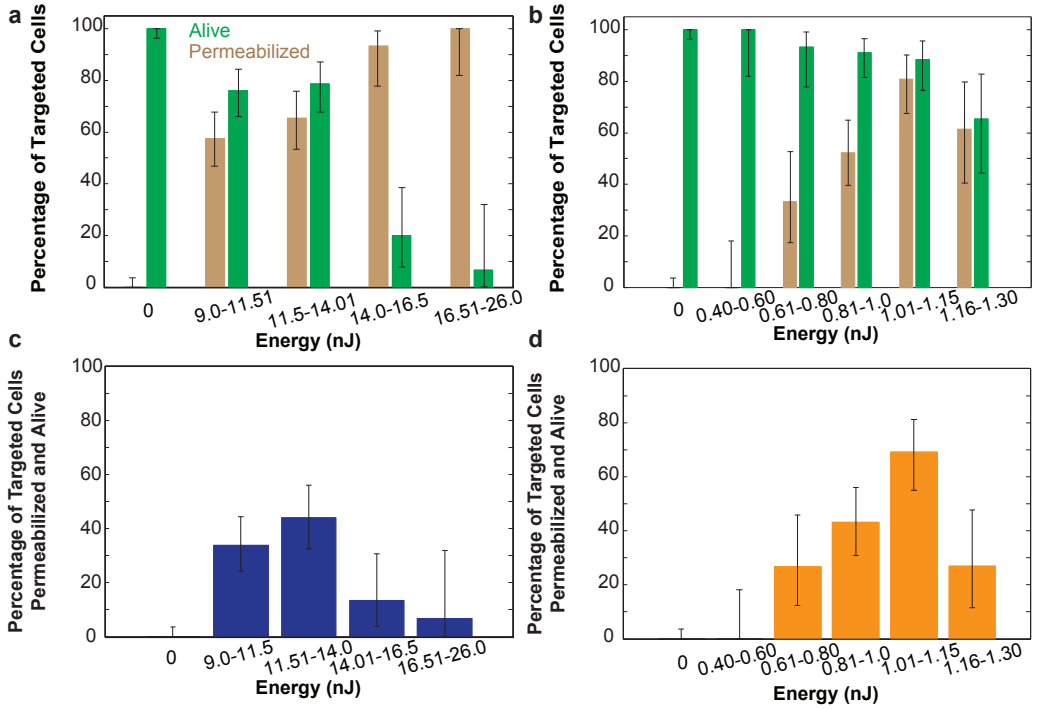

Figure 8.2: Cell viability and permeabilization probability as a function of irradiation energy.

The percentage of cells that were permeabilized and the percentage that were viable after irradiation, considered separately, across a range of energies for pulses from the amplifier (a) and oscillator (b). The percentage of cells that were both permeabilized and viable after 90 min. as a function of irradiation energy for amplifier (c) and oscillator (d) irradiation.

(Fig. 8.2c) and reached 70% for 1.0 nJ pulse energy for the oscillator irradiation (Fig. 8.2d).

8.4.2 Modeling of dye efflux after optoporation

A simple diffusion-based model was used to estimate laser-produced hole radii in both laser regimes. Briefly, we considered a laser-produced hole of radius r in the cell membrane that is much smaller than the cell diameter. We further assumed that the hole radius was constant in time while the pore was open, then rapidly closed. This model predicts the initial decrease in dye concentration, ϕ, inside the cell to be an exponential decay (see Section 8.6):

$$\phi(t) = \phi_0 \exp(-t/\tau) \tag{8.1}$$

where ϕ_0 is the initial concentration of dye within the cell and τ is the diffusive time constant for the hole. For viscosity, η_0, dye molecule radius of gyration, R_g, membrane thickness, e, cell volume, V_{cell}, temperature, T, and Boltzmann constant, k_B, τ is given by (see Section 8.6):

$$\tau = \frac{6\eta_0 R_g e V_{cell}}{k_B T r^2} \tag{8.2}$$

We fit the initial decay of fluorescence (linearly proportional to dye concentration) after optoporation to (8.1) and used (8.2) to determine the initial hole radius (Fig. 8.3a). We further estimated an effective hole opening time, t_{hole}, which was taken as the time it would take for the concentration to decay to the final value observed after membrane resealing, ϕ_∞, assuming a constant hole radius, i.e.

$$t_{hole} = \tau \log\left(\frac{\phi_0}{\phi_\infty}\right) \tag{8.3}$$

In both laser regimes, hole radii increased with increasing laser energy, and holes produced with the 1-kHz laser were larger, on average, than holes produced with the 76-MHz laser (Fig. 8.3b and c, respectively). In the optimal energy range for the amplifier pulses where the greatest percentage of targeted cells were permeablized and

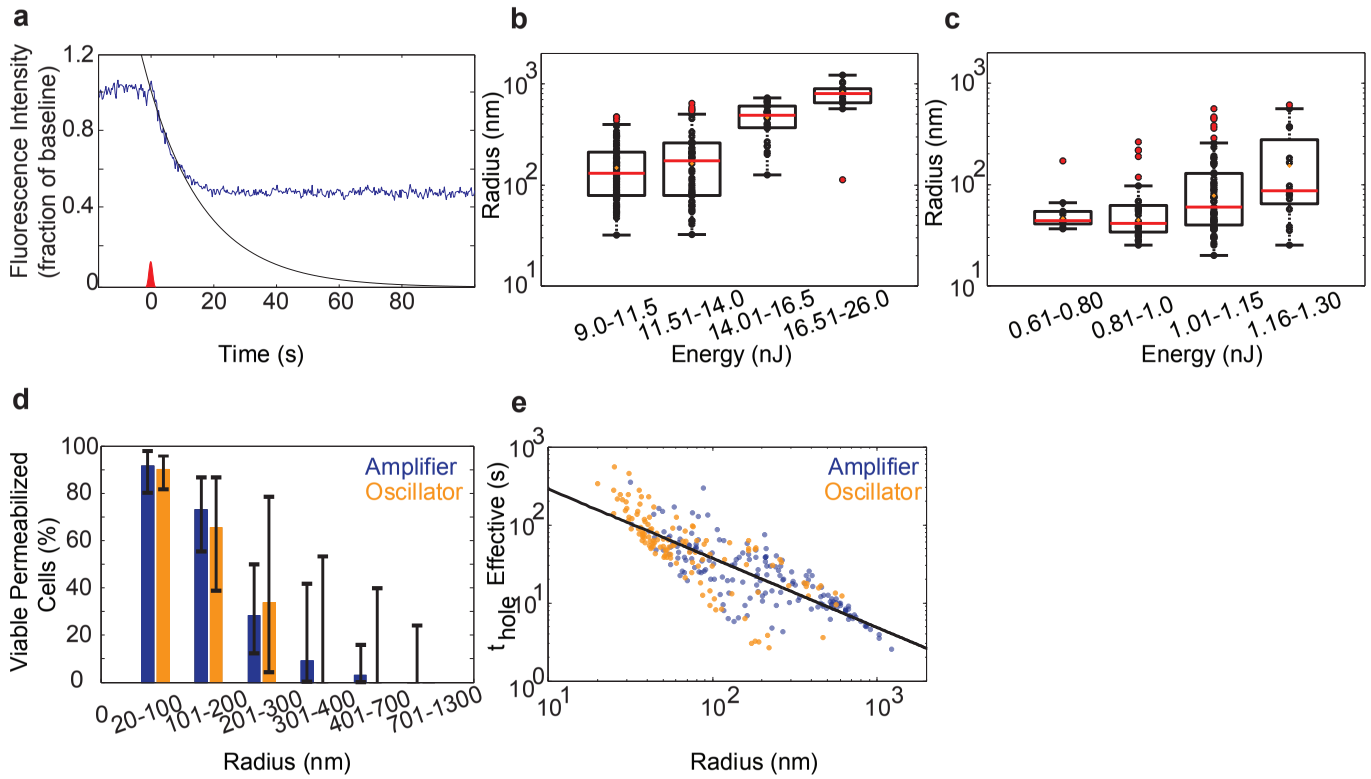

Figure 8.3: Quantification of membrane pore size and opening time.

Fitting (*black curve*) of the initial decay in intracellular fluorescence intensity (*blue trace*) after optoporation (a) was used to determine the radius of the membrane pore across a range of energies for both amplifier (b) and oscillator (c) pulses. Cell viability decreased with increasing pore radius for both amplifier and oscillator irradiation (d). Paradoxically, the effective time the pore was open, thole decreased with increasing pore size (e). A power law given by (8.4) was fit to the data.

viable (∼12 nJ), the hole radii were 160 ± 115 nm (mean +/- std. dev.). For the oscillator pulses at optimal energy (∼1.0 nJ), the holes had radii of 77 ± 55 nm. Hole radius was a strong predictor of cell viability for both amplifier and oscillator pulses (Fig. 8.3d).

We found phenomenologically that the approximate duration the pore was open, t_{hole}, scaled as a power law with the initial radius (Fig. 8.3e):

$$t_{hole} = ar^{\gamma} \tag{8.4}$$

where a and γ were determined by a least squares fit. We found $a = 4.0 \pm 3 \times 10^4$ s and $\gamma = -1.60.2$ where r was measured in nm. Surprisingly, larger holes were observed to reseal more quickly in optoporated cells that remained viable.

8.4.3 Cell volume transiently increased after optoporation

Cells expressing GFP were irradiated using optimal energy ranges and three-dimensional 2PEF stacks were taken at baseline, 30 s, and 5 min after irradiation to determine changes in cell volume that resulted from optoporation. Cells exhibited a protrusion at the target location on the membrane for both the amplifier and oscillator laser pulses shortly after membrane irradiation, which then retracted back over time (Fig. 8.4a-c, amplifier example). On average, the protrusion produced by the amplifier was larger than that produced by the oscillator, resulting in a larger volume increase after irradiation (Fig. 8.4d).

8.4.4 DNA plasmid accumulated on the plasma membrane of cells targeted with amplified laser pulses

To understand the movement of DNA plasmids after optoporation, we irradiated cells in the presence of fluorescently-labeled DNA plasmid. Cells targeted with

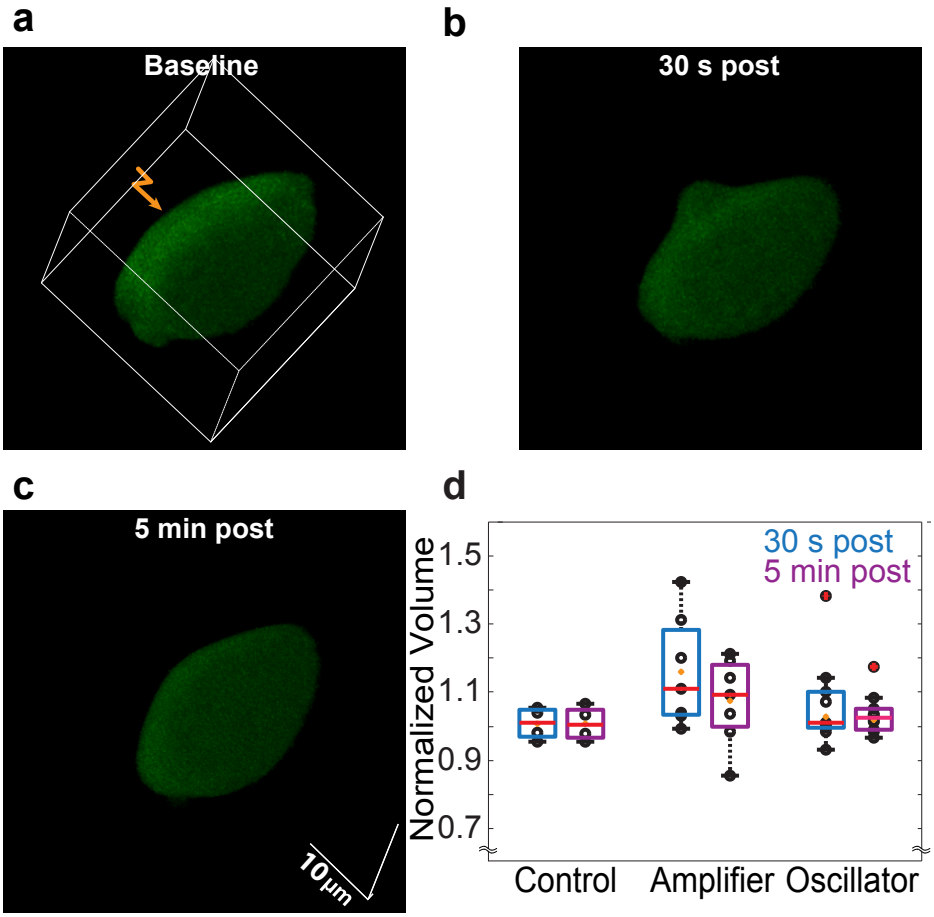

Figure 8.4: Cell shape and volume changes after optoporation.
Three-dimensional image stacks were used to compute cell volumes before and over time after optoporation (a-c). Images correspond to optoporation with 2 pulses of 12.0-nJ energy from the amplifier. Changes in cell volume over time for control cells and cells optoporated with amplifier or oscillator laser sources (d).

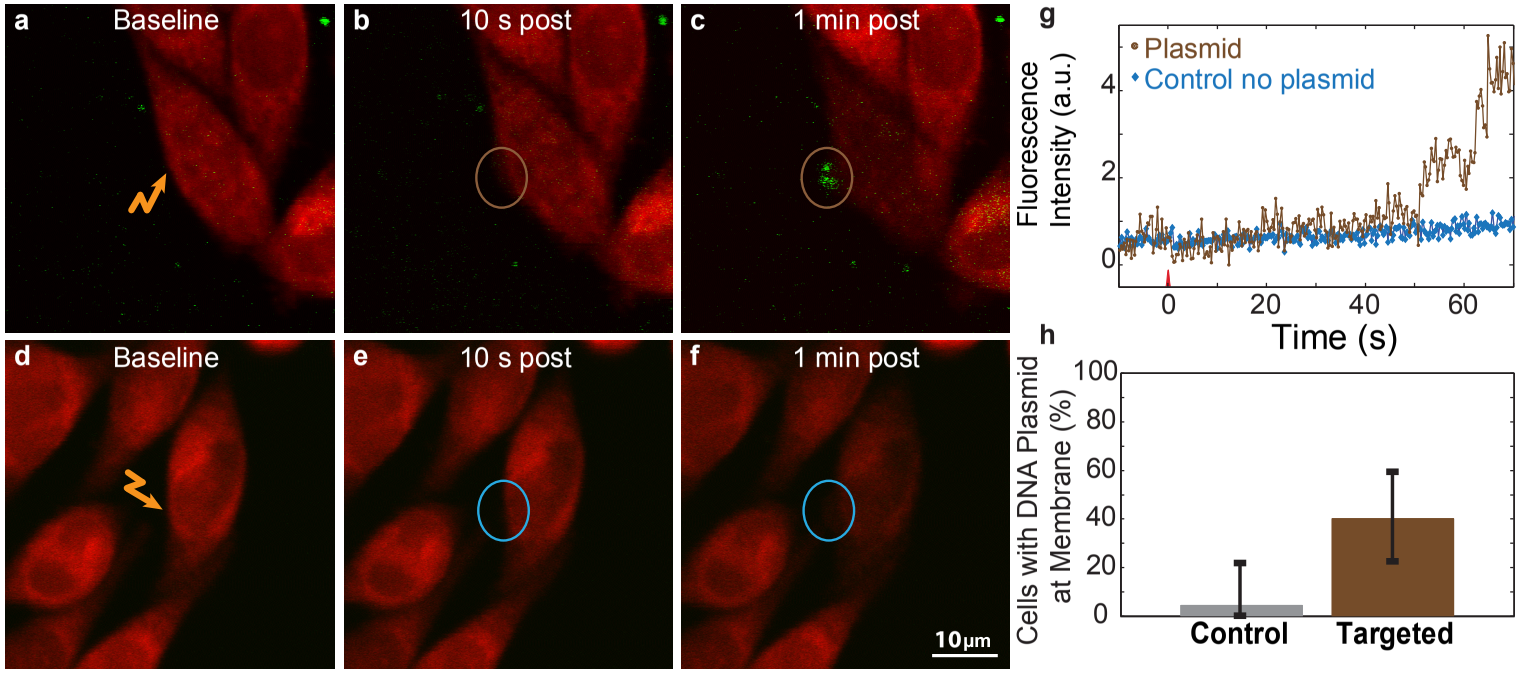

Figure 8.5: Accumulation of DNA plasmid on the irradiated section of the cell membrane.
Fluorescently-labeled DNA plasmid (*green*) accumulated at the site of irradiation (2, 12-nJ pulses from the amplifier) along the plasma membrane of cells (labeled with calcein red-orange (*red*)) (a-c). No increase in fluorescence intensity at the targeted site was observed in cells irradiated without labeled plasmid present (d-f). The accumulation of labeled plasmid occurred slowly over time (g). The fraction of cells that exhibited accumulation of labeled plasmid at the membrane for cells that were (*targeted*) and were not (*control*) optoporated with amplified pulses (h).

the amplifier exhibited increased fluorescence at the site of membrane irradiation, suggesting membrane accumulation of DNA at the irradiated location (Fig. 8.5a-c). In comparison, cells irradiated by amplified pulses in the absence of labeled plasmid showed negligible increase in fluorescence (Fig. 8.5 e-g). Plasmid accumulation at the plasma membrane began about 20-60 s after membrane irradiation (Fig. 8.5d). Forty percent of cells (12 of 30) irradiated in the presence of labeled DNA plasmid exhibited a localized increase in fluorescence at the irradiated site on the membrane, while only 4% of cells that were not irradiated showed an increase (Fig. 8.5h; $p = 0.004$, students t-test) The signal to noise of 2PEF imaging of the labeled plasmid was not sufficient to resolve plasmid entry into the cell. In control experiments with the oscillator, we observed a localized increase in autofluorescence at the target location on the plasma membrane, which precluded similar measurements of DNA plasmid movement after oscillator-based optoporation.

8.4.5 Single cells were transfected using both laser systems

Single cells were optoporated in the presence of a DNA plasmid that coded for the production of GFP, and expression was assessed at 24 and 48 hours after optoporation. Both single cells (Fig. 8.6a, amplifier example) and cells that had divided post optoporation (Fig. 8.6b and c, oscillator example) were observed after single cell transfection for each laser system. The transfection efficiency, defined as targeted cells that both survived and expressed GFP, was approximately 25% (30%) for the amplified (oscillator) laser pulses when using the optimal energies determined above (Fig. 8.6d). The spontaneous transfection without laser irradiation was negligibly low (< 1 in 10^6 cells).

8.5 DISCUSSION

We investigated pore dynamics and cell viability after femtosecond laser optoporation with two different laser irradiation regimes: a train of millions of low-energy pulses at high repetition rate (the dominant approach in previous work) and two higher-energy, isolated pulses. The mechanisms that lead to pore formation are quite different in these two regimes, with cumulative damage across many pulses arising from low density plasma dominating in the former case and ablative damage from a high density plasma by each pulse governing the latter [6]. We identified optimal laser parameters for optoporation in both regimes, defined by both successful permeabilization of the membrane and viability of the cell. We found that cell viability after optoporation, indicated by both enzymatic function and membrane integrity at 90 min. after irradiation, was completely dependent on resealing of the laser-produced pore over 10 s after irradiation for both laser irradiation regimes. Using trains of low-energy pulses, the laser energy we identified for optimal rates of optoporation ($\sim$1 nJ) agrees well with that found in previous work for similar focusing conditions and exposure times [3], and successful pore formation was achieved in about 70% of targeted cells[1]. The 12-nJ pulse energy found to be optimal for isolated, higher-energy pulses is above the breakdown threshold for water at the 1.0-NA focusing used here, supporting an ablative mechanism for pore formation. In this case, a lower fraction of targeted cell, about 45% were successfully optoporated, and cell viability dropped rapidly with increases in pulse energy above the optimal range.

By carefully measuring and modeling the efflux of a small dye out of optoporated cells, we quantified the size and dynamics of the laser-created pore. For both irradiation regimes, the pore size increased with laser energy. Pore size was, on average, about twice as large at the energy associated with optimal optoporation for higher-energy, isolated pulses (160-nm radius) as for trains of low-energy pulses (80-nm radius). For the same hole radii, however, the two irradiation regimes resulted in a similar

[1]Pore formation was assayed by dye leak-out, independent of DNA transfection.

percentage of cells permeabilized and viable. Collectively, these data suggest that the total area of the laser-produced pore, independent of the irradiation regime used to form it, dictated the acute resealing behavior of the pore and therefore the long-term viability of the cell.

Interestingly, the rate for successful DNA transfection was similar between the two laser systems, at about 30%. This suggests that a larger fraction of cells successfully optoporated with trains of low-energy pulses do not take up the DNA plasmid as compared to cells optoporated using isolated, higher-energy pulses. The DNA plasmid is much larger than the small molecule dye we used to indicate permeabilization, and we found that the average pore size created with trains of low-energy pulses is smaller than that produced with isolated, higher-energy pulses. Taken together, this suggests that perhaps pore sizes were on the small side for successful entry of enough DNA plasmid into the cell when optoporated with trains of low-energy pulses. In any case, the $\sim$30% transfection rate agrees well with recent experiments that carefully quantify transfection rates.

Although we ignore any dynamic changes in the pore radius in our model (until it is assumed to rapidly snap closed), our predictions for initial dye efflux agree well with experimental data. Our model proposes diffusion as the transport driver, allowing us to make quantitative predictions about the rates of transport of different solute molecules. For example, we observed significant efflux of calcein dye molecules, but a much more limited transport of GFP protein, which has a larger radius of gyration (data not shown). In fact, the GFP efflux was below the detection threshold for optoporation with a train of millions of low-energy pulses. In contrast, efflux of GFP was observed after optoporation with isolated, higher-energy pulses, consistent with the larger pore radius produced. From the pore size estimates based on calcein efflux, we were able to predict the amount of GFP efflux experimentally observed (data not shown), confirming that diffusion is the dominant driver of solute transport through the pore.

As mentioned above, our model is limited compared to previous models by Puc et al. [13] and Wang et al. [14] because it did not account for hole resealing dynamics.

Incorporating a robust theory of the pore dynamics is difficult, however, because more is at play than passive membrane dynamics. Previous research by Brochard-Wyart et al. [15] and Karatekin et al. (2003) described the dynamic behavior of transient pores in giant unilamellar vesicles. A complete explanation was achieved by considering competing effects of surface tension, line tension, and relaxation of the Laplace pressure by fluid leak out through the transient pore. Importantly, such models predict a pore lifetime that is an increasing function of initial pore size. In stark contrast, we find that larger pores actually close faster in cells that successfully resealed after optoporation. This result strongly suggests that the passive sealing processes used to describe the pore dynamics in vesicles will be inadequate for cells. Indeed, other researchers have shown that resealing of transected neurites is a calcium-mediated, active process [16]. We note, however, that there is some selection bias in our results, as we must only include cells that did successfully reclose in this analysis and it is possible that for larger diameter pores, only the ones that reclosed quickly were able to reclose at all.

The mechanism for DNA plasmid entry into optoporated cells has been assumed to be diffusion. From our measurements, we have excellent estimates of the radius of the pore and the duration the pore is typically open. We calculated how many plasmids of 4.7 kb would diffuse into the cell as a function of pore size, assuming the size-dependent pore duration derived from our data and shown in Fig. 8.3e. We find that, for the 100 nm pore size associated with optimal optoporation efficiency that the concentration of DNA plasmids inside the cell will be only about 10^{-3} of the extracellular concentration (Fig. 8.7). For typical concentrations of plasmid used in these experiments, this suggests that just a few copies of the DNA enter the cell. This should be compared to the hundreds to thousands of copies of DNA plasmid that are estimated to enter the cell using electroporation or reagents like Lipofectomine. Because of intracellular barriers that degrade or block cytoplasmic DNA from reaching the nucleus and expressing, it is unclear that just a few plasmids entering the cell via. diffusion is sufficient to drive transgene expression.

Under irradiation with higher-energy, isolated pulses we found that DNA plasmid

accumulates on the plasma membrane at the irradiated site (Fig. 8.5). Several factors may play a role in this. First, the cell strongly depolarizes after optoporation [3], lowering the barrier for negatively-charged DNA to adhere to the cell membrane. Second, the ablated patch of the cell membrane likely requires some time, perhaps long after the pore has resealed, to fully regain a normal complement of proteins and to otherwise regain normal structure and function. This, in turn may create a permissive environment for DNA to adhere at the damaged spot. Over time, the DNA adhered to the cell membrane would likely be endocytosed, thus providing an alternative mechanism for DNA plasmid entry after optoporation. Because of signal-to-noise limitations, we were, unfortunately, unable to follow the DNA that adhered to the cell membrane over time to see if it was endocytosed. It is possible that a similar accumulation of DNA at the irradiated site of the membrane occurred when we targeted cells with a train of millions of low-energy pulses, but we were unable to resolve the DNA plasmid accumulation at the membrane after irradiation in this regime due to a localized increase in autofluorescence at the target location on the membrane that would mask the signal from DNA accumulation. A similar mechanism was observed for electroporation mediated DNA entry, with DNA plasmid sticking to the plasma membrane and then being endocytosed into the cell about 30 min. later [17]. The plasmid accumulation on the membrane only occurred at the electropermeabilized side of the cell facing the cathode. Our observation of plasmid interaction with the targeted patch of the plasma membrane may suggest common mechanisms for plasmid entry in optoporation and electroporation. If delayed endocytosis is, in fact, a mechanism for DNA entry, this would have implications for the best choice of parameters for laser transfection. Perhaps many small patches of membrane that are rendered sticky for DNA by irradiation would provide higher transfection efficiencies.

In conclusion, we have built on a quantitative understanding of pore creation and resealing after optoporation across two distinct regimes of irradiation with femtosecond lasers. In addition, we have identified mechanisms for DNA plasmid entry after optoporation that rely on DNA adherence to patches of cell membrane altered by

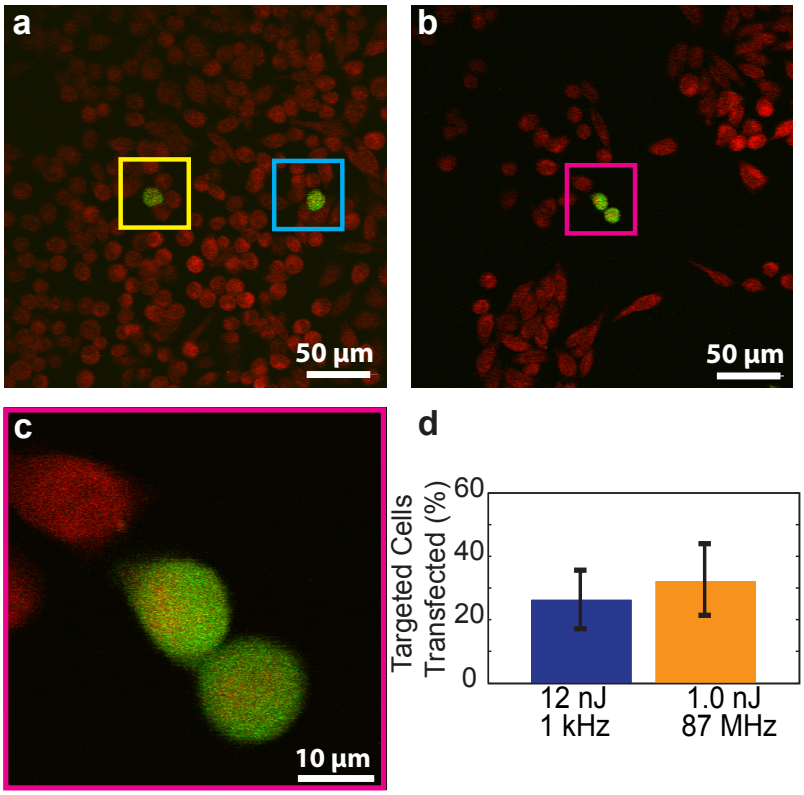

Figure 8.6: Transfection of cells with oscillator and amplifier laser pulses. Cells were targeted in media containing plasmids coding for eGFP. Cells were targeted with either two 12-nJ pulses from the amplifier (a) or 3.8×10^6 1.0-nJ pulses from the oscillator (b,c). All cells were labeled using calcein red-orange (*red*) with transfected cells expressing GFP (*green*). To avoid double counting due to cell division after transfection (b,c), cells were sparsely targeted (a). Transfection efficiencies were determined for both laser sources and were not statistically different (d).

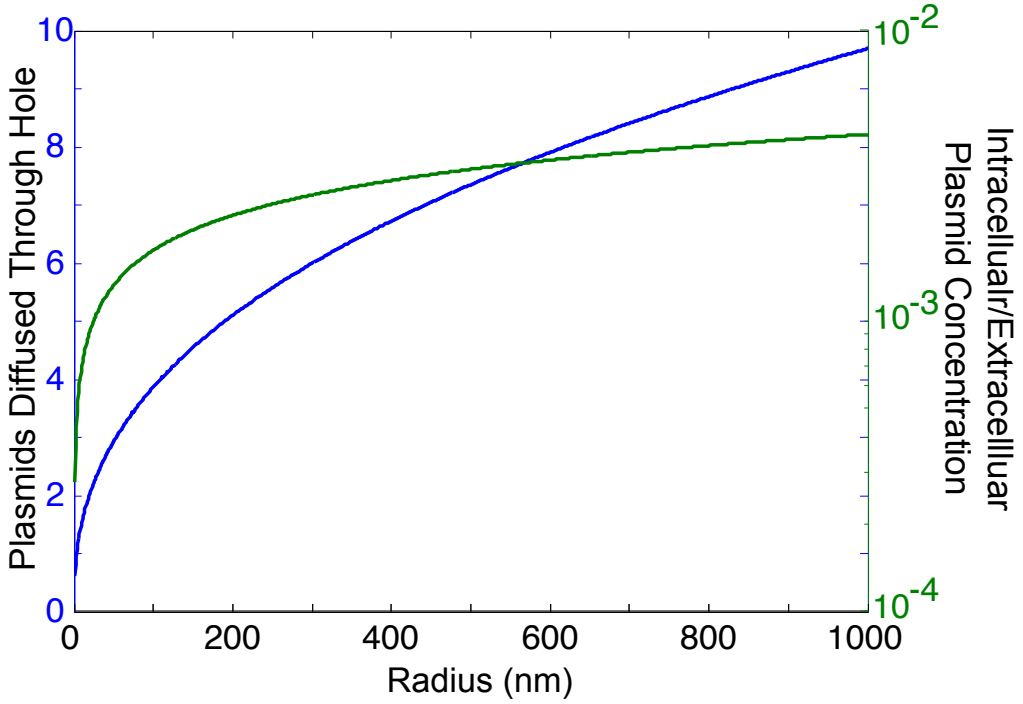

Figure 8.7: Calculated diffusive entry of DNA plasmids through laser-created pores. On the basis of the experimental fit for the time the pore remains open, t_{hole}, as a function of pore radius, r, and the dependence of the diffusion time, τ, on radius we estimated the intracellular DNA plasmid concentration in terms of the fraction of extracellular plasmid concentration (*green*; right-hand axis) assuming only diffusive entry. The blue curve depicts the number of plasmids that enter the cell (left-hand axis), for the extracellular plasmid concentration used in this work (10 μg/ml). Pore radii associated with optimal transfection efficiency were around 100-200 nm, predicting the entry of only 2-3 plasmid copies by diffusion.

irradiation and later endocytosis. Importantly, the demonstration of transfection using higher-energy, isolated femtosecond laser pulses in cultured cells sets the stage for future in vivo optoporation studies without the limitations of potential thermal tissue damage that would be likely when using a train of millions of low-energy pulses. We anticipate that these findings will be critical for the development of a minimally invasive, high fidelity transfection technique that can be used in vivo and has the potential to probe complex diseases through precise genetic manipulation of single cells in a living organism.

REFERENCES

[1] UK Tirlapur and K König. Cell biology - Targeted transfection by femtosecond laser. *Nature*, 418(6895):290–291, 2002.

[2] D Stevenson, B Agate, X Tsampoula, P Fischer, CTA Brown, W Sibbett, A Riches, F Gunn-Moore, and K Dholakia. Femtosecond optical transfection of cells: viability and efficiency. *Opt Express*, 14(16):7125–7133, 2006.

[3] J Baumgart, W Bintig, A Ngezahayo, S Willenbrock, H. Murua Escobar, W Ertmer, H Lubatschowski, and A Heisterkamp. Quantified femtosecond laser based opto-perforation of living GFSHR-17 and MTH53a cells. *Opt Express*, 16(5):3021–3031, 2008.

[4] Aisada Uchugonova, Karsten Koenig, Rainer Bueckle, Andreas Isemann, and Gabriel Tempea. Targeted transfection of stem cells with sub-20 femtosecond laser pulses. *Opt Express*, 16(13):9357–9364, 2008.

[5] Craig McDougall, David J Stevenson, Christian. TA Brown, Frank Gunn-Moore, and Kishan Dholakia. Targeted optical injection of gold nanoparticles into single mammalian cells. *J Biophotonics*, 2(12):736–743, 2009.

[6] A Vogel, J Noack, G Huttman, and G Paltauf. Mechanisms of femtosecond laser nanosurgery of cells and tissues. *Appl Phys B-Lasers O*, 81(8):1015–1047, 2005.

[7] F Stracke, I Rieman, and K König. Optical nanoinjection of macromolecules into vital cells. *J Photoch Photobio B*, 81(3):136–142, 2005.

[8] Cheng Peng, Robert E Palazzo, and Ingrid Wilke. Laser intensity dependence of femtosecond near-infrared optoinjection. *Phys. Rev. E*, 75(4):–, 2007.

[9] CB Schaffer, N Nishimura, EN Glezer, AMT Kim, and E Mazur. Dynamics of femtosecond laser-induced breakdown in water from femtoseconds to microseconds. *Opt Express*, 10(3):196–203, 2002.

[10] Nozomi Nishimura, Nathanael L Rosidi, Costantino Iadecola, and Chris B Schaffer. Limitations of collateral flow after occlusion of a single cortical penetrating arteriole. *J Cerebr Blood F Met*, 30(12):1914–1927, 2010.

[11] N Nishimura, CB Schaffer, B Friedman, PS Tsai, PD Lyden, and D Kleinfeld. Targeted insult to subsurface cortical blood vessels using ultrashort laser pulses: three models of stroke. *Nat Meth*, 3(2):99–108, 2006.

[12] Nathanael L Rosidi, Joan Zhou, Sanket Pattanaik, Peng Wang, Weiyang Jin, Morgan Brophy, William L Olbricht, Nozomi Nishimura, and Chris B Schaffer.

Cortical Microhemorrhages Cause Local Inflammation but Do Not Trigger Widespread Dendrite Degeneration. *Plos One*, 6(10):e26612, 2011.

[13] M Puc, T Kotnik, LM Mir, and D Miklavcic. Quantitative model of small molecules uptake after in vitro cell electropermeabilization. *Bioelectrochemistry*, 60:1–10, 2003.

[14] M Wang, O Orwar, and SG Weber. Single-cell transfection by electroporation using an electrolyte/plasmid-filled capillary. *Analytical chemistry*, 81(10):4060–4067, 2009.

[15] F Brochard-Wyart, PG De Gennes, and O Sandre. Transient pores in stretched vesicles: role of leak-out. *Physica A: Statistical Mechanics and its Applications*, 278(1-2):32–51, 2000.

[16] CS Spaeth, EA Boydston, LR Figard, A Zuzek, and GD Bittner. A Model for Sealing Plasmalemmal Damage in Neurons and Other Eukaryotic Cells. *J Neurosci*, 30(47):15790–15800, 2010.

[17] M Golzio, J Teissie, and MP Rols. Direct visualization at the single-cell level of electrically mediated gene delivery. *Proceedings of the National Academy of Sciences of the United States of America*, 99(3):1292–1297, 2002.

8.6 APPENDIX: Model of dye efflux from an optoporated cell

To model the efflux of cytoplasmic dye from a cell after optoporation, we used Ficks first law of diffusion, where the diffusion flux, $\mathbf{J}$, is given by:

$$\mathbf{J} = -D\nabla\phi \tag{8.5}$$

where D is the diffusion constant. We approximated the gradient as being one-dimensional across the cell membrane, and we took the concentration of dye, ϕ, inside the cell to be uniform at all times and positions within the cell. We further approximated the derivative as a finite difference over the membrane thickness, e:

$$\frac{d\phi}{dx} \approx \frac{\Delta\phi}{\Delta x} = \frac{\phi}{e} \tag{8.6}$$

The change in the number of dye molecules, N, inside the cell was equal to the flux through a pore of radius, r:

$$\frac{dN}{dt} = \mathbf{J}\pi r^2 \tag{8.7}$$

Dividing by the cell volume, V_{cell}, and using (8.5) and (8.6), we have:

$$\frac{d\phi}{dt} = -\frac{D\pi r^2}{eV_{cell}}\phi \tag{8.8}$$

Assuming a constant radius for the pore, this equation is integrated to give:

$$\phi(t) = \phi_0 \exp(-t/\tau) \tag{8.9}$$

where ϕ_0 is the initial concentration of dye within the cell and τ is the diffusion time constant for the pore and is given by, $eV_{cell}/D\pi r^2$. From the Stokes-Einstein relation,

$$D = \frac{k_B T}{6\pi\eta_0 R_g} \tag{8.10}$$

where η_0, is viscosity, R_g is the radius of gyration of the molecular, T is temperature, and k_B is the Boltzmann constant, we arrive at,

$$\tau = \frac{6\eta_0 R_g e V_{cell}}{k_B T r^2} \tag{8.11}$$

We fit the initial decrease in cellular fluorescence (which is proportional to the concentration) to (8.9). Using $R_g = 0.6$ nm for calcein dye, $\eta_0 = 1$ cP (nominal value for water), $e = 10$ nm (nominal membrane thickness), $k_B = 1.38 \times 10^{23}$ J•K^{-1}, $T = 298$ K, and $V_{cell} = 1.2 \times 10^3$ μm^3 (based on volume measurements from image stacks), we use (8.11) to determine the initial hole radius, r.

CHAPTER 9

CONCLUDING THOUGHTS AND FUTURE DIRECTIONS

9.1 Summary and Reflection: Are we any further ahead?

At the end of one's doctoral training, it is instructive to pause and ask what has been accomplished throughout one's years of study. And so, the question hangs, "What have we learned through considerable investment of time and resources?"

First, we have demonstrated label-free third harmonic generation (THG) imaging of myelin, a key central nervous system (CNS) component that is notoriously difficult to image using exogenous labeling strategies. The value of this work was impressed upon me only lately in both email and phone conversations with Dr. Benjamin Odermann, a recently hired faculty member at the University of Bonn, Germany. He is a neuroscientist who has seen the value of modern microscopy techniques, and was particularly interested in using THG imaging of myelin as an assay in his laboratory for studies in zebrafish models. It is truly exciting to see the development of a technique start to progress from a technical demonstration to routine experimental assay. It is my hope that others follow suit in adopting this technique to study myelin-associated diseases of the central nervous system, including multiple sclerosis (MS) and demyelination of axons in an injured environment, such as spinal cord injury (SCI).

Whereas our studies of THG imaging of myelin have gained in interest over time, our studies of longitudinal spinal cord injury have had considerable interest even prior to publication. Our poster presentation at the 2010 Society for Neuroscience Annual Meeting engendered considerable interest. Manuscripts and parts drawings were provided wherever requested, and studies using our chamber and procedure are already well under way. For example, Daniel Côté at Laval University, Québec, Canada has adopted our technique for CARS studies of experimental autoimmune encephalomyelitis (EAE), the leading murine model of MS. Since MS is accompanied

by motor loss and paralysis, our chamber has not only provided the ability to perform longitudinal imaging, but also has aided in preventing accidental and potentially confounding SCI resulting from unavoidable compromised vertebral integrity caused by laminectomy. As was outlined in Chapter 2, the ability to perform time-lapse imaging of the spinal cord is invaluable to studies of disease dynamics and therapeutic efficacy, and our chamber has dramatically improved the ability to achieve this goal. It is our hope that this chamber will receive widespread use by researchers across a broad range of spinal cord studies.

Our study on spinal cord blood flow and microvascular architecture is meant to fill a critical hole in our understanding of both healthy and injured spinal cord. From an evolutionary biology perspective, the similarities between mouse, rat, rhesus, and human spinal cords suggests a common evolutionary pressure driving the network structures we see. In particular, characterization of the network structure necessarily raises the question of what feature has been optimized, and subject to which constraints. For example, Corson [1] has presented a generalized flow network model which minimizes energy dissipation while facing the constraint of a fixed amount of "material" from which the vasculature is constructed. In his model, he accounted for fluctuating (as opposed to steady-state) sources and found that, under certain constraint parameters, the optimal network strongly resembled the tree-like transport structures found in biological systems. Under different sets of constraint parameters, net-like structures were observed to optimize the system. Similarly, the spinal cord, like the brain, requires constant high-rate perfusion and is able to autoregulate this perfusion [2] across a wide range of systemic blood pressures. However, this perfusion is also balanced by the high density of neurons requiring perfusion and the limited volume of the vertebral canal, suggesting that perfusion optimization subject to fixed volume constraints may apply here as well.

We have systematically mapped the spinal cord microvasculature, quantified vessel topological connections, and quantified network structure. We have also performed *in vivo* measurements of blood flow which have given insights into spinal blood drainage

and the ischemic susceptibility of the spinal cord to dorsal spinal veinous (DSV) occlusion. These findings provide a solid baseline and reference for future studies, which we will discuss in the next section.

To date, we have extensively verified the existence of a nonlinear optical reflection signal, laying the essential ground work for a new and exciting microscopy. As with all proposed nonlinear microscopies, the plethora of nonlinear mixing effects that are possible for a combination of input frequencies requires careful and methodical identification of any proposed technique. Our preliminary data have verified our predictions, providing the impetus to evaluate NORM as a true microscopy.

Finally, our work on optoporation brings a new level of understanding and optimization to a field which has relied primarily on phenomenological studies. We have systematically mapped transfection efficiency, cell viability, and transport kinetics across pulse energy for two diverse laser systems. Given the potential of optoporation for *in vivo* cellular transfection, it is essential to know optimal laser parameters in a controlled *in vitro* setting before proceeding to the complex milieu of tissue. In addition, the time required for *in vivo* animal preparations, including cranial or spinal surgery, plasmid microinjection, and subsequent imaging and transfection makes *in vivo* studies cost-prohibitive as an optimization platform. Thus, starting with an optimized system provides the necessary parameters with which to begin *in vivo* trials, the subject of another current PhD student's thesis.

To answer the question at the beginning of this section, I believe a resounding "yes" may be answered without special pleading. We have developed robust assays and experimental platforms for future studies of biological interest. These techniques are not esoteric findings or isolated to the expertise of one lab, but can be and are being implemented around the world, as evidenced by the requests we have received for drawings, parts, and recommendations. Within our own lab, they also serve to have opened doors to new and exciting studies, upon which I will now offer some insights and speculations.

9.2 Future Directions

9.2.1 THG Imaging of Peripheral Nerve

We have demonstrated that THG microscopy is a strong source of contrast for imaging myelin in the mouse CNS [3](Chapter 4). One surprising outcome of this study was that THG can be efficiently generated with low-NA objectives in myelin in both the CNS and peripheral (see Fig. 9.1) nervous system (PNS), enabling a large field of view (FOV) to be imaged (Fig. 9.1b). Moreover, since low-NA objectives have a large confocal parameter ($\sim$ 50 μm) compared to large-NA objectives ($\sim$ 1-2 μm), they are much less sensitive to motion artifact, a feature which is of value in a clinical setting. Nevertheless, THG can also be generated using large NA objectives, which allow for greater optical sectioning and detailed resolution (Fig. 9.1d,e) where desired.

One potential application of low-NA THG imaging of PNS myelin is in prostate cancer surgery. According to the American Cancer Society [5], over 240 000 cases of prostate cancer (CaP) will be diagnosed in the United States in 2012, resulting in over 28 000 deaths. To date, radical prostatectomy remains the gold standard of care [6]. Unfortunately, this procedure causes damage to or loss of the cavernous nerve, resulting in erectile dysfunction (ED). Procedures which attempt to spare neurovascular bundles (NVB) have seen a marked improvement in sparing of erectile function, yet still results in complete loss of function in nearly 25 % of patients, or limited recovery in almost half of patients [6] after 18 months of post-operative recovery. Limited recovery was seen between years 3 and 5, with the greatest improvement seen in cases of total ED [7].

In part, nerve preservation is hindered by the ability of the surgeon to visualize nerves in real time, as well as the conflicting requirements of NVB sparing and tumor margin mapping. Recent work using phage display [8] has been shown to robustly label peripheral nerves fluorescently in mice, although this technique requires considerable effort in isolation of the correct peptide fragment, and its associated cost of amplification

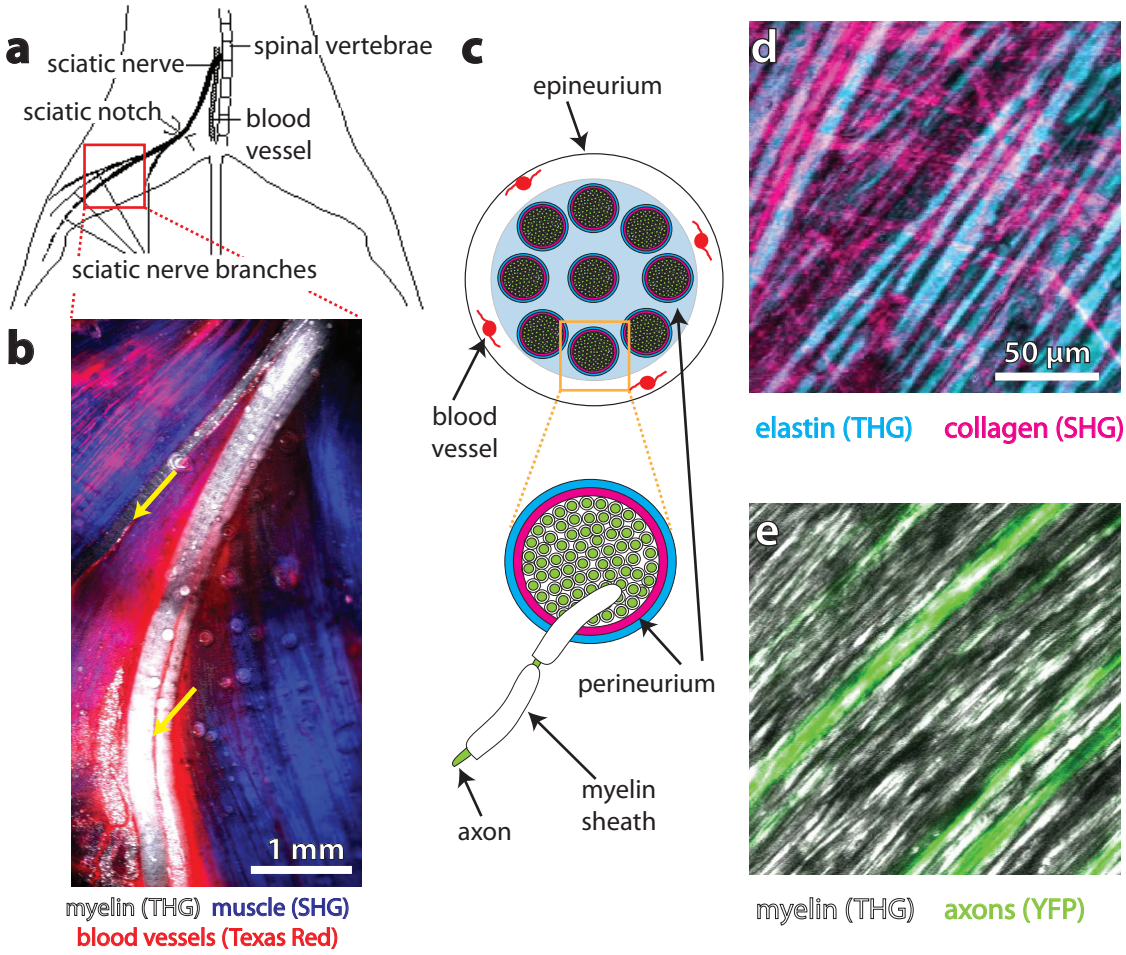

Figure 9.1: In vivo imaging of the mouse PNS.
Exposure of a mouse thigh (a) allowed for isolation of the sciatic nerve and its branches (a; box) [4], making possible low-NA objective imaging (b) of muscle (*blue*), sciatic nerve (*white*), and Texas Red-labeled blood vessels (red; yellow arrows) in vivo. Imaging of the nerve (c) using high resolution imaging showed collagen from SHG (*magenta*) and presumably elastin from THG (*cyan*) in the perineurium (d). Myelin from THG (*white*) and a subset of axons in a transgenic mouse expressing yellow fluorescent protein (YFP) imaged using 2PEF (*green*) enabled direct visualization of nerve bundles (e). Diagram in (a) is reproduced with permission from John Wiley & Sons, initially published as Weinstein, D. E. and Wu, R. 2001. Isolation and Purification of Primary Schwann Cells. Current Protocols in Neuroscience. 3.17.13.17.9.

to quantities sufficient for human dosing [4].. Coherent Anti-Stokes Raman Scattering (CARS) microscopy has also been demonstrated in ex vivo imaging of cavernous nerve [9] in human tissue. This technique relies on the high lipid content of myelin fibers

and the lipid-specificity of CARS imaging to outline the nerve. However, the extreme technical challenges associated with CARS microscopy make its clinical application difficult. In particular, CARS requires two synchronized, picosecond duration pulsed laser systems and very tight focusing to generate an image.

Because TH signal is generated from a single laser source, it is easily combined with other multi-photon imaging modalities such as 2-photon excited fluorescence (2PEF) and second harmonic generation (SHG). Neither SHG nor THG requires a resonant energy level to be produced, and both are produced by endogenous tissue structures without the need for exogenous dyes or labeling strategies. This property also makes THG non-invasive and cost-effective in a clinical setting. When combined with 2PEF and tumor-specific fluorescent labeling strategies [10] for margin mapping, a multi-modal endoscope that included THG for imaging myelin could provide a powerful surgical tool that both ensured appropriate margin mapping while maximizing NVB sparing. In fact, this very idea has been the subject of a recent grant proposal in collaboration with Dr. Chris Xu (Applied and Engineering Physics, Cornell University).

A first step in this process will be to perform imaging of whole mouse prostate and sciatic nerve in situ using a simultaneous combination of THG, SHG, and 2PEF. Since THG is produced effectively from myelin in the CNS [3], and we have demonstrated myelin imaging in the PNS, THG could be used specifically to visualize the cavernous nerve. However, unlike the CNS, fat storage in the periphery will also provide strong THG signal [11]. It will therefore be imperative to demonstrate that nerve can be distinguished morphologically and contextually. To do so, the use of transgenic animals expressing fluorescent reporter proteins in peripheral nerves would allow for co-localization of THG with labeled axon bundles. SHG of the surrounding collagen structures could also provide relevant context, such as the perineurium and/or muscle. Blinded identification of nerve from THG/SHG images will be compared to simultaneous 2PEF images with labeled axons.

Since THG is a coherent effect, THG signal does not saturate like 2PEF. However, it depends critically on laser pulse parameters. In general, THG image contrast is

improved when lasers with large pulse energy (30 nJ) and small (1-10 MHz) pulse repetition rates are used. In both cases, careful attention must be paid to linear (thermal) damage by tissue heating occurring at large average powers and nonlinear tissue ablation, which occurs at large pulse energies. In addition, since for 1040-nm excitation wavelength, the TH is in the near UV and UV-mediated damage must be considered.

To determine optimum laser parameters for imaging, it will be important to first evaluate THG contrast in sciatic nerve *ex vivo*. Characterization would need to include pulse repetition rates between 1 and 10 MHz with pulse energies up to the NA-dependent thermal and nonlinear damage thresholds. Pulses should be compressed to as short as possible to maximize peak power, which will improve signal strength but will not affect damage thresholds below 1 ps [12].

To evaluate the safety of the laser regimes, *in vivo* imaging of exposed sciatic nerve and cavernous nerve by continuously scanning the nerves for 1-hour at each set of high-contrast laser parameters can be performed. At the end of each session, exposed tissue could be excised, digested, and examined for DNA fragmentation using DNA electrophoresis. Positive identification of fragmented DNA is indicative of phototoxicity. In parallel, gross histopathology of excised tissue could be examined to look for acute structural photodamage. Laser parameters will then be chosen on the basis of maximum image contrast with minimal tissue damage.

To demonstrate the value of THG imaging for NVB sparing, studies in which a surgeon performed partial and radical prostactemoy in mouse models of CaP would be of value. Two models [13, 14] use simian virus 40 large tumor antigen (SV40-Tag) to selectively induce neoplasia in mouse prostate, closely resembling human CaP. Since these sites of neoplasia manifest themselves as early as 10 weeks, straight forward evaluation of NVB sparing in partial prostatectomies in early onset CaP and radical prostatectomies in late stage CaP is possible. Anterograde labeling of the cavernous nerve at the spinal nerve prior to animal sacrifice could be used to assess distal sparing of the cavernous nerve in both partial and radical prostatectomy models. In partial resections, quantitative scoring of end-point histological sections will be used to

determine surgical efficacy in terms of tumor margin mapping. Statistical comparisons between animals operated on with and without THG imaging will establish the value of this imaging modality.

Apart from humans, dogs are the only known species to spontaneously acquire CaP in an age-related manner [15]. For this reason and anatomical similarities, they have been used as a larger animal model of pre-clinical prostate surgery, especially with regards to NVB sparing [16–18]. As a follow-up study to mouse models of CaP, we propose to evaluate THG imaging of cavernous nerve as a surgical tool in canine models of radical prostatectomy.

9.2.2 Deep *In Vivo* Imaging in the Mouse Spinal Cord

We have demonstrated longitudinal imaging of the mouse spinal cord using a novel implanted chamber [19] (Chapter 5). However, due to the short scattering length of myelin, imaging depth has typically been limited to 50 μm or less. As a consequence, only axons from the dorsal root ganglia (DRG) in the most superficial layer of the spinal cord are routinely visible. This particular class of neuron has cell bodies outside of the spinal cord and sends projections both centrally and peripherally. With respect to regeneration, the neurons robustly regenerate processes on the peripheral side but do not on the central side. In fact, lesioning the peripheral projections of DRG 1-2 weeks prior to lesioning the central projections results in growth of centrally projected axons past the lesion site [20]. This dualistic nature of the DRG projections adds a confounding factor to regeneration studies, and raises questions about the transferability of therapeutic strategies developed for DRG axon regeneration to "purely central" neurons. Finally, since DRG send afferent, sensory projections only, treatment of DRG axons does nothing to mitigate the underlying paralysis.

In contrast, the corticospinal tracts (CSTs) [1] can have cell bodies in layer V of the primary motor cortex that extend all the way to motor neurons in the ventral horn of the spinal cord [21], fully contained within the CNS. These tracts are partly responsible for voluntary motor control and injury results in paralysis, making their regeneration of primary interest in SCI regeneration studies. For example, in rats, improved CST sprouting following administration of neurotophin-3 (NT-3) [22] and olfactory ensheathing cell transplantation have been seen [23]. Another study using Alzet osmotic pumps to deliver a humanized IN-1 antibody fragment showed CST regeneration across the lesion site with robust sprouting caudal to the lesion [24]. More recently, progress has been made in a mouse model of SCI by suppressing PTEN [25], resulting in regeneration of CSTs across a lesion site and the observation of new synapse formation. In all cases, these studies have relied on post-mortem histology to assess the extent of regeneration, losing critical information about the mechanism and dynamic interactions that have led to these results.

Another critical motor tract is the rubrospinal tract (RST), descending from the red nucleus and residing in the dorsolateral aspect of the mouse spinal cord [26, 27]. Sparing of these tracts is highly correlated with improved motor outcome [28], and pre-clinical studies [29–31] have shown that these tracts respond well to neurotrophic factors following injury.

Clearly, studies of CST and RST regeneration would benefit from the repeated, time-lapse imaging approach currently accessible to studies of DRG axons. However, the mouse dorsal corticospinal tracts (dCSTs) are located approximately 300-500 μm below the dorsal surface of the spinal cord [26] (see Fig. 9.2.2c), making their optical access without surgical damage to the spinal cord impossible. The RSTs are located more laterally and slightly closer to the surface ($\sim$200 μm), but still beyond multi photon imaging ranges. At the same time, invasive surgery would result in experimental

[1] As a rule, spinal tract nomenclature follows the rule that the first part of the word denotes the tract origin (i.e. cell body location) and the second part denotes the axonal destination. So, corticospinal means "from the cortex to the spinal cord", while spinothalamic tracts refer to projections of spinal cord neurons to the thalamus.

artifacts, including ischemic and inflammatory damage. One possibility for a minimally invasive surgery has been demonstrated in the rodent cortex by Chia et al. [32]. A right triangular prism with a mirror on the hypotenuse was inserted into the rodent cortex, effectively translating the imaging plane from xy to yz. Tissue disruption was limited to within 100 μm of the prism surface.

We have replicated this technique in the mouse spinal cord (Fig. 9.2.2) in conjunction with our spinal chamber described elsewhere [19]. Briefly, we used a triangular blade to create a small incision in the dorsal spinal cord just lateral of the mideline. A 1 mm x 1mm right triangular mirrored prism was inserted (Fig. 9.2.2a) into the spinal cord and sealed in place with Kwik-Sil elastomer, as for the spinal chamber. Subsequent imaging (Fig. 9.2.2 b-c) showed intact and well-perfused blood vessels just 50 μm from the site of insertion (Fig. 9.2.2d).

Using this technique, the maximum depth from the spinal cord surface that can be imaged is determined by the prism dimensions rather than the scattering length of the tissue, in this case, 1 mm. The lateral extent of imaging is set by the scattering length of the local tissue environment, and will vary depending on whether imaging is taking place in the gray matter or white matter, with the latter being much more scattering than the former. In our study, we implanted the prism facing the dCSTs. However, rotation of the prism by 180° would allow for similar imaging of the RST. Combining this technique with our imaging chamber extends the promise of longitudinal imaging to the more critical motor tracts.

However, this approach is not without its challenges. First, the dCSTs are a highly-myelinated set of axons in the dorsal spinal cord that sit at the boundary of the gray commissure. Thus, imaging *into* the dCST is bound to be limited by the same scattering limitations as imaging below the dorsal columns. Nevertheless, imaging of at least superficial dCST axons would present a considerable advance towards understanding motor pathway regeneration. Similar challenges exist for the RST, but their closer proximity to the gray matter [26] may allow a more distal placement of the prism, and thus less disturbance at the imaging site. Careful placement of both the prism position

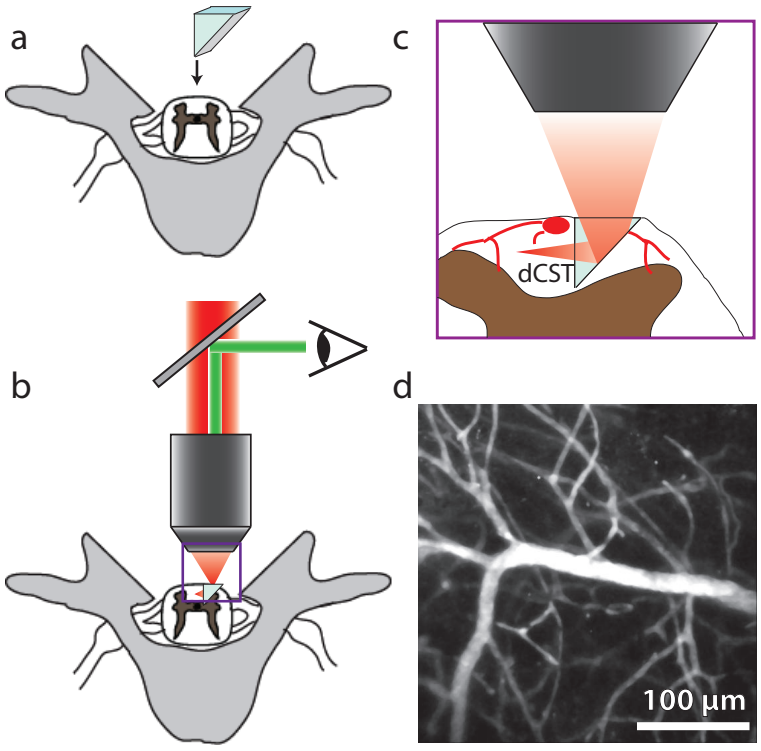

Figure 9.2: An implanted prism allows for deeper imaging in the mouse spinal cord. After exposing a vertebral segment by performing a dorsal laminectomy, a small incision in the spinal cord is made and a right isosceles triangle is inserted (a). Subsequent multi-photon microscopy (b) allows for imaging in the yz plane when scanning in the xy plane (c), potentially enabling access to the dorsal corticospinal tracts (dCSTs). We have currently demonstrated imaging of intact, perfused blood vessels (d) 1 day post-implantation.

and angle will be critical for optimum imaging.

Second, insertion of the prism itself will result in unavoidable SCI. This tissue disruption is also likely to carry a secondary injury response, including inflammation and potentially ischemia. Similar histological studies to those of Chia et al. [32] will need to be performed to assess the extent of tissue injury in the spinal cord. Any effect of the implantation on regenerative outcome will similarly need to be assessed.

Despite these challenges, deep imaging in the spinal cord is essential for probing motor recovery and pursuing therapies targeted at relieving paralysis. Depth limitations in the brain have been overcome by the use of implanted prisms [32] as well

as implanted microendoscopes [33], and extension of these techniques to the spinal cord is a natural and necessary next step for SCI studies.

9.2.3 Angle-Resolved Nonlinear Optical Reflection Microscopy (AR-NORM)

In our current construction of NORM (Chapter 7), signal is preferentially collected from normal incidence, with diminishing collection efficiency for off-normal angles of incidence. As a consequence, we anticipate image "shadows" in curved surfaces. There are two methods we could use to mitigate this problem.

First, we could introduce a displacement, δ, of the probe beam from the optic axis. For an objective of effective focal length, f, this would result in an incident angle given by

$$\theta = \arctan(\frac{\delta}{f}) \tag{9.1}$$

By scanning over a rage of δ, the extent of shadowing could be reduced, resulting in a truer representation of tissue structure.

Alternatively, we could replace our existing photodiode with a position-sensitive photodiode, (PDP90A; Thor Labs, Inc.). This sensor has sub-micron resolution, and any non-normal incidence would result in a detectable displacement of the reflected beam. This detection scheme would effectively achieve the same result as our first proposed scheme, except because we measure displacement, δ, directly, there is no need to scan. The image intensity, I_{RN} would therefore be renormalized according to

$$I_{RN} = \frac{I_0}{\cos(\theta)} = \frac{I_0}{\cos(\delta/f)} \tag{9.2}$$

where I_0 is the reflectance intensity. This change would be easily implemented and improve the interpretation of NORM images.

9.2.4 Improved Transfection Efficiency Using Polyethylene Glycol

In our studies of optoporation, we have experimentally determined the optimum pulse energies for cellular transfection using two different pulse-repetition rate lasers. This optimum–for both laser systems– comes as a trade-off between high transfection efficiency, favoring large holes and thus large pulse energy, and cell viability, favoring smaller holes and lower pulse energies. One of the paradoxes found in this study was that simple membrane modeling [34, 35] that balances an edge tension against surface tension and Laplace pressure predicts that larger holes take longer to close than smaller holes, while our observations showed that–for holes that closed on acute time scales– larger holes closed more quickly than small holes.

One resolution of this paradox is that membrane resealing is not a passive membrane processecently, Spaeth et al. [36] have shown that calcium (Ca^{2+}) mediates membrane sealing in neurites following transection, and other studies [37] suggest a Ca^{2+}-dependent mechanism for cell membrane resealing more generally. Thus, since Ca^{2+} diffusion into the cell happens more quickly for a large hole, it is plausible that this activates the sealing process more quickly. Conversely, smaller holes allow a slower influx of Ca^{2+}, and thus take longer to seal. The diffusion coefficient of Ca^{2+}, D, is concentration-dependent and ranges between 13 $\mu m^2/s$ and 50 $\mu m^2/s$ for 0.1-0.5 μM free Ca^{2+} [38]. Using $D = 20\ \mu m^2/s$, we estimate for the larger holes in our study ($r_0 \sim 300$ nm; $\tau \sim 10$ s) that–considering diffusive effects only and ignoring any intracellular buffering– the concentration of intracellular Ca^{2+} had completely equilibrated with the extracellular concentration by the time the hole resealed, while for smaller holes ($r_0 \sim 30$ nm; $\tau \sim 100$ s), the intracellular Ca^{2+} concentration had only reached $\sim$50% of the extracellular concentration. These estimates lend support to the Ca^{2+}-dependent sealing hypothesis.

In any case, an excess of intracellular Ca^{2+} will result in activation of cytochrome

c and initiate the apoptotic cascade. As a caveat, recall that in determining hole sealing time as a function of hole radius we selected only those cells which did, in fact, reseal after being permeabilized. However, larger holes had reduced viability, meaning that we have systematically excluded a large number of holes that did *not* reseal on experimental timescales. This selection bias may mask some of true intracellular dynamics that occur for large holes. Nevertheless, the validity of the Ca^{2+}-dependent sealing hypothesis could be readily tested by irradiating cells using the optimum laser pulses in media containing physiological Ca^{2+} and Ca^{2+}-free media. If our hypothesis is true, large holes should no longer seal quickly.

While interesting in terms of cellular mechanisms, perhaps of greater practical value is the discovery of Spaeth et al. [39] that addition of 3.7 mM polyethylene glycol (PEG) to the extracellular solution can result in much faster axonal resealing following axotomy, with nearly instantaneous sealing achieved in Ca^{2+}-containing media and 100 % sealing probability. Since our ultimate goal for optoporation is in vivo transfection, which requires time-consuming surgery and precise microinjections, any increase in cellular viability from improved sealing would be an enormous boon. This improvement is especially important for studies of small-scale neural networks, for which the accidental killing of neurons during transfection may have confounding effects on subsequent measurements. In addition, tissue scattering makes the estimation of the incident laser energy at the cell membrane difficult, since the laser light is attenuated by higher-lying layers of tissue. In our current study, in the absence of scattering or other complicating features, laser-permeabilized cells had a maximum viability of approximately 70 %. Thus, if the addition of PEG to the cellular media results in faster sealing, it is possible that constraints on laser power could be relaxed while maintaining a much higher cellular viability.

To test this latter hypothesis, the experiments performed to date should be repeated with the addition of varying concentrations of PEG. Optimization of PEG concentration will need to be determined such that cell resealing and viability is increased by faster membrane sealing while maintaining a window sufficient for DNA transfection.

Ultimately, these experiments should be demonstrated *in vivo*.

9.3 Conclusion

With these reflections and future directions in mind, it is time to bring this work to a close. I have immensely enjoyed and been stimulated by my work in the Schaffer group over the last few years. Chris has been an incredible mentor, under whom I have learned a great deal about life in academia, including scientific rigor, academic politics, and teaching pedagogy. In particular, his willingness to invest time and resources in projects of mutual interest to him and myself has provided an environment conducive to true scientific exploration and intellectual growth, and made nearly all of the projects in this thesis a reality.

To those who follow up on this thesis where I am obliged to leave off, either on one of the proposed avenues in this chapter or on novel endeavors of their own, I have a few short pieces of advice which have been helpful to me.

First, avoid tunnel vision. Your project is not that interesting in and of itself. It's value is tied, in part, to its perception and impact within a larger scientific community. Therefore, you must repeatedly present your work as part of a larger whole. In fact, one of the greatest challenges in presenting your work is to argue that it *really is* important; we all abhor "the horror of the same old thing" [40]. This goal cannot be achieved if you restrict yourself to literature and seminars dealing only within the narrow confines of your own experiments. Read broadly. Listen broadly. Discuss your work with colleagues outside of your field, and do not hide behind your lack of formal training. Your ability to integrate diverse ideas can only improve the quality of your project and stimulate your thinking to new and interesting ideas.

Second, the principal investigator under whom you work is not, contrary to popular opinion, infallible (sorry Chris). A professor's years of experience, depth and breadth of learning, and collaborative dealings are of immense value to you as a student. However,

like all human beings, some of his/her ideas are inaccurate, skewed, or just plain wrong. Part of becoming a mature researcher is your ability to develop your own ideas and respectfully and professionally disagree. Keep in mind that not all of your ideas are winners either.

Third, work hard and work smart. There is no substitute for hard work. Period. However, working smartly can dramatically increase the output of hard work. For example, taking the time to learn basic Matlab programming can substantially speed your rate of repetitive and menial data analysis.

Finally, do not be in a great hurry to publish or merely finish your degree. I am not saying that it is wise to dawdle, but merely that publishing good work and learning a great deal in the process of doing so is to be preferred to smaller incremental studies. The most useful (and most cited) papers are those which fully address a key question by a series of well-thought-out experiments rather than presenting a mere disembodied result. Moreover, your Ph.D. is a terrific opportunity to interact with the sharpest minds of our time, both within your field and outside of it. Rushing your Ph.D. simply to be done sooner is to deny yourself the fullness of higher academic education.

This concludes both this thesis and along with it, the last of my foreseeable formal education.

And now, O School, thy time has past
'Tis time to say "Farewell".
But thou, Fair Learning, hold me fast
Be my companion still.

REFERENCES

[1] F Corson. Fluctuations and redundancy in optimal transport networks. *Phys. Rev. Lett.*, 104(4):48703, 2010.

[2] R Hickey, M S Albin, L Bunegin, and J Gelineau. Autoregulation of spinal cord blood flow: is the cord a microcosm of the brain? *Stroke*, 17(6):1183–1189, 1986.

[3] Matthew J Farrar, Frank W Wise, Joseph R Fetcho, and Chris B Schaffer. In Vivo Imaging of Myelin in the Vertebrate Central Nervous System Using Third Harmonic Generation Microscopy. *Biophys J*, 100(5):1362–1371, 2011.

[4] R Wu and DE Weinstein. Isolation and Purification of Primary Schwann Cells. *Current Protocols in Neuroscience, Wiley, New York*, 1999.

[5] American Cancer Society. Prostate Cancer. pages 1–85, 2012.

[6] F Van der Aa, S Joniau, D De Ridder, and H Van Poppel. Potency after unilateral nerve sparing surgery: a report on functional and oncological results of unilateral nerve sparing surgery. *Prostate Cancer Prostatic Dis*, 6(1):61–65, 2003.

[7] Farhang Rabbani, Jeffrey Schiff, Michael Piecuch, Luis Herran Yunis, James A Eastham, Peter T Scardino, and John P Mulhall. Time Course of Recovery of Erectile Function After Radical Retropubic Prostatectomy: Does Anyone Recover After 2 Years? *The Journal of Sexual Medicine*, 7(12):3984–3990, 2010.

[8] Michael A Whitney, Jessica L Crisp, Linda T Nguyen, Beth Friedman, Larry A Gross, Paul Steinbach, Roger Y Tsien, and Quyen T Nguyen. Fluorescent peptides highlight peripheral nerves during surgery in mice. *Nat Biotechnol*, pages 1–7, 2011.

[9] L Gao, H Zhou, MJ Thrall, F Li, Y Yang, Z Wang, P Luo, KK Wong, GS Palapattu, and STC Wong. Label-free high-resolution imaging of prostate glands and cavernous nerves using coherent anti-Stokes Raman scattering microscopy. *Biomedical optics express*, 2(4):915–926, 2011.

[10] QT Nguyen, ES Olson, TA Aguilera, T Jiang, M Scadeng, LG Ellies, and RY Tsien. Surgery with molecular fluorescence imaging using activatable cell-penetrating peptides decreases residual cancer and improves survival. *Proceedings of the National Academy of Sciences of the United States of America*, 107(9):4317–4322, 2010.

[11] D Débarre, W Supatto, AM Pena, A Fabre, T Tordjmann, L Combettes, MC Schanne-Klein, and E Beaurepaire. Imaging lipid bodies in cells and tissues using third-harmonic generation microscopy. *Nat Meth*, 3(1):47–53, 2005.

[12] AC Tien, S Backus, H Kapteyn, M Murnane, and G Mourou. Short-pulse laser damage in transparent materials as a function of pulse duration. *Phys. Rev. Lett.*, 82(19):3883–3886, 1999.

[13] IG Maroulakou, M Anver, L Garrett, and JE Green. Prostate and Mammary Adenocarcinoma in Transgenic Mice Carrying a Rat C3(1) Simian-Virus-40 Large Tumor-Antigen Fusion Gene. *Proceedings of the National Academy of Sciences of the United States of America*, 91(23):11236–11240, 1994.

[14] NM Greenberg, F Demayo, MJ Finegold, D Medina, WD Tilley, JO Aspinall, GR Cunha, AA Donjacour, RJ Matusik, and JM Rosen. Prostate-Cancer in a Transgenic Mouse. *Proceedings of the National Academy of Sciences of the United States of America*, 92(8):3439–3443, 1995.

[15] PJ Russell and DJ Voeks. Animal models of prostate cancer. *Methods in molecular medicine*, 81:89–112, 2003.

[16] NK Janzen, KR Han, KT Perry, JW Said, PG Schulam, and AS Belldegrun. Feasibility of nerve-sparing prostate cryosurgery: Applications and limitations in a canine model. *J Endourol*, 19(4):520–525, 2005.

[17] Troy Richard John Gianduzzo, Jose R Colombo, Ehab El-Gabry, Georges-Pascal Haber, and Inderbir S Gill. Anatomical and Electrophysiological Assessment of the Canine Periprostatic Neurovascular Anatomy: Perspectives as a Nerve Sparing Radical Prostatectomy Model. *The Journal of Urology*, 179(5):2025–2029, 2008.

[18] A Ong, L Su, I Varkarakis, T Inagaki, R Link, S Bhayani, A Patriciu, B Crain, and P Walsh. Nerve sparing radical prostatectomy: effects of hemostatic energy sources on the recovery of cavernous nerve function in a canine model. *The Journal of Urology*, 172(4):1318–1322, 2004.

[19] Matthew J Farrar, Ida M Bernstein, Donald H Schlafer, Thomas A Cleland, Joseph R Fetcho, and Chris B Schaffer. Chronic in vivo imaging in the mouse spinal cord using an implanted chamber. *Nat Meth*, 9(3):297–U113, 2012.

[20] S Neumann and CJ Woolf. Regeneration of dorsal column fibers into and beyond the lesion site following adult spinal cord injury. *Neuron*, 23(1):83–91, 1999.

[21] Eric R Kandel, James H Schwartz, and Thomas M Jessell. *Principles of Neuroscience*. McGraw-Hill, New York, NY, 4 edition, 2000.

[22] L Schnell, R Schneider, R Kolbeck, YA Barde, and ME Schwab. Neurotrophin-3 Enhances Sprouting of Corticospinal Tract During Development and After Adult Spinal-Cord Lesion. *Nature*, 367(6459):170–173, 1994.

[23] Y Li, PM Field, and G Raisman. Regeneration of adult rat corticospinal axons induced by transplanted olfactory ensheathing cells. *J Neurosci*, 18(24):10514–10524, 1998.

[24] C Brosamle, AB Huber, M Fiedler, A Skerra, and ME Schwab. Regeneration of lesioned corticospinal tract fibers in the adult rat induced by a recombinant, humanized IN-1 antibody fragment. *J Neurosci*, 20(21):8061–8068, 2000.

[25] Kai Liu, Yi Lu, Jae K Lee, Ramsey Samara, Rafer Willenberg, Ilse Sears-Kraxberger, Andrea Tedeschi, Kevin Kyungsuk Park, Duo Jin, Bin Cai, Bengang Xu, Lauren Connolly, Oswald Steward, Binhai Zheng, and Zhigang He. PTEN deletion enhances the regenerative ability of adult corticospinal neurons. *Nat Neurosci*, 13(9):1075–U64, 2010.

[26] Charles Watson, George Paxinos, and Gulgun Kayalioglu. *The Spinal Cord*. Elsevier Ltd., Burlington, MA, 2009.

[27] Huazheng Liang, George Paxinos, and Charles Watson. The red nucleus and the rubrospinal projection in the mouse. *Brain Struct Funct*, 217(2):221–232, 2011.

[28] MG Fehlings and CH Tator. The relationships among the severity of spinal cord injury, residual neurological function, axon counts, and counts of retrogradely labeled neurons after experimental spinal cord injury. *Exp Neurol*, 132(2):220–228, 1995.

[29] Marc J Ruitenberg, Bas Blits, Paul A Dijkhuizen, Erik T te Beek, Arne Bakker, Joop J van Heerikhuize, Chris W Pool, Wim T J Hermens, Gerard J Boer, and Joost Verhaagen. Adeno-associated viral vector-mediated gene transfer of brain-derived neurotrophic factor reverses atrophy of rubrospinal neurons following both acute and chronic spinal cord injury. *Neurobiol Dis*, 15(2):394–406, 2004.

[30] MJ Ruitenberg, GW Plant, FPT Hamers, J Wortel, B Blits, PA Dijkhuizen, WH Gispen, GJ Boer, and J Verhaagen. Ex vivo adenoviral vector-mediated neurotrophin gene transfer to olfactory ensheathing glia: effects on rubrospinal tract regeneration, lesion size, and functional recovery after implantation in the injured rat spinal cord. *The Journal of neuroscience*, 23(18):7045–7058, 2003.

[31] Y Liu, D Kim, BT Himes, SY Chow, T Schallert, M Murray, A Tessler, and I Fischer. Transplants of fibroblasts genetically modified to express BDNF promote regeneration of adult rat rubrospinal axons and recovery of forelimb function. *The Journal of neuroscience*, 19(11):4370–4387, 1999.

[32] TH Chia and MJ Levene. Microprisms for In Vivo Multilayer Cortical Imaging. *J Neurophysiol*, 102(2):1310–1314, 2009.

[33] RPJ Barretto, TH Ko, JC Jung, TJ Wang, G Capps, AC Waters, Y Ziv, A Attardo, L Recht, and MJ Schnitzer. Time-lapse imaging of disease progression in deep brain areas using fluorescence microendoscopy. *Nat Med*, 17(2):223–228, 2011.

[34] E Karatekin, O Sandre, and F Brochard-Wyart. Transient pores in vesicles. *Polymer International*, 52(4):486–493, 2003.

[35] F Brochard-Wyart, PG De Gennes, and O Sandre. Transient pores in stretched vesicles: role of leak-out. *Physica A: Statistical Mechanics and its Applications*, 278(1-2):32–51, 2000.

[36] C S Spaeth, E A Boydston, L R Figard, A Zuzek, and G D Bittner. A Model for Sealing Plasmalemmal Damage in Neurons and Other Eukaryotic Cells. *J Neurosci*, 30(47):15790–15800, 2010.

[37] P McNeil. Membrane repair redux: redox of MG53. *Nat Cell Biol*, 11(1):7–9, 2009.

[38] N.L. Allbritton, T. Meyer, and L. Stryer. Range of messenger action of calcium ion and inositol 1, 4, 5-trisphosphate. *Science*, 258(5089):1812–1815, 1992.

[39] CS Spaeth, T Robison, and JD Fan. Cellular mechanisms of plasmalemmal sealing and axonal repair by polyethylene glycol and methylene blue. *J Neurosci*, 2012.

[40] CS Lewis. *The Screwtape Letters & Screwtape Proposes a Toast*. Macmillan, New York, NY, 1961.

APPENDIX A

PERMISSIONS

NATURE PUBLISHING GROUP LICENSE TERMS AND CONDITIONS

Jul 03, 2012

This is a License Agreement between Matthew J Farrar ("You") and Nature Publishing Group ("Nature Publishing Group") provided by Copyright Clearance Center ("CCC"). The license consists of your order details, the terms and conditions provided by Nature Publishing Group, and the payment terms and conditions.

All payments must be made in full to CCC. For payment instructions, please see information listed at the bottom of this form.

License Number	2941530558536
License date	Jul 03, 2012
Licensed content publisher	Nature Publishing Group
Licensed content publication	Nature Reviews Neuroscience
Licensed content title	Therapeutic interventions after spinal cord injury
Licensed content author	Sandrine Thuret, Lawrence D. F. Moon and Fred H. Gage
Licensed content date	Aug 1, 2006
Volume number	7
Issue number	8
Type of Use	reuse in a thesis/dissertation
Requestor type	academic/educational
Format	print and electronic
Portion	figures/tables/illustrations
Number of figures/tables/illustrations	1
High-res required	no
Figures	Box 1
Author of this NPG article	no
Your reference number	
Title of your thesis / dissertation	NONLINEAR OPTICAL TECHNIQUES FOR IMAGING AND MANIPULATING THE MOUSE CENTRAL NERVOUS SYSTEM
Expected completion date	Aug 2012
Estimated size (number of	400

pages)

Total 0.00 USD

Terms and Conditions

Terms and Conditions for Permissions

Nature Publishing Group hereby grants you a non-exclusive license to reproduce this material for this purpose, and for no other use, subject to the conditions below:

1. NPG warrants that it has, to the best of its knowledge, the rights to license reuse of this material. However, you should ensure that the material you are requesting is original to Nature Publishing Group and does not carry the copyright of another entity (as credited in the published version). If the credit line on any part of the material you have requested indicates that it was reprinted or adapted by NPG with permission from another source, then you should also seek permission from that source to reuse the material.

2. Permission granted free of charge for material in print is also usually granted for any electronic version of that work, provided that the material is incidental to the work as a whole and that the electronic version is essentially equivalent to, or substitutes for, the print version. Where print permission has been granted for a fee, separate permission must be obtained for any additional, electronic re-use (unless, as in the case of a full paper, this has already been accounted for during your initial request in the calculation of a print run). NB: In all cases, web-based use of full-text articles must be authorized separately through the 'Use on a Web Site' option when requesting permission.

3. Permission granted for a first edition does not apply to second and subsequent editions and for editions in other languages (except for signatories to the STM Permissions Guidelines, or where the first edition permission was granted for free).

4. Nature Publishing Group's permission must be acknowledged next to the figure, table or abstract in print. In electronic form, this acknowledgement must be visible at the same time as the figure/table/abstract, and must be hyperlinked to the journal's homepage.

5. The credit line should read:
   Reprinted by permission from Macmillan Publishers Ltd: [JOURNAL NAME] (reference citation), copyright (year of publication)
   For AOP papers, the credit line should read:
   Reprinted by permission from Macmillan Publishers Ltd: [JOURNAL NAME], advance online publication, day month year (doi: 10.1038/sj.[JOURNAL ACRONYM].XXXXX)

   Note: For republication from the *British Journal of Cancer*, the following credit lines apply.

Reprinted by permission from Macmillan Publishers Ltd on behalf of Cancer Research UK: [JOURNAL NAME] (reference citation), copyright (year of publication) For AOP papers, the credit line should read:
Reprinted by permission from Macmillan Publishers Ltd on behalf of Cancer Research UK: [JOURNAL NAME], advance online publication, day month year (doi: 10.1038/sj.[JOURNAL ACRONYM].XXXXX)

6. Adaptations of single figures do not require NPG approval. However, the adaptation should be credited as follows:

   Adapted by permission from Macmillan Publishers Ltd: [JOURNAL NAME] (reference citation), copyright (year of publication)

   Note: For adaptation from the *British Journal of Cancer*, the following credit line applies.
   Adapted by permission from Macmillan Publishers Ltd on behalf of Cancer Research UK: [JOURNAL NAME] (reference citation), copyright (year of publication)

7. Translations of 401 words up to a whole article require NPG approval. Please visit http://www.macmillanmedicalcommunications.com for more information. Translations of up to a 400 words do not require NPG approval. The translation should be credited as follows:

   Translated by permission from Macmillan Publishers Ltd: [JOURNAL NAME] (reference citation), copyright (year of publication).

   Note: For translation from the *British Journal of Cancer*, the following credit line applies.
   Translated by permission from Macmillan Publishers Ltd on behalf of Cancer Research UK: [JOURNAL NAME] (reference citation), copyright (year of publication)

We are certain that all parties will benefit from this agreement and wish you the best in the use of this material. Thank you.

Special Terms:

v1.1

If you would like to pay for this license now, please remit this license along with your payment made payable to "COPYRIGHT CLEARANCE CENTER" otherwise you will be invoiced within 48 hours of the license date. Payment should be in the form of a check or money order referencing your account number and this invoice number RLNK500811559.
Once you receive your invoice for this order, you may pay your invoice by credit card. Please follow instructions provided at that time.

Make Payment To:
Copyright Clearance Center
Dept 001
P.O. Box 843006
Boston, MA 02284-3006

For suggestions or comments regarding this order, contact RightsLink Customer Support: customercare@copyright.com or +1-877-622-5543 (toll free in the US) or +1-978-646-2777.

Gratis licenses (referencing $0 in the Total field) are free. Please retain this printable license for your reference. No payment is required.

ELSEVIER LICENSE
TERMS AND CONDITIONS

Jun 28, 2012

This is a License Agreement between Matthew J Farrar ("You") and Elsevier ("Elsevier") provided by Copyright Clearance Center ("CCC"). The license consists of your order details, the terms and conditions provided by Elsevier, and the payment terms and conditions.

All payments must be made in full to CCC. For payment instructions, please see information listed at the bottom of this form.

Supplier	Elsevier Limited The Boulevard,Langford Lane Kidlington,Oxford,OX5 1GB,UK
Registered Company Number	1982084
Customer name	Matthew J Farrar
Customer address	526 Campus Rd. Ithaca, NY 14853
License number	2921940890006
License date	Jun 04, 2012
Licensed content publisher	Elsevier
Licensed content publication	Experimental Neurology
Licensed content title	Chondroitin sulphate proteoglycans: Key modulators of spinal cord and brain plasticity
Licensed content author	K. Bartus,N.D. James,K.D. Bosch,E.J. Bradbury
Licensed content date	May 2012
Licensed content volume number	235
Licensed content issue number	1
Number of pages	13
Start Page	5
End Page	17
Type of Use	reuse in a thesis/dissertation
Intended publisher of new work	other
Portion	figures/tables/illustrations
Number of figures/tables/illustrations	1
Format	both print and electronic
Are you the author of this Elsevier article?	No

Will you be translating?	No
Order reference number	Figure 2
Title of your thesis/dissertation	NONLINEAR OPTICAL TECHNIQUES FOR IMAGING AND MANIPULATING THE MOUSE CENTRAL NERVOUS SYSTEM
Expected completion date	Aug 2012
Estimated size (number of pages)	400
Elsevier VAT number	GB 494 6272 12
Permissions price	0.00 USD
VAT/Local Sales Tax	0.0 USD / 0.0 GBP
Total	0.00 USD
Terms and Conditions	

INTRODUCTION

1. The publisher for this copyrighted material is Elsevier. By clicking "accept" in connection with completing this licensing transaction, you agree that the following terms and conditions apply to this transaction (along with the Billing and Payment terms and conditions established by Copyright Clearance Center, Inc. ("CCC"), at the time that you opened your Rightslink account and that are available at any time at http://myaccount.copyright.com).

GENERAL TERMS

2. Elsevier hereby grants you permission to reproduce the aforementioned material subject to the terms and conditions indicated.

3. Acknowledgement: If any part of the material to be used (for example, figures) has appeared in our publication with credit or acknowledgement to another source, permission must also be sought from that source. If such permission is not obtained then that material may not be included in your publication/copies. Suitable acknowledgement to the source must be made, either as a footnote or in a reference list at the end of your publication, as follows:

"Reprinted from Publication title, Vol /edition number, Author(s), Title of article / title of chapter, Pages No., Copyright (Year), with permission from Elsevier [OR APPLICABLE SOCIETY COPYRIGHT OWNER]." Also Lancet special credit - "Reprinted from The Lancet, Vol. number, Author(s), Title of article, Pages No., Copyright (Year), with permission from Elsevier."

4. Reproduction of this material is confined to the purpose and/or media for which permission is hereby given.

5. Altering/Modifying Material: Not Permitted. However figures and illustrations may be altered/adapted minimally to serve your work. Any other abbreviations, additions, deletions and/or any other alterations shall be made only with prior written authorization of Elsevier Ltd. (Please contact Elsevier at permissions@elsevier.com)

6. If the permission fee for the requested use of our material is waived in this instance, please be advised that your future requests for Elsevier materials may attract a fee.

7. Reservation of Rights: Publisher reserves all rights not specifically granted in the combination of (i) the license details provided by you and accepted in the course of this licensing transaction, (ii) these terms and conditions and (iii) CCC's Billing and Payment terms and conditions.

8. License Contingent Upon Payment: While you may exercise the rights licensed immediately upon issuance of the license at the end of the licensing process for the transaction, provided that you have disclosed complete and accurate details of your proposed use, no license is finally effective unless and until full payment is received from you (either by publisher or by CCC) as provided in CCC's Billing and Payment terms and conditions. If full payment is not received on a timely basis, then any license preliminarily granted shall be deemed automatically revoked and shall be void as if never granted. Further, in the event that you breach any of these terms and conditions or any of CCC's Billing and Payment terms and conditions, the license is automatically revoked and shall be void as if never granted. Use of materials as described in a revoked license, as well as any use of the materials beyond the scope of an unrevoked license, may constitute copyright infringement and publisher reserves the right to take any and all action to protect its copyright in the materials.

9. Warranties: Publisher makes no representations or warranties with respect to the licensed material.

10. Indemnity: You hereby indemnify and agree to hold harmless publisher and CCC, and their respective officers, directors, employees and agents, from and against any and all claims arising out of your use of the licensed material other than as specifically authorized pursuant to this license.

11. No Transfer of License: This license is personal to you and may not be sublicensed, assigned, or transferred by you to any other person without publisher's written permission.

12. No Amendment Except in Writing: This license may not be amended except in a writing signed by both parties (or, in the case of publisher, by CCC on publisher's behalf).

13. Objection to Contrary Terms: Publisher hereby objects to any terms contained in any purchase order, acknowledgment, check endorsement or other writing prepared by you, which terms are inconsistent with these terms and conditions or CCC's Billing and Payment terms and conditions. These terms and conditions, together with CCC's Billing and Payment terms and conditions (which are incorporated herein), comprise the entire agreement between you and publisher (and CCC) concerning this licensing transaction. In the event of any conflict between your obligations established by these terms and conditions and those established by CCC's Billing and Payment terms and conditions, these terms and conditions shall control.

14. Revocation: Elsevier or Copyright Clearance Center may deny the permissions described in this License at their sole discretion, for any reason or no reason, with a full refund payable to you. Notice of such denial will be made using the contact information provided by you. Failure to receive such notice will not alter or invalidate the denial. In no event will Elsevier or Copyright Clearance Center be responsible or liable for any costs, expenses or damage incurred by you as a result of a denial of your permission request, other than a refund of the amount(s) paid by you to Elsevier and/or Copyright Clearance Center for denied permissions.

LIMITED LICENSE

293

The following terms and conditions apply only to specific license types:

15. **Translation**: This permission is granted for non-exclusive world **English** rights only unless your license was granted for translation rights. If you licensed translation rights you may only translate this content into the languages you requested. A professional translator must perform all translations and reproduce the content word for word preserving the integrity of the article. If this license is to re-use 1 or 2 figures then permission is granted for non-exclusive world rights in all languages.

16. **Website**: The following terms and conditions apply to electronic reserve and author websites:
Electronic reserve: If licensed material is to be posted to website, the web site is to be password-protected and made available only to bona fide students registered on a relevant course if:
This license was made in connection with a course,
This permission is granted for 1 year only. You may obtain a license for future website posting,
All content posted to the web site must maintain the copyright information line on the bottom of each image,
A hyper-text must be included to the Homepage of the journal from which you are licensing at http://www.sciencedirect.com/science/journal/xxxxx or the Elsevier homepage for books at http://www.elsevier.com , and
Central Storage: This license does not include permission for a scanned version of the material to be stored in a central repository such as that provided by Heron/XanEdu.

17. **Author website** for journals with the following additional clauses:

All content posted to the web site must maintain the copyright information line on the bottom of each image, and the permission granted is limited to the personal version of your paper. You are not allowed to download and post the published electronic version of your article (whether PDF or HTML, proof or final version), nor may you scan the printed edition to create an electronic version. A hyper-text must be included to the Homepage of the journal from which you are licensing at http://www.sciencedirect.com/science/journal/xxxxx . As part of our normal production process, you will receive an e-mail notice when your article appears on Elsevier's online service ScienceDirect (www.sciencedirect.com). That e-mail will include the article's Digital Object Identifier (DOI). This number provides the electronic link to the published article and should be included in the posting of your personal version. We ask that you wait until you receive this e-mail and have the DOI to do any posting.

Central Storage: This license does not include permission for a scanned version of the material to be stored in a central repository such as that provided by Heron/XanEdu.

18. **Author website** for books with the following additional clauses:
Authors are permitted to place a brief summary of their work online only.
A hyper-text must be included to the Elsevier homepage at http://www.elsevier.com . All content posted to the web site must maintain the copyright information line on the bottom of each image. You are not allowed to download and post the published electronic version of your chapter, nor may you scan the printed edition to create an electronic version.

Central Storage: This license does not include permission for a scanned version of the material to be stored in a central repository such as that provided by Heron/XanEdu.

19. **Website** (regular and for author): A hyper-text must be included to the Homepage of the journal from which you are licensing at http://www.sciencedirect.com/science/journal/xxxxx. or for books to the Elsevier homepage at http://www.elsevier.com

20. **Thesis/Dissertation**: If your license is for use in a thesis/dissertation your thesis may be submitted to your institution in either print or electronic form. Should your thesis be published commercially, please reapply for permission. These requirements include permission for the Library and Archives of Canada to supply single copies, on demand, of the complete thesis and include permission for UMI to supply single copies, on demand, of the complete thesis. Should your thesis be published commercially, please reapply for permission.

21. **Other Conditions**:

v1.6

If you would like to pay for this license now, please remit this license along with your payment made payable to "COPYRIGHT CLEARANCE CENTER" otherwise you will be invoiced within 48 hours of the license date. Payment should be in the form of a check or money order referencing your account number and this invoice number RLNK500791979.
Once you receive your invoice for this order, you may pay your invoice by credit card. Please follow instructions provided at that time.

Make Payment To:
Copyright Clearance Center
Dept 001
P.O. Box 843006
Boston, MA 02284-3006

For suggestions or comments regarding this order, contact RightsLink Customer Support: customercare@copyright.com or +1-877-622-5543 (toll free in the US) or +1-978-646-2777.

Gratis licenses (referencing $0 in the Total field) are free. Please retain this printable license for your reference. No payment is required.

NATURE PUBLISHING GROUP LICENSE TERMS AND CONDITIONS

Jun 28, 2012

This is a License Agreement between Matthew J Farrar ("You") and Nature Publishing Group ("Nature Publishing Group") provided by Copyright Clearance Center ("CCC"). The license consists of your order details, the terms and conditions provided by Nature Publishing Group, and the payment terms and conditions.

All payments must be made in full to CCC. For payment instructions, please see information listed at the bottom of this form.

License Number	2918891155016
License date	May 30, 2012
Licensed content publisher	Nature Publishing Group
Licensed content publication	Nature Reviews Neuroscience
Licensed content title	In vivo imaging of the diseased nervous system
Licensed content author	Thomas Misgeld and Martin Kerschensteiner
Licensed content date	Jun 1, 2006
Volume number	7
Issue number	6
Type of Use	reuse in a thesis/dissertation
Requestor type	academic/educational
Format	print and electronic
Portion	figures/tables/illustrations
Number of figures/tables/illustrations	1
High-res required	no
Figures	Figure 1: Advantages of in vivo imaging in neurological disease models
Author of this NPG article	no
Your reference number	
Title of your thesis / dissertation	NONLINEAR OPTICAL TECHNIQUES FOR IMAGING AND MANIPULATING THE MOUSE CENTRAL NERVOUS SYSTEM
Expected completion date	Aug 2012
Estimated size (number of pages)	400
Total	0.00 USD
Terms and Conditions	

Terms and Conditions for Permissions

Nature Publishing Group hereby grants you a non-exclusive license to reproduce this material for this purpose, and for no other use, subject to the conditions below:

1. NPG warrants that it has, to the best of its knowledge, the rights to license reuse of this material. However, you should ensure that the material you are requesting is original to Nature Publishing Group and does not carry the copyright of another entity (as credited in the published version). If the credit line on any part of the material you have requested indicates that it was reprinted or adapted by NPG with permission from another source, then you should also seek permission from that source to reuse the material.

2. Permission granted free of charge for material in print is also usually granted for any electronic version of that work, provided that the material is incidental to the work as a whole and that the electronic version is essentially equivalent to, or substitutes for, the print version. Where print permission has been granted for a fee, separate permission must be obtained for any additional, electronic re-use (unless, as in the case of a full paper, this has already been accounted for during your initial request in the calculation of a print run). NB: In all cases, web-based use of full-text articles must be authorized separately through the 'Use on a Web Site' option when requesting permission.

3. Permission granted for a first edition does not apply to second and subsequent editions and for editions in other languages (except for signatories to the STM Permissions Guidelines, or where the first edition permission was granted for free).

4. Nature Publishing Group's permission must be acknowledged next to the figure, table or abstract in print. In electronic form, this acknowledgement must be visible at the same time as the figure/table/abstract, and must be hyperlinked to the journal's homepage.

5. The credit line should read:
   Reprinted by permission from Macmillan Publishers Ltd: [JOURNAL NAME] (reference citation), copyright (year of publication)
   For AOP papers, the credit line should read:
   Reprinted by permission from Macmillan Publishers Ltd: [JOURNAL NAME], advance online publication, day month year (doi: 10.1038/sj.[JOURNAL ACRONYM].XXXXX)

   Note: For republication from the *British Journal of Cancer*, the following credit lines apply.
   Reprinted by permission from Macmillan Publishers Ltd on behalf of Cancer Research UK: [JOURNAL NAME] (reference citation), copyright (year of publication) For AOP papers, the credit line should read:
   Reprinted by permission from Macmillan Publishers Ltd on behalf of Cancer Research UK: [JOURNAL NAME], advance online publication, day month year (doi: 10.1038/sj.[JOURNAL ACRONYM].XXXXX)

6. Adaptations of single figures do not require NPG approval. However, the adaptation should be credited as follows:

   Adapted by permission from Macmillan Publishers Ltd: [JOURNAL NAME]

(reference citation), copyright (year of publication)

Note: For adaptation from the *British Journal of Cancer*, the following credit line applies.
Adapted by permission from Macmillan Publishers Ltd on behalf of Cancer Research UK: [JOURNAL NAME] (reference citation), copyright (year of publication)

7. Translations of 401 words up to a whole article require NPG approval. Please visit http://www.macmillanmedicalcommunications.com for more information. Translations of up to a 400 words do not require NPG approval. The translation should be credited as follows:

   Translated by permission from Macmillan Publishers Ltd: [JOURNAL NAME] (reference citation), copyright (year of publication).

   Note: For translation from the *British Journal of Cancer*, the following credit line applies.
   Translated by permission from Macmillan Publishers Ltd on behalf of Cancer Research UK: [JOURNAL NAME] (reference citation), copyright (year of publication)

We are certain that all parties will benefit from this agreement and wish you the best in the use of this material. Thank you.

Special Terms:

v1.1

If you would like to pay for this license now, please remit this license along with your payment made payable to "COPYRIGHT CLEARANCE CENTER" otherwise you will be invoiced within 48 hours of the license date. Payment should be in the form of a check or money order referencing your account number and this invoice number RLNK500789444.
Once you receive your invoice for this order, you may pay your invoice by credit card. Please follow instructions provided at that time.

Make Payment To:
Copyright Clearance Center
Dept 001
P.O. Box 843006
Boston, MA 02284-3006

For suggestions or comments regarding this order, contact RightsLink Customer Support: customercare@copyright.com or +1-877-622-5543 (toll free in the US) or +1-978-646-2777.

Gratis licenses (referencing $0 in the Total field) are free. Please retain this printable license for your reference. No payment is required.

NATURE PUBLISHING GROUP LICENSE TERMS AND CONDITIONS

Jun 28, 2012

This is a License Agreement between Matthew J Farrar ("You") and Nature Publishing Group ("Nature Publishing Group") provided by Copyright Clearance Center ("CCC"). The license consists of your order details, the terms and conditions provided by Nature Publishing Group, and the payment terms and conditions.

All payments must be made in full to CCC. For payment instructions, please see information listed at the bottom of this form.

License Number	2918911353159
License date	May 30, 2012
Licensed content publisher	Nature Publishing Group
Licensed content publication	Nature Neuroscience
Licensed content title	Microglial Cx3cr1 knockout prevents neuron loss in a mouse model of Alzheimer's disease
Licensed content author	Martin Fuhrmann, Tobias Bittner, Christian K E Jung, Steffen Burgold, Richard M Page, Gerda Mitteregger
Licensed content date	Mar 21, 2010
Volume number	13
Issue number	4
Type of Use	reuse in a thesis/dissertation
Requestor type	academic/educational
Format	print and electronic
Portion	figures/tables/illustrations
Number of figures/tables/illustrations	1
High-res required	no
Figures	Figure 1: Microglial CX3CR1-dependent neuron loss in 5xTg mice
Author of this NPG article	no
Your reference number	
Title of your thesis / dissertation	NONLINEAR OPTICAL TECHNIQUES FOR IMAGING AND MANIPULATING THE MOUSE CENTRAL NERVOUS SYSTEM
Expected completion date	Aug 2012
Estimated size (number of pages)	400
Total	0.00 USD
Terms and Conditions	

Terms and Conditions for Permissions

Nature Publishing Group hereby grants you a non-exclusive license to reproduce this material for this purpose, and for no other use, subject to the conditions below:

1. NPG warrants that it has, to the best of its knowledge, the rights to license reuse of this material. However, you should ensure that the material you are requesting is original to Nature Publishing Group and does not carry the copyright of another entity (as credited in the published version). If the credit line on any part of the material you have requested indicates that it was reprinted or adapted by NPG with permission from another source, then you should also seek permission from that source to reuse the material.

2. Permission granted free of charge for material in print is also usually granted for any electronic version of that work, provided that the material is incidental to the work as a whole and that the electronic version is essentially equivalent to, or substitutes for, the print version. Where print permission has been granted for a fee, separate permission must be obtained for any additional, electronic re-use (unless, as in the case of a full paper, this has already been accounted for during your initial request in the calculation of a print run). NB: In all cases, web-based use of full-text articles must be authorized separately through the 'Use on a Web Site' option when requesting permission.

3. Permission granted for a first edition does not apply to second and subsequent editions and for editions in other languages (except for signatories to the STM Permissions Guidelines, or where the first edition permission was granted for free).

4. Nature Publishing Group's permission must be acknowledged next to the figure, table or abstract in print. In electronic form, this acknowledgement must be visible at the same time as the figure/table/abstract, and must be hyperlinked to the journal's homepage.

5. The credit line should read:
   Reprinted by permission from Macmillan Publishers Ltd: [JOURNAL NAME] (reference citation), copyright (year of publication)
   For AOP papers, the credit line should read:
   Reprinted by permission from Macmillan Publishers Ltd: [JOURNAL NAME], advance online publication, day month year (doi: 10.1038/sj.[JOURNAL ACRONYM].XXXXX)

   Note: For republication from the *British Journal of Cancer*, the following credit lines apply.
   Reprinted by permission from Macmillan Publishers Ltd on behalf of Cancer Research UK: [JOURNAL NAME] (reference citation), copyright (year of publication) For AOP papers, the credit line should read:
   Reprinted by permission from Macmillan Publishers Ltd on behalf of Cancer Research UK: [JOURNAL NAME], advance online publication, day month year (doi: 10.1038/sj.[JOURNAL ACRONYM].XXXXX)

6. Adaptations of single figures do not require NPG approval. However, the adaptation should be credited as follows:

   Adapted by permission from Macmillan Publishers Ltd: [JOURNAL NAME]

(reference citation), copyright (year of publication)

Note: For adaptation from the *British Journal of Cancer*, the following credit line applies.
Adapted by permission from Macmillan Publishers Ltd on behalf of Cancer Research UK: [JOURNAL NAME] (reference citation), copyright (year of publication)

7. Translations of 401 words up to a whole article require NPG approval. Please visit http://www.macmillanmedicalcommunications.com for more information. Translations of up to a 400 words do not require NPG approval. The translation should be credited as follows:

   Translated by permission from Macmillan Publishers Ltd: [JOURNAL NAME] (reference citation), copyright (year of publication).

   Note: For translation from the *British Journal of Cancer*, the following credit line applies.
   Translated by permission from Macmillan Publishers Ltd on behalf of Cancer Research UK: [JOURNAL NAME] (reference citation), copyright (year of publication)

We are certain that all parties will benefit from this agreement and wish you the best in the use of this material. Thank you.

Special Terms:

v1.1

If you would like to pay for this license now, please remit this license along with your payment made payable to "COPYRIGHT CLEARANCE CENTER" otherwise you will be invoiced within 48 hours of the license date. Payment should be in the form of a check or money order referencing your account number and this invoice number RLNK500789496.
Once you receive your invoice for this order, you may pay your invoice by credit card. Please follow instructions provided at that time.

Make Payment To:
Copyright Clearance Center
Dept 001
P.O. Box 843006
Boston, MA 02284-3006

For suggestions or comments regarding this order, contact RightsLink Customer Support: customercare@copyright.com or +1-877-622-5543 (toll free in the US) or +1-978-646-2777.

Gratis licenses (referencing $0 in the Total field) are free. Please retain this printable license for your reference. No payment is required.

ELSEVIER LICENSE
TERMS AND CONDITIONS

Jun 28, 2012

This is a License Agreement between Matthew J Farrar ("You") and Elsevier ("Elsevier") provided by Copyright Clearance Center ("CCC"). The license consists of your order details, the terms and conditions provided by Elsevier, and the payment terms and conditions.

All payments must be made in full to CCC. For payment instructions, please see information listed at the bottom of this form.

Supplier	Elsevier Limited The Boulevard,Langford Lane Kidlington,Oxford,OX5 1GB,UK
Registered Company Number	1982084
Customer name	Matthew J Farrar
Customer address	526 Campus Rd. Ithaca, NY 14853
License number	2933590949612
License date	Jun 21, 2012
Licensed content publisher	Elsevier
Licensed content publication	Biophysical Journal
Licensed content title	In Vivo Imaging of Myelin in the Vertebrate Central Nervous System Using Third Harmonic Generation Microscopy
Licensed content author	Matthew J. Farrar,Frank W. Wise,Joseph R. Fetcho,Chris B. Schaffer
Licensed content date	2 March 2011
Licensed content volume number	100
Licensed content issue number	5
Number of pages	10
Start Page	1362
End Page	1371
Type of Use	reuse in a thesis/dissertation
Portion	full article
Format	both print and electronic
Are you the author of this Elsevier article?	Yes
Will you be translating?	No
Order reference number	
Title of your	NONLINEAR OPTICAL TECHNIQUES FOR IMAGING AND

thesis/dissertation	MANIPULATING THE MOUSE CENTRAL NERVOUS SYSTEM
Expected completion date	Aug 2012
Estimated size (number of pages)	400
Elsevier VAT number	GB 494 6272 12
Permissions price	0.00 USD
VAT/Local Sales Tax	0.00 USD / GBP
Total	0.00 USD
Terms and Conditions	

INTRODUCTION

1. The publisher for this copyrighted material is Elsevier. By clicking "accept" in connection with completing this licensing transaction, you agree that the following terms and conditions apply to this transaction (along with the Billing and Payment terms and conditions established by Copyright Clearance Center, Inc. ("CCC"), at the time that you opened your Rightslink account and that are available at any time at http://myaccount.copyright.com).

GENERAL TERMS

2. Elsevier hereby grants you permission to reproduce the aforementioned material subject to the terms and conditions indicated.

3. Acknowledgement: If any part of the material to be used (for example, figures) has appeared in our publication with credit or acknowledgement to another source, permission must also be sought from that source. If such permission is not obtained then that material may not be included in your publication/copies. Suitable acknowledgement to the source must be made, either as a footnote or in a reference list at the end of your publication, as follows:

"Reprinted from Publication title, Vol /edition number, Author(s), Title of article / title of chapter, Pages No., Copyright (Year), with permission from Elsevier [OR APPLICABLE SOCIETY COPYRIGHT OWNER]." Also Lancet special credit - "Reprinted from The Lancet, Vol. number, Author(s), Title of article, Pages No., Copyright (Year), with permission from Elsevier."

4. Reproduction of this material is confined to the purpose and/or media for which permission is hereby given.

5. Altering/Modifying Material: Not Permitted. However figures and illustrations may be altered/adapted minimally to serve your work. Any other abbreviations, additions, deletions and/or any other alterations shall be made only with prior written authorization of Elsevier Ltd. (Please contact Elsevier at permissions@elsevier.com)

6. If the permission fee for the requested use of our material is waived in this instance, please be advised that your future requests for Elsevier materials may attract a fee.

7. Reservation of Rights: Publisher reserves all rights not specifically granted in the combination of (i) the license details provided by you and accepted in the course of this licensing transaction, (ii) these terms and conditions and (iii) CCC's Billing and Payment terms and conditions.

8. License Contingent Upon Payment: While you may exercise the rights licensed immediately upon issuance of the license at the end of the licensing process for the transaction, provided that you have disclosed complete and accurate details of your proposed use, no license is finally effective unless and until full payment is received from you (either by publisher or by CCC) as provided in CCC's Billing and Payment terms and conditions. If full payment is not received on a timely basis, then any license preliminarily granted shall be deemed automatically revoked and shall be void as if never granted. Further, in the event that you breach any of these terms and conditions or any of CCC's Billing and Payment terms and conditions, the license is automatically revoked and shall be void as if never granted. Use of materials as described in a revoked license, as well as any use of the materials beyond the scope of an unrevoked license, may constitute copyright infringement and publisher reserves the right to take any and all action to protect its copyright in the materials.

9. Warranties: Publisher makes no representations or warranties with respect to the licensed material.

10. Indemnity: You hereby indemnify and agree to hold harmless publisher and CCC, and their respective officers, directors, employees and agents, from and against any and all claims arising out of your use of the licensed material other than as specifically authorized pursuant to this license.

11. No Transfer of License: This license is personal to you and may not be sublicensed, assigned, or transferred by you to any other person without publisher's written permission.

12. No Amendment Except in Writing: This license may not be amended except in a writing signed by both parties (or, in the case of publisher, by CCC on publisher's behalf).

13. Objection to Contrary Terms: Publisher hereby objects to any terms contained in any purchase order, acknowledgment, check endorsement or other writing prepared by you, which terms are inconsistent with these terms and conditions or CCC's Billing and Payment terms and conditions. These terms and conditions, together with CCC's Billing and Payment terms and conditions (which are incorporated herein), comprise the entire agreement between you and publisher (and CCC) concerning this licensing transaction. In the event of any conflict between your obligations established by these terms and conditions and those established by CCC's Billing and Payment terms and conditions, these terms and conditions shall control.

14. Revocation: Elsevier or Copyright Clearance Center may deny the permissions described in this License at their sole discretion, for any reason or no reason, with a full refund payable to you. Notice of such denial will be made using the contact information provided by you. Failure to receive such notice will not alter or invalidate the denial. In no event will Elsevier or Copyright Clearance Center be responsible or liable for any costs, expenses or damage incurred by you as a result of a denial of your permission request, other than a refund of the amount(s) paid by you to Elsevier and/or Copyright Clearance Center for denied permissions.

LIMITED LICENSE

The following terms and conditions apply only to specific license types:

15. **Translation**: This permission is granted for non-exclusive world **English** rights only unless your license was granted for translation rights. If you licensed translation rights you may only translate this content into the languages you requested. A professional translator must perform all translations and reproduce the content word for word preserving the integrity

of the article. If this license is to re-use 1 or 2 figures then permission is granted for non-exclusive world rights in all languages.

16. **Website**: The following terms and conditions apply to electronic reserve and author websites:
Electronic reserve: If licensed material is to be posted to website, the web site is to be password-protected and made available only to bona fide students registered on a relevant course if:
This license was made in connection with a course,
This permission is granted for 1 year only. You may obtain a license for future website posting,
All content posted to the web site must maintain the copyright information line on the bottom of each image,
A hyper-text must be included to the Homepage of the journal from which you are licensing at http://www.sciencedirect.com/science/journal/xxxxx or the Elsevier homepage for books at http://www.elsevier.com , and
Central Storage: This license does not include permission for a scanned version of the material to be stored in a central repository such as that provided by Heron/XanEdu.

17. **Author website** for journals with the following additional clauses:

All content posted to the web site must maintain the copyright information line on the bottom of each image, and the permission granted is limited to the personal version of your paper. You are not allowed to download and post the published electronic version of your article (whether PDF or HTML, proof or final version), nor may you scan the printed edition to create an electronic version. A hyper-text must be included to the Homepage of the journal from which you are licensing at http://www.sciencedirect.com/science/journal/xxxxx . As part of our normal production process, you will receive an e-mail notice when your article appears on Elsevier's online service ScienceDirect (www.sciencedirect.com). That e-mail will include the article's Digital Object Identifier (DOI). This number provides the electronic link to the published article and should be included in the posting of your personal version. We ask that you wait until you receive this e-mail and have the DOI to do any posting.

Central Storage: This license does not include permission for a scanned version of the material to be stored in a central repository such as that provided by Heron/XanEdu.

18. **Author website** for books with the following additional clauses:
Authors are permitted to place a brief summary of their work online only.
A hyper-text must be included to the Elsevier homepage at http://www.elsevier.com . All content posted to the web site must maintain the copyright information line on the bottom of each image. You are not allowed to download and post the published electronic version of your chapter, nor may you scan the printed edition to create an electronic version.

Central Storage: This license does not include permission for a scanned version of the material to be stored in a central repository such as that provided by Heron/XanEdu.

19. **Website** (regular and for author): A hyper-text must be included to the Homepage of the journal from which you are licensing at http://www.sciencedirect.com/science/journal/xxxxx. or for books to the Elsevier homepage at http://www.elsevier.com

20. **Thesis/Dissertation**: If your license is for use in a thesis/dissertation your thesis may be

submitted to your institution in either print or electronic form. Should your thesis be published commercially, please reapply for permission. These requirements include permission for the Library and Archives of Canada to supply single copies, on demand, of the complete thesis and include permission for UMI to supply single copies, on demand, of the complete thesis. Should your thesis be published commercially, please reapply for permission.

21. **Other Conditions**: Permission is granted to submit your article in electronic format. This license permits you to post this Elsevier article online on your Institution's website if the content is embedded within your thesis. You are also permitted to post your Author Accepted Manuscript online however posting of the final published article is prohibited. Please refer to Elsevier's Posting Policy for further information:
http://www.elsevier.com/wps/find/authors.authors/postingpolicy

v1.6

If you would like to pay for this license now, please remit this license along with your payment made payable to "COPYRIGHT CLEARANCE CENTER" otherwise you will be invoiced within 48 hours of the license date. Payment should be in the form of a check or money order referencing your account number and this invoice number RLNK500803816.
Once you receive your invoice for this order, you may pay your invoice by credit card. Please follow instructions provided at that time.

Make Payment To:
Copyright Clearance Center
Dept 001
P.O. Box 843006
Boston, MA 02284-3006

For suggestions or comments regarding this order, contact RightsLink Customer Support: customercare@copyright.com or +1-877-622-5543 (toll free in the US) or +1-978-646-2777.

Gratis licenses (referencing $0 in the Total field) are free. Please retain this printable license for your reference. No payment is required.

From: "Goldweber, Paulette - Hoboken" <pgoldweb@wiley.com>
Subject: RE: Republication/Electronic Request Form
Date: July 2, 2012 3:47:54 PM EDT
To: "mjf258@cornell.edu" <mjf258@cornell.edu>

Dear Matthew:

Thank you for your request. John Wiley & Sons, Inc. has no objections to your proposed reuse of this material.

Permission is hereby granted for the use requested subject to the usual acknowledgements (title, volume number, issue number, year, page numbers. Copyright [year and owner]. And the statement “This material is reproduced with permission of John Wiley & Sons, Inc.”). Any third party material is expressly excluded from this permission. If any of the material you wish to use appears within our work with credit to another source, authorization from that source must be obtained.

This permission does not include the right to grant others permission to photocopy or otherwise reproduce this material except for accessible versions made by non-profit organizations serving the blind, visually impaired and other persons with print disabilities.

Sincerely,

Paulette Goldweber
Associate Manager, Permissions
Global Rights
John Wiley & Sons, Inc.
ph: 201-748-8765
f: 201-748-6008
pgoldweb@wiley.com

-----Original Message-----
From: PermissionsUS@wiley.com on www.wiley.com [mailto:webmaster@wiley.com]
Sent: Friday, June 29, 2012 10:04 AM
To: Permissions - US
Subject: Republication/Electronic Request Form

A01_First_Name: Matthew
A02_Last_Name: Farrar
A03_Company_Name: Cornell University
A04_Address: 526 Campus Rd., B54 Weill Hall
A05_City: Ithaca
A06_State: New York
A07_Zip: 14853
A08_Country: United States
A09_Contact_Phone_Number: 6072558102
A10_Fax:
A11_Emails: mjf258@cornell.edu
A12_Reference:
A13_Book_Title: Current Protocols in Neuroscience
A40_Book_or_Journal: Journal
A14_Book_Author:
A15_Book_ISBN:
A16_Journal_Month: May
A17_Journal_Year: 2001
A18_Journal_Volume: 3.17.1–3.17.9
A19_Journal_Issue_Number: n/a
A20_Copy_Pages: Figure 3.17.1
A21_Maximum_Copies: 350
A22_Your_Publisher: Cornell University
A23_Your_Title: NONLINEAR OPTICAL TECHNIQUES FOR IMAGING AND MANIPULATING THE MOUSE CENTRAL NERVOUS SYSTEM
A24_Publication_Date: August 2012
A25_Format: print,E-Book
A41_Ebook_Reader_Type: Adobe pdf
A26_If_WWW_URL:
A27_If_WWW_From_Adopted_Book:
A28_If_WWW_Password_Access:

A45_WWW_Users:
A29_If_WWW_Material_Posted_From:
A30_If_WWW_Material_Posted_To:
A42_If_Intranet_URL:
A32_If_Intranet_From_Adopted_Book:
A33_If_Intranet_Password_Access:
A48_Intranet_Users:
A34_If_Intranet_Material_Posted_From:
A35_If_Intranet_Material_Posted_To:
A50_If_Software_Print_Type:
A60_If_Other_Type:
A37_Comments_For_Request: Request for use of single figure in thesis. Article was published in print August 1999.